

Ministry of Higher Education and Scientific Research
Hassiba Benbouali University of Chlef
Faculty of Civil Engineering and Architecture
Department of Civil Engineering



THESIS

Submitted to obtain the diploma of

DOCTORATE 3RD CYCLE LMD

Speciality: **Civil Engineering**

Option: **Structures & Geotechnics**

By

Sabrina BENYETTOU ORIBI

Topic

Instability behaviour of steel beams with web openings under extreme fire conditions

(Comportement à l'instabilité de poutres métalliques à ouvertures d'âme sous des conditions extrêmes d'incendie)

Defended on 28/10/2023 in front of the jury composed of:

BRANCI Taieb	Professor	University of Chlef	Chairman
BENAROUS Abdallah	Professor	Université de Blida 1	Examiner
DJEBLI Benyagoub	MCA	University of Tiaret	Examiner
LAMRI Belkacem	Professor	University of Chlef	Rapporteur
KADA Abdelhak	MCA	University of Chlef	Co-Rapporteur
MESQUITA MR Luis	Professor	IPB (Portugal)	Invited

ACKNOWLEDGEMENT

First, all my praise and thanks are to the Almighty Allah, who has relentlessly blessed and protected me along this path. For countless sleepless nights, his sustaining grace brought me to the achievement of this milestone.

I want to take this opportunity to express my deepest gratitude to my supervisors, Prof. Belkacem LAMRI, Prof. Abdelhak KADA, and Prof. Luis Mesquita, for their unwavering support, invaluable advice, and guidance throughout the entire process of completing this work. I am grateful for their patience and understanding as I navigated my way through the research world. Special thanks to my PhD co-supervisor, Prof. Luis Mesquita, for not only welcoming me as a volunteer researcher at the Polytechnic Institution of Bragança (Portugal) but also for constantly pushing me to achieve more during our endless discussions and spirited debates. I am truly indebted to them for their encouragement and dedication, especially during the final stages of manuscript writing.

I would like to express my sincere gratitude to the members of the PhD committee, namely Prof. Branci Taieb, Prof. Benarous Abdallah, and Prof. Djebli Benyagoub, for graciously accepting the responsibility of evaluating my research.

I would like to express my sincere gratitude to the dedicated researchers, PhD candidates, designers, managers, technicians, engineers, and directors who played a crucial role in making my PhD journey in Algeria and Portugal successful. The ESTIG Department of IPB (Portugal) is undoubtedly a remarkable institution for collaborative research, where diverse perspectives are valued and ideas are carefully considered, debated, refined, and improved. Their unwavering support and warm hospitality greatly contributed to my academic growth and development.

On a more personal level, I would like to express my heartfelt gratitude to every single teacher who has ever taught me a letter, a lesson, a principle, or a moral attitude. I mention all my teachers inside and outside of my home university.

I would also like to thank the Ministry of Higher Education and Scientific Research (MESRS) of Algeria for their generous support in funding my PhD studies. Their contribution, with reference number 714/PNE/Doctorant/Portugal/2019-2020, has been invaluable and instrumental in completing my program. Thank you for investing in my education and future.

DEDICATIONS

بِسْمِ اللَّهِ الرَّحْمَنِ الرَّحِيمِ

In the name of ALLAH, the All- Beneficent, the Ever Merciful

This dissertation dedication is devoted first to the strongest person I know: me.

My parents are my biggest source of inspiration. I am grateful for your faith in me, even when I doubted myself. Your unconditional love, motivation, and prayer accompanied me through this arduous journey. This achievement would not have been achievable without your guidance and assistance. This work has a special fidelity to you. You have demonstrated that anything can be accomplished with hard work and dedication. Thanks for staying with me until the end of this work. I love you so much.

To my husband and his family, who have been an inestimable source of strength, support, and encouragement for me during this extended voyage. I am truly fortunate to have you as my partner on this journey of life.

I am forever grateful to my family, sisters, and brothers whose boundless love, encouragement, and support have guided me through the completion of my PhD journey. Your presence in my life has meant everything to me. To my dear friends Khadidja, Wahiba, Aziza, and Abetare, your unwavering support and strength have been an invaluable source of motivation during times of trial and challenge. Your friendship brings me solace and joy, and I cannot thank you enough. To all my other friends, I am filled with gratitude for your unwavering love and companionship throughout my journey. You hold a special place in my heart, and I am blessed to have you in my life. Thank you for being such amazing friends.

This entire work is also devoted to my supervisors, Prof. Belkacem LAMRI, Prof. Abdelhak KADA, and Prof. Luis MESQUITA, a sign of standing appreciation for their wise guidance, constructive feedback, and sincere support. Thanks a lot for your precious time and your direction, which enabled me to develop my capabilities and reach this satisfying destination.

My endless gratitude to each of you for making this journey special and memorable!

ABSTRACT

Recently, there has been an upswing in building construction that utilise sustainable designs and the effective use of raw materials. As a result, there has been a surge of research with the goal of optimising the geometrical configuration of web-opening steel sections to meet cost-effectiveness in structural design. There is still a need for research in improving the design method for perforated unrestrained steel beams to evaluate their behaviour in terms of lateral torsional buckling (LTB).

This research will delve into the behaviour of cellular beams that are at risk of instability-induced failure. Analysis of the beams using Eurocode will be conducted, along with numerical modelling using ANSYS software, to explore how they react to both room temperature and elevated temperatures. The study will also encompass the effect of the numerical coupling and the thickness of the endplates on the elastic and buckling simulations of the cellular beams, considering the initial geometric imperfections and material nonlinearities.

A parametric study was conducted to examine the effects of variations in temperature, cross-section geometry, and web aperture configurations for simply supported beams exposed to a uniform bending load and a distributed load. Buckling curves for cellular beams were determined by comparing FE reduction factors with those prescribed by Eurocode 3 parts 1 and 2 for the equivalent solid steel beams and Eurocode 3 parts 1–13 for cellular beams.

The study demonstrates that using numerical coupling in the elastic and buckling simulations cancels out local cross-section buckling, enabling the detection of the LTB mode without it being superimposed or combined with other buckling modes. On the other hand, in the parametric study, the analyses depicted the following failure modes at ambient and elevated temperatures: LTB and LTB+ plastification of the two T-section for end moments and yielding of the top tee section's flange, web post-buckling (WPB), Vierendeel mechanism (VM) and LTB for a distributed load. Other combined failure modes have also been observed.

For intermediate and high non-dimensional slenderness, the Eurocode 3 curve, using an equivalent solid beam, gives better predictions.

Considering the numerical results and Eurocode formulae, a new proposed formula for the plateau length of the LTB curves was obtained. The comparison of the predicted results using both numerical and simplified design methods reveals that the proposed formulae have reduced the discrepancy and enhanced the LTB curve to better assess the cellular beams' behaviour.

Keywords: Cellular beam, Instability, LTB, failure mode, Fire; Eurocodes, Numerical modelling; Imperfections; Residual stresses

RESUME

De nouveaux développements dans la construction de bâtiments ont été observés pour atteindre les critères de conception durable et l'utilisation efficace des matières premières. Cela a conduit à une augmentation des recherches récentes sur l'optimisation des configurations géométriques des sections en acier à ouverture d'âme pour répondre à la rentabilité dans la conception structurelle. L'amélioration de la méthode de conception des poutres en acier perforées non retenues pour évaluer leur comportement en cas de flambement latéral en torsion (LTB) reste un besoin de recherche.

Dans ce travail de recherche, les poutres cellulaires sujettes à la rupture en raison de l'instabilité seront étudiées analytiquement par l'Eurocode et numériquement par la méthode des éléments finis en utilisant le logiciel ANSYS pour étudier leur comportement à des températures ambiantes et élevées en raison du feu. L'étude comprendra également l'effet du couplage numérique et de l'épaisseur des plaques d'extrémité sur les simulations élastiques et de flambage des poutres cellulaires, en tenant compte des imperfections géométriques initiales et des non-linéarités des matériaux.

Une étude paramétrique a été réalisée sur la température, la géométrie de la section transversale et les configurations de l'ouverture de l'âme pour les poutres en appui simple soumises à une flexion uniforme et à une charge distribuée. Les courbes de flambement des poutres cellulaires ont été évaluées en comparant les facteurs de réduction FE avec ceux de la courbe de flambement recommandée par les deux premières parties de l'Eurocode 3 pour les poutres en acier solide équivalentes, et l'Eurocode 3 parties 1-13 pour les poutres cellulaires.

L'étude montre que l'utilisation du couplage numérique pendant les simulations élastiques et de flambement annule le flambement local de la section transversale et permet de capturer le mode LTB sans qu'il soit superposé ou combiné à d'autres modes de flambement. D'autre part, dans l'étude paramétrique, les analyses ont montré les modes de ruptures suivants à des températures ambiantes et élevées : LTB et LTB+ plastification des deux sections en T pour une charge de flexion uniforme et la plastification de la semelle de la section du té supérieur, flambement d'âme (WPB), mécanisme Vierendeel (VM) et LTB pour une charge répartie. D'autres modes de défaillance combinés ont également été observés. Pour un élancement intermédiaire et élevé, la courbe d'Eurocode 3, utilisant une poutre solide équivalente, donne de meilleures prédictions.

En considérant les résultats numériques et les formules d'Eurocode 3, une nouvelle formule proposée pour la longueur du plateau des courbes LTB a été obtenue. La comparaison entre les résultats numériques et les résultats prédits par la méthode de conception simplifiée montre que les formules proposées ont réduit la divergence et amélioré la courbe LTB pour mieux évaluer le comportement des poutres cellulaires.

Mots clés : Poutre cellulaire, Instabilité, LTB, Mode de ruine, Incendie ; Eurocodes, Modélisation numérique ; Imperfections ; Contraintes résiduelles.

ملخص

تمت ملاحظة التطورات الجديدة في تشييد المباني لتحقيق معايير التصميم المستدام والاستخدام الفعال للمواد الخام. أدى ذلك إلى زيادة في الأبحاث الحديثة حول تحسين التكوينات الهندسية للعوارض الفولاذية ذات فتحات لتلبية الفعالية من حيث التكلفة في التصميم الإنشائي. لا يزال تحسين طريقة تصميم العوارض الفولاذية غير المقيدة والتي تحتوي على فتحات لتقييم سلوكها في ظل الالتواء الجانبي (LTB) حاجة بحثية.

في هذا البحث، ستتم دراسة العوارض الفولاذية المعرضة للفشل بسبب عدم الاستقرار تحليليًا بواسطة Eurocode و عددًا بطريقة العناصر المحدودة باستخدام برنامج ANSYS للتحقق من سلوكها في درجات الحرارة المحيطة والمرتفعة بسبب الحريق. ستشمل الدراسة أيضًا تأثير الاقتران العددي وسماكة الصفائح النهائية على المحاكاة المرنة والالتواء للعوارض الفولاذية، مع الأخذ في الاعتبار العيوب الهندسية الأولية وعدم خطية المادة.

تم إجراء دراسة بارامترية على درجة الحرارة وهندسة المقطع العرضي وخصائص الفتحات للعوارض المدعومة ببساطة والمعرضة لعزم دوران متساوي أو حمولة موزعة بشكل متجانس. تم تقييم منحنيات الالتواء للعوارض الفولاذية من خلال مقارنة عوامل اختزال FE مع تلك الخاصة بمنحني الالتواء الموصي به من قبل الجزأين الأولين من EUROCODE 3 للحزم الفولاذية الصلبة المكافئة، و Eurocode 3 part 1-13 للحزم الفولاذية ذات فتحات.

تُظهر الدراسة أن استخدام الاقتران العددي أثناء عمليتي كل من المحاكاة المرنة والالتواء، يلغي الالتواء المحلي للمقطع العرضي، ويسمح بالتقاط وضع LTB دون تراكمه أو دمج مع أوضاع التواء أخرى. من ناحية أخرى، في الدراسة البارامترية، نتج عن التحليلات أوضاع الفشل التالية في درجات الحرارة المحيطة والمرتفعة: LTB و (P+2T) + LTB plastification عند تطبيق عزم الدوران، ولدونة شفة المقطع ال Tee العلوي (B-1T)، التواء على مستوى اللوحات العرضية ما بين الفتحات (WPB) وآلية (VM) Vierendeel و LTB للحمل الموزع. كما لوحظت أنماط فشل مجتمعة أخرى. بالنسبة إلى للعوارض الفولاذية ذات نحافة متوسطة وعالية، يوفر منحني Eurocode 3، باستخدام عوارض صلبة مكافئة، تنبؤات أفضل.

بالنظر إلى النتائج العددية وصيغ Eurocode، تم الحصول على صيغة مقترحة جديدة ل plateau length لمنحنيات LTB. تُظهر المقارنة بين النتائج المتوقعة لطريقة التصميم الرقمية والمبسطة أن الصيغ المقترحة قللت من التناقض وحسنت منحني LTB لتقييم سلوك العوارض الفولاذية ذات فتحات بشكل أفضل.

كلمات مفتاحية: عوارض ذات فتحات متعددة؛ عدم الاستقرار؛ LTB؛ وضع الفشل؛ النار؛ Eurocodes؛ النمذجة الرقمية؛ العيوب؛ الضغوط المتبقية.

PUBLICATIONS

The current PhD research has resulted in the following journal papers, and international and national conference papers:

Journal papers

1. Benyettou Oribi, S., Kada, A., Lamri, B., Mesquita, L.M., "Investigation of residual stresses on the fire resistance of unrestrained cellular beams", *ce/papers* 4(2-4) (2021) 1386-1394. <https://doi.org/10.1002/cepa.1436>.
2. Benyettou Oribi, S., Kada, A., Lamri, B., Mesquita, L., "Behaviour of cellular steel beams at ambient and high-temperature conditions", *Journal of Constructional Steel Research* 207 (2023) 107969. <https://doi.org/10.1016/j.jcsr.2023.107969>.

International Conferences

1. Benyettou Oribi, S., Kada, A., Lamri, B., "Investigation sur le comportement des poutres d'acier sous l'effet des températures élevées", 2^{ème} Conférence Internationale de Construction Métallique et Mixte, (CICOMM-2018), Alger, Algérie, 9-10/10/2018.
2. Benyettou Oribi, S., Kada, A., Lamri, B., "Modélisation numérique du comportement non linéaire des poutres mixtes sous l'effet d'un incendie", 8^{ème} Symposium International sur la Construction en Zones Sismiques, (SICZS-2018), Chlef, Algérie, 13/10/2018.
3. Benyettou Oribi, S., Kada, A., Lamri, B., Mesquita, L., "Numerical analysis of lateral torsional buckling of steel I-beams with and without web-openings under fire", 5th IBERIAN-LATIN AMERICAN CONGRESS ON FIRE SAFETY (5 CILASCI), Porto, Portugal, 15-16/07/2019, P. 893-903.
4. Benyettou Oribi, S., Kada, A., Lamri, B., Mesquita, L., "Investigation of residual stresses on the fire resistance of unrestrained cellular beams", The 9th European Conference on Steel and Composite Structures, Euro steel SHEFFIELD 2021, Sheffield, England, 1-3/09/2021.
5. Benyettou Oribi, S., Kada, A., Lamri, B., Mesquita, L., "Influence of initial imperfections on the lateral torsional buckling of cellular beams under fire", 3^{ème} Conférence Internationale de Construction Métallique et Mixte CICOMM'2023, Oran, Algeria, 13-14/03/2023.

National Conferences

1. Benyettou Oribi, S., Kada, A., and Lamri, B., "Investigation du comportement de poutres de plancher mixte a ouvertures d'âme sous des conditions extrêmes d'incendie", 2`emes journées des doctorants de la faculté de GCA, 18/05/2017, Chef, Algeria.
2. Benyettou Oribi, S., Kada, A., and Lamri, B., "Investigation du comportement de poutres de plancher mixte a ouvertures d'âme sous des conditions extrêmes d'incendie", 3`emes journées des doctorants de la faculté de GCA, 20/06/2018, Chef, Algeria.

CONTENTS

ACKNOWLEDGEMENT	iii
DEDICATIONS	iii
ABSTRACT	v
RESUME	vii
ملخص	ix
PUBLICATIONS	x
CONTENTS.....	xii
LIST OF FIGURES	xvi
LIST OF TABLES	xix
LIST OF SYMBOLS	xx
LIST OF ACRONYMS	xxvii
GENERAL INTRODUCTION.....	1
1.1. Motivation and Background	2
1.2. Objectives & Research questions	3
1.3. Limitations	4
1.4. Dissertation summary	4
CHAPTER 1. LITERATURE REVIEW	6
1.1. Overview of steel cellular beams	7
1.2. Production process	8
1.3. Factors influencing stability of steel beams: Geometric and material imperfections. 11	
1.3.1. Geometric imperfections	11
1.3.2. Structural imperfection: Residual stress	14
1.4. Instability modes of cellular beams.....	19

1.4.1.	Global bending mechanism	20
1.4.2.	Global shear mechanism.....	21
1.4.3.	Lateral torsional buckling	21
1.4.4.	Vierendeel mechanism VM	23
1.4.5.	Web-post horizontal shear	24
1.4.6.	Web-post buckling	25
1.4.7.	Web-post crippling due to compression	26
1.4.8.	Rupture of a welded joint in a web post	26
1.5.	Finite element method FEM	27
1.6.	State of research on the instability behaviour of steel beams with web openings under extreme fire conditions	30
CHAPTER 2. FIRE SAFETY AND STEEL STRUCTURES		35
2.1.	Overview of Fire	36
2.2.	Fire modelling: the ISO-834 standard fire curve	38
2.3.	Properties of steel structures at high temperature	40
2.3.1.	Mechanical properties	40
2.3.2.	Thermal properties	44
2.4.	Analysis of temperature changes in steel.....	47
2.5.	Fire resistance verification.....	48
2.6.	Design rules for the resistance of steel solid and cellular beams	49
2.6.1.	Design guidelines	49
2.6.2.	Geometric properties of gross and net cross-sections	50
2.6.3.	Classification of cross-sections.....	54
2.6.4.	Design resistance at ambient temperature	57
2.6.5.	Design resistance at elevated temperature.....	66
CHAPTER 3. SIMULATION AND ANALYSIS OF STEEL SOLID AND CELLULAR BEAMS IN ANSYS		69
3.1.	Methodology	70
3.2.	Parametric analysis and case studies _ Model 1	70
3.3.	Parametric analysis and case studies _ Model 2	72
3.3.1.	Assumptions.....	73
3.3.2.	Geometric parameters of studied cases	73
3.4.	Numerical model, boundary conditions, and imperfections	75

3.4.1. Model I	75
3.4.2. Model II	78
3.5. Influence of web openings on critical temperature and displacement of steel beams _ Model I	86
3.6. Investigations on beams with multiple web openings in a fire situation with and without imperfections _ Model I	87
3.7. Imperfections and residual stresses' effects on cellular beam LTB _ Model I	89
3.8. Effect of profile section geometry.....	91
3.9. Study of the effect of residual stresses on the fire resistance of unrestrained cellular beams _ Model II	92
CHAPTER 4. ANALYSIS FOR GLOBAL LT BUCKLING AND INTERACTING FAILURE MODES	99
4.1. Introduction.....	100
4.2. LTB elastic critical moment.....	100
4.3. Effects of coupling and end plates' thickness on the collapse resistance of cellular beams 102	
4.4. Buckling curves and normalised moment resistance	105
4.5. LTB behaviour and failure modes at ambient temperature	106
4.6. LTB behaviour and failure modes under fire condition	116
4.7. Development of a new plateau length of the LTB curves for cellular beams	126
4.8. Comparison of Eurocode and proposed methods for LTB resistance of a cellular beam under distributed load	129
GENERAL CONCLUSION	132
5.1. General conclusion	133
5.2. Suggestions for future research.....	135
BIBLIOGRAPHY	136
ANNEXES	146
ANNEX A. Elastic critical moment of cellular beams_DL.....	147
ANNEX B. Von mises stress distribution of steel beams - end moment load.....	155
ANNEX C. Von mises stress distribution of solid beams - distributed load.....	172

LIST OF FIGURES

Figure 1-1. Fabrication process of steel cellular beams [11].	9
Figure 1-2. Steel beams with different opening shapes [12].	10
Figure 1-3. Geometric imperfections: a) Global, b-c) local [20].	12
Figure 1-4. Residual stress distribution for hot-rolled members, a) proposed by ECCS in [35], b-c) model proposed in 1998. Extracted from [13].	16
Figure 1-5. Residual stress distribution for hot-rolled members proposed by the ECCS in [39]. Extracted from [10].	17
Figure 1-6. proposed residual stress patterns for cellular and castellated members [10].	18
Figure 1-7. Residual stress distribution models, a) for solid beam, b-c) for cellular beam.	19
Figure 1-8. Global bending mechanism in perforated beams [53].	21
Figure 1-9. Shear failure of the perforated cross-section [2].	21
Figure 1-10. Pure lateral torsional buckling failure mode in steel cellular beam [57].	22
Figure 1-11. The 1T and 2T approaches for the calculation of the lateral-torsional buckling resistance of steel cellular beam [10].	22
Figure 1-12. Vierendeel failure mode [61], b-c) plastic hinges, Vierendeel bending and effective length [62].	23
Figure 1-13. Web-post yielding due to horizontal shear [55].	24
Figure 1-14. a) Double curvature of the web-post interpreted as web-post buckling [63], b) Stresses identified on the web-post [55], c) Effective length for closely spaced openings [3].	25
Figure 1-15. Web-post crippling due to compression [65].	26
Figure 1-16. Rupture of a welded joint in a web post [45].	27
Figure 1-17. a) A finite element model of a prosthetic hand for weightlifting. b) Completed prototype of a prosthetic hand, attached to a bar. Extracted from [67].	28
Figure 2-1. The four stages of fire development.	37
Figure 2-2. Standard and hydrocarbon fire curves	40
Figure 2-3. stress strain relationship for steel at elevated temperature (reproduced from Eurocode 3 part 1-2 [4])	42
Figure 2-4. Reduction factors for the strain-stress relationship of carbon steel at elevated temperature (reproduced from [4])	43
Figure 2-5. Stress- strain relationship of carbon steel S355 at elevated temperature.	44
Figure 2-6. Temperature-dependent relative thermal elongation of carbon steel	45

Figure 2-7. Specific heat of carbon steel as a function of the temperature	46
Figure 2-8. Thermal conductivity of carbon steel as a function of the temperature	47
Figure 2-9. Geometric properties of cellular steel beams	50
Figure 2-10. Maximum width-to-thickness ratios for compression parts.....	55
Figure 2-11. Internal forces and moments acting on Tees.....	65
Figure 2-12. Top left quarter of model section.	65
Figure 3-1. Geometric parameters of the studied beams, cellular beam with ACB+ adaptation.	71
Figure 3-2. Geometric parameters of parent sections: (a) 610UB101, (b) IPE600.....	71
Figure 3-3. IPE450, cross-section geometric dimensions (mm).	72
Figure 3-4. SHELL181 element geometry [6].....	75
Figure 3-5. Stress-strain relationships for carbon steel at high temperatures (a) S430, (b) S275.	76
Figure 3-6. Finite element models of cellular beam: (a) with distributed load, (b) with end moment.	77
Figure 3-7. Displacement vs. time of Pin-rolled steel beam.....	78
Figure 3-8. Mesh configuration of FEM and boundary conditions for IPE base profile cellular steel beams ($L = 3$ m, $H/h=1.4$, $a_0/h = 1.2$, and $S/a_0=1.4$)	80
Figure 3-9. Pure bending moments	80
Figure 3-10. Geometric imperfections in (a) solid beam, (b) cellular beam.	81
Figure 3-11. Residual stress distributions of rolled sections, S355: (a) solid beam; $H=1.3$ h, (b) cellular beam; $H=1.3$ h, $a_0=0.8$ h.	82
Figure 3-12. Layout and organization of the finite element model implemented in ANSYS. .	83
Figure 3-13. Sketch of LTB test according to Sonck et al. [24].	84
Figure 3-14. Comparison between numerical and experimental tests. Load versus vertical displacement.....	85
Figure 3-15. Studied steel beams from left to right, P1, P2, P3, respectively.....	86
Figure 3-16. Mid-span vertical displacement vs. temperature.....	87
Figure 3-17. Cellular beam and equivalent hexagonal beam.....	88
Figure 3-18. Vertical displacement vs. critical temperature under ISO834 fire.	89
Figure 3-19. Moment resistances of cellular beam vs. temperatures, (a) with end moment load, (b) with distributed load.....	90
Figure 3-20. Vertical (VD) and lateral displacements (LD) of cellular beams vs. temperature: (a) with an End moment, (b) with a distributed load.....	91

Figure 3-21. Influence of profile section geometry, (a) $L=3$ m, (b) $L=8$ m.	92
Figure 3-22. Lateral torsional buckling resistance with different openings spacing $H/h = 1.3$, $a_0/h = 0.8$, $S/a_0 = 1.1, 1.4, 1.7$	94
Figure 3-23. Lateral [LD] and vertical [VD] displacements of cellular beams as a function of applied load with $H/h = 1.3$, $a_0/h = 0.8$, $S/a_0 = 1.1$	95
Figure 3-24. LTB moment resistance of cellular beams varying in height with $a_0/h = 0.8$, $S/a_0 = 1.1$	96
Figure 3-25. LTB moment resistance of cellular beam varying in opening diameter $a_0/h = 0.8, 1.0, 1.2$	97
Figure 3-26. Analytical and numerical LTB elastic critical moments percental differences for solid and cellular beams at $\theta = 20^\circ\text{C}$ and $\theta = 500, 700^\circ\text{C}$	102
Figure 4-1. Comparison between numerical normalized collapse moments and LTB analytical reduction factors versus non-dimensional slenderness at $\theta = 20^\circ\text{C}$	107
Figure 4-2. Detected failure modes.	110
Figure 4-3. Normalized FE collapse moment resistances versus vertical displacements of cellular beams at ambient temperature.	110
Figure 4-4. (a) Collapse moment resistance against cellular beam lengths at $\theta = 20^\circ\text{C}$ with $H/h = 1.3, 1.4$, and 1.5 ; $a_0/h = 1.2$; $S/a_0 = 1.4$. (b) Corresponding Von misses stress at failure for cellular beams with L of 3, 5, and 8 m.	113
Figure 4-5. Comparison between numerical and analytical reduction factors for LTB against non-dimensional slenderness (a-b) at $\theta = 500^\circ\text{C}$, (c-d) at $\theta = 700^\circ\text{C}$	118
Figure 4-6. Detected failure modes at $\theta = 500^\circ\text{C}$	120
Figure 4-7. Detected failure modes at $\theta = 700^\circ\text{C}$	121
Figure 4-8. (a) LTB moment resistance versus cellular beam length at $\theta = 500^\circ\text{C}$ with $H/h = 1.3, 1.4$, and 1.5 ; $a_0/h = 1.2$; $S/a_0 = 1.4$. (b) Corresponding Von misses stress at failure for cellular beams with L of 3, 5, 8 m from left to right.	122
Figure 4-9. (a) LTB moment resistance versus cellular beam length at $\theta = 700^\circ\text{C}$ with $H/h = 1.3, 1.4$, and 1.5 ; $a_0/h = 1.2$; $S/a_0 = 1.4$. (b) Corresponding Von misses stress at failure for cellular beams with L of 3, 5, 8 m from left to right.	123
Figure 4-10. Comparisons of numerical results, analytical results predicted by the Eurocode 3 (in red colour), and theoretical results predicted by the proposed equation (in blue colour).	129
Figure 4-12. Comparison between the proposed and the EC3 methods for a cellular beam with $H/h = 1.3$, $a_0/h = 1.0$, $S/a_0 = 1.7$	130

LIST OF TABLES

Table 1-1. Application-specific variations in geometrical dimensions of cellular beams [1]. ...8	8
Table 2-1. The relationship between stress and strain for carbon steel at elevated temperatures (reproduced from [4])	41
Table 2-2. Reduction factors for stress-strain relationship of carbon steel at elevated temperatures (reproduced from EN 1993-1-2 [4])	42
Table 2-3. Maximum width-to-thickness ratios for compression parts.....	55
Table 2-4. Recommended values for imperfection factors for lateral torsional buckling curves [3]	59
Table 2-5. Recommended values for lateral torsional buckling curves for cross-sections [3] ..	59
Table 2-6. Values of factors C1, C2, and C3 for moment diagrams due to type of load and support conditions [103]	61
Table 2-7. Values of the severity factor, β	67
Table 2-8. Correction factors k_c for the new proposal [22].....	67
Table 3-1. Geometric characteristics of the studied cases	72
Table 3-2. Geometric and loading data for solid and cellular steel beam cases.	74
Table 3-3. Properties of the steel 610UB101 cross-section.....	77
Table 3-4. Comparison between the reference model and FE model results	78
Table 3-5. Mesh sensitivity analysis, cases with $H/h = 1.3h$, $a_0/h = 0.8$, $S/a_0 = 1.1$, $L = 5$.m	79
Table 3-6. Geometric details of test specimens	85
Table 3-7. Vertical displacements and critical temperatures of the simulated beams.	86
Table 3-8. Displacements and critical temperatures of the different beams studied.....	88
Table 3-9. LTB moment resistance of cellular beams with and without residual stresses from numerical results, $H/h = 1.3$, $a_0/h = 0.8$, and $S/a_0 = 1.1$	93
Table 3-10. Effect of coupling, thickness, and existence of end plates, on the CB's collapse mode.	104
Table 4-1. Summary of the failure modes related to the investigated cases at ambient temperature.....	114
Table 4-2. Summary of the failure modes related to the investigated cases at $\theta = 500$ °C.	124
Table 4-3. Summary of the failure modes related to the investigated cases at $\theta = 700$ °C	125
Table 4-4. Performance ratio between FE and predicted results for $H/h = 1.3$	128
Table 4-5. Cellular beam design verification.....	129

LIST OF SYMBOLS

Latin letters

Ambient condition

a_0	Overall length of an opening; web opening diameter
A	Cross-sectional area of I section
A_f	Area of one flange
A_w	Area of a web
A_{wT}	The cross-sectional area of web of the Tee
A_T	Cross sectional area of one Tee section
A_v	Shear area for rolled I and H sections, load parallel to web
$A_{v,T}$	Shear area for rolled Tee section
$A_{\phi,f}$	The cross-sectional area of the flange of the inclined Tee
$A_{\phi,wT}$	The cross-sectional area of web of the inclined Tee
$A_{\phi,T}$	The cross-sectional area of the inclined Tee
$A_{\phi,v}$	Shear area for rolled inclined Tee section
a_t	The ratio of the effective length of the Tee at the opening
b	The overall breadth, width of a cross section
b_s	Length of sinusoidal part of opening
c	Factor depending on f_y
C	The width of a part of a cross-section
C_1	Factor depending on the loading
C_2	Factor depending on the end restraint conditions
d	Depth of straight portion of a web measured from the root radius
d_0	Overall length of an opening; web opening diameter
d'	The distance between centroid of the top and the bottom Tee sections along the vertical centre line
d_t	Depth of outstand of Tee section measured from the root radius
E	Modulus of elasticity
$\{F\}$	Force vector
$\{F_a\}$	Vector of the applied loads
$\{F_t^{nr}\}$	Vector of restoring loads corresponding to the element internal loads
f	Modification factor for χ_{LT}

f_y	The yield strength at 20 [°C]
$f_{y,f}$	The yield strength of the top and bottom flanges
$f_{y,w}$	The yield strength of the web
G	Shear modulus
H	The final height of the cellular beam
h	Depth of a parent cross section
h_ϕ	The height of the inclined Tee section
h_0	Depth of opening (or diameter of circular opening)
h_w	Web depth of sloid web section
h_{wT}	Web depth of one Tee-section
i	Subscript representing the current equilibrium iteration
I_y	Second moment of area about the major axis y-y
$I_{y,2T}$	Second moment of area of 2T sections at an opening about the major axis y-y
I_z	Second moment of area about the minor axis z-z
$I_{z,2T}$	Second moment of area of 2T sections at an opening about the minor axis z-z
I_w	Warping constant
$I_{w,2T}$	Warping constant for 2T sections
I_t	St. Venant torsional constant
$I_{t,2T}$	St. Venant torsional constant for 2T sections
$[K]$	Stiffness matrix
$\{K_i^T\}$	Jacobian stiffness matrix
k_c	Correction factor for moment distribution
L	Total beam length
l_e	Effective width: the length subject to buckling
l_f	The distance between loads
$M_{b,Rd}$	Design buckling resistance moment
M_{cr}	Elastic critical moment for lateral-torsional buckling
M_{Ed}	Design bending moment
$M_{Ed}(x)$	Design bending moment at a distance x from the support
M_{EC3}	Eurocode Moment resistance
M_{FE}	Numerical moment resistance
$M_{\phi,Ed}$	Design value of the bending moment in the Tee section at an angle ϕ from the vertical centre line

M_{Rd}	The plastic moment resistance of the gross cross-section $M_{pl,Rd}$ For normal temperature design
$M_{c,Rd}$	Design resistance for bending about one principal axis of the gross section
$M_{el,Rd}$	The elastic moment resistance
$M_{pl,Rd,2T}$	Design plastic bending resistance of two Tee
$M_{\phi,Rd,1T}$	The moment resistance resisting the Vierendeel moment in the Tee section at an angle ϕ from the vertical centre line
$M_{wp,Rd}$	The design resistance of the web-post
n	Number of openings along the beam
N_{Ed}	Design normal force
$N_{\phi,Ed}$	Design value of the axial force in the Tee section at an angle ϕ from the vertical centre line
$N_{Rd,1T}$	Design values of the resistance to normal forces
$N_{\phi,Rd,1T}$	The axial force resistance of the Tee section at an angle ϕ from the vertical centre line
$N_{wp,Rd}$	Web-post buckling resistance
r	Root radius
[S]	Stress stiffness matrix
S	Centre to centre spacing of adjacent openings
S_0	Edge to edge spacing of openings (= S-a ₀)
S_e	Width of end post between the connection and the nearer edge of the first Opening
t	Time
t_f	Flange thickness
t_w	Web thickness
{u}	Nodal displacement vector
$V_{pl,Rd}$	Design plastic shear resistance
$V_{pl,Rd,2T}$	Design plastic shear resistance of the two Tee section
$V_{\phi,pl,Rd}$	The design plastic shear resistance of the Tee section at an angle ϕ from the vertical centre line
V_{Ed}	Design shear force
$V_{Ed}(x)$	Design value of the shear force acting on the beam at the opening
$V_{\phi,Ed}$	Design value of the shear force in the Tee section at an angle ϕ from the

	vertical centre line
$V_{wp,Rd}$	The design longitudinal shear resistance of the web-post
w	Edge-to-edge spacing of openings ($= S - a_0$)
w_0	Width of end post between the connection and the nearer edge of the first opening
$W_{pl,y}$	Plastic section modulus
$W_{pl,y,2T}$	Plastic section modulus of perforated section
$W_{\phi,pl,1T}$	Plastic section modulus of the inclined Tee section
x	Distance between the end support and the vertical centre line of the opening
\bar{y}	The distance from the top edge to centroid of the Tee section along the vertical centre line of the hole
\bar{y}_{ϕ}	The distance from the top edge to centroid of the inclined Tee section along the vertical centre line of the hole
Z_c	The distance from the local centroid of the area of one Tee to the global centroid
Z_{pl}	The distance between the plastic neutral axis and the extreme fibre of the steel flange of a Tee section
$Z_{\phi,pl}$	The distance between the plastic neutral axis and the extreme fibre of the steel flange of the inclined Tee

Fire condition

A_m	The surface area of the member
C_a	Specific heat of steel
$E_{a,\theta}$	The slope of the linear elastic range for steel at elevated temperature θ_a
$E_{fi,d,t}$	The design effect of actions for the fire situation, determined in accordance with EN 1991-1-2, including the effects of thermal expansions and deformations;
f	Modification factor for $\chi_{LT,fi}$
$f_{p,\theta}$	The proportional limit for steel at elevated temperature θ_a
$f_{y,\theta}$	The effective yield strength of steel at elevated temperature θ_a
$\dot{h}_{net,c}$	Heat transfer by convection
$\dot{h}_{net,d}$	The design value of the net heat flux
$\dot{h}_{net,r}$	Heat transfer by radiation
k_c	Correction factor for moment distribution

$k_{E,\theta}$	Slope of linear elastic range at the steel temperature θ_a reached at time t
$k_{E,\theta.com}$	The reduction factor for the slope of the linear elastic range at the maximum steel temperature in the compression flange $\theta_{a.com}$ Reached at time t .
$K_{p,\theta}$	Proportional limit relative to yield strength at at the steel temperature θ_a
k_{sh}	Correction factor for the shadow effect
$k_{y,\theta}$	The reduction factor for the yield strength of steel at the steel temperature θ_a , reached at time t
$k_{y,\theta.com}$	The reduction factor for the yield strength of steel at the maximum temperature in the compression flange $\theta_{a.com}$ Reached at time t .
$M_{b.fi.t.Rd}$	The design buckling resistance moment at time t .
$M_{fi.\theta.Rd}$	The design moment resistance of the cross-section for a uniform temperature θ_a Which is equal to the uniform temperature θ_a At time t in a cross-section which is not thermally influenced by the supports.
$M_{fi.\theta.Rd.2T}$	Design plastic bending resistance of two Tee for a uniform temperature θ_a
$M_{fi.t.Rd}$	The design moment resistance at time t
$N_{fi.\theta.Rd}$	The design resistance of a tension member for a uniform temperature θ_a
$R_{fi.d.t}$	The corresponding design resistance in the fire situation.
$t_{fi,d}$	The design value of the fire resistance
$t_{fi,requ}$	The required fire resistance time
V	The volume of the member
$V_{fi.t.Rd}$	The design shear resistance at time t
$V_{fi.t.Rd.2T}$	The design shear resistance at time t of two Tee section

Greek letters

Ambient condition

α_{LT}	Imperfection factor
β	Correction factor for the lateral torsional buckling curves for rolled and welded sections
γ_{M0}	Partial factor for resistance of cross-sections whatever the class is
γ_{M1}	Partial factor for resistance of members to instability assessed by member checks
Δu_i	A correction of the current displacement vector $\{u_i\}$
ε	Factor depending on f_y

λ_1	The slenderness value to determine the relative slenderness
λ_i	The eigenvalue of number i
$\bar{\lambda}$	Non dimensional slenderness
$\bar{\lambda}_{LT}$	Non dimensional slenderness for lateral torsional buckling
$\bar{\lambda}_{LT,0}$	Plateau length of the lateral torsional buckling curves for rolled and welded sections
ν	The Poisson coefficient
$\sigma_{\text{compression}}$	Residual stress in compression
σ_{c1}	The compressive stress at the flange tips
σ_{c2}	The compressive stress in the center of the web
$\sigma_{\text{res,max}}$	Maximum residual stresses
$\sigma_{\text{res,web}}$	Tension residual stress in the web
σ_t	The tensile stress at the web to flange junction
σ_{tension}	Residual stress in tension
ν	Poisson's ratio in elastic stage
ϕ	Angle in which the location of the critical section
Φ	A value for determining the χ coefficient
Φ_{LT}	Value to determine the reduction factor χ_{LT}
χ_{LT}	Reduction factor for lateral-torsional buckling.
$\chi_{LT,mod}$	Modified reduction factor for lateral-torsional buckling
ψ	Ratio of moments in segment
$\{\psi\}_i$	Eigenvector of displacement of number i

Fire condition

α	Imperfection factor
α_c	Coefficient of heat transfer by convection
$\gamma_{M,fi}$	The partial factor for the relevant material property, for the fire situation.
Δl	The temperature induced expansion
Δt	The time interval
$\Delta\theta_{a,t}$	The increase of temperature during the time interval Δt
ε_f	The emissivity of the fire
ε_m	The surface emissivity of the member
$\varepsilon_{y,\theta}$	Yield strain
$\varepsilon_{u,\theta}$	Ultimate strain

$\varepsilon_{t,\theta}$	Limiting strain for yield strength
θ	The temperature
θ_a	The steel temperature [$^{\circ}\text{C}$].
$\theta_{cr,d}$	The design value of the critical material temperature
θ_d	The design value of material temperature
θ_g	Gas temperature in the fire compartment
θ_m	The surface temperature of the member
θ_r	The effective radiation temperature of the fire environment
λ_a	The thermal conductivity of steel
$\bar{\lambda}_{LT,\theta.com}$	Non dimensional slenderness for lateral torsional buckling in the fire design situation
ρ	Unit mass of steel
σ	The Stephan Boltzmann constant
Φ	The configuration factor
$\Phi_{LT,\theta.com}$	Value to determine the reduction factor χ_{LT} In the fire design situation
$\chi_{LT,fi}$	The reduction factor for lateral-torsional buckling in the fire design situation
$\chi_{LT,fi.mod}$	Modified reduction factor for lateral-torsional buckling
Ψ	Ratio between the moments applied in the extremities

LIST OF ACRONYMS

BEM	Boundary element method
B-1T	Bending of the top tee section's flange
CE	Couples' node to node degrees of freedom. Master node dof's are independent and slave nodes dof's are dependent. Rigid connection.
CP	Directly Couples the node-to-node degrees of freedom. The prime node's dof during matrix formulation are used and dof's of other node ignored.
CEN	European Committee for Standardization
CSBS	Cellular steel beams
D	Distributed load
Diff (%)	Percentage difference
DOF	Degree of freedom
EC3	Eurocode 3
ECCS	European Convention for Constructional Steelwork
EN	European standard
ENV	European pre-standard
EP	End plate
EXP	Experimental
F	Load
FE	Finite element
FEA	Finite element analysis
FDM	Finite difference method
FEM	Finite element method
FVM	Finite volume method
HC	Hydrocarbon curve
ISO 834	Conventional fire curve
LD	Lateral displacement
LTB	Lateral-torsional buckling
M	End moment load
NLGMA	Non-linear geometric analysis

P-2T	Plastification of two tee sections
PrEN	European pre-standard
Py	Plastic yielding
q	Load
ROT	Rotation
SCI	Steel construction institute
1T	One tee section
2T	Two tee section
TS	Tee section
U	Displacement
VD	Vertical displacement
VM	Vierendeel mechanism
W/CP	With coupling procedure
W/EP.1t _f	With end plates of thickness 1t _f
W/EP.2t _f	With end plates of thickness 2t _f
W/O.CP	Without coupling procedure
W/O.EP	Without endplate
WB	Web buckling
WP	Web post
WPB	Web-post buckling
WPBS	Web-post buckling by shear

GENERAL INTRODUCTION

1.1. Motivation and Background

Today, with the ameliorations implemented in the design standards, analysis tools and manufacturing, cellular steel beams bring sustainable and innovative alternative solutions for modern building construction to achieve longer spans and open spaces, plus the extra benefit of enclosing integrated services in the beam's depth.

This type of beam is fabricated by thermally cutting and rearranging European hot-rolled sections, resulting in two shifted sections that create evenly spaced round web openings. The resulting beam is generally 40–50% deeper than the parent section, with 50% higher section modulus and bearing capacity, 125% heightened inertia, and stiffness, while maintaining the same overall weight [1]. The size of the openings depends on the specific application and structural requirements. This leads to fewer floor zones and simplifies construction, allowing the structure to remain elegant, and making the installation of mechanical and electrical services easier.

However, it must be considered that the presence of these openings in the web of the beam affects their failure behaviour and can lead to new failure modes, such as buckling of the web post between openings or yielding around the openings in a Vierendeel mechanism or altering the modes that already exist in beams without openings, named as solid beams, such as the beam's lateral torsional buckling, LTB. Therefore, a thorough study of its behaviour is required as its performance depends on beam properties such as geometry, fabrication, and installation quality.

Although this kind of beam is increasingly being used around the world, cellular beam design is not covered in detail in Eurocode 3, a standard created to address steel structure and components designs. Thus, the designer must rely on the manufacturer's manuals or scientific studies to elaborate the calculations. There is still no reliable codified design method for beams with web openings. A codified design guide was provided in National Annex N of ENV 1993-1-1:1992/A2:1998 [2], which was later superseded due to reliability issues. To remedy this deficiency, there is a proposal to supplement the standard, Eurocode 3 part 1-13 [3], which deals with the design of rolled and fabricated steel beam sections with openings in the web, but it is not yet in use.

Steel beam members require a base level of resistance against fire [4] to prevent precocious failure when unprotected and if this is not met the sections for solid beams may be protected. A new normative appendix, Annex F, on Beams with Large Web Openings, is included in the

updated first draft of prEN 1993-1-2 [5], in which the section factors for the cellular beam's different failure modes in the fire were the focal point. Nevertheless, no provision was made for the LTB mechanical response under fire considering geometric imperfections effects, residual stresses, material, and geometric nonlinearities. Therefore, the goal of this research work is to understand and analyse the behaviour, resistance, and modes of instability of such beams in normal and fire conditions, with a focus on the lateral torsional buckling failure mode, thereby increasing knowledge about this topic and possibly contributing to the future standardization of this type of structural element.

1.2. Objectives & Research questions

There is a need for more research on the LTB resistance of cellular steel beams and especially when failure modes and their interaction are to be considered and when the adequate LTB curve is chosen.

In this dissertation, numerical models will be developed to predict the instability behaviour, especially the lateral torsional buckling, LTB, of unrestrained cellular steel beams and their effective solid beams at ambient temperature and increasing elevated temperatures due to fire. The study also will be focused on the depicted interacting failure modes, web-post buckling; Vierendeel mechanism; yielding of the Tee section. For this purpose, the simulations will be carried out with the finite element software ANSYS APDL [6] including the initial geometrical imperfections, residual stresses, and geometric and material nonlinearities. Additional boundary conditions, so that the beams cannot deflect laterally throughout the beam span or twist at the supports will be introduced.

To determine the most appropriate buckling curve for the cellular beam of the proposed model, the LTB curve of the effective solid beam will be chosen for the calculation of the LTB resistance of the cellular beam according to EC3-1-1 [7] and confronted with the results got when using the specific LTB curve recommended by [3] for cellular beam.

A parametric study will be conducted to identify the influence of loading type, variation of cross-section dimensions, opening geometric characteristics, steel beam length and non-dimensional slenderness on the fire resistance and failure loads of a cellular beam, including associated instabilities, as well as the consequent stress distribution across its span.

The adequacy of the calculation of cellular beam resistance by the simplified methods of Eurocode 3 Part 1-1 [7], Eurocode 3 Part 1-2 [4], Eurocode 3 Part 1-13 [3] and the SCI-P355 [8] guide, will be verified by comparison with numerical results.

As a result of this research, a new plateau length for the LTB curves of cellular beams based on their geometric parameters will be proposed.

This work seeks to answer the following research questions:

- How do the use of numerical coupling and endplates during the elastic and buckling simulations affect the buckling mode and the moment resistance at collapse?
- What effect do web openings have on the collapse load and global LTB resistance of the cellular beam at ambient and elevated temperatures?
- What are the geometric parameters that limit the occurrence of LTB on cellular beams at ambient and elevated temperatures?

1.3. Limitations

Because the topic of the instability behaviour of steel beams with web openings under ambient temperature and extreme fire conditions is so broad, some limitations will be put forward:

- Cellular beams with I hot-rolled profile, which is symmetric about the weak axis.
- Regular large circular openings are the main configuration of openings that are used, openings placed centrally in the depth of the section.
- Beams are loaded by a pure bending moment or a mechanically distributed load.
- The beams are simply supported at the ends by fork supports.
- The LTB for cellular beams is mainly affected by residual stresses applied along the cross-section.

1.4. Dissertation summary

The work is divided into five chapters. The first chapter is the present introduction, which offers an overall generalization of the issue and sets out the foundation and the aims of the study.

Chapter 1 gives an overview of the literature on the topic of the work, where explains in detail the characterization of the cellular beam, with information on production methods and typical applications, and identifies the instability phenomena that might occur in beams with web

apertures. It briefly gives a general overview of the finite element method. It also displays the synthesis of the bibliographic research, which presents the findings of recent studies on the subject in question.

In Chapter 2, we recall the main definitions related to the characteristics and behaviour of steel at elevated temperatures according to the second part of Eurocode 3. Then attention is given to the design methods of steel solid and cellular beams at ambient and elevated temperature according to the two first parts of Eurocode 3, Eurocode 3 Part 1-13 and to the SCI-S355 design guide.

In Chapter 3, we focus on the numerical methodology used to simulate the behavior of steel beams subjected to ambient and elevated temperatures. This includes a description of the cases studied, as well as the modelling of steel solids and cellular beams in ANSYS software. We also address the challenges encountered during simulation convergence and provide an explanation for how these issues were resolved. Furthermore, this chapter discusses the influence of web openings on the critical temperature and displacement of steel beams. Additionally, we examine the effects of imperfections and residual stresses on the lateral-torsional buckling (LTB) of cellular beams and the fire resistance of unrestrained cellular beams. The impact of profile section geometry is also analyzed in this section.

Chapter 4 presents analytical and numerical simulations of the LTB resistance of cellular beams, including a study of the elastic critical moment and the influence of coupling and end plate thickness on collapse resistance at different temperatures. A parametric study was also conducted to analyze LTB and interacting failure modes. The results and their comparison using various design methods are discussed in depth. Based on these findings, a new proposal for the LTB curves of cellular beams is presented.

Finally, chapter 5 summarizes the main conclusions that can be drawn from the research carried out and gives recommendations for future research to better understand the behaviour of this type of beam.

CHAPTER 1. LITERATURE REVIEW

1.1. Overview of steel cellular beams

The cellular beam, a modern version of the traditional “castellated beam”, is defined as expanded steel sections with circular openings. They are specially crafted to suit the requirements of a particular position in a certain building project. Their manufacturing process gives them certain qualities. It is essential to evaluate whether these features suit the building project in question.

One of its most prominent features is its high strength-to-weight ratio. Steel cellular beams are highly resilient, can withstand high loads, and have a low dead weight. This makes them ideal for supporting heavy loads in construction projects.

The grid arrangement with its wide span reduces the number of columns needed, thereby allowing greater architectural liberty. Additionally, it reduces the number of components required for fabrication and assembly, as well as the structural depth of the floor, resulting in a lighter building [1].

Cellular steel beams are also highly versatile, as they can be manufactured in various shapes and sizes due to the cutting line performed. This versatility enables them to be used in the creation of various structures, ranging from simple foundations to complex bridges and buildings. The dimensions of these beams vary depending on the purpose for which they are used and are shown in Table 1-1, with a_0 representing the diameter of the hole opening, h being the height of the solid beam profile that creates the cellular beam, S being the distance between the openings, and H being the final height of the cellular beam. Despite the higher cost of fabricating cellular beams due to cutting and welding processes compared to conventional beam, the current advancement in computer controlled cutting and welding technology allows for highly precise and cost-effective production [9]. Cellular beams come in a variety of steel grades. Typically, floor beams require higher-grade steels such as S355 and S460, with S355 usually being adequate for roof beams.

Table 1-1. Application-specific variations in geometrical dimensions of cellular beams [1].

Application	Objective	a_0/h	S/a_0	H/h
Roof support systems Footbridges Wide-span purlins	Optimisation of the height/weight ratio	1.0 – 1.3	1.1 – 1.3	1.4 – 1.6
Floor support systems Parking structures Beams for offshore structures	Optimization of load/weight ratio	0.8 – 1.1	1.2 – 1.7	1.3 – 1.4

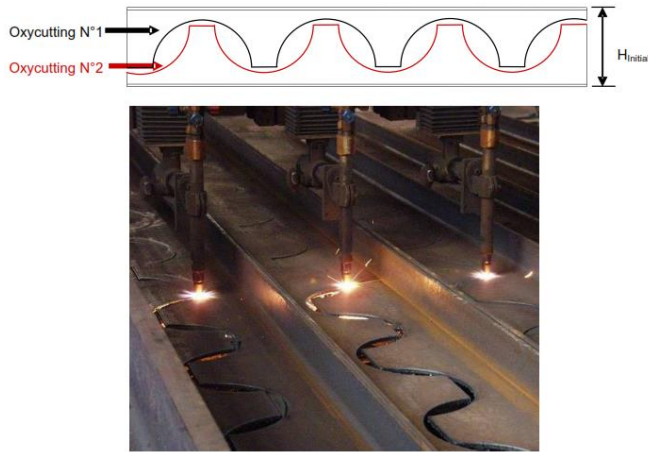
1.2. Production process

Beams with web openings are made from a standard hot-rolled I- or H-sections and there are three distinct approaches for their production [8].

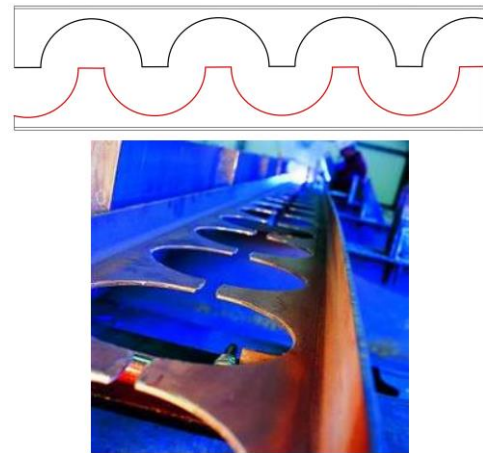
The first method involves creating openings directly in the web of a laminated steel profile, these openings are isolated. As a result, the original profile is preserved, but the area is reduced, which leads to a decrease in its resistance capacity.

The second method involves forming fabricated sections from three plates welded together to form an I-section, with the possibility of obtaining asymmetric or tapered geometries. Openings are cut in the web of an I-section, either before to or after its formation, and this method can be used for isolated openings or for regularly spaced openings. It is also possible to define sheets with specific characteristics, such as curvatures, shapes, and hole spacing. This process is applied by Fabsec (UK).

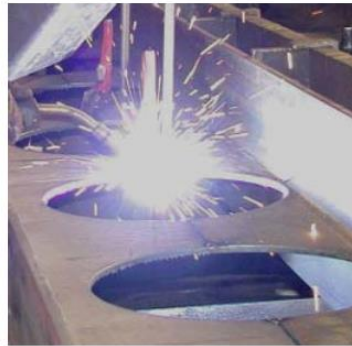
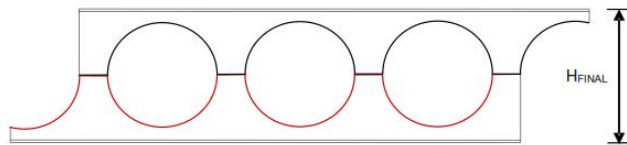
Another commonly used process involves flame cutting the web of a hot-rolled H or I-shaped section according to a certain pattern and then welding the resulting two sections together tip-to-tip. This process yields a member that is 40-60% higher than the original I-section and offers a wide variety of geometric possibilities, ranging from tapered beams with a varying moment of inertia to web-opening shapes to asymmetric beams [10]. The cutting pattern and the properties of the top and bottom halves of the beam can be altered to achieve these variations. ArcelorMittal (Luxembourg) and Westok (UK) are two of the many manufacturers of steel cellular and castellated members that employ this method in production. In our work, we will focus solely on beams manufactured using this process.



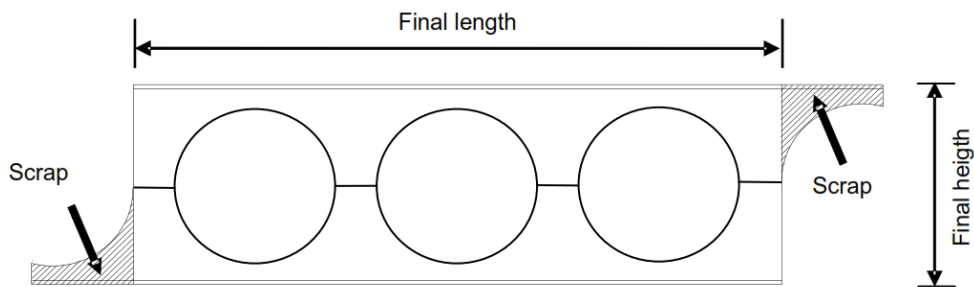
a) Oxycutting of the parent profile



b) Separation and positioning of the two parts of the parent profile.



c) Welding of the two parts of the parent profile



d) Final geometry of the cellular beam

Figure 1-1. Fabrication process of steel cellular beams [11].

These beams can be of constant or variable inertia, has a constant height or is tapered, with or without counter bends, with symmetrical or asymmetrical cross-sections with different shapes of openings. They are presented successively as follows:

Tapered cellular beams are created by cutting the web of the beam at an angle to the centroidal line and then flipping one of the T-sections before welding them together. This type of beam is a reliable choice for a variety of structures, such as long cantilevers (stadium stands) and continuous beams (footbridges, frame rafters, etc.) [1].

Curved or cambered beams are made by altering the cutting pattern to form different top and bottom tees, which are then bent to the desired radius and welded. These beams can be utilized to handle architectural or practical needs, for example, matching roof inclines or adapting to the flexing of the section due to its own weight and dead load from the floor slab [1].

Asymmetrical profiles can be made by welding together the top and bottom T-sections of different profiles or even different steel grades. These configurations are particularly advantageous for composite design, as they enable the most effective utilization of steel in the beam [1]. For this work, only doubly symmetric cellular beams will be taken into consideration.

Depending on the type and function of the beams, the openings can vary considerably in shape: circular, hexagonal, Angelina, octagonal, rectangular, elongated, sinusoidal and extended hexagonal shaped openings. Furthermore, customized holes can be created to meet the specific requirements of a project, and various holes can be combined in the same beam [2, 3]. This variety of hole shapes influences the beam's strength, as changing the total height increases its stiffness, altering the location of the stresses to which the beam is subjected, and the amount of material present in its section changes its failure mode.

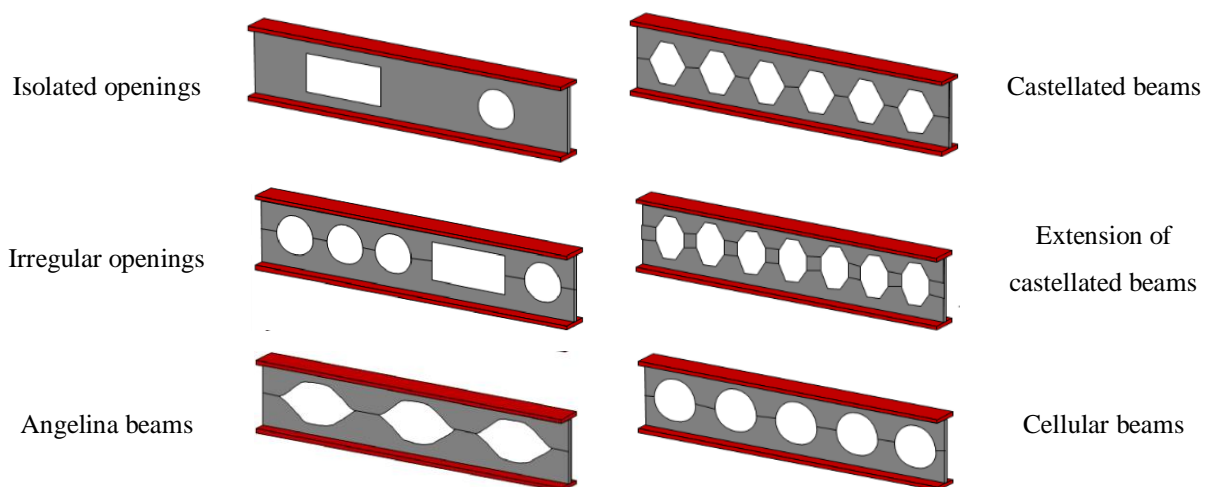


Figure 1-2. Steel beams with different opening shapes [12].

Large web openings cause a considerable decrease in the shear resistance of beams, because of the loss of a major portion of the web yet lead to a lesser decrease in bending resistance [8]. In this work, the behaviour of beams with large circular web openings will be analysed.

When it comes to designing steel structures, it is important to consider the imperfections that may be present in the individual elements that are composed, which can reduce the strength of the structure. These imperfections can be caused by the manufacturing process [10], because of the sudden cooling of the heated steel, as well as storage and transportation to the assembly site [13].

Imperfections can be divided into three categories: geometric, material, and structural. Geometric imperfections include variations in the dimensions of a structure or a member, a lack of verticality of a structure and straightness, and a lack of flatness of a member. Material imperfections refer to the variation in material properties as well as the presence of residual stresses. Structural imperfections include variations in support/ boundary conditions if any, and eccentricities of load application [7]. In this study, analysing the buckling of the cellular beam is of primary importance. To this end, the effects of geometric imperfections and residual stresses are carefully evaluated.

1.3. Factors influencing stability of steel beams: Geometric and material imperfections.

Imperfections to be considered are of two kinds geometric and structural which are linked to the prescribed straightness tolerances of the beam and induced stresses, and both are included in the design by [7]. Imperfections in cellular beams have a considerable impact on structural performance, lowering load-carrying capacity [14, 15]. Residual stresses can have a significant effect on the structural performance, causing localized plastic deformations that reduce stiffness and lead to a decrease in the element's load-bearing capacity [16].

1.3.1. Geometric imperfections

From a practical perspective, geometrical imperfections are related to the tolerances that steel constructors must adhere to. These include the geometrical manufacturing tolerances prescribed by the European standard EN 1993-1-1:2005 [7] and the assembly and execution tolerances related to the assembly method.

From a scientific perspective, the geometrical imperfections must be considered when computing the geometrical and material non-linear failure load of a structural element. To this end, the recommendations of the standard EN1993-1-5: 2006 [17] in Annex C suggest, if no better option is available, to use the geometrical imperfections that correspond to the most likely critical buckling mode and apply an amplitude of 80% of the geometrical fabrication tolerances. According to [7] the structural integrity of frames and bracing systems must be addressed considering both global and local imperfections.

According to Martins et al . [18] and Rossi et al. [19], geometrical imperfections, such as initial curvature, in beams, alters the traditional buckling problem and transforms it into a load-displacement problem, which stands in opposition to the problem of bifurcation of the equilibrium. Thus, geometric imperfections must be considered when performing numerical analysis to ensure accurate results are obtained, a requirement that is necessary to accurately predict the behaviour of steel structures. Teixeira et al. [20] concluded in their study that geometric imperfection shape has a marked effect on the outcomes of the simulation, both qualitatively in terms of altering failure modes and quantitatively by increasing the overall resistance due to web bending. The three main geometric imperfections shape they identified in castellated and cellular beams were global bending of the longitudinal axis of the beam about the weak-axis of inertia (Figure 1-3a); bending of the web (Figure 1-3b); and misalignment between the upper and lower halves of the beam at the welded section (Figure 1-3c).

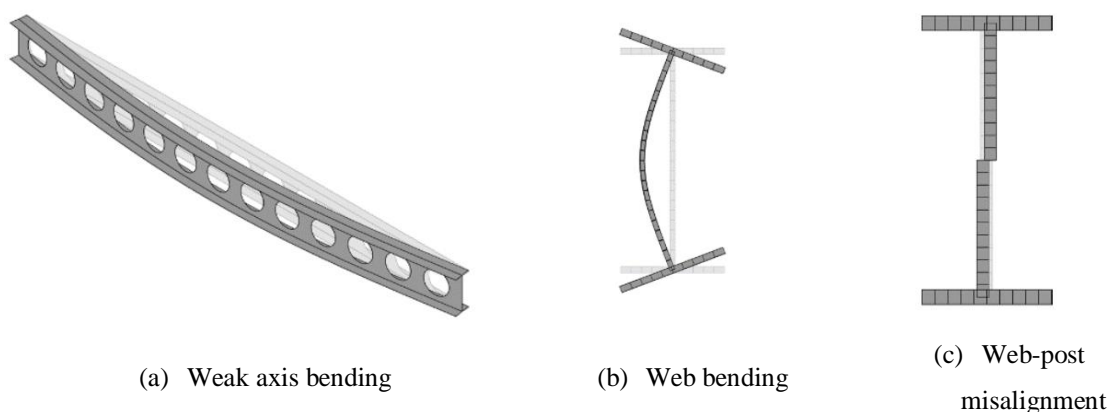


Figure 1-3. Geometric imperfections: a) Global, b-c) local [20].

1.3.1.1. Global geometric imperfection

Global imperfections are required to describe global beam instabilities as lateral torsional buckling [21]. Since the lateral torsional buckling is characterized by a combination of

horizontal and vertical displacement, as well as rotation of the section, it is reasonable to consider that the horizontal straightness of the compressed flanges that it is important to know [13]. The displacement of the beam axial axis along its length can often be approximated by a half of a sinusoidal curve, with the maximum amplitude at the beam centre being equal to a value of $L/1000$, [10, 20, 22-25]. This is represented mathematically by the equation (1) in [26].

$$y(x) = \frac{L}{1000} \sin\left(\frac{\pi x}{L}\right) \quad (1)$$

Where L is the beam length and x the length variation.

Using this formulation, the exact coordinates of the beam points with the imperfection can be determined. According to formulation (1), with a sinusoidal function, the imperfection will result in zero values at the ends of the beam ($x=0$ or $x=L$) and maximum values at mid-span at $x= L/2$.

Along with this displacement, the lack of verticality of the beam's cross section can be considered by assigning it an initial rotation around the axial axis with a maximum value of $L/1000$ radians at mid-span, as mentioned in [22, 27].

1.3.1.2. Local geometric imperfection

Local geometric imperfections can be found in the web-post between two openings of a cellular beam, and their value may differ depending on the beam's height. In the Eurocode 3 standard [17], a value of $H/200$ for numerical calculation is proposed. Where H is the final cellular beam's height.

In Durif et al.'s [21] research study, experimental tests and numerical modelling were conducted to analyse cellular beams with sinusoidal openings. The out-of-plane imperfection of the web-post was measured at various cross sections along the beam's length to obtain the local geometric imperfection. The measurements showed an initial imperfection with C-shaped maximum magnitude equal to $H/430$, compared to the Eurocode-proposed value of $H/200$. The same shape of initial imperfection with different magnitudes was found in all the cross sections.

In the ArcelorMittal catalogue for ACB® and Angelina™ beam sections [1, 28], the specified tolerance for initial imperfections in the web post is $H/100$ if H is greater than or equal to 600mm and 4mm or less if H is less than 600mm. This is corroborated by a numerical

research study on LTB in cellular beams performed by Ferreira et al. [25], which established $H/100$ as the maximum value for sections with $L/H < 10$ and $H > 600\text{mm}$ and recommended not to exceed 4mm for sections with $H < 600\text{mm}$.

For the study of structural instability in a non-linear analysis the numerical model must be provided with imperfections that can trigger the instability. The initiation of buckling failure is enabled by imperfections; however, these imperfections must be of small magnitude to prevent disruption of the main responses of the beam [15]. Therefore, for the modelling of LTB of steel beams, no local geometrical imperfections are needed [16, 20, 27], provided that the different plates of the cross-section do not belong to the "slender" range (i.e., no "Class 4" elements), as they have a minimal impact on the global buckling of the beam as recommended by the literature [27]. Boissonade et al. [27] suggested that using eigenmodes as the initial imperfect shape is appropriate, provided that the initial amplitude is carefully scaled (e.g. $L / 1000$).

An alternative to using global and local geometric imperfections in beams in finite element models is to apply imperfection following the buckling analysis of eigenvalues and eigenvectors, allowing for the worst-case scenarios of global and local buckling modes to be found. The analysis is a linear perturbation procedure. As a result, the coordinates of the beam elements are altered to account for this additional imperfection [29]. The eigenvalues and eigenvectors method can be used to predict the theoretical buckling resistance of an idealized elastic structure. To obtain this result, the basic structural configuration is calculated by considering the loads and constraints; each load is associated with a buckling mode, which represents the shape of the structure under the critical load [30].

1.3.2. Structural imperfection: Residual stress

A stress pattern from the fabrication process with amplitudes equivalent to the mean (anticipated) values may serve as a representation of structural imperfections in terms of residual stresses [17].

Since 1960, great advancements have been made in the knowledge of residual stresses on welded plates [31], welded sections [32], hot-rolled sections [33], and welded sections with oxy-cut plates [34] in the field of steel construction. This knowledge has been taken up by the European Convention on Metal Construction (ECCS) in its publication [35], which defines

the bases of the residual stress models according to the type of element and the manufacturing process used.

Residual stresses are known as internal stresses that can exist in a member that is not subjected to external loads, during the manufacture, heat is introduced at the cutting and welding areas influencing the already existing residual strains [36]. Their sign and variance are depending on the cooling conditions and cross-section geometry. A suitable heat treatment can be used to remove residual stress, but this is usually too costly to be a viable option. An alternative method is mechanical processes like cold regularization, which can reduce the impact of stress [35].

1.3.2.1. Solid beams

The formation of residual stresses in I-section members that have been hot-rolled can be attributed to the uneven cooling of the beams after they have been manufactured in the rolling mill, resulting in the thermal contraction of the material. After the hot-rolling and cooling processes, the elements may no longer be within the recommended standard for linearity. Consequently, a process of regularization of the flatness in the cold is necessary, resulting in a new pattern of residual stresses, particularly in the flange of the beam [37]. In the following, the two main types of residual stress distribution are summarized.

In 1972, Alpsten, G. [38] conducted theoretical studies that served as the basis for a first model of residual stress in medium-sized rolled sections proposed by Young [36] in the same year. This model was adopted by the European Convention for Constructional Steelwork (ECCS) in 1976 [35] and featured a static equilibrium distribution of mean stresses with a parabolic shape, as depicted in Figure 1-4a. Typically, the flanges will be in compression at the tips and in tension at the flange centres, while the web's residual stresses may be either positive or negative, depending on the cooling parameters and the cross-section's geometry [36].

Where, the peak stress values are obtained from:

$$\sigma_{c1} = 165 \left[1 - \frac{ht_w}{2.4 bt_f} \right] [MN/m^2]$$

$$\sigma_{c2} = 100 \left[1.5 - \frac{ht_w}{2.4 bt_f} \right] [MN/m^2]$$

$$\sigma_t = 100 \left[0.7 - \frac{ht_w}{2bt_f} \right] [MN/m^2]$$

Where: σ_{c1} is the compressive stress at the flange tips; σ_{c2} is the compressive stress in the centre of the web; σ_t is the tensile stress at the web to flange junction; h is the web depth; t_w is the web thickness; b is the flange breadth, t_f is the flange thickness.

Notably, this model is independent of the material's yield strength, and the highest values are primarily a function of the geometry of the section. A new parabolic distribution model was proposed in 1998 that was capable of distinguishing between small and large profiles, as seen in Figure 1-4b-c. This model simplifies the influence of section geometry on residual stresses by categorizing profiles based on h/b , [13].

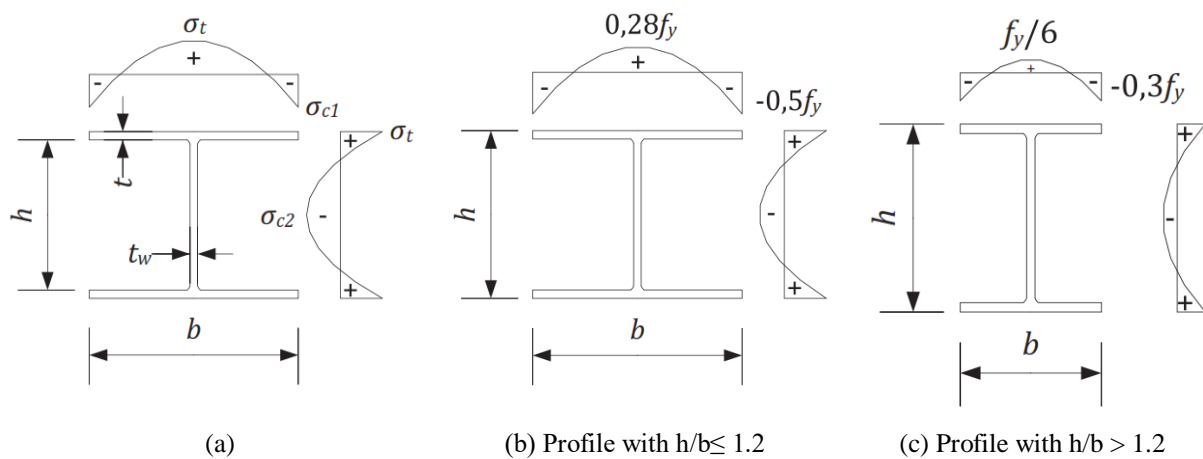


Figure 1-4. Residual stress distribution for hot-rolled members, a) proposed by ECCS in [35], b-c) model proposed in 1998. Extracted from [13].

ECCS [39] proposed a simplified model for rolled sections which involves the use of a triangular linear distribution, which is the most frequently used in numerical simulations and is indicated in Figure 1-5. This model stands in contrast to the parabolic residual stress distributions which, while they appear to better reflect experimental measurements, are not as widely applied. Profiles with $h/b \leq 1.2$ have maximum residual stresses in tension and compression of $0.5 \cdot f_y$, while those with $h/b > 1.2$ have maximum values of $0.3 \cdot f_y$.

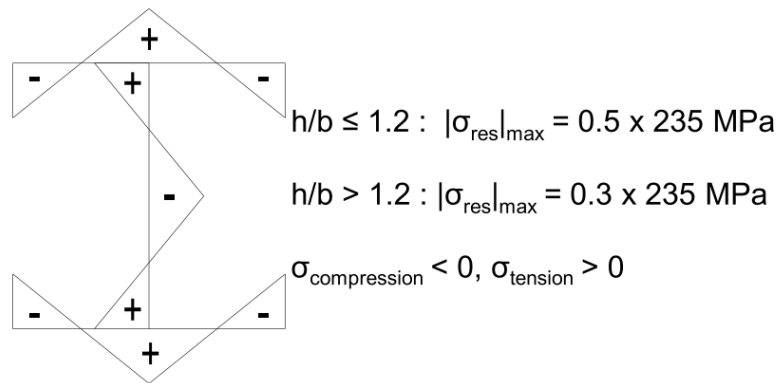


Figure 1-5. Residual stress distribution for hot-rolled members proposed by the ECCS in [39]. Extracted from [10].

1.3.2.2. Cellular beams

Accurately quantifying the residual stress present in various components has been a major area of research [40], with the goal of incorporating the results into improved design guidelines and advanced numerical models.

The residual stresses present in the solid beam are modified when the thermal cutting process, such as ox cutting or plasma cutting, is performed on the web to produce the holes of the cellular beams, added to the welding process of the halves where heat is introduced again [24, 27]. According to Sonck et al. (2014), Sonck 2014 [10, 16], this could potentially have a negative impact on the existing residual stresses in the parent sections and thus the LTB resistance. Nseir et al. [41] highlighted the complexity of the state of residual stresses in cellular beams and proposed a solution to account for their effects by adopting the amplitude $L/500$. Ellobody [23] developed a 3-D nonlinear finite element model for cellular steel beams, accounting for residual stress and geometric imperfections. However, they assumed the distribution of residual stresses in the cellular beam to be the same as in the solid beam, justifying that the cutting process had been conducted carefully.

Sonck et al. [16] studied the behaviour of cellular steel beams about the distribution of residual stresses after the manufacturing process both experimentally and numerically. The authors confirmed that there was a rise in the maximum residual stress of compression and redistribution of the maximum tensile residual stress in the web.

Sonck 2014 [10] conducted experimental tests of solid beams made of S235 steel grade and IPE160 hot rolled cross-section to create a residual stress model for cellular and castellated beams. The cellular member specimens were made by oxycutting circular openings around

the hexagonal openings in completed castellated members. The author's proposed residual stress patterns depend on the depth-to-width ratio h/b of the parent section originating the cellular beam and the intensity of its yield stress. The ECCS pattern [39], as shown in Figure 1-5, is employed as the original residual stress pattern for the parent section.

Because residual stresses in the flanges have the greatest influence on global buckling resistance, the residual stress variations in the flanges are the same as in the original section, and these stresses are balanced by the tensile stresses in the web. The residual stress magnitudes in the flanges are calculated by applying a residual stress decrease of 30 MPa at the flange tips and 20 MPa at the flange centres to parent section members with an original residual stress amplitude of 70 MPa ($\approx 0.3 \times 235$ MPa) for $h/b > 1.2$ and 120 MPa ($\approx 0.5 \times 235$ MPa) for $h/b = 1.2$. So, with the ratio $h/b > 1.2$, at the flange tips a compressive stress of 150 MPa results, and at the center 100 MPa tensile stress. Similarly, with $h/b \leq 1.2$, at the flange tips a compressive stress of 100 MPa results, and at the center 50 MPa tensile stress, as shown in Figure 1-6.

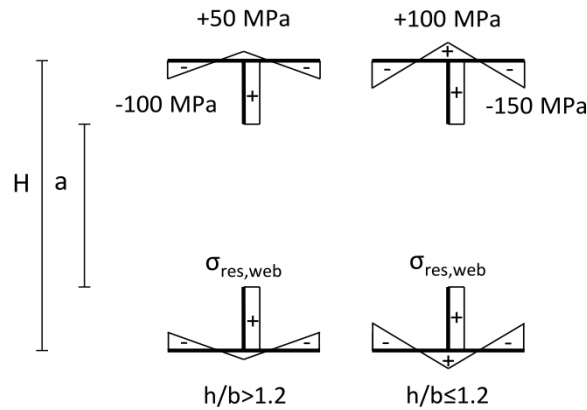


Figure 1-6. proposed residual stress patterns for cellular and castellated members [10].

To make a uniform residual stress pattern that would be the same across the beam's length, the tensile stress in the web was set to match the tensile stress in the web zone of the Tee section. The magnitude of the tensile residual stress in the web ($\sigma_{res,web}$) is calculated according to equation (2), dependent on the geometry of the beam [10].

$$\sigma_{res,web} = 50 \text{ MPa} \times \frac{bt_f}{(H - t_f - a_0) t_w} \quad (2)$$

In Sonck et al [42], Kwani et al. [43], the ECCS (1984) proposal for solid beams, which involves a triangular distribution of stress with the peak stresses dependent on the yield strength, is taken into consideration in a simpler residual stress pattern model for cellular

beams. In this model, it is thought that the stresses in the web are zero due to the process of introducing the holes dissipates the constraint in the web. Consequently, the residual stresses in the flange are the primary factor in torsional lateral buckling and bending buckling.

Silva et al. [44] recently conducted numerical investigations on residual stresses, which suggested new models that account for the cutting and welding phases of the plates used in the manufacturing of steel cellular beams. The conclusion was that residual stresses on the web have no effect on either the beam's resistance capacity or failure modes. The present work adopts residual stress patterns, Figure 1-7, from Silva et al. [44] and were used as incoming data in the following parts which relate to the studies of the lateral torsional buckling.

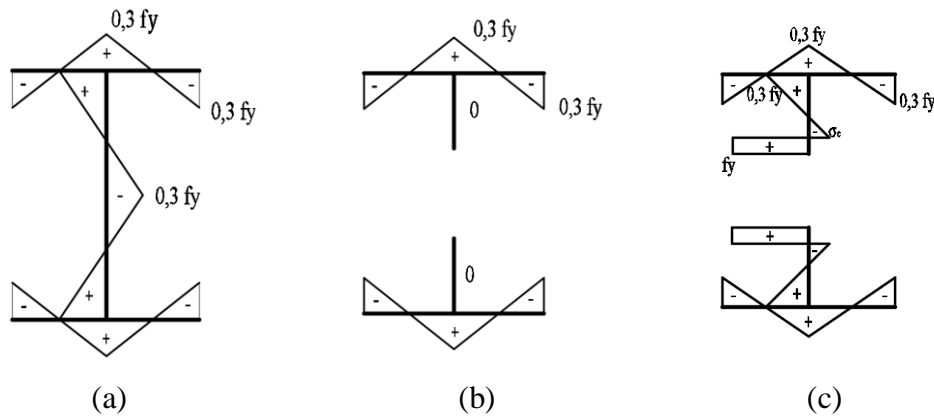


Figure 1-7. Residual stress distribution models, a) for solid beam, b-c) for cellular beam

1.4. Instability modes of cellular beams

Cellular beams with large web openings exhibit different failure modes. Research done by [45] have identified six types of failure for castellated beams, which could be associated in nature with solid beams for global failure or exclusively to beams with web openings for local failure. For the case of cellular beams, several authors have investigated the different failure modes [23, 41, 46-49] and they have shown that they are influenced by beam geometry, web slenderness, opening dimensions, type of loading, as well as the availability of lateral supports. The following is a summary of the various failure mechanisms:

Global failure modes

- pure bending
- pure shear
- lateral-torsional buckling

Local instability modes

- shear buckling (which may govern for slender webs [8])
- local flange buckling
- local web buckling

Failure at opening locations

- local Vierendeel bending (dependent on the shear transfer across the opening)
- tee buckling (not for circular openings)

Web-post failure modes

- web-post horizontal shear
- web-post bending (governing between closely spaced rectangular openings)
- web-post buckling (dependent on the slenderness of the web-post and the shear resistance of the web-post between adjacent openings)
- web-post crippling due to compression
- Rupture of a welded joint in a web post.

Vierendeel mechanism and web post buckling are collapse modes that occur specifically because of the presence of the openings, whereas shear and moment strength modes already exist in solid beams but with different values because of the openings [10].

Elsawaf et al. [50] indicated in their research study that the failure modes for steel beams with openings in fire, which is not laterally restraint, are the same as at room temperature and are mainly related to web post buckling and Vierendeel mechanism, both of which are local buckling.

This section focuses on the behaviour and failure mechanisms of cellular beams that differ from plain-webbed beams. Failure modes that are generally comparable to those found in standard sections are only briefly addressed.

1.4.1. Global bending mechanism

This failure mechanism, also known as the flexure mechanism, may occur when a beam is subjected to pure bending moments and minimal vertical shear. In a manner akin to what is seen in solid beams with bending forces, the tee-sections above and below the holes yield to tension and compression until they become completely plastic. Despite the presence of the

holes, which interrupt the propagation of plastic zones on the central axis of the beam, the tee sections become fully plastic [45, 51-53], see Figure 1-8.

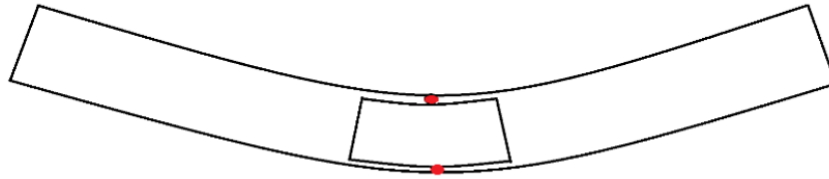
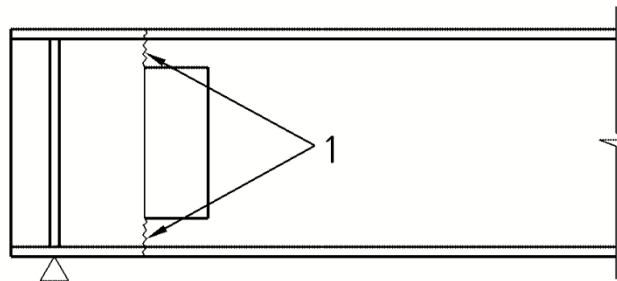


Figure 1-8. Global bending mechanism in perforated beams [53].

1.4.2. Global shear mechanism

It is uncommon for perforated beams to experience shear failure, and this is only limited to a very small length of opening, which lies in a very high shear region [54]. When considering bending and shear mechanisms separately, they are rarely the critical modes of failure in cellular beams, as demonstrated by [55]. Generally, openings in uniformly loaded, simply supported beams may fail due to the combined effect of bending and shear. However, if an opening is present at a location of high shear (near the support), the web area is eliminated, reducing the shear capacity of the section, and increasing the possibility of failure due to pure shear [53], as shown Figure 1-9.



1: Shear Plastification

Figure 1-9. Shear failure of the perforated cross-section [2].

1.4.3. Lateral torsional buckling

Lateral torsional buckling (LTB) is a failure mechanism that can be observed in both solid and cellular beams that are not axially loaded. Without adequate lateral support, this mode will usually dominate over the flexure mechanism [55]. It can also occur during the construction phase of composite beams or for composite beams subjected to a negative bending moment [10]. As in solid web beams, the out-of-plane movement of the beam without any web distortions describes this mode of failure [45, 51, 56]. Cellular beams, due to their increased

relative height of the cross section compared to a solid web beam, are more likely to experience this type of failure [10]. Figure 1-10 depicts the typical LTB failure mode in a cellular beam.

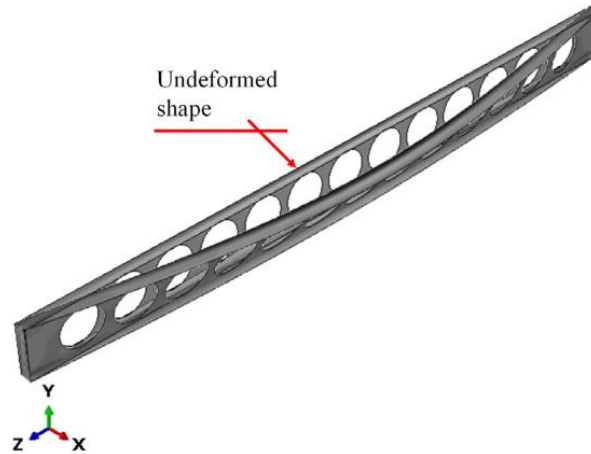


Figure 1-10. Pure lateral torsional buckling failure mode in steel cellular beam [57].

The current design of LTB failure is in a state of conflict [24, 42]. Two distinct groups of design guidelines for lateral-torsional buckling, based on 1T or 2T approaches [10], Figure 1-11. The 1T approach considers the LTB failure moment to be the flexural buckling failure moment of the compressed tee section at the opening, while the 2T approach applies the same formula as for a plain-webbed member, but by calculating the cross-sectional characteristics at the opening's centre location [42, 45]. According to [10, 41], the 1T approach is very conservative. The existing 2T design methodology is numerically confirmed in the study of [24] to be suitable for calculating the critical buckling moment M_{cr} , and the LTB resistance. It is used in the most current design guideline proposals for lateral torsional buckling of cellular elements [24, 44, 58], although the buckling curve choice differs amongst the various proposals. The present work will be done with the second approach, which involves determining the characteristics at the centre of the web opening.

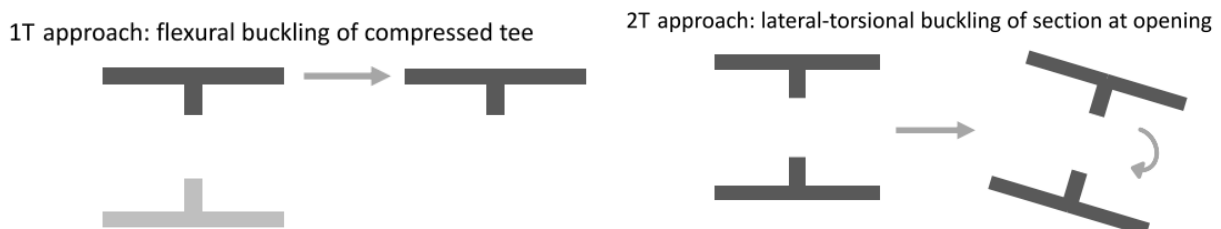


Figure 1-11. The 1T and 2T approaches for the calculation of the lateral-torsional buckling resistance of steel cellular beam [10].

1.4.4. Vierendeel mechanism VM

The presence of a shear force of high magnitude is the primary factor in this failure mode [45]. In fact, this is an extension of the flexure mechanism, but with the addition of shear V [55]. Vierendeel bending is produced by the transmission of shear forces throughout openings to equal the rate of variation in bending moment along the beam [59, 60]. Plastic hinges are formed in the vicinity of the holes, causing deformation of the tee sections in the manner of a parallelogram [51], causing crushing, or tearing at the weakest points [52].

This mechanism is often critical in short-span members, where shear dominates, and wide openings with large secondary bending moments or shallow T-sections with low plastic resistance [45].

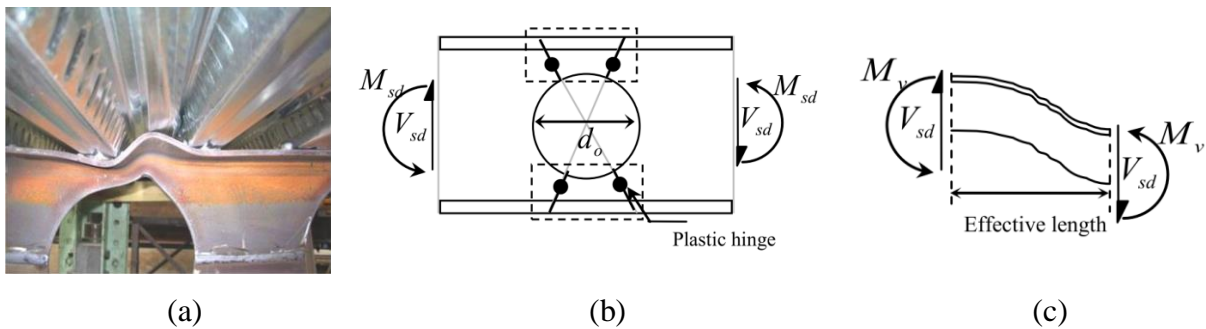


Figure 1-12. Vierendeel failure mode [61], b-c) plastic hinges, Vierendeel bending and effective length [62].

When applied shear is present on a castellated beam, the tee sections situated above and below the openings must be able to carry the applied shear and the primary and secondary moments. The conventional bending moment experienced at the beam cross-section is referred to as the primary moment, whereas the secondary moment (also known as the Vierendeel moment) is the result of the action of the shear force over the horizontal length of the opening. Therefore, as the horizontal length of the opening decreases, the magnitude of the second moment will decrease accordingly. The location of this failure typically occurs at the opening under greatest shearing force, or if multiple openings are under the same maximum shear, then the one with the greatest moment will be the critical one [51].

It is necessary to evaluate the interaction of the global shear and moment at each web opening along the beam's length due to the changing global bending moment and shear forces, this can help in pointing the critical opening [60]. The location of the critical section (angle ϕ) is largely influenced by the presence of a slab in composite construction and, as well as by the parameters of the spacing between openings (S/a_0), the slenderness of the openings $a_0/(t_w \epsilon)$

with $\varepsilon = \sqrt{(235/f_y)}$, the steel grade, and the symmetry or dissymmetry of the section [47]. Generally, this critical section can be inclined around 20 to 25° [63].

To prevent this kind of failure, the Vierendeel bending resistance of the tee section must be higher than the Vierendeel bending moments. This bending resistance is the sum of the moment resistances at the four corners, plus the overall moment and shear load, which also contribute to the computation of the resistance [62]. Further information on the internal force distribution can be found in the works of Bitar et al. [47], and Lawson and Hicks [8].

The formation of Vierendeel mechanisms has been studied for cellular beams, as well as for beams with other web openings shapes [46, 48, 49, 61, 62].

1.4.5. Web-post horizontal shear

In cellular beam, multiple openings close together implies interactions of forces between openings at the level of web post, this interaction can be illustrated mainly through the presence of a horizontal shear force which balances the differential axial forces between two openings, causing Plasticization of Web-post by Horizontal Shear.

In a cellular beam, the applied vertical shear induces a horizontal shear force in the web post between adjacent openings which can lead the web post to fail by yielding or rupturing at the weld line in its middle [52], as can be seen in Figure 1-13. Horizontal shear forces are developed in the web-post to transfer the incremental tension force to the bottom Tee [55, 59]. The resistance to this failure type depends on the welded joint surface and the yield stress of the steel [10]. It might be decisive for closely spaced openings (narrow posts) [8].

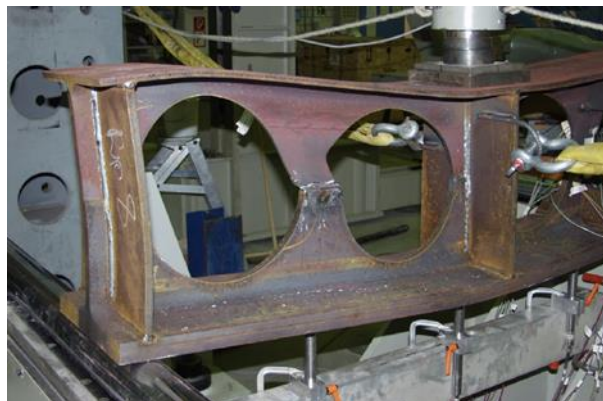


Figure 1-13. Web-post yielding due to horizontal shear [55].

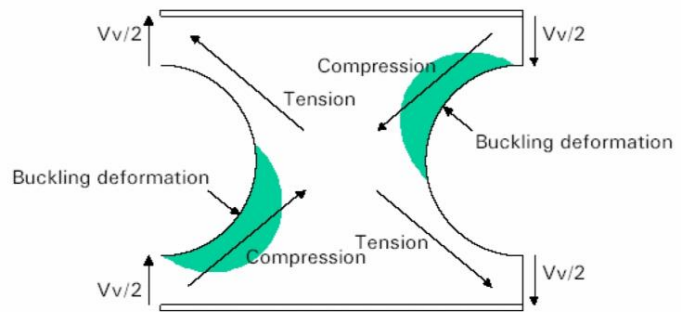
1.4.6. Web-post buckling

Web-post buckling occurs when the shear force causes compression stresses that destabilize the web-post, causing it to twist around its vertical axis and take on a deformed shape [64]. The out-of-plane double-curvature shape of the web-post is characteristic of this instability [63], Figure 1-14a. The web post experiences double curvature bending, which is associated with a horizontal shear force along its height. One inclined edge of the opening will be stressed in tension, while the opposite side will experience compression and buckling, resulting in a twisting effect along the post's height [51], Figure 1-14b.

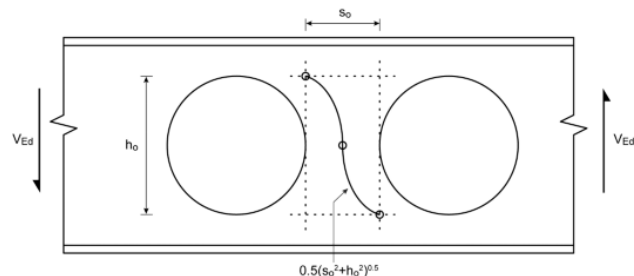
The tendency of a beam to buckle depends directly on the width of its web post (S_0), i.e., the space between the edges of the openings. Based on this, the SCI355 [8] classified beams into two categories, those with widely spaced openings ($S_0 > a_0$), and those with closely spaced openings ($S_0 < 0.5 a_0$). The effective width (l_e), which is the length subject to buckling, is illustrated in Figure 1-14(c) and calculated differently for each category: $l_e = 0.7a_0$ for widely spaced openings [8], and $l_e = 0.5\sqrt{(S_0^2 + a_0^2)}$ for closely spaced openings [3, 8]. The effects of web post buckling can be disregarded for widely spaced openings when $a_0/t_w \leq 25$, as per SCI 355 [8].



(a)



(b)



(c)

Figure 1-14. a) Double curvature of the web-post interpreted as web-post buckling [63], b) Stresses identified on the web-post [55], c) Effective length for closely spaced openings [3].

1.4.7. Web-post crippling due to compression

This form of failure, known as web post buckling due to compression, is like the crippling of the web in a plain webbed beam [45]. It occurs when local loads or reaction forces are applied directly to the web-post. The web post that buckles due to compression does not experience torsion, as opposed to a web post that buckles due to shear [51, 52], as illustrated in Figure 1-15. This failure mode was reported in the experiments conducted by Husain et al. [65]. To avoid this mode of buckling, high concentrated load should not be placed directly above the web-post region [53, 55]. Otherwise, it can be prevented by placing transverse stiffeners at the location of the transverse forces or filling the openings [24].



Figure 1-15. Web-post crippling due to compression [65].

1.4.8. Rupture of a welded joint in a web post

Rupture of the welded joint between two beam holes can occur if the length of the weld is shortened to reduce the magnitude of the secondary moment in the tee-sections [45]. Vierendeel mechanisms are more likely to occur in beams with long horizontal hole lengths, resulting in long welds. Conversely, short weld lengths can lead to failure of the welded joints due to exceeding the horizontal yield stress [51].

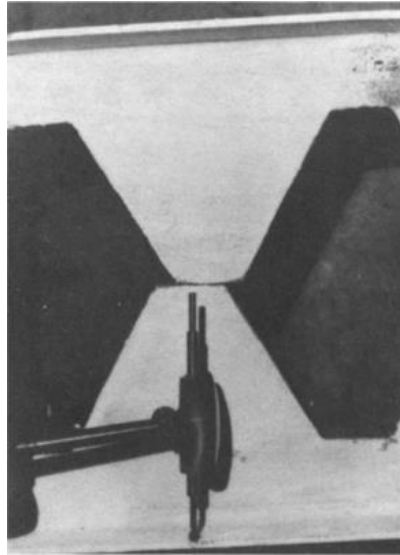


Figure 1-16. Rupture of a welded joint in a web post [45]

1.5. Finite element method FEM

A physical problem, which can be modelled mathematically using a set of differential equations, boundary conditions, and initial conditions for non-stationary problems, can be solved using both analytical and numerical approaches. Analytical methods are generally based on simplifying assumptions about the geometry, behaviour, and type of objects being studied, which limits their ability to accurately simulate the behaviour of a real system. With the advancement of computer technology, numerical methods have become increasingly popular for solving problems formulated by systems of partial differential equations with boundary conditions without requiring simplifying assumptions about the shape or behaviour of the materials involved. Examples of numerical methods include the finite element method (FEM), the finite volume method (FVM), the finite difference method (FDM), the boundary element method (BEM), and mesh-free methods.

The present work will utilize the Finite Element Method (FEM) to numerically solve the problem. This method enables the linear or nonlinear behaviour of the structure to be analysed and allows for the evolution in time and/or space of one or more variables representing the physical behaviour of a problem to be obtained [66]. It is an excellent method for calculating displacements, stresses, and strains under a set of loads.

Deeply, the finite element method (FEM), also referred to as "finite element analysis (FEA)", is a powerful computational technique used to obtain approximate solutions to a variety of "real-world" engineering problems involving complex domains subjected to general boundary

conditions [67]. Typical topics of interest in this field include structural analysis, fluid mechanics, heat transfer, electrostatics, and the study of electromagnetic fields.

The FEM is based on a simple concept: to subdivide (discretise) a complex shape into numerous elementary subdomains of simple geometric form (finite elements) interconnected at points called nodes, see Figure 1-17. The mechanical behaviour of each element is considered separately, and then assembled in such a way that force balance and displacement compatibility are satisfied at each node. FEM uses simple approximations of the unknown variables in each element to transform the partial differential equations into algebraic equations. These nodes and elements do not necessarily have any physical meaning but are chosen to achieve an accurate approximation of the desired solution.

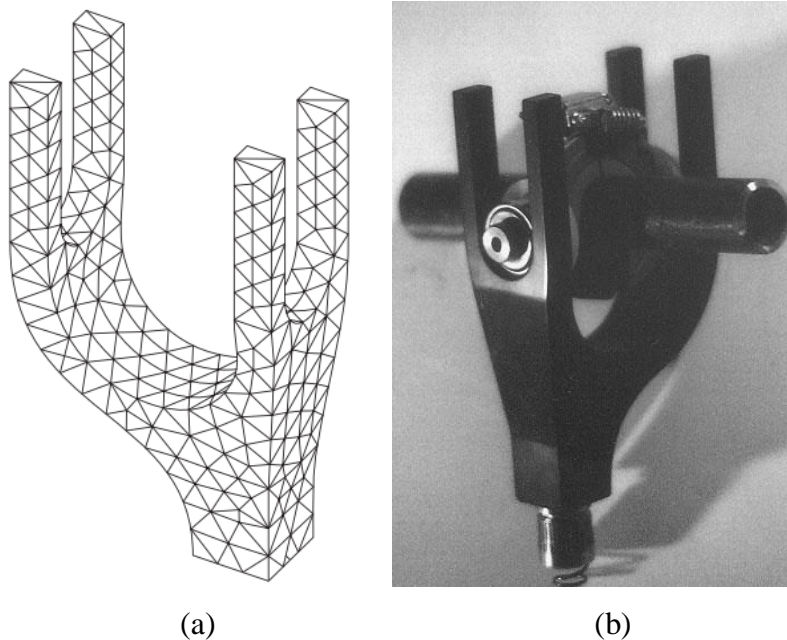


Figure 1-17. a) A finite element model of a prosthetic hand for weightlifting. b) Completed prototype of a prosthetic hand, attached to a bar. Extracted from [67].

The procedure for finite element analysis involves defining the physical problem (structural, heat, flow, etc.), creating a mathematical model using differential equations, specifying material properties, loading, and boundary conditions, and then selecting an appropriate element type (1D truss element, beam element, 2D shell element, plate element, or 3D solid element) and determining the mesh density (number of elements) and solution parameters. The loading and boundary conditions must then be represented, followed by selecting the type and method of solution (linear, nonlinear, structural static analysis, modal analysis, transient dynamic analysis, buckling analysis, contact, steady-state thermal analysis, transient thermal

analysis), and then obtaining the results (displacement, stress, strain, natural frequency, temperature, time history, pressure), [68].

The development of solutions to engineering problems through Finite Element Analysis (FEA) necessitates the use of either a bespoke computer program tailored to the FEA formulation, or a commercially available general-purpose FEA program such as ANSYS. ANSYS offers a comprehensive package for multi-purpose analysis and is employed across a broad range of engineering disciplines. The software ANSYS Mechanical APDL was used to perform the analysis of the proposed problem in this study.

In a case where a linear structural static analysis is to be performed, the overall equilibrium equation is done by equation (3), [69].

$$[K]\{u\} = \{F\} \quad (3)$$

Where: $[K]$ is the stiffness matrix, $\{u\}$ is the nodal displacement vector and $\{F\}$ is the force vector.

The current work employs a doubly nonlinear system, both geometrically and materially, because large displacements are examined, and the tangent of the stress-strain curve is not always constant.

The Newton-Raphson method is employed by this program to perform the static analysis of a nonlinear system, solving it incrementally and iteratively from the standpoint of updating the load and stiffness matrix, and can be written as [69]:

$$[K_i^T]\{\Delta u_i\} = \{F^a\} - \{F_i^{nr}\} \quad (4)$$

$$\{u_{i+1}\} = \{u_i\} + \{\Delta u_i\} \quad (5)$$

Where: $[K_i^T]$ is the Jacobian (tangent) stiffness matrix, “i” is a subscript representing the current equilibrium iteration, $\{\Delta u_i\}$ is a correction of the current displacement vector $\{u\}$, $\{F_a\}$ is the vector of the applied loads and $\{F_i^{nr}\}$ is the vector of restoring loads corresponding to the element internal loads.

The simulation buckling analysis is performed for a linear elastic analysis, which means that the tangent of the stress-strain curve is constant. The buckling problem is formulated as an eigenvalue problem [69]:

$$([K] + \lambda_i[S])\{\psi\}_i = \{0\} \quad (6)$$

Where: $[K]$ is the stiffness matrix, λ_i is the eigenvalue of number i , $[S]$ is the stress stiffness matrix, $\{\psi\}_i$ is the eigenvector of displacement of number i .

1.6. State of research on the instability behaviour of steel beams with web openings under extreme fire conditions

Steel cellular beams are a relatively new type of structural technology that offers a range of advantages compared to traditional solid or open web designs. Given the expanding use of steel-cellular beams, their behaviour in fires has become an increasingly important consideration. Although research in this field has grown significantly, many designs for this type of structure are still based on standards for traditional solid beams. To date, numerous studies have been conducted to assess the mechanical performance of these beams, including their collapse modes and reactions under high-temperature conditions. The outcomes of several of these studies are presented herein, with most of them being based on experimental testing and/or numerical simulations.

In 2004, Baily was the first to conduct a fire test on unloaded solid and cellular beam samples with a primal concern of comparing the temperature elevation and distribution between protected and unprotected sections. The experiments conducted in this paper indicate that the web-post temperatures of a protected cellular beam are significantly higher than the temperatures of an identical solid beam. It has been hypothesized that this increase is caused by the intumescent char being "pulled back" from the circumference of the hole. Additionally, it was found that the disparity between web-post temperatures and the bottom flange of the cellular beam is contingent upon on the type and thickness of intumescent coating used [70].

In 2006, Darlene Rini investigated the structural response of a long span cellular beam with varying section geometries when subjected to various temperature-time curves. Utilizing a nonlinear, finite element computational analysis of a steel-frame composite structure incorporating a long span cellular beam with a composite deck, the paper aimed to identify buckling behaviour, midspan displacements, and connection forces of the long-span cellular beam and to compare these results to a similar I-shaped member with no web openings. The findings revealed that long-span cellular beams subjected to fire can experience two buckling events before undergoing large displacement behaviour and catenary action. Additionally,

global, and local responses to such beams are mainly affected by local web stiffness, especially in the pre-buckling stage [71].

In 2007, Nadjai et al. [72] conducted an experimental and analytical research study at the FireSERT, University of Ulster, to investigate the behaviour of full-scale composite floor cellular steel beams in fire conditions. Based on the that experimental study findings, Vassart et al. [73] proposed an analytical calculation method to determine the WPB strength of cellular beams during fires.

In 2009, Vassart conducted a study to develop an analytical model with the purpose of predicting the critical temperature of cellular beams made of hot-rolled sections in a fire. Through conducting tests and simulations with isolated cellular beams in a fire, a new analytical model was developed because of the research [11].

Subsequently, in 2011, Naili et al presents an experimental and numerical study of three full-scale composite floor cellular steel beams, each comprising different steel geometries and loading conditions, at elevated temperatures. These beams featured both circular and elongated web openings. The analysis was conducted using finite element models accounting for material and geometrical non-linearity. The results were then compared with experimental data and existing design software from the Steel Construction Institute (SCI) [74].

Mesquita et al. [75], Kada Abdelhak [76], and Lamri et al. [77], Presented the results of a series of experimental tests of unloaded solid and cellular beams with circular apertures in fire conditions with and without intumescent fire protection. The influence of intumescent thickness, hole diameter, and web post width on cellular beams is also investigated. The tests are carried out in accordance with EN13381-8 for solid beams protected by intumescent paint and prEN13381-9 for cellular beams protected by intumescent paint. The results of the experiment suggest that intumescent coating increases fire resistance time in both solid and cellular beams due to its application, indicating its effectiveness.

Ellobody et al. examined the structural performance of composite frames with castellated and non-castellated steel beams with profiled steel sheeting under fire conditions. Research revealed that frames fitted with castellated steel beams exhibited less vertical mid-span deflection and improved ratios of span to maximum deflection when compared to frames without these beams [78].

The research of Wang et al. [79] investigated the fire-resistance capacity and web-post buckling behavior of UB cellular steel beams with and without protection. Their results

indicated that the level of protection along the perimeter of the hole has a significant effect on the temperature distribution of the web post, thus influencing its buckling behavior. In agreement, Nadjai et al. [80] established that intumescent coatings are most efficient for fire prevention on steel cellular beams.

Only a few research has been done on the subject of the LTB mechanical response under fire, considering geometric imperfections effects, residual stresses, material, and geometric nonlinearities [73, 81]. Recent investigations are yet to reach a full understanding of the LTB resistance and failure modes with the factors mentioned above [44, 82-84]. In their numerical study, Kada et al. [85] studied the effects of fire on the flexure of beams with either hexagonal or circular web apertures while considering different uniform load levels.

In 2019, the research work proposed by Mustasin focused on the behaviour of composite perforated beams in fire conditions and developed a virtual hybrid simulation approach to facilitate this investigation. The simulation combined the OpenSees, OpenFresco and Abaqus softwares to model the response of structural elements exposed to fire while taking account of the surrounding structure in the form of axial and rotational restraint. The accuracy of the model was validated using available fire test data, and the results showed the importance of including the effects from the remaining structure in the simulation. This virtual hybrid simulation framework was then used to investigate the influence of influential parameters such as type of fire, opening layout, restraint conditions, and material and geometric details. Furthermore, a series of analytical expressions were developed to modify the ambient temperature design standards for perforated beams and account for the effects of fire [53].

Silva et al. [44] studied changes in the LTB response of solid and cellular steel beams with temperature, exploring potential associations between certain geometric parameters. They showcased that beams with a smaller tee height may succumb to the Vierendeel mechanism (VM), whereas those with greater dimensions could fail due to web-post buckling (WPB).

Correa de Faria et al. [84] proposed new approaches for assessing the lateral-torsional buckling resistance of cellular steel beams in both room temperature and fire conditions. The proposed approaches followed European rules (EC3-1-1:2005 and EC3-1-2:2005) and consisted of a single formula for both conditions. A numerical model was constructed and validated using literature numerical and experimental results, with comparison to four experiments on cellular beams subjected to lateral-torsional buckling in room temperature conditions [16, 24, 41, 86]. Similarly, the model was evaluated in a fire situation by

comparison to three experiments on steel plain-webbed beams. In the parametric study, twenty different hot-rolled parent sections, six different groups of diameters and spacing of apertures, various values of slenderness, two types of structural steels, a room temperature condition, and seven target temperatures between 200°C and 800°C were all analysed.

The new approaches are based on the maximum capacity of the cross-section at the centre of the opening, which is defined by the member's class, steel reduction factors at flange temperature, and a modified reduction factor for LTB ($\chi_{LT,\theta,Prop}$), which integrates both material and geometric factors, as per the following formula:

$$M_{Rk,\theta} = \chi_{LT,\theta,Prop} W_y f_y k_{y,\theta} \quad (7)$$

$$\chi_{LT,\theta,Prop} = \left[\frac{1}{\Phi_{LT,\theta,Prop} + \sqrt{\Phi_{LT,\theta,Prop}^2 - \bar{\lambda}_{LT,\theta}^2}} \leq \left\{ 1 / \bar{\lambda}_{LT,0}^2 \right\} \kappa_0 \right] \quad (8)$$

$$\Phi_{LT,\theta,Prop} = 0,5 \left[1 + \alpha_\theta (\bar{\lambda}_{LT,\theta} - \bar{\lambda}_{LT,0}) + \bar{\lambda}_{LT,\theta}^{1,9} \right] \quad (9)$$

Where: W_y is the appropriate section modulus, f_y is the yield strength, $k_{y,\theta}$ is the reduction factor for the yield strength corresponding to the flange temperature, κ_0 is a correction factor.

The topic of the elastic critical moment for cellular beams under non-uniform bending was taken on as well. It has been shown that numerical and analytical results on the elastic critical moment vary considerably (reaching 10% under uniform bending, 25% under non-uniform bending) for cellular beams with non-dimensional slenderness lower than 2.0 at room temperature and 3.0 in fire situations, due to web distortion and interaction between local modes and the LTB buckling [84].

Benyettou et al. [83] surveyed numerically the LTB failure mode of beams having closely spaced large openings and the influence of parameters such as length, height of the cross-section, opening diameter and the impact of residual imperfections on their fire resistance.

In 2021, Justino et al. [87] proposed a semi-empirical method for calculating the shear strength of web-post buckling by shear (WPBS) in castellated steel beams. This method was based on making an analogy between the compressed diagonal of the web post and the strut model. Subsequently, Kotabati et al. [88] conducted a study to determine the governing failure criteria (deflection, flexural, and shear) of cellular steel beams (CSBs) at both ambient

and elevated temperatures. This study was undertaken under a standard fire curve and a non-uniform bending, with the beam depth fixed and the spacing between apertures chosen to prevent local web-post failure. Kotapati et al. [89] then investigated the behaviour of laterally supported CSBs exposed to the ISO 834 fire under three- and four-sided conditions. Their research findings showed that the number of openings, effect size, spacing of the openings, and different load ratios and fire exposure conditions, all have a significant effect on the fire-resistance time of CSBs at elevated temperatures and deflection at the stage of failure.

In 2023, Kotabati proposed a novel approach for designing laterally unrestrained cellular steel beams subjected to a moment gradient at elevated temperatures. Experiments as well as numerical simulations are used to investigate how different beam sizes, spacings, slenderness's, and boundary conditions affect the beam's lateral-torsional buckling resistance. The resulting design proposal is compared with the existing Eurocode 3 part 1-2 and is found to be safer and more accurate, growing from a statistical analysis of the results [90].

1.7. Conclusions

In summary, the cellular beam is a modern version of the traditional "castellated beam" with circular openings and specialized manufacturing for specific building projects. Its high strength-to-weight ratio, wide-span grid arrangement, and versatility make it ideal for supporting heavy loads and allowing architectural freedom. Although the cutting and welding processes make fabrication more expensive, advancements in technology have made production more precise and cost-effective. These beams come in various sizes and steel grades, with higher grades typically used for floor and roof beams.

Beam production methods and variations in web openings can affect the resistance and functionality of steel structures. In this work, we focus on beams created by flame cutting and welding sections together. These beams can have variable inertia, tapered shapes, and different hole patterns. Imperfections in the manufacturing process and material properties can also impact the strength of the beam. We will specifically analyse the LT buckling behaviour of beams with large circular web openings, taking into consideration geometric and residual stresses.

CHAPTER 2. FIRE SAFETY AND STEEL STRUCTURES

2.1. Overview of Fire

To accurately evaluate the structural performance during a fire, it is essential to comprehend the thermal conditions that the structure will experience [71]. Fire is described as a three-element equation composed of fuel, an oxidizer such as oxygen, and a heat source [91].

When a fire starts, it goes through a phase of development, typically marked by a rise in temperature, followed by a regression phase with a corresponding drop in temperature. Depending on the method of ignition and the type of fuel, the development process will be faster or slower. The severity of the fire and duration of these phases depend on several parameters, including the quantity and distribution of combustible materials (fire load), speed of combustion, ventilation, compartment geometry, and thermal properties of the compartment walls [91].

Within a confined space, such as a building, a fire can be divided into four distinct stages-ignition, growth, fully developed, and decay, each of which has a different duration [91, 92].

- First stage – Ignition (Incipient)

The ignition (Incipient) stage is when it is critical to combat a fire as it can be most easily suppressed and will cause the least amount of damage. When the four elements required to sustain a fire - fuel, heat, oxygen, and chemical reaction - unite, and the fuel reaches its ignition temperature, the fire begins. Control can be achieved by using a fire extinguisher; however, the rate of combustion mainly depends on the kind of fuel, its size, ventilation, and the type of ignition source. During the smouldering fire stage, the temperature is focused on the point of ignition and the first gases and smoke are released.

- Second stage – Growth

Once a fire starts in the growth stage, it consumes more fuel and creates more heat and smoke. During the second phase, when the fire is still localized but has grown in brightness, the radiation or contact of the flames reaches nearby materials, hot gases fill the volume, and if left unchecked can quickly reach Flash-over “a sudden ignition of everything combustible in a contained area, it generally corresponds to a temperature of 500 to 600°C”. Recognizing an early fire at this stage is critical as control becomes harder and there is little time to put it out.

- Third stage – Fully Developed

The fire has spread, and the maximum amount of fuel and oxidizers have been consumed, producing the highest heat release rate. A fully developed fire is the hardest to suppress, as it

is at the highest temperatures and causing the most heat damage. If you have not been able to suppress the fire before reaching this stage, then the odds of stopping it are much smaller.

- Fourth stage – Decay

The decay phase of a fire is characterized by a decrease in fire intensity and temperature as available fuel is consumed, resulting in nothing left to burn and eventually causing the fire to become either a smoulder or non-existent.

Through understanding each of these stages and their durations, appropriate countermeasures can be taken to ensure a fire does not cause any significant damage. The graph below outlines the temperature rise in a compartment over time, outlining the various phases of a fire's development.

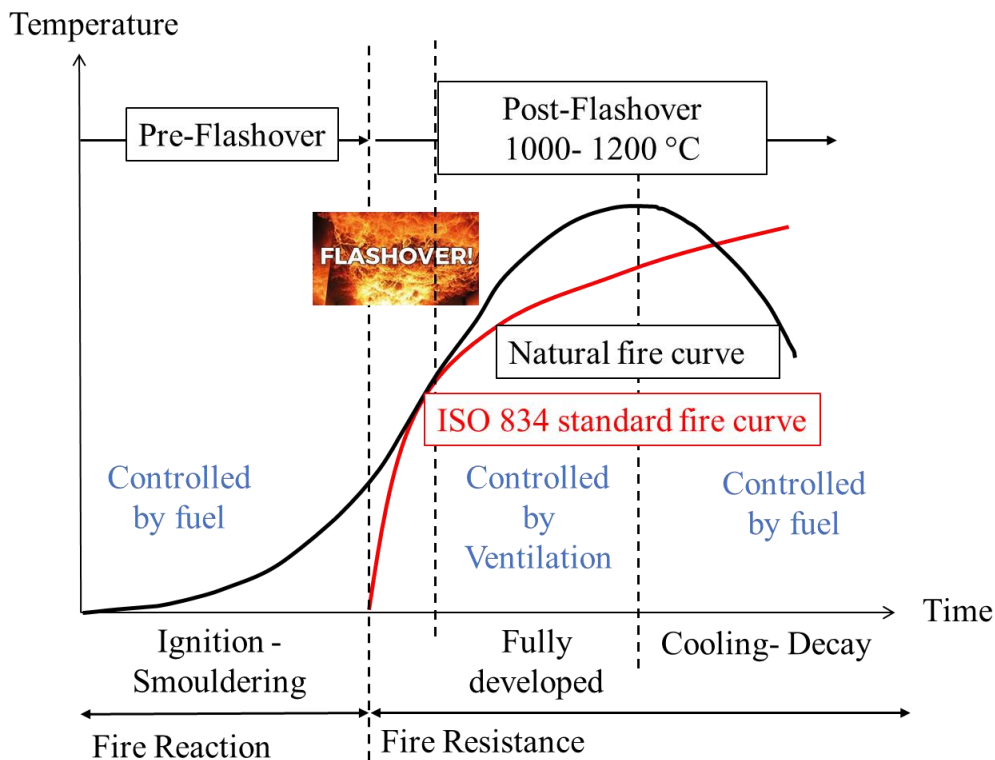


Figure 2-1. The four stages of fire development.

The main goals of fire safety are to ensure the security of people and their belongings by guarding against fire-related hazards. These objectives involve preserving the lives of building dwellers, defending fire fighters, and safeguarding the building and the buildings around it [91]. In order to realize these objectives, fire regulations must be observed and multiple steps must be taken.

When it comes to fire safety, steel has many advantages: it is non-combustible, strong, ductile, homogeneous, and isotropic. Steel does not burn, does not give off toxic fumes or smoke, and has long spans compared to other materials. It is also able to return to its pre-fire performance levels once cooled, making evaluation, reinforcement, and rehabilitation possible instead of demolition. Its ability to deform plastically also enhances safety and its consistent performance ensures predictable behaviour which can be quantified through calculation [93].

The fire resistance of columns, beams, walls, and slabs must prevent the propagation of fire and the collapse of the structure so that extinguishing operations can be carried out without excessive risk to firefighters [92].

2.2. Fire modelling: the ISO-834 standard fire curve

The most straightforward way of representing a fire is to use nominal curves, which accurately depict variations in gaseous temperatures over time. Historically, nominal curves were developed and employed to experimentally test construction elements to determine their relative resistance to and reaction against fire. Such curves are invaluable in the design process of fire safety for buildings, and the current regulatory requirement to model the temperature variation during a fire is the internationally recognized ISO 834 curve, otherwise known as the conventional fire curve, ISO fire or standard fire.

The standard time-temperature curve describing the flashover room fire scenario ("cellulosic fire") begins with a strong temperature rise in the first minute and reaches a maximum temperature of around 1000 °C after 90 minutes [94]. Unlike in a natural fire, as shown in Figure 2-1, where the fire load is burned at a certain time and thus results in a decrease in temperatures, the temperatures in this scenario never drop.

According to Eurocode EN1991-1-2 [95], the ISO standard for fire is described by the following equation:

$$\theta_g = 20 + 345 \log_{10}(8t + 1) \quad (10)$$

Where: θ_g is the gas temperature in the fire compartment (°C); t is the time (min); the coefficient of heat transfer by convection is $\alpha_c = 25 \text{ W/m}^2\text{k}$.

If a fire breaks out in a compartment near the edge of the building, flames may spread out from the façade. These flames can be long enough to heat up the outside face of the building on the floor above the fire compartment. To protect the building from the re-entry of the fire,

the external fire spread curve should be taken into consideration. This curve is based on the cooling effect of the air surrounding the building [96]. According to EN 1991-1-2 [95], the external fire curve is given by equation (11):

$$\theta_g = 660(1 - 0.687 e^{-0.32 t} - 0.313 e^{-3.8 t}) + 20 \quad (11)$$

Where θ_g is the gas temperature near the member ($^{\circ}\text{C}$), the coefficient of heat transfer by convection is $\alpha_c = 25 \text{ W/m}^2\text{k}$.

The standard fire curve is based on the rate at which general building materials and their contents combust. It has been used for many years, however, it soon became clear that the burning rates of some materials, like gasoline and chemicals, exceeded the rate at which timber would burn. To address this need, an alternative approach for testing structures and materials employed in the petrochemical industry was developed, resulting in the creation of the Hydrocarbon Curve. This hydrocarbon curve is applicable to cases where smaller petroleum fires may result, like car fuel tanks, petrol or oil tankers, and certain chemical tankers [97]. According to Eurocode EN1991-1-2 [95], the progression of the temperature of the Hydrocarbon (HC) fire curve is represented by the following equation.

$$\theta_g = 1080(1 - 0.325 e^{-0.167 t} - 0.675 e^{-2.5 t}) + 20 \quad (12)$$

Where the coefficient of heat transfer by convection is $\alpha_c = 50 \text{ W/m}^2\text{K}$.

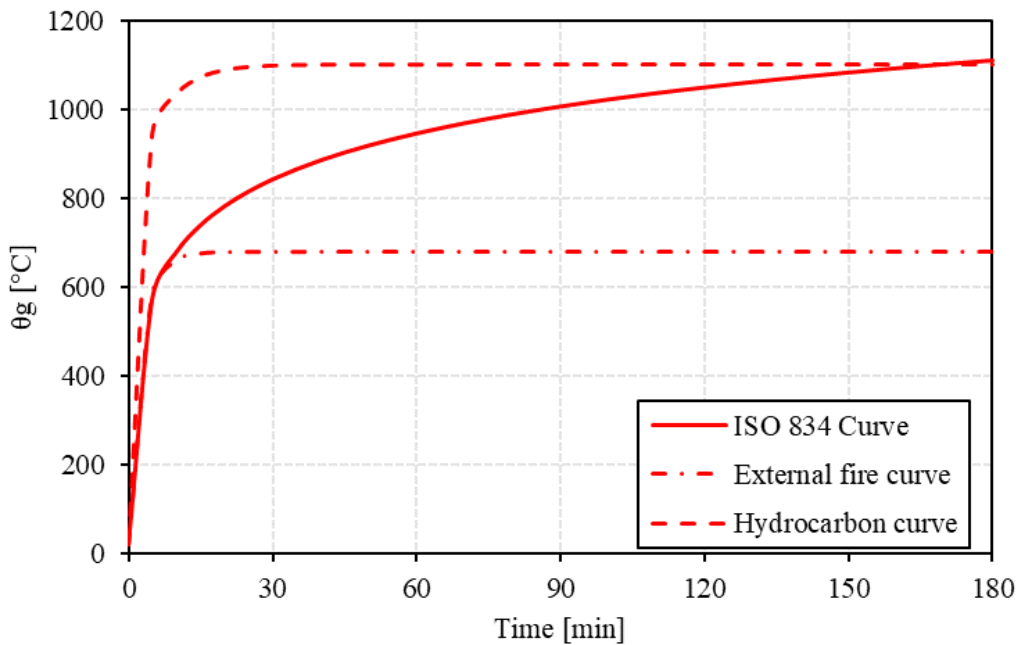


Figure 2-2. Standard and hydrocarbon fire curves

2.3. Properties of steel structures at high temperature

Assessing the fire behaviour of structural elements requires knowledge of material properties at elevated temperatures, such as stress-strain relationships, modulus of rigidity, strength, deformation properties, and thermal elongation as a function of temperature, among others.

To gain a better understanding of what happens to steel and composite structures in a fire, it is essential to be aware of the behaviour of the mechanical properties of different steel grades at high temperatures. Generally, simpler material models are used to gauge the fire resistance of steel structures. However, for a more precise calculation, it is critical to rely on accurate material data when using finite element or finite strip analyses [98].

When exposed to fire, steel's temperature increases, reducing its strength and stiffness. This material response to fire can cause deformations and potential failure, depending on the loads applied, temperature profile, and support conditions. The severity of the fire, section factor (area of exposed steel), and amount and type of applied fire protection materials all influence the amount of temperature increase in steel [71].

Part 1-2 of Eurocode 3 [4] deals with the design of steel structure-general rules for the verification of resistance to fire. It supplements Eurocode 3 part 1-1 [7], which tackles the subject of steel structure design at room temperature, indicating distinctions and supplemental requirements of the influence of high temperatures on the structure material. It is essential to investigate the material in high-temperature situations because mechanical parameters such as modulus of elasticity, ultimate stress and yield stress change depending on the temperature to which it is exposed.

The study of steel behaviour at high temperatures makes it possible to accurately evaluate beam instability. The mechanical and thermal properties of steel, as presented in Eurocode 3 Part 1-2 [4], are then sequentially explained.

2.3.1. Mechanical properties

2.3.1.1. Strength and deformation properties

The strength and deformation properties of steel at elevated temperatures should be obtained from the stress-strain relationship given in Table 2-1 and shown in Figure 2-3.

The stress-strain diagram of steel at elevated temperatures, displayed in Figure 2-3, contains four distinct sections: Phase 1 exhibiting a linear response with a temperature-dependent elastic modulus ($E_{a,\theta}$) up to the proportional limit ($f_{p,\theta}$) which marks the point at which the curve changes from elastic to plastic. Phase 2 demonstrating an elliptical transition and shows the appearance of the yield stress of the material, it begins at the proportional limit ($f_{p,\theta}$), up until the maximum strength ($f_{y,\theta}$) is obtained at a strain of $\varepsilon_{y,\theta}$ (2%). Phase 3 exhibiting a constant stress level between $\varepsilon_{y,\theta}$ and $\varepsilon_{t,\theta}$ (which is defined in the Eurocode as 15%) which disregards the strain hardening of the steel. Phase 4 displaying a linear weakening to zero at the ultimate strain $\varepsilon_{u,\theta}$ (20% in the Eurocode) represents the rupture of the material, the loss of its strength, [99, 100].

Table 2-1. The relationship between stress and strain for carbon steel at elevated temperatures (reproduced from [4])

Strain range	Stress σ	Tangent modulus
$\varepsilon \leq \varepsilon_{p,\theta}$	$\varepsilon E_{a,\theta}$	$E_{a,\theta}$
$\varepsilon_{p,\theta} < \varepsilon < \varepsilon_{y,\theta}$	$f_{p,\theta} - c + (b/a) \left[a^2 - (\varepsilon_{y,\theta} - \varepsilon)^2 \right]^{0.5}$	$\frac{b(\varepsilon_{y,\theta} - \varepsilon)}{a \left[a^2 - (\varepsilon_{y,\theta} - \varepsilon)^2 \right]^{0.5}}$
$\varepsilon_{y,\theta} \leq \varepsilon \leq \varepsilon_{t,\theta}$	$f_{y,\theta}$	0
$\varepsilon_{t,\theta} < \varepsilon < \varepsilon_{u,\theta}$	$f_{y,\theta} \left[1 - (\varepsilon - \varepsilon_{t,\theta}) / (\varepsilon_{u,\theta} - \varepsilon_{t,\theta}) \right]$	-
$\varepsilon = \varepsilon_{u,\theta}$	0.00	-
Parameters	$\varepsilon_{p,\theta} = f_{p,\theta} / E_{a,\theta}$ $\varepsilon_{y,\theta} = 0.02$	$\varepsilon_{t,\theta} = 0.15$ $\varepsilon_{u,\theta} = 0.20$
Functions	$a^2 = (\varepsilon_{y,\theta} - \varepsilon_{p,\theta})(\varepsilon_{y,\theta} - \varepsilon_{p,\theta} + C / E_{a,\theta})$ $b^2 = C (\varepsilon_{y,\theta} - \varepsilon_{p,\theta}) E_{a,\theta} + C^2$ $C = \frac{(f_{y,\theta} - f_{p,\theta})^2}{(\varepsilon_{y,\theta} - \varepsilon_{p,\theta}) E_{a,\theta} - 2 (f_{y,\theta} - f_{p,\theta})}$	

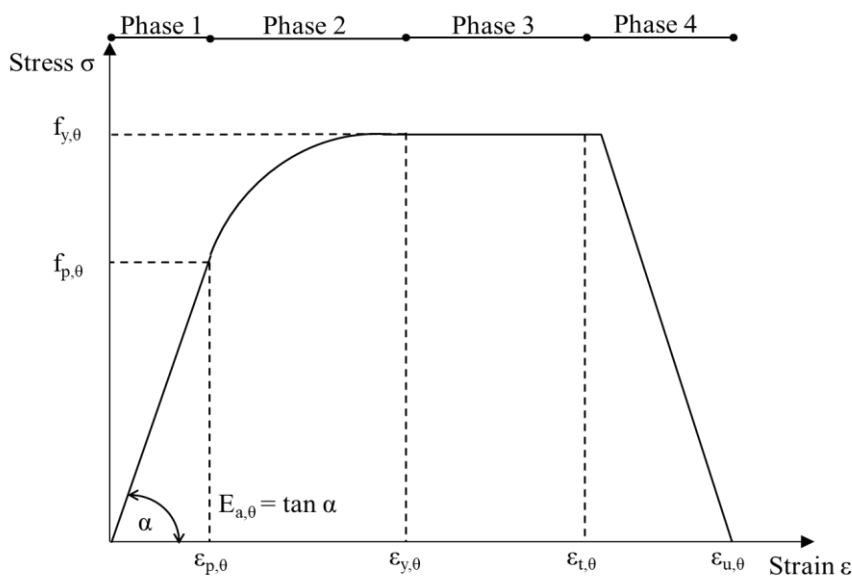


Figure 2-3. stress strain relationship for steel at elevated temperature (reproduced from Eurocode 3 part 1-2 [4])

These relationships are established based on the following three key factors:

- Effective yield strength, relative to yield strength at 20 °C: $k_{y,\theta} = f_{y,\theta} / f_y$
- Proportional limit relative to yield strength at 20 °C: $k_{p,\theta} = f_{p,\theta} / f_y$
- Slope of linear elastic range, relative to slope at 20°C: $k_{E,\theta} = E_{a,\theta} / E_a$

The reduction factors that are dependent on the temperature for these parameters are displayed in Table 2-2, and graphically in Figure 2-4.

Table 2-2. Reduction factors for stress-strain relationship of carbon steel at elevated temperatures (reproduced from EN 1993-1-2 [4])

Steel temperature θ_a	Reduction factors at temperature θ_a relative to the value of f_y or E_a at 20 °C		
	Reduction factor (relative to f_y) for effective yield strength $K_{y,\theta} = f_{y,\theta} / f_y$	Reduction factor (relative to f_y) for proportional limit $K_{p,\theta} = f_{p,\theta} / f_y$	Reduction factor (relative to E_a) for the slope of the linear elastic range $K_{E,\theta} = E_{a,\theta} / E_a$
20 °C	1.000	1.000	1.000
100 °C	1.000	1.000	1.000
200 °C	1.000	0.807	0.900
300 °C	1.000	0.613	0.800
400 °C	1.000	0.420	0.700
500 °C	0.780	0.360	0.600
600 °C	0.470	0.180	0.310

700 °C	0.230	0.075	0.130
800 °C	0.110	0.050	0.090
900 °C	0.060	0.0375	0.0675
1000 °C	0.040	0.0250	0.0450
1100 °C	0.020	0.0125	0.0225
1200 °C	0.000	0.0000	0.0000

Note: For intermediate values of the steel temperature, linear interpolation may be used.

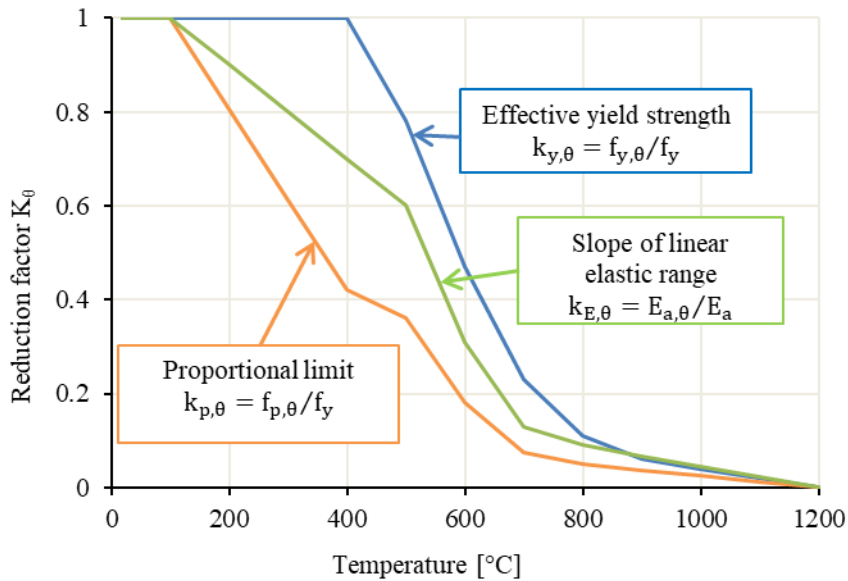


Figure 2-4. Reduction factors for the strain-stress relationship of carbon steel at elevated temperature (reproduced from [4])

The current work is based on the properties of S355 steel, and the curves of the stress-strain relationship at various temperatures are illustrated in Figure 2-5.

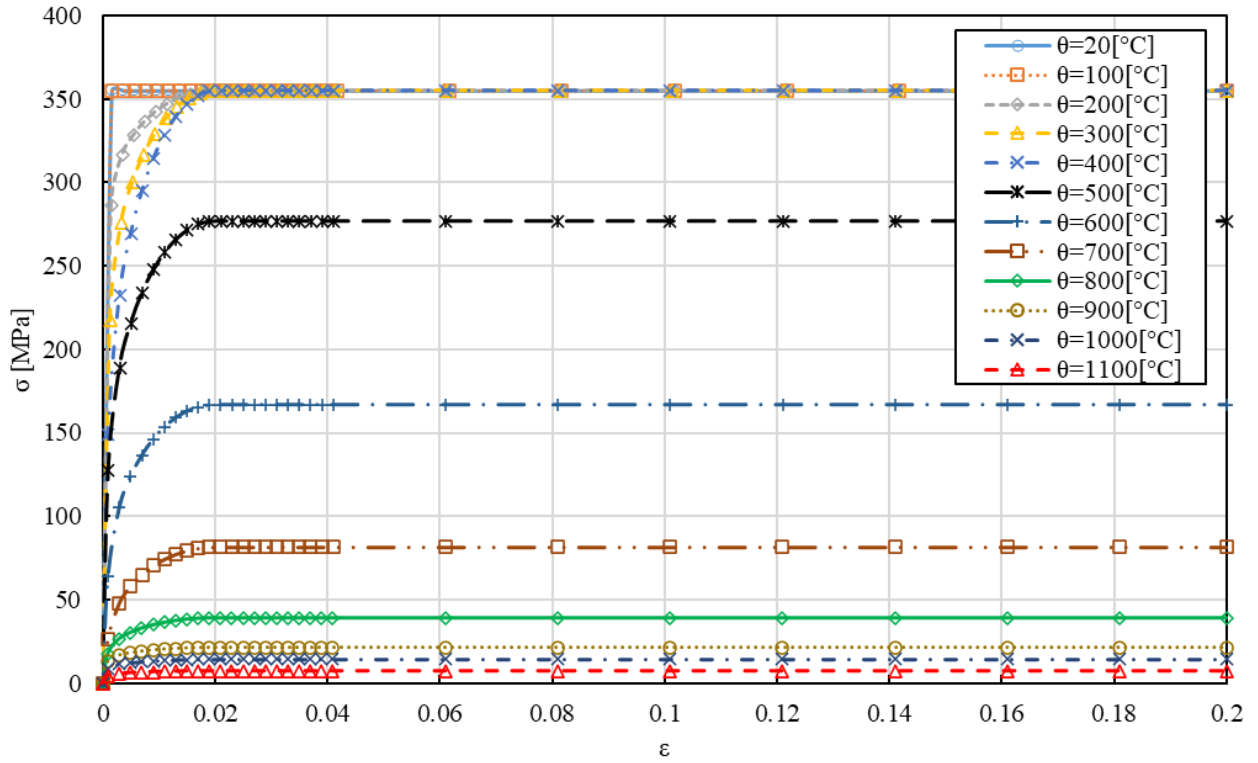


Figure 2-5. Stress- strain relationship of carbon steel S355 at elevated temperature.

2.3.1.2. Unit mass

The unit mass of steel is unaffected by changes in temperature and can be assumed to remain the same being equal to $\rho_a = 7850 \text{ kg/m}^3$ [4].

2.3.2. Thermal properties

2.3.2.1. Thermal elongation

When the temperature of a material changes, its size will either expand or shrink depending on the type of material. This phenomenon is known as "thermal expansion" and is defined as the alteration in shape, area, or volume of a material due to temperature variation. The cause of thermal expansion is the increased energy of the molecules and atoms that make up the material, resulting in them pushing further apart as they are heated, causing the material to expand. The thermal elongation of steel ($\Delta l/l$) is characterized in increments corresponding to its temperature as outlined by the standard [4], in equation (13). By following these equations for each temperature interval, the graph in Figure 2-6 is constructed.

$$\begin{aligned}
 20 \text{ }^\circ\text{C} \leq \theta_a < 750 \text{ }^\circ\text{C} \quad \Delta l/l &= 1.2 \times 10^{-5} \theta_a + 0.4 \times 10^{-8} \theta_a^2 - 2.416 \times 10^{-4} \\
 750 \text{ }^\circ\text{C} \leq \theta_a < 860 \text{ }^\circ\text{C} \quad \Delta l/l &= 1.1 \times 10^{-2}
 \end{aligned}
 \tag{13}$$

$$860\text{ }^{\circ}\text{C} \leq \theta_a < 1200\text{ }^{\circ}\text{C} \quad \Delta l/l = 2 \times 10^{-5} \theta_a - 6.2 \times 10^{-3}$$

Where: l is the length at 20°C ; Δl is the temperature induced elongation; θ_a is the steel temperature ($^{\circ}\text{C}$).

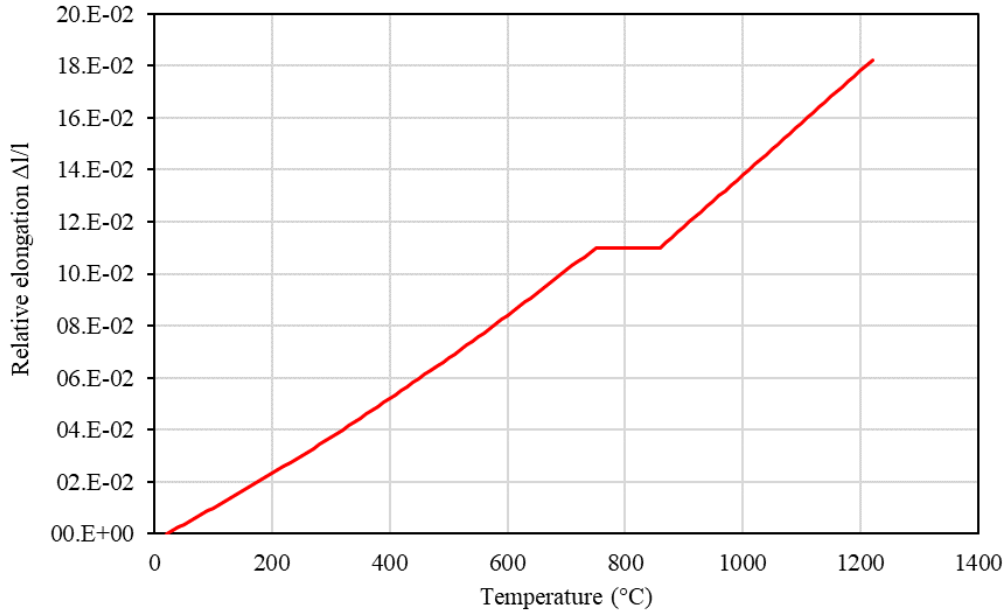


Figure 2-6. Temperature-dependent relative thermal elongation of carbon steel

2.3.2.2. Specific heat

The specific heat capacity of a substance is a measure of how much energy is required to increase the temperature of a unit mass (1 kg) of the material by 1 degree Celsius ($^{\circ}\text{C}$). It is affected by two parameters: the amount of a substance there is, mass, and the material itself. The specific heat capacity of a material indicates how its temperature will change when energy is applied, with a larger specific heat capacity indicating that more energy is required to produce the same temperature change. In other words, the specific heat capacity of a substance determines the amount of energy necessary to heat it by a certain amount. It is determined as a function of temperature according to the expression (14) [4]. Graphically, the variation of the specific heat with temperature using these expressions is illustrated in Figure 2-7.

$$20\text{ }^{\circ}\text{C} \leq \theta_a < 600\text{ }^{\circ}\text{C} \quad C_a = 425 + 7.73 \times 10^{-1} \theta_a - 1.69 \times 10^{-3} \theta_a^2 + 2.22 \times 10^{-6} \theta_a^3 \text{ J/kgK} \quad (14)$$

$$600\text{ }^{\circ}\text{C} \leq \theta_a < 735\text{ }^{\circ}\text{C} \quad C_a = 666 + \frac{13002}{738 - \theta_a} \text{ J/kgK}$$

$$735\text{ }^{\circ}\text{C} \leq \theta_a < 900\text{ }^{\circ}\text{C} \quad C_a = 545 + \frac{17820}{\theta_a - 731} \text{ J/kgK}$$

$$900\text{ }^{\circ}\text{C} \leq \theta_a < 1200\text{ }^{\circ}\text{C} \quad C_a = 650 \text{ J/kgK}$$

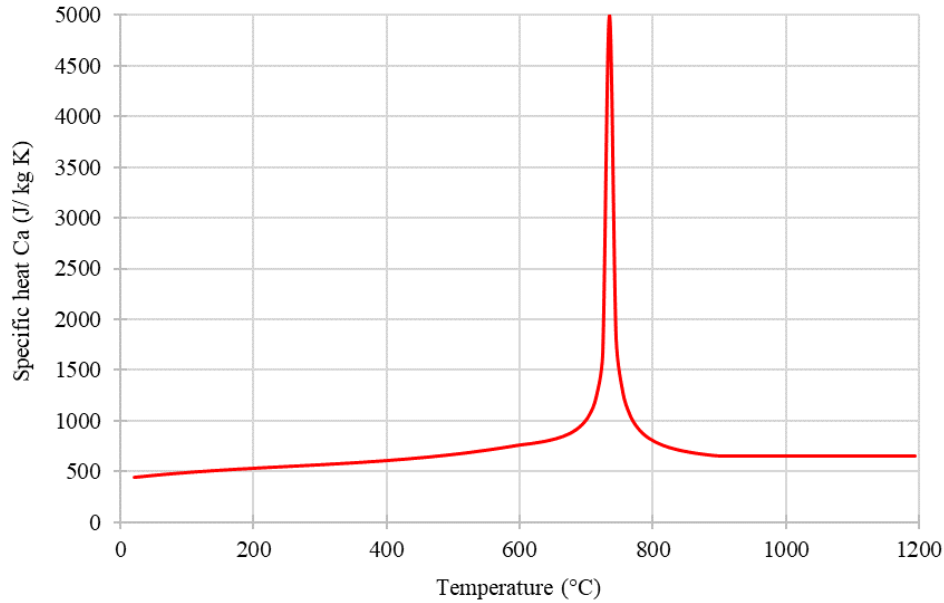


Figure 2-7. Specific heat of carbon steel as a function of the temperature

2.3.2.3. Thermal conductivity

Thermal conductivity refers to the ability of a material to conduct/or transfer heat from one location to another without the material itself undergoing any displacement. The thermal conductivity of steel λ_a (W/mK) is determined by equation (15). Graphically, its variation with temperature is shown in Figure 2-8.

$$\begin{aligned} 20\text{ }^{\circ}\text{C} \leq \theta_a < 800\text{ }^{\circ}\text{C} & \quad \lambda_a = 54 - 3.33 \times 10^{-2} \theta_a \text{ W/mK} \\ 800\text{ }^{\circ}\text{C} \leq \theta_a < 1200\text{ }^{\circ}\text{C} & \quad \lambda_a = 27.3 \text{ W/mK} \end{aligned} \tag{15}$$

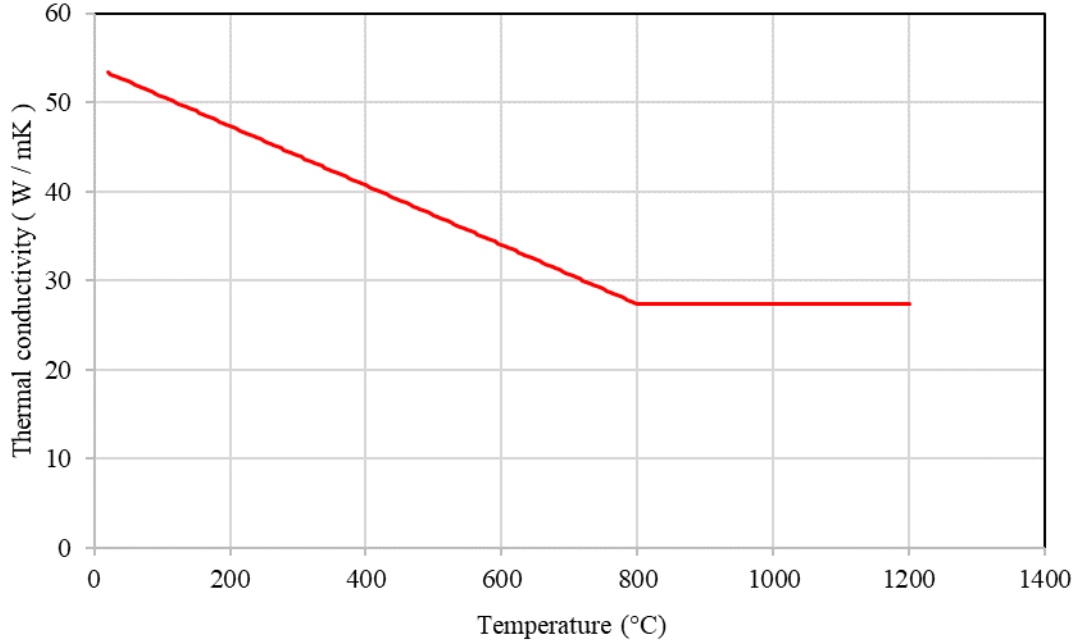


Figure 2-8. Thermal conductivity of carbon steel as a function of the temperature

2.4. Analysis of temperature changes in steel

In an unprotected steel member, for an equivalent uniform temperature distribution in the cross section, the increase of temperature $\Delta\theta_{a,t}$ in a small time interval Δt (up to 5 seconds) depends on the net amount of heat which the section acquires during this time. The increase is given according to the following equation [4, 101]:

$$\Delta\theta_{a,t} = k_{sh} \frac{A_m/V}{c_a \rho_a} \dot{h}_{net,d} \Delta t \tag{16}$$

Where: k_{sh} is correction factor for the shadow effect and is set to unity for conservative results. For I-section under normal fire conditions, it is given by equation (17), and for all other cases it is given as in equation (18).

$$k_{sh} = 0.9 [A_m/V]_b / [A_m/V] \tag{17}$$

$$k_{sh} = [A_m/V]_b / [A_m/V] \tag{18}$$

Where:

$[A_m/V]_b$ denotes the box value of the section factor. A_m/V is the section factor for unprotected steel members (1/m), it represents the effect of the geometry of the steel section and the

condition of its exposure to fire [102]; A_m is the surface area of the member per unit length (m^2/m), V is the volume of the member per unit length (m^3/m);

c_a is the specific heat of steel (J/kgK) (see section 2.3.2.); ρ_a is the unit mass of steel (kg/m^3), see section (2.3.1.); $\dot{h}_{net,d}$ is the design value of the net heat flux per unit area (W/m^2); Δt is the time interval in seconds.

The thermal action on a structural member is the heat flux into the member [101]. On the fire exposed surfaces, the net heat flux $\dot{h}_{net,d}$ to the surface of a member is given in equation (19) as the sum of the heat transfer by convection $\dot{h}_{net,c}$ and radiation $\dot{h}_{net,r}$ [95].

$$\dot{h}_{net,d} = \dot{h}_{net,c} + \dot{h}_{net,r} \quad (19)$$

Where: $\dot{h}_{net,c}$ is the net convective heat flux component and is given by equation (20).

$$\dot{h}_{net,c} = \alpha_c (\theta_g - \theta_m) \quad (W/m^2) \quad (20)$$

θ_m is the surface temperature of the member ($^{\circ}C$).

$\dot{h}_{net,r}$ is the net radiative heat flux component per unit surface area and is given by equation (21).

$$\dot{h}_{net,r} = \phi \cdot \varepsilon_m \cdot \varepsilon_f \cdot \sigma \cdot [(\theta_r + 273)^4 - (\theta_m + 273)^4] \quad (W/m^2) \quad (21)$$

Where: Φ is the configuration factor; σ is the Stephan Boltzmann constant (equals to $5.67 \cdot 10^{-8} W/m^2K^4$); ε_m is the surface emissivity of the member; ε_f is the emissivity of the fire; and θ_r is the effective radiation temperature of the fire environment ($^{\circ}C$).

2.5. Fire resistance verification

For mechanical analysis, Eurocode 1 Part 1-2 defines three types of fire safety verification domains with which the structure must comply [95].

- Time domain: the structure must have a fire resistance time that exceed the design time required, which varies based on the building's level of occupancy. For larger buildings, hosting a greater number of users, a prolonged fire resistance time should be provided to allow for an adequate evacuation period.

$$t_{fi,d} \geq t_{fi,requ} \quad (22)$$

Where: $t_{fi,d}$ is the design value of the fire resistance; $t_{fi,requ}$ is the required fire resistance time.

- Strength domain: At the point in time required to account for a potential fire situation, the element's resistance must be greater than the calculated values of the effects of the fire-situation actions at the same instant. This ensures that a safety margin is always imposed, and that the first domain is met.

$$R_{fi,d,t} \geq E_{fi,d,t} \quad (23)$$

Where: $R_{fi,d,t}$ is the design value of the resistance of the member in the fire situation; $E_{fi,d,t}$ is the design value of the relevant effects of actions in the fire situation, both at time t .

- Temperature domain: leads you through the design process for a material temperature lower than its critical temperature.

$$\theta_d \leq \theta_{cr,d} \quad (24)$$

Where: θ_d is the design value of material temperature; $\theta_{cr,d}$ is the design value of the critical material temperature.

2.6. Design rules for the resistance of steel solid and cellular beams

2.6.1. Design guidelines

Some general guidance on the design of beams with web openings is provided in: Annex N “Ouvertures dans les âmes” of Eurocode NF EN1993-1-1 (2002) [2]; SCI publication P355 (2011), “Design of composite beams with large web openings: in accordance with Eurocodes and the UK National Annexes” [8]; the new Eurocode part currently under development: draft EN1993-1-13 – CEN/TC 250/SC 4 N 1839 (2017), “Web Openings in Steel Beams EC3 Part 1-13”[3]; and, within the scope of EN 1993-1-13, a new normative appendix, Annex F, on Beams with Large Web Openings, is included in the updated first draft of pr-EN 1993-1-2 [5], in which the section factors for the different failure mechanisms of the cellular beam in fire were the focal point.

For this research, solid and cellular beams were designed using the expressions laid out in Eurocode 3 Part 1-1 [7]. Since the standard does not include any explicit expressions for designing cellular beams, this was supplemented by the provisions of the SCI Guide P355 [8], along with guidance from academic literature in the form of referenced articles. The SCI P355 provides detailed manuals on the design of cellular beams as well as methods for their

strength determination based on the principles and terminology of Eurocodes 3 and 4, which have been experimentally verified.

2.6.2. Geometric properties of gross and net cross-sections

The geometrical characteristics of a cellular beam fluctuate depending on what is needed in the design, so this alteration in size is researched in this paper to recognize its impact on the ultimate strength. Because of this, it is essential to assign names to each beam component. Figure 2-9 comprehensively illustrate the components of a cellular beam and the key dimensions.

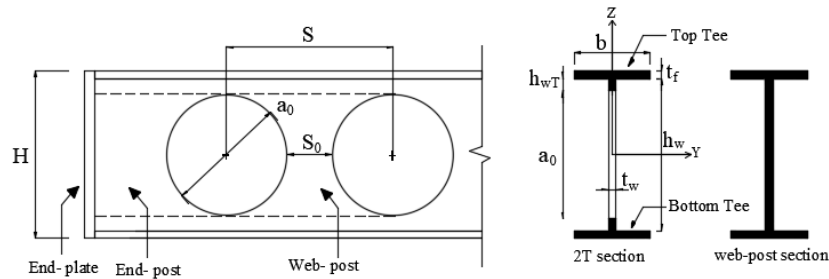


Figure 2-9. Geometric properties of cellular steel beams

The geometric dimensions of the above shown beam are overall breadth (b); flange thickness (t_f); web thickness (t_w); web opening diameter (a_0); final height (H); web depth of solid web section ($h_w = H - 2 * t_f$); web depth of one Tee-section ($h_{wT} = h_w/2 - a_0/2$); spacing between the web openings (S); web post width (S_0). The net section corresponds to the 2T cross-section at the opening's location in a cellular beam, and the gross section is the I-cross section's overall area, excluding any holes within the cross section.

The 2T approach is adopted for the strength calculations of the cross-section of a symmetrical cellular beam, with the corresponding characteristics computed at the centre of the opening of its web.

Equations (25) to (53) can be used to calculate the geometry characteristics including gross, net, and inclined cross-sections, without accounting for the radius of constancy between the web and the flange.

2.6.2.1. Gross cross-section

- Area of web

$$A_w = h_w * t_w \quad (25)$$

- Area of one flange

$$A_f = b * t_f \quad (26)$$

- Cross-sectional area

$$A = A_f + A_w \quad (27)$$

- Shear area for rolled I and H sections, load parallel to web [7]

$$A_V = A - 2 b t_f + t_w \times t_f \quad (28)$$

- Plastic section modulus

$$W_{pl.y} = \frac{t_w H^2}{4} + (b - t_w)(H - t_f)t_f \quad (29)$$

- Second moment of area about the major axis y-y

$$I_y = \frac{1}{12} [bH^3 - (b - t_w)(H - 2t_f)^3] \quad (30)$$

- Second moment of area about the minor axis z-z

$$I_z = \frac{1}{12} [2 t_f b^3 + (H - 2 t_f) t_w^3] \quad (31)$$

- St. Venant torsional constant

$$I_t = \frac{2}{3} (b - 0.63 t_f) t_f^3 + \frac{1}{3} (H - 2 t_f) t_w^3 + 2 \left(\frac{t_w}{t_f} \right) (0.145) \left[\frac{(t_w/2)^2 + (t_f)^2}{t_f} \right]^4 \quad (32)$$

- warping constant

$$I_w = \frac{t_f b^3}{24} \times (H - t_f)^2 \quad (33)$$

2.6.2.2. Net cross-section

- Area of web

$$A_{wT} = h_{wT} * t_w \quad (34)$$

- Area of one flange

$$A_f = b * t_f \quad (35)$$

- Cross-sectional area

$$A_T = A_f + A_{wT} \quad (36)$$

- Shear area for rolled Tee section, load parallel to web

$$A_{V.T} = A_T - b t_f + (t_w) \frac{t_f}{2} \quad (37)$$

- Plastic section modulus

$$W_{pl.y.2T} = (A_T Z_c) * 2 \quad (38)$$

Where: Z_c is the centroid of a Tee Section and calculated as the following:

$$Z_c = \frac{(A_f (h_w + t_f)/2 + A_{wT}(h_{wT}/2 + a_0/2))}{(A_f + A_{wT})} \quad (39)$$

- The distance between the plastic neutral axis and the extreme fibre of the steel flange of a Tee section [8]

$$z_{pl} = (A_f + A_{w.T})/(2b) \quad (40)$$

- Second moment of area of a Tee section, $I_{y,1T}$, and of the cross-section, $I_{y,2T}$, about the major axis y-y [58]

$$I_{y,1T} = \frac{b t_f^3}{12} + A_f \left(\frac{h_w}{2} + \frac{t_f}{2} \right)^2 + \frac{t_w h_{wT}^3}{12} + A_{wT} \left(\frac{h_{wT}}{2} + \frac{a_0}{2} \right)^2 \quad (41)$$

$$I_{y.2T} = 2 I_{y.1T} \quad (42)$$

- Second moment of area of a Tee section, $I_{z.1T}$, and of the cross-section, $I_{z.2T}$, about the minor axis z-z [58]

$$I_{z.1T} = \frac{t_f b^3}{12} + \frac{h_w t_w^3}{12} \quad (43)$$

$$I_{z.2T} = 2 I_{z.1T} \quad (44)$$

- St. Venant torsional constant [58]

$$I_{t.2T} = \frac{2}{3} b_f t_f^3 + \frac{1}{3} (h_w - a_0) t_w^3 \quad (45)$$

- warping constant [58]

$$I_{w.2T} = \frac{t_f b_f^3 (h_w + t_f)^2}{24} - \frac{(a_0 t_w)^3}{144} \quad (46)$$

2.6.2.3. Inclined cross-section

- The height of section [11]

$$h_\phi = (H/2)/\cos\phi - a_0/2 \quad (47)$$

- Area of web [11]

$$A_{\phi.w.T} = (h_\phi - t_f/\cos\phi) * t_w \quad (48)$$

- Area of one flange [11]

$$A_{\phi.f} = b * (t_f/\cos\phi) \quad (49)$$

- Cross sectional area

$$A_{\phi.T} = A_{\phi.f} + A_{\phi.w.T} \quad (50)$$

- Shear area for rolled inclined Tee section [11]

$$A_{\phi,V} = A_{\phi,T} - b(t_f/\cos\phi) + (t_w + 2r)(t_f/2\cos\phi) \quad (51)$$

- Plastic section modulus

$$w_{\phi,pl,1T} = A_{\phi,w,T} \left(0.5 \left(h_{\phi} - \left(\frac{t_f}{\cos\phi} \right) \right) + \left(\frac{t_f}{\cos\phi} \right) - z_{\phi,pl} \right) + A_{\phi,f} \left(0.5 \left(\frac{t_f}{\cos\phi} \right) - z_{\phi,pl} + \frac{z_{\phi,pl}^2}{(t_f/\cos\phi)} \right) \quad (52)$$

- The distance between the plastic neutral axis and the extreme fibre of the steel flange of the inclined Tee [62]

$$z_{\phi,pl} = (A_{\phi,f} + A_{\phi,w,T})/(2b) \quad (53)$$

2.6.3. Classification of cross-sections

The purpose of cross section classification is to determine how much the resistance and rotation capacity of cross sections is limited by its local buckling resistance [7].

There are four classes of cross-sections, from the heaviest to the slenderest:

- Class 1 cross-sections are those that can form a plastic hinge with the rotational capacity required from plastic analysis while maintaining resistance.
- Class 2 cross sections are those that can evolve their plastic moment resistance $M_{pl,Rd}$ but, because to local buckling, have limited rotation capacity.
- Class 3 cross sections are the ones in which, assuming an elastic distribution of stresses, the stress in the extreme compression fibre of the steel member can exceed the yield strength, but local buckling is likely to prevent the plastic moment resistance from developing. The plastic moment resistance is reduced to the elastic moment resistance $M_{el,Rd}$.
- Class 4 cross sections have local buckling before the cross section achieves yield stress in one or more areas.

2.6.3.1. Gross cross section

The class to which a cross-section belongs depends on the width-thickness ratio of its compressed web or flanges, the loading type (compression, bending, compound bending) and the yield strength of the material. According to [7], the cross-section can be classified as presented in Table 2-3.

Table 2-3. Maximum width-to-thickness ratios for compression parts

		Class 1		Class 2		Class 3	
A member in bending	Web-post $d/t_w \leq$	72 ϵ		83 ϵ		124 ϵ	
A member in compression	Flange $c/t_f \leq$	9 ϵ		10 ϵ		14 ϵ	
$\epsilon = \sqrt{235/f_y}$		f_y	235	275	355	420	460
		ϵ	1.00	0.92	0.81	0.75	0.71

Where: d is the depth of straight portion of a web measured from the root radius, $d = h - 2 * (t_f + r)$; C is the width of a part of a cross-section (flange), $c = (b - t_w)/2 - r$, r is the root radius; ϵ : factor depending on f_y , see Figure 2-10.

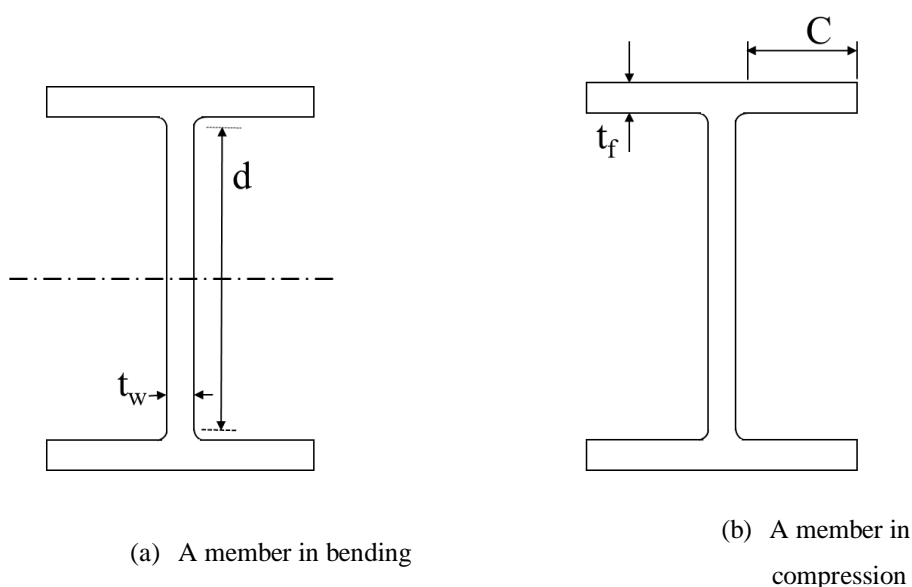


Figure 2-10. Maximum width-to-thickness ratios for compression parts.

2.6.3.2. Net cross-section

To establish the resistance of perforated sections in particular, classification criteria was defined first in Appendix N, §§N.1.7.2 (3), of the previous version ENV of the Eurocodes [2]

in terms of the yield level at failure and the possibility of occurrence of local buckling at the compressed upper tee. According to this classification, perforated cross-sections were classified according to the web outstand of the Tee at the opening. Considering the same assumptions, the web outstand at the opening classification was then developed [3] based on a loading type criterion: Tees subject to global bending or to Vierendeel bending.

Each cellular beam's section classification at an opening position is established for an angle $\phi=0^\circ$ [11].

- Section classification of Tees subject to global bending

It is sufficient for the unstiffened webs of tees above and below apertures to be class 2 or 3 in the absence of mechanism Vierendeel.

In pure bending, where the section has flanges of class 1 or 2, the unstiffened web outstand at the opening can be considered as Class 2 by omitting the outstand depth, d_t , in compression higher than $10 t_w \varepsilon$. Where the flange is Class 3, the unstiffened web outstand can be considered as Class 3 by omitting the outstand depth, d_t , in compression higher than $14 t_w \varepsilon$.

- Tees sections classification subjected to Vierendeel bending.

For local verification of shear transmission at the opening by Vierendeel bending, the outstand part of the web-post is classified in respect to the ratio of the Tee's effective length at the opening, a_t , to the outstand depth, d_t .

The parameter, a_t , varies depending on the form of the apertures where:

$$a_t = a_0 \text{ for rectangular openings}$$

$$a_t = 0.7 a_0 \text{ for circular and hexagonal openings}$$

$$a_t = a_0 - 0.3 h_0 \text{ for elongated circular openings}$$

$$a_t = b_0 + 0.5 b_s \text{ sinusoidal and extended hexagonal openings.}$$

The criterion for classification is then defined as follows:

- Class 3 web outstands should be classified as Class 2 if the following conditions are met:

$$\text{For: } a_t > 32 t_w \varepsilon, d_t \leq \frac{10 t_w \varepsilon}{\sqrt{1 - \left(\frac{32 t_w \varepsilon}{a_t}\right)^2}}$$

Class 3 web outstands should be classified as Class 2 when $a_t \geq 32 t_w \varepsilon$.

- Class 4 web outstands should be classified as Class 3 if the following conditions are met:

$$\text{For } a_t > 36\epsilon t_w, d_t \leq \frac{14 t_w \epsilon}{\sqrt{1 - \left(\frac{36 t_w \epsilon}{a_t}\right)^2}}$$

Class 4 web outstands should be classified as Class 3 when $a_t \geq 36\epsilon t_w$.

For Class 4 web outstands, the limiting value of d_t for a Class 3 web can be used to compute the effective elastic section characteristics.

Design according to [12, 13] is conducted when considering the final height H for the solid/cellular cross sections with the same class 1 or 2 as the original parent section.

2.6.4. Design resistance at ambient temperature

2.6.4.1. Plastic bending design resistance

The plastic bending design resistance ($M_{pl,Rd}$) for solid cross-section is based on the formulation available in EC3-1-1 clause 6.2.5 [7], which is determined by its geometric dimensions and by the yield stress of the material it is composed of.

$$M_{c,Rd} = M_{pl,Rd} = \frac{w_{pl,y} f_y}{\gamma_{M0}} \quad (54)$$

Where: f_y is the yield strength at 20 °C, γ_{M0} is partial factor for resistance of cross-sections whatever the class is equal to 1.

For the cellular beam in section of two tees, the flexural bending design resistance is calculated following the same methodology as for the solid beam calculation, as specified by equation (55).

$$M_{PL,Rd,2T} = w_{pl,2T} f_y / \gamma_{M0} = 2 A_T Z_c f_y / \gamma_{M,0} \quad (55)$$

Where: $w_{pl,2T}$ is the plastic section modulus of the two Tee sections; Z_c is the distance between the local centroid of one Tee section's area and the global one; A_T is the area of one Tee section, A_f is the area of the flange of one Tee; A_{wT} is the area of the web of one Tee section, as outlined in section 2.6.2.

When dealing with circular openings, the design bending resistance of the web-post is greatly influenced by the width of the web-post, as the wider the post, the lower its slenderness ratio

and thus the higher its resistance. To ensure the highest degree of resistance, the design bending resistance should be taken as its elastic value, as defined by equation (56) [8].

$$M_{wp,Rd} = \frac{S_0^2 t_w f_y}{6\gamma_{M,o}} \quad (56)$$

2.6.4.2. Plastic shear resistance

The design plastic shear resistance for gross cross-section, $V_{pl,Rd}$, is determined as by EC3-1-1 clause 6.2.6, and include the shear resistance for net cross-section [7]. This dictates that the shear strength should be computed using the shear area of the beam cross-section (A_v , $A_{v,T}$) and its yield strength.

$$V_{pl,Rd} = \frac{A_v (f_y / \sqrt{3})}{\gamma_{M0}} \quad (57)$$

$$V_{pl,Rd,2T} = 2 A_{v,T} (f_y / \sqrt{3}) / \gamma_{M0} \quad (58)$$

Where: A_v and $A_{v,T}$ are the shear areas for rolled I and H sections and of one tee section, respectively.

When determine the design longitudinal shear resistance of the web-post, equation (59) considers not only the yield stress, but also the area of the web post, as it is the area that resists this effect [8].

$$V_{wp,Rd} = \frac{(S_0 t_w) f_y / \sqrt{3}}{\gamma_{M0}} \quad (59)$$

2.6.4.3. Lateral torsional buckling resistance

For solid and cellular members, the lateral torsional buckling resistance ($M_{b,Rd}$) of a laterally unrestricted beam is determined using the equation (**Error! Reference source not found.**) [3, 7]. The only difference lies in the values assigned to the geometric section's parameters, such as the torsion constant and warping constant, which have already been specified earlier.

$$M_{b,Rd} = \chi_{LT} w_{pl,y} \frac{f_y}{\gamma_{M1}} \quad (60)$$

Where: $w_{pl,y}$ is the plastic section modulus of the gross and the 2T sections respectively; γ_{M1} is a partial safety factor equal to 1; χ_{LT} is the reduction factor for lateral-torsional buckling

which can be calculated according to the “general case” of EC3, and given by equation (Error! Reference source not found.).

$$\chi_{LT} = \frac{1}{\Phi_{LT} + \sqrt{\Phi_{LT}^2 - \bar{\lambda}_{LT}^2}} \quad \text{but } \chi_{LT} \leq 1.0 \quad (61)$$

With $\Phi_{LT} = 0.5[1 + \alpha_{LT}(\bar{\lambda}_{LT} - 0.2) + \bar{\lambda}_{LT}^2]$, α_{LT} the imperfection factor related the appropriate buckling curve, defined by Table 2-4, and $\bar{\lambda}_{LT}$ is the appropriate non-dimensional slenderness given by equation (62).

$$\bar{\lambda}_{LT} = \sqrt{\frac{w_{pl,y} f_y}{M_{cr}}} \quad (62)$$

Table 2-4. Recommended values for imperfection factors for lateral torsional buckling curves [3]

Buckling curve	a	b	c	d
Imperfection factor α_{LT}	0.21	0.34	0.49	0.76

To determine which curve to use for a given section geometry and beam type, one should consult Table 5.

Table 2-5. Recommended values for lateral torsional buckling curves for cross-sections [3]

Cross-section	Limits	Buckling curve
Rolled I-sections	$h/b \leq 2$	a
	$h/b > 2$	b
Welded I-sections	$h/b \leq 2$	c
	$h/b > 2$	d
Other cross--sections	-	d

M_{cr} is the elastic critical moment calculated as the maximum value of bending moment supported by a beam free from any type of imperfections [103]. M_{cr} for the net section is determined by the beam geometry, support conditions, and moment diagram, and is calculated taking into account the torsion constant (I_t), and the warping constant (I_w) according to [58] using the following equation (63) .

$$M_{cr} = C_1 \frac{\pi^2 EI_z}{(k_z L)^2} \left\{ \sqrt{\left[\left(\frac{k_z}{k_w} \right)^2 \frac{I_w}{I_z} + \frac{(k_z L)^2 GI_t}{\pi^2 EI_z} + (C_2 Z_g)^2 \right]} - C_2 Z_g \right\} \quad (63)$$

With $G = E/[2(1 + \nu)]$, G being the shear modulus, E the Young modulus, ν the Poisson's coefficient, I_z is the second moment of area about the weak axis, k_z and k_w are effective length factors, L is the beam length between points which have lateral restraint, C_1 , C_2 are factors depending on the loading and end restraint conditions, I_w is the warping constant, I_t is the torsion constant, Z_g is the distance between the point of load application and the shear centre.

The values of k_z and k_w are equal to 1.0 for the case where fork support is present at both ends, which prevents lateral displacements and torsion-type rotation. When the bending moment diagram is linear along a segment of a member delimited by lateral restraints, or when the transverse load is applied in the shear centre, $C_2 Z_g = 0$. The latter expression should be simplified to:

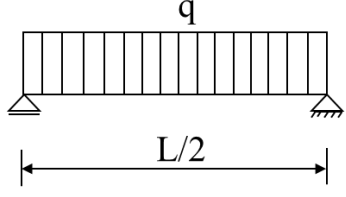
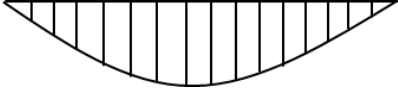
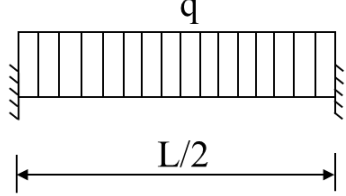
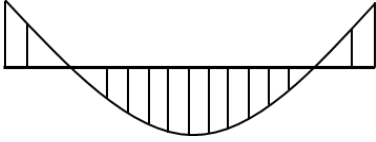
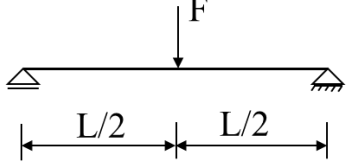
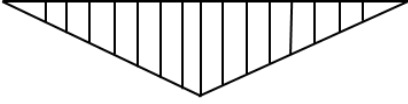
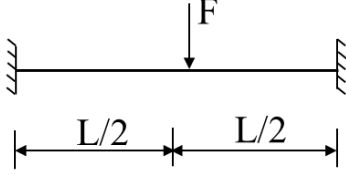
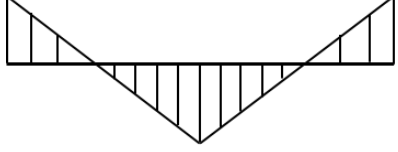
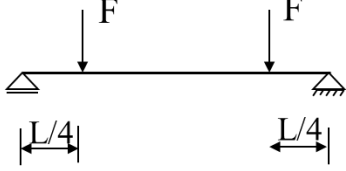

$$M_{cr} = C_1 \frac{\pi^2 EI_z}{(L)^2} \left\{ \sqrt{\left[\frac{I_w}{I_z} + \frac{(L)^2 GI_t}{\pi^2 EI_z} \right]} \right\} \quad (64)$$

The values of the C_1 , C_2 , and C_3 Factors, which are dependent on the loading and restraint conditions, can be found in Table 2-6. For beam with end moments loading, C_1 factor equals to 1. And for the beams with distributed loading, C_1 and C_2 took values of 1.132 and 0.459 respectively.

CHAPTER 2. FIRE SAFETY AND STEEL STRUCTURES

Table 2-6. Values of factors C1, C2, and C3 for moment diagrams due to type of load and support conditions

[103]

Type of load and support conditions	Moment diagram	Value of k	Value of factors		
			C ₁	C ₂	C ₃
		1.0 0.5	1.132 0.972	0.459 0.304	0.525 0.980
		1.0 0.5	1.285 0.712	1.562 0.652	0.753 1.070
		1.0 0.5	0.365 1.070	0.553 0.432	1.730 3.050
		1.0 0.5	1.565 0.938	1.267 0.715	2.640 4.800
		1.0 0.5	1.046 1.010	0.430 0.410	1.120 1.890

2.6.4.4. Web post buckling resistance

The capacity of a web post subjected to buckling is influenced by a variety of geometric characteristics, such as the size and shape of the opening (whether it is circular or rectangular), the width and thickness of the web-post, and the asymmetry of the positioning of the opening in the height of the beam [8, 104]. Its strength, $N_{wp,Rd}$, is computed using Equation (65) from [8].

$$N_{wp,Rd} = \chi \frac{S_0 t_w f_y}{\gamma_{M1}} \quad (65)$$

Where χ is the reduction factor associated with the buckling mode considered and is defined in [7] as:

$$\chi = \frac{1}{\Phi + \sqrt{\Phi^2 - \bar{\lambda}^2}} \text{ but } \chi \leq 1.0 \quad (66)$$

$$\Phi = 0.5[1 + \alpha(\bar{\lambda} - 0.2) + \bar{\lambda}^2] \quad (67)$$

Where ϕ is a value for determining the χ coefficient, λ is the normalized slenderness, and α is the imperfection factor.

The normalized slenderness is calculated based on the width of the web post, depending on whether the openings are widely or closely spaced. It is recommended that Curve "b" be chosen for determining the imperfection factor α in cellular beams of hot rolled sections, while Curve "c" should be chosen for cellular beams manufactured from steel plates [8].

- For widely spaced circular openings:

$$\bar{\lambda} = \frac{2.5 h_0}{t_w} \frac{1}{\lambda_1} \quad (68)$$

- For closely spaced circular openings

$$\bar{\lambda} = \frac{1.75\sqrt{S_0^2 + h_0^2}}{t_w} \frac{1}{\lambda_1} \quad (69)$$

λ_1 being the slenderness value to determine the relative slenderness, and is defined in EN 1993-1-1 by equations (70) [8] as being:

$$\lambda_1 = \sqrt{(E/f_y)} = 94 \varepsilon \quad (70)$$

$$\varepsilon = \sqrt{(235/f_y)} \quad (71)$$

Where: ε is a factor depending on f_y .

2.6.4.5. Resistance of the tees in Vierendeel mechanism

Under the Vierendeel action, four plastic hinges in the Tee-sections above and below the web holes forms, resulting in the 'Vierendeel' mechanism. In order to define the scope of the rules of computing the load carrying capacity of a cellular beam based on Vierendeel failure, the

annex N from Eurocode EN 1993-1-1:2002 [2] addresses a method of calculation for the net section resistance, but lacks the consideration of the verification of the local conditions at the openings. As an alternative, methods are provided for rolled beams with circular and sinusoidal openings, in which the forces and resistances can be checked in increments around or along the openings, making them suitable for computer methods. In addition, an improved method for Vierendeel bending that applies to circular openings has been introduced in the new Eurocode part : draft EN1993-1-13 [3].

Due to the global bending moment M_{Ed} and shear force V_{Ed} at the centre line of the aperture, Figure 2-11, the perforated section at angle ϕ is subjected to three co-existing actions: axial force $N_{\phi,Ed}$, shear force $V_{\phi,Ed}$ and local bending moment $M_{\phi,Ed}$, Figure 2-12. Equilibrium of these local actions in the tee section is determined using a linear interaction formula in accordance with [3]:

$$\frac{N_{\phi,Ed}}{N_{\phi,Rd,1T}} + \frac{M_{\phi,Ed}}{M_{\phi,Rd,1T}} \leq 1.0 \quad (72)$$

Where: $N_{\phi,Rd,1T}$, $M_{\phi,Rd,1T}$ are design resistances of the Tee section at an angle ϕ from the vertical centre line. $N_{\phi,Ed}$, $M_{\phi,Ed}$ are design values of the axial force and bending moment, respectively in the Tee section at an angle ϕ from the vertical centre line.

The $N_{\phi,Ed}$, $M_{\phi,Ed}$ is calculated in accordance with [62] given by equations (74) and (75) respectively, noting that the resistance of each inclined section at an angle ϕ is measured by changing this angle from $-\phi_{max}$ to $+\phi_{max}$ in increment of 1° to 5° , so that ϕ_{max} is calculated as presented in Equation (73). The perforated sections moment can be defined according to sides, with the lower moment side (LMS) on the left and the high moment side (HMS) on the right (HMS).

$$\Phi_{max} = \text{Arctg} \left(\frac{a_0 + w}{2 * h_m} \right) = \text{Arctg} \left(\frac{S}{H} \right) \quad (73)$$

$$N_{\phi,Ed} = (N_{Ed}) \cos \phi - (V_{Ed}/2) \sin \phi \quad (74)$$

$$M_{\phi,Ed} = (V_{Ed}/2)(H/2 - \bar{y}_\phi \cos \phi) \tan \phi + (N_{Ed})(\bar{y}_\phi \cos \phi - \bar{y}) \quad (75)$$

N_{Ed} , V_{Ed} , and M_{Ed} are the global forces that distributed between the upper and lower members to the right of an opening, Figure 2-12, in which, N_{Ed} is the design value of the axial force in the Tee section at the vertical centre line due to the global bending action calculated

by equation (76); M_{Ed} is the design value of the bending moment at the centreline of the opening calculated by equation (77); V_{Ed} is the design value of the shear force acting on the beam at the opening calculated by equation (78).

$$N_{Ed} = M_{Ed}/d' \quad (76)$$

$$M_{Ed}(x) = q(Lx/2 - x^2/2) \quad (77)$$

$$V_{Ed}(x) = q(L/2 - x) \quad (78)$$

Where: q is the load bearing capacity at the inclined section; d' is the vertical centre line distance between the centroid of the top and bottom Tee sections, $d' = H - 2\bar{y}$; \bar{y} is the distance from the top edge to centroid of a tee section along the vertical centre line of the hole; \bar{y}_ϕ is the distance from the top edge to centroid of a tee section along a line at angle θ from vertical calculated as following [62]:

$$\bar{y}_\phi = \frac{b(t_f/\cos\phi)^2 + t_w(h_\phi^2 - (t_f/\cos\phi)^2)}{2A_{\phi,T}} \quad (79)$$

The axial force resistance of the tee section of a cellular beam, $N_{Rd,1T}$ is calculated using the equation (80), in the same way that the compression resistance of a cross section is calculated in the standard EN 1993-1-1 clause 6.2.4 [7]. Thus, the axial force resistance of the Tee section at an angle ϕ from the vertical centre line can be calculated by equation (80).

$$N_{Rd,1T} = A_T f_y / \gamma_{M0} \quad (80)$$

$$N_{\phi,Rd,1T} = A_{\phi,T} f_y / \gamma_{M0} \quad (81)$$

Where: $A_{\phi,T}$ is the cross-sectional area of a inclined tee section (see Section 2.6.2).

According to SCI-P355 clause 3.4.4 [8], the plastic bending resistance of a top or bottom Tee section in the absence of axial force can be determined using expression (82). Similarly, the bending resistance resisting the Vierendeel bending moment in the Tee section at an angle ϕ from the vertical centre is calculated in the form of the equation (83).

$$M_{Rd,1T} = \frac{W_{pl,1T} f_y}{\gamma_{M0}} \quad (82)$$

$$M_{\phi,Rd,1T} = W_{\phi,pl,1T} f_y / \gamma_{M0} \quad (83)$$

Where: $w_{\theta,pl,1T}$ is plastic section modulus of an inclined Tee section; $z_{\phi,pl}$ is the distance between the plastic neutral axis and the extreme fibre of the steel flange of the inclined Tee section (see Section 2.6.2. .

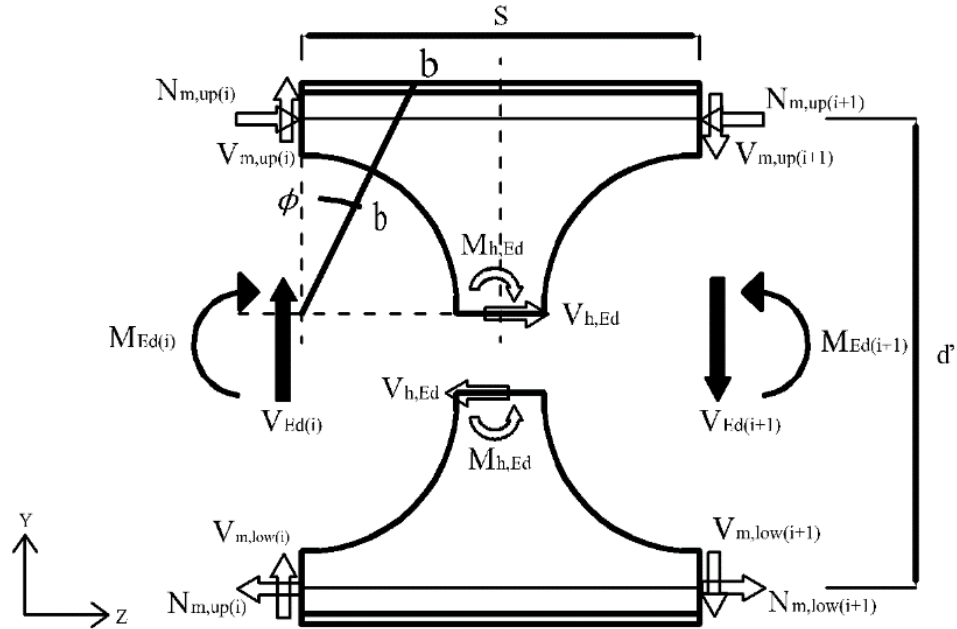


Figure 2-11. Internal forces and moments acting on Tees.

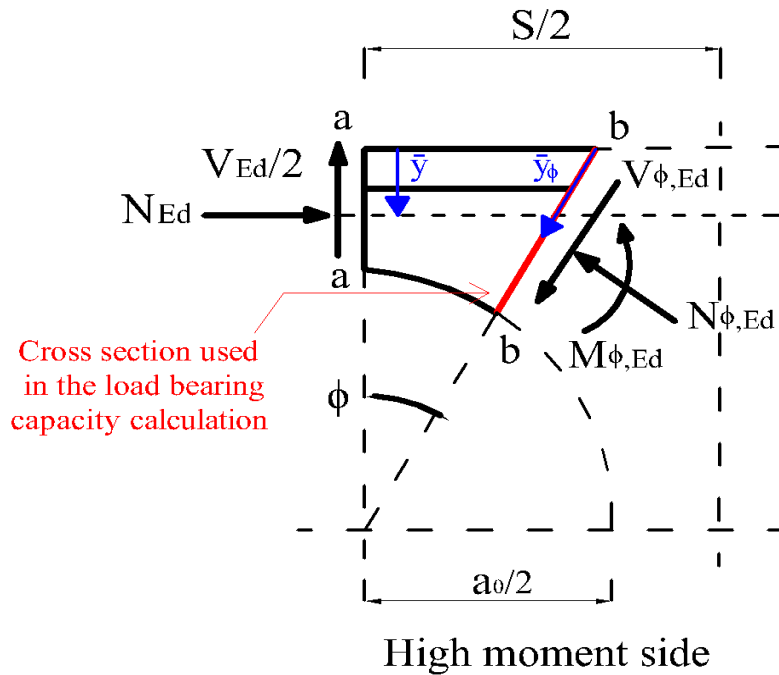


Figure 2-12. Top left quarter of model section.

2.6.5. Design resistance at elevated temperature

The simplified rule for the design resistance in a fire situation is determined from the one of the normal situation taking into consideration steel's mechanical characteristics at high temperatures [4]. The flexural design resistance of the gross, net, and inclined sections, at a specific elevated temperature θ is obtained by multiplying the above mentioned resistances at 20 °C, by the reduction factor for the yield strength of steel at temperature θ , reached at time t , $k_{y,\theta}$, and replacing γ_{M0} , γ_{M1} by $\gamma_{M,fi}$, in which $\gamma_{M,fi}$ is the partial factor for the relevant material property for the fire situation. The elastic critical moment $M_{cr,\theta}$ of the cross-sections at elevated temperature is obtained by multiplying the previously mentioned resistance M_{cr} at 20 °C by the reduction factor for the slope of the linear elastic range at the steel temperature θ , $k_{E,\theta}$.

2.6.5.1. Lateral torsional buckling

The lateral torsional buckling resistance, $M_{b,fi,t,Rd}$ of gross section and $M_{b,fi,t,Rd,2T}$ of net section, is computed as for normal conditions considering the reduction factor in the fire situation, $\chi_{LT,fi}$ [4]. Similarly, $\chi_{LT,fi}$ is calculated using formulae at ambient temperature, where:

$$\Phi_{LT,\theta,com} = 0.5 \left[1 + \alpha \bar{\lambda}_{LT,\theta,com} + (\bar{\lambda}_{LT,\theta,com})^2 \right] \quad (84)$$

$$\alpha = 0.65 \sqrt{235/f_y} \quad (85)$$

$$\bar{\lambda}_{LT,\theta,com} = \bar{\lambda}_{LT} [k_{y,\theta,com}/k_{E,\theta,com}]^{0.5} \quad (86)$$

$k_{E,\theta,com}$ is the reduction factor for the slope of the linear elastic range at the maximum steel temperature in the compression flange $\theta_{a,com}$ reached at time t .

New design formulations for α and $\chi_{LT,fi}$, equations (87) and (88), to consider the bending moment distribution, the type of cross section, and steel grade are introduced to improve the design efficiency [22].

$$\alpha = \beta \sqrt{235/f_y} \quad (87)$$

$$\chi_{LT,fi,mod} = \frac{\chi_{LT,fi}}{f} \leq 1.0 \quad \text{with } f = 1 - 0,5(1 - k_c) \quad (88)$$

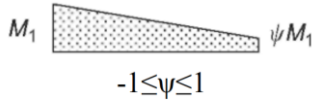

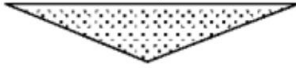

Where: β is the severity factor and is obtained from the Table 2-7

Table 2-7. Values of the severity factor, β

Cross-section	Limits	β	
		S235, S275, S355, S420	S460
Rolled I section	$h/b \leq 2$	0.65	0.70
	$h/b > 2$	0.75	0.80
Welded I section	$h/b \leq 2$	0.70	0.75
	$h/b > 2$	0.80	0.85
Other cross-sections	-	0.80	0.85

$\chi_{LT,fi,mod}$ is a modified reduction factor, k_c is a correction factor set to coincide as closely as possible with a representative sample of numerical results from the survey, as taken from Table 2-8.

Table 2-8. Correction factors k_c for the new proposal [22].

Moment distribution	Class 1, 2, and 3 sections
	K_c
 M_1  ψM_1 $-1 \leq \psi \leq 1$	$0.6 + 0.3 \psi + 0.15 \psi^2$ but $K_c \leq 1$
	0.79
	0.91

Note: for other bending diagrams $K_c = 1$.

2.6.5.2. Lateral torsional buckling: Pattamad et al. formulation.

To develop calculation rules, there are some analytical models developed to represent the lateral torsional buckling resistance of cellular beams [58]. Based on the formulations provided in [4] and [58], the main analytical formulas for calculating the LTB resistance of a cellular beam at elevated temperature are presented below:

$$M_{b,fi,t,Rd,CB} = K_{LB} * M_{b,fi,t,Rd,EC3} \tag{89}$$

Where $M_{b,fi,t,Rd,EC3}$ is the design lateral torsional buckling resistance according to [4].

K_{LB} is a correction factor for the design of cellular beams with non-dimensional slenderness < 2.5 as mentioned by [58].

With shear loads (Distributed load):

$$k_{LB} = \min(0.16 * (A_f / A_w) + 0.66, 1) / \max((-0.1 * \bar{\lambda}_{LT} + 0.13), 0.9) \quad (90)$$

Without shear loads (End moment load):

$$k_{LB} = 1 / (-0.01 * \bar{\lambda}_{LT} + 1.05) \quad (91)$$

2.7. Conclusions

Guidance on designing beams with web openings can be found in Eurocode NF EN1993-1-1, SCI publication P355, draft EN1993-1-13 – CEN/TC 250/SC 4 N 1839, at ambient temperature, and the updated first draft of pr-EN 1993-1-2, under fire conditions, which includes a new normative appendix on beams with large web openings. For this research, solid and cellular beams were designed using Eurocode 3 Part 1-1, supplemented by the provisions of the SCI Guide P355 and guidance from academic literature. The SCI P355 provides detailed manuals on the design of cellular beams and their strength determination according to Eurocodes. This research work investigates the impact of varying the geometrical characteristics of a cellular beam on its ultimate strength. The 2T approach is used for strength calculations, with characteristics computed at the centre of the web opening.

**CHAPTER 3. SIMULATION AND
ANALYSIS OF STEEL SOLID AND
CELLULAR BEAMS IN ANSYS**

3.1. Methodology

Our strategy for this work is to research the critical moment and torsional lateral deflection resistance obtained using the ANSYS computer program and compare it to the simplified calculation methods outlined in Eurocode 3 and SCI Guide P355 and identify any potential failure modes. We will also analyse the impact of changing the geometrical parameters of the cellular beam. In doing so, we will use a numerical model that considers global and local imperfections of the beam due to eigenvalues and eigenvectors, as well as residual stresses in the flange. To ensure accuracy, we will keep the temperature consistent throughout the simulation and gradually increase the load to discover the load the beam can handle at these initial conditions.

3.2. Parametric analysis and case studies _ Model 1

All the studied cases are based on numerical modelling and an empirical design method, as referenced by Peter J et al [105] and K.F. Chung et al [54], to compare the results obtained.

Table 3-1 presents the cases studied to compare the solid and cellular beams and to determine the effect of changing each geometric dimension on the instability mode and the ultimate strength of the beam.

Case 1 comes to determine the Influence of web openings on temperature and displacement of steel beams. Three types of beams were investigated: a solid beam (P1), a beam with two openings (P2), and a beam with six openings (P3) (Chung type), using the same notations for the geometric parameters of the cellular beams as those of ACB+ and assuming that the beams are prevented against buckling Figure 3-1. The three beams are based on UB 457x152x52 [54] with a span of 7.5 m, loaded by a uniformly distributed load $Q = 35 \text{ kN/m}$, and with circular holes of diameter $a_0/h = 0.75$ set symmetrically in reference to the centre of the beam with 1.0 m spacing from end supports. S275 steel with a yield strength of $f_y = 275 \text{ MPa}$ was employed. The influence of the width of the web-post on the characteristics of the beams are characterized by the ratio e/a_0 , which will be the parameter studied. The characteristics of the beams are described in Table 3 [106].

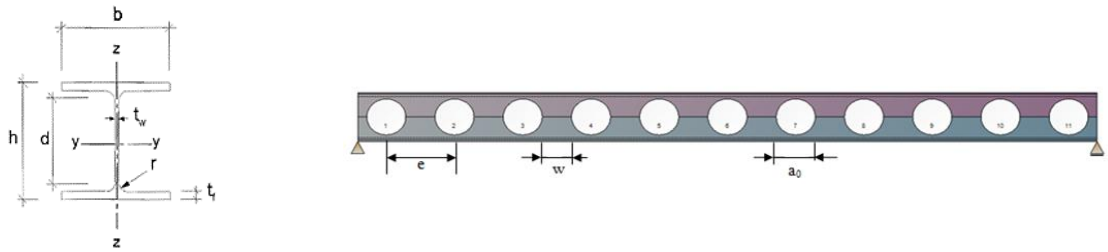


Figure 3-1. Geometric parameters of the studied beams, cellular beam with ACB+ adaptation.

Case 2 is used to investigate beams with multiple web openings in a fire situation, both with and without imperfections. This case study was conducted on three types of beams: a solid beam, a cellular beam, and a beam with hexagonal openings, all of them were based on the same cross-section profile (UB457x152x52) as in Case 1. The geometric parameters of the beams are provided in Table 3-1 [106].

Case 3 is used to define the influence of imperfections and residual loads on cellular beam local buckling. The simulations used the British universal beam 610UB101, with parameters $a_0/h = 0.8$, $H/h = 1.3$, and $w/a_0 = 0.3$, the holes were spaced at regular intervals [9]. The cross-section height was $h = 602$ mm, with a breadth of $b = 228$ mm. The beams were subjected to a constant temperature as well as an increasing uniformly distributed load (U) or end moment (M) that varied with time ($q = 100t$) until they collapsed [107].

Case 4 is used to investigate how the geometry of the profile section affects the LTB resistance. The British universal beam 610UB101 and the European I-beam IPE600 were selected for the simulations. The IPE600 section was chosen to have similar geometric dimensions to the 610UB101 section, as both are inscribed within the same rectangle [107], see Figure 3-2. The spacing between holes e/a_0 was changed between $= 1.2, 1.3$, and 1.5 .

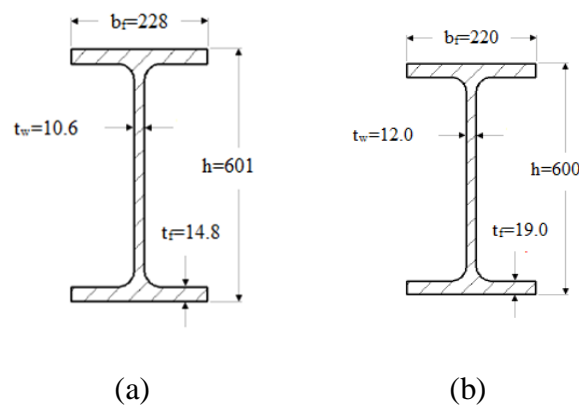


Figure 3-2. Geometric parameters of parent sections: (a) 610UB101, (b) IPE600.

CHAPTER 3. SIMULATION AND ANALYSIS OF STEEL SOLID AND CELLULAR BEAMS IN ANSYS

Table 3-1. Geometric characteristics of the studied cases

Cases	Profile	Beam	L	H	a ₀	e	e/a ₀	Openings	f _y	Q
			m	mm	mm	m		number		
Case 1	UB457x15 2x52	P1	7.5	449.8	0	-	-	0	275	DL 35 (kN/m)
		P2			337.35	5.5	16.30	2		
		P3			337.5	1	2.96	6 (CHUNG model)		
Case 2	UB457x15 2x52	PS	7.5	449.8	337.5	0.5	1.482	15	275	DL 35 (kN/m)
		P Cell								
		P Hex								
Case 3	610UB101		8	782.6	481.6	0.621	1.289	12	430	q = 100t DL M
Case 4	610UB101		8	782.6	481.6	0.577	1.2	12	430	q = 100t DL M
						0.722	1.5			
						0.722	1.5			
Case 4	IPE600		8	780.0	480	0.576	1.2	12	430	q = 100t M
						0.624	1.3			
						0.720	1.5			

3.3. Parametric analysis and case studies _ Model 2

To carry out the analysis, a standard profile, is used for the simulations. The chosen profile is the IPE 450, employed both for solid beam models and for the beam producing the cellular one; these dimensions are shown in Figure 3-3.

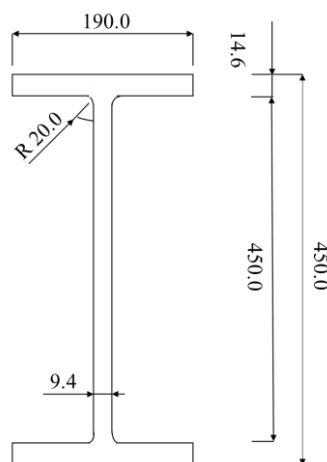


Figure 3-3. IPE450, cross-section geometric dimensions (mm).

This research focuses on the parametric study of IPE450 hot-rolled profiles with Class 1 and 2 cross-sections for simply supported solid and cellular steel beams subjected to LTB based upon the given assumptions.

3.3.1. Assumptions

Regarding the parameters of the beam model in the numerical simulations, the following assumptions are made based on the EC3-1-13 [3], the SCI reference [8], and the ArcelorMittal catalogue [1] :

- Cellular beams with I profile, which are symmetric about the weak axis, with $h_{wT} > t_f + 30$ mm, the ratio of the depth of top and bottom Tees $0.5 \leq h_{wT,b} / h_{wT,t} \leq 3$, [8];
- Regular circular openings are the main configuration of openings that are used, openings placed centrally in the depth of the section $h_{wT,b} / h_{wT,t} = 1$, with web-post width; $a_0/12$ or $50 \text{ mm} < s_0 < 0.75 a_0$ [1],
- Large web apertures of $1.25 a_0 < H < 1.75 a_0$ [1],
- Closely spaced circular openings: edge to edge spacing $s_0 < a_0$ and the minimum end-post width s_e is $0.5 s_0$ [3], $s_e \geq 0.5 a_0$ [8],
- The LTB for cellular beams is mainly affected by residual stresses applied along the cross-section.

3.3.2. Geometric parameters of studied cases

In the examined related cases, SB and CB, the beam span L , cross-section depth H , and load type for both solid and cellular beams, as well as opening width a_0 , spacing S for the latter, are all considered, as indicated in Table 3-2. The beams were subjected to two separate load cases: end moments (M) and uniform distribution (D). Geometrical parameters for cellular beams were varied proportionally to the parent section height, h , and to the opening diameter, a_0 , as shown in Table 3-2. To include geometries at the lowest, intermediate, and high ranges of a_0/h and S/a_0 within the recommended range of assumptions, different opening sizes and spacing were chosen.

CHAPTER 3. SIMULATION AND ANALYSIS OF STEEL SOLID AND CELLULAR BEAMS IN ANSYS

Table 3-2. Geometric and loading data for solid and cellular steel beam cases.

Beam	Parent steel profile	Loading type	H	a_0	S	L (m)
Solid	SB	M	1.3h	-	-	2, 3, 4, 5, 6, 8, 10, 12, 14
			1.4h			
			1.5h			
		D	1.3h			
			1.4h			
			1.5h			
Cellular	CB	M	1.3h	0.8h	1.1 a_0	1.5, 2, 3, 4, 5, 6, 8, 10, 12, 14
			1.4h	1.0h	1.4 a_0	
			1.5h	1.2h	1.7 a_0	
		D	1.3h	0.8h	1.1 a_0	
			1.4h	1.0h	1.4 a_0	
			1.5h	1.2h	1.7 a_0	

The cellular beam models are designated for LT buckling analysis based on their geometrical characteristics. The section is indicated by the first symbol on the label, while the opening ratio (a_0/h) and spacing ratio (S/a_0) are represented by the second and third symbols, respectively. Thus, the label CB-0.8-1.1 refers to the cellular beam of an IPE450 cross-section with $a_0/h=0.8$ and $S/a_0=1.1$.

The inelastic buckling is influenced by the geometry and position of the web opening [15]. It is worth taking notice that, in all the examples investigated, the number of openings is always odd, thus one cell is always located at the beam's mid-span, making the 2T-section endure the maximum bending moment. Applied temperatures include room temperature (20 °C), as well as two extreme temperatures (500 °C and 700 °C), which were chosen to anticipate a fire situation.

The temperatures of 500°C, 600°C and 700°C are selected to represent a range of commonly utilized critical temperatures when designing solid beams, as specified by Eurocode 3 Part 1-2. Additionally, an ambient temperature of 20°C is used as a basis for comparison in ascertaining the strength of beams exposed to elevated temperatures.

The steel grade S355 ($f_y = 355$ (MPa)) was used for all beams with a typical value of elasticity modulus of 210 (GPa), and Poisson's ratio of 0.3.

3.4. Numerical model, boundary conditions, and imperfections

All numerical simulations performed were carried out in ANSYS software (Ansys, 2022 R1), using the numerical model made up of shell elements to study the LTB resistance of laterally unrestrained beams, with and without web openings. Shell elements are suitable for representing thin structures, corresponding to structures in which one dimension is notably smaller than the other two dimensions [6].

3.4.1. Model I

3.4.1.1. Model description

SHELL elements serve as the foundation for Model I. Each node of this element has six degrees of freedom, three for translation along the x, y, and z axes and three for rotations about these axes. The number of integration points for each layer is set to three by default, however, by exploiting the non-linear properties of the material, the element is constituted of two integration points in each direction of the plane and five integration points in the thickness, see Figure 3-4 .

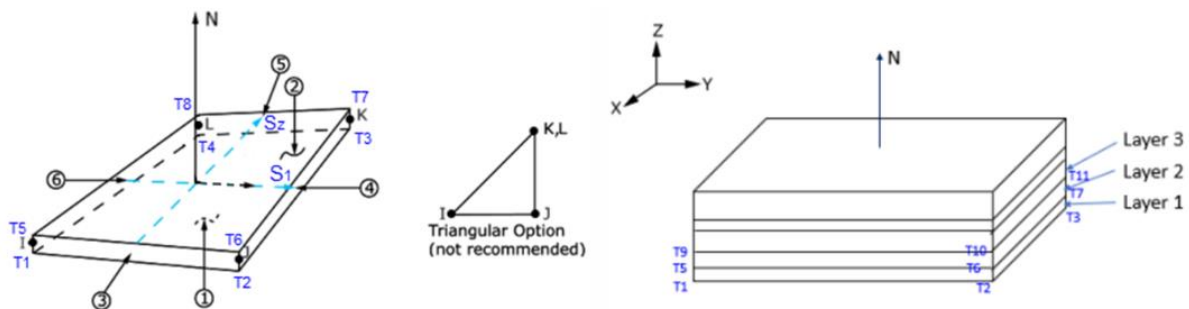
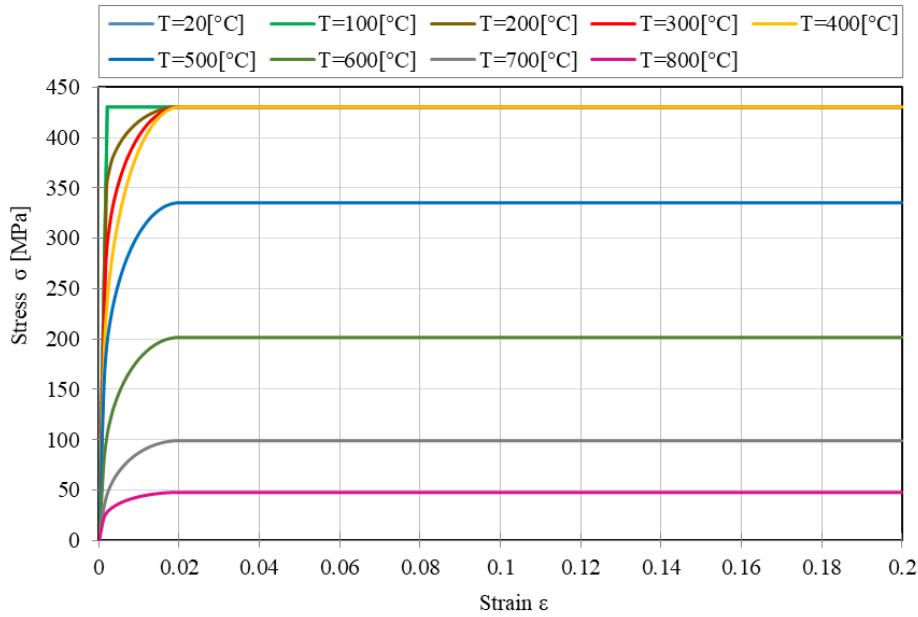


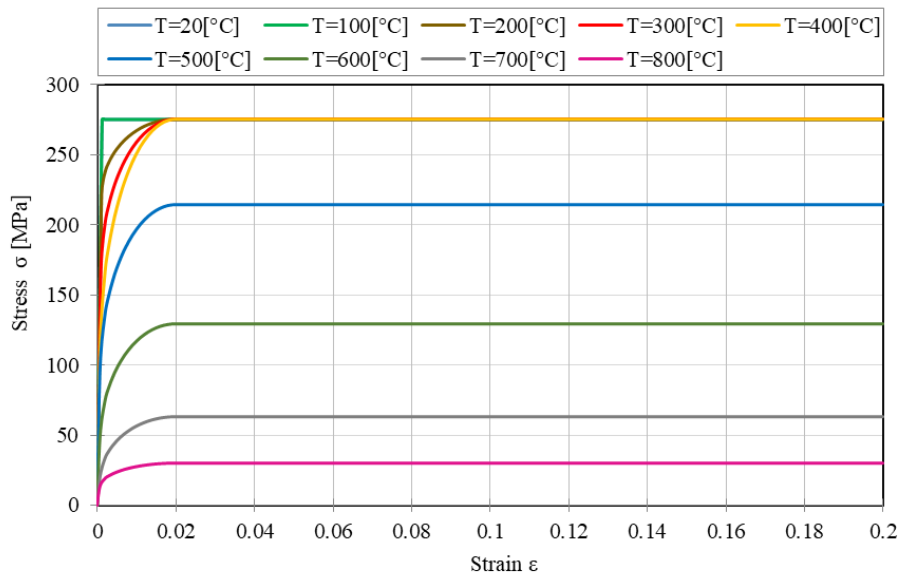
Figure 3-4. SHELL181 element geometry [6].

Mesh sensitivity research was performed, and the findings for a mesh with 8 elements in the base, 16 elements in the web, and 100 elements along the length were obtained, with the inclusion of plates at both ends of thickness $1 * t_f$. The radius of gyration is ignored. The cross section is plotted by the coordinates of the profile's average surface.

This model allows for calculations with high displacements while accounting for material and geometric non-linearities. The non-linearity of the material was determined using the stress-strain relationship comes from Eurocode 3 Part 1-2 [4] and is shown schematically in Figure 3-5 (a) for validation and Figure 3-5 (b) for the other simulations.



(a)



(b)

Figure 3-5. Stress-strain relationships for carbon steel at high temperatures (a) S430, (b) S275.

Structural imperfections are introduced using characteristic values such as an initial sinusoidal imperfection with a value of $L/1000$ for the solid beam [39] and $d/200$ for the cellular and hexagonal beams [108].

Two types of loading are considered, end moment (M) was modelled by a couple of loads acting on the flange's nodes, and a distributed load (D) on the centre line of the top flange with the two end nodes receiving half the force given to the other nodes, see Figure 3-6.

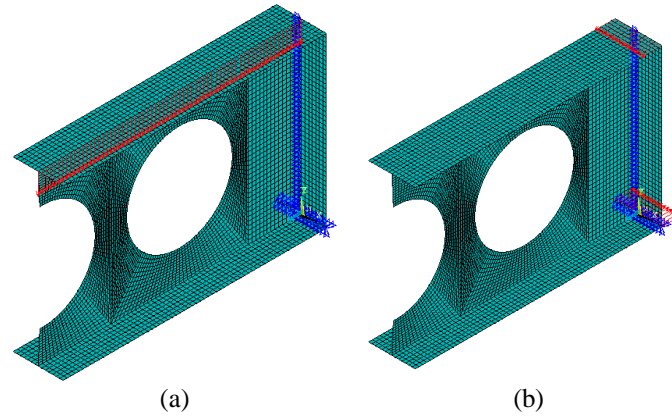


Figure 3-6. Finite element models of cellular beam: (a) with distributed load, (b) with end moment.

3.4.1.2. Validation of the FEM

The starting point is an investigation of a simply supported steel beam, which has already been treated by Seputro [105]. The case studied is a 610UB101 isostatic beam with an 8 m span, a distributed load of 25 kN/m and a temperature rise of 10 [°C/min]. Under ambient conditions, the yield strength of the steel used in this study is 430 GPa, the Young's modulus is $E=210$ GPa and the Poisson's ratio is $\nu = 0.3$. The properties of the section are shown in Table 3-3. Properties of the steel 610UB101 cross-section.

Table 3-3. Properties of the steel 610UB101 cross-section

Profile	h	b	t_w	t_f	A	$W_{pl,y}$	L	E_a	f_y	ν
	mm	mm	mm	mm	Cm^2	Cm^3	m	GPa	Mpa	
610UB101	602	228	10.6	14.8	130	2900	8.0	210	430	0.3

The comparative study is carried out based on the critical temperature and the mid-span displacement of steel beams in a fire situation to assess the adequacy of the numerical results obtained compared to the results obtained by Peter J. et al [109] with different types of support conditions, pin-rolled and fixed-fixed beam. The values of displacements U_y and critical temperature θ_{cr} are presented in Figure 3-7 and Table 3-4.

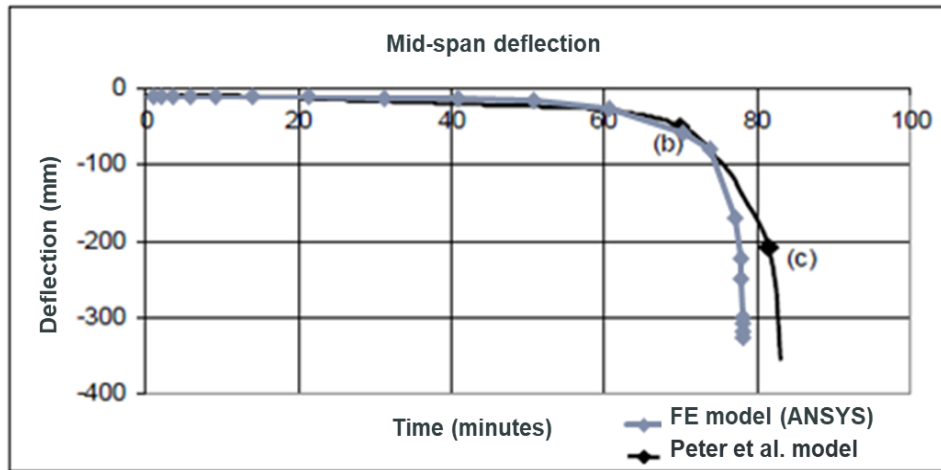


Figure 3-7. Displacement vs. time of Pin-rolled steel beam.

The numerical model was found to be accurate in its representation of the mechanical behaviour of the beams until failure, as evidenced by the comparison of the displacement-time curves and critical temperatures. Therefore, it can be used as a validated numerical model for our study, see Table 3-4.

Table 3-4. Comparison between the reference model and FE model results

	Pin-roller beam		Fixed-fixed beam	
	u_y mm	θ_{cr} °C	u_y Mm	θ_{cr} °C
Peter et al. reference model [109]	-380.00	830.00	-223.00	880.00
FE model	-382.30	800.58	-207.00	892.96

3.4.2. Model II

3.4.2.1. Element type selection and mesh sensitivity analysis

The 3D four-node shell element type SHELL181, with full integration, was used, without considering the fillet radius between the web and the flanges.

For comparison, mesh sensitivity analyses using both the elastic buckling moment and ultimate collapse moment were conducted with elements sizes of 30 mm, 20 mm, and 15 mm, see Table 3-5. The numerical results are compared with the elastic critical moment and the LTB moment resistance given by Eurocode, as defined in Section 2.6. From these simulations, an element size of 20 mm, see Figure 3-8, for all simulations was chosen, considering the required accuracy and acceptable computation times.

CHAPTER 3. SIMULATION AND ANALYSIS OF STEEL SOLID AND CELLULAR
BEAMS IN ANSYS

Table 3-5. Mesh sensitivity analysis, cases with $H/h= 1.3h$, $a_0/h=0.8$, $S/a_0=1.1$, $L=5.m$

Analysis type	M_{EC3} (kN.m)	Element size	M_{FE} (kN.m)	M_{FE} / M_{EC3}
Elastic buckling analysis	453.855	15 mm	457.103	1.007
		20 mm	458.043	1.009
		30 mm	460.116	1.014
Nonlinear analysis (NLGMA)	320.635	15 mm	355.288	1.108
		20 mm	355.599	1.109
		30 mm	356.785	1.113

3.4.2.2. Constraints

The beam cross-section is represented by the coordinates of the midplane of the profile. The beam geometry is orientated according to the coordinate system shown in Figure 3-8. The span is directed along the Z-axis, the y-axis and X-axis are in the plane of the cross section, while Y-axis is parallel to the web and the X-axis is parallel to the flanges. The origin of the (X; Y) axes is situated at the intersection between the web and the bottom flange at the right end of the beam.

Beam end conditions, designed to create "fork" type supports, are modelled by restraining the two ends by, the vertical displacements (U_y) on the bottom flange, the lateral, out-of-plane, displacements (U_x) along the web, the rotation along Z (ROTZ) on the bottom flange and the web, Figure 3-8.

All nodes at mid-span are axially restrained (U_z) to maintain the symmetry, and the rotation (ROTX) of nodes of beam ends sections are coupled to the chosen master node at the web centre defining a rigid region (CE), where the given master node's rotation is the same for all nodes. End plates are added to the beam to prevent local web crippling and section plastification. These plates must be able to transfer vertical shear and enable beam end rotations without creating large moments [110]. For cases involving short and high section cellular beams, where the first buckling mode is local buckling or a combination of local and distortional buckling, instead of lateral torsional buckling, the coupling (CP) degree of freedom, set for the ROTZ, was applied during the Eigen buckling analyses along the entire span of the beam studied with distance of $S/2$ and $H/2$ for cellular and solid beams, respectively, to fortify the web against local buckling and thus stimulate the collapse mode of LTB.

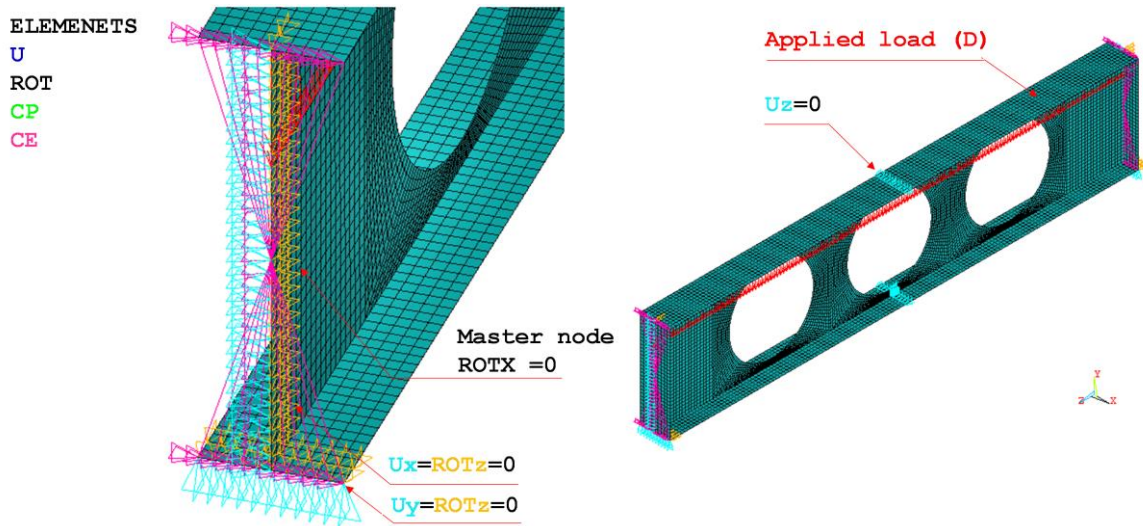


Figure 3-8. Mesh configuration of FEM and boundary conditions for IPE base profile cellular steel beams ($L = 3$ m, $H/h=1.4$, $a_0/h = 1.2$, and $S/a_0=1.4$)

3.4.2.3. Loads

The model was subjected to pure bending moments, M , achieved by two uniform forces at the top and bottom flanges of the beam's end sections, or a mechanically distributed load, D , applied to the nodes of the top flange centreline, see Figure 3-8 and Figure 3-9.

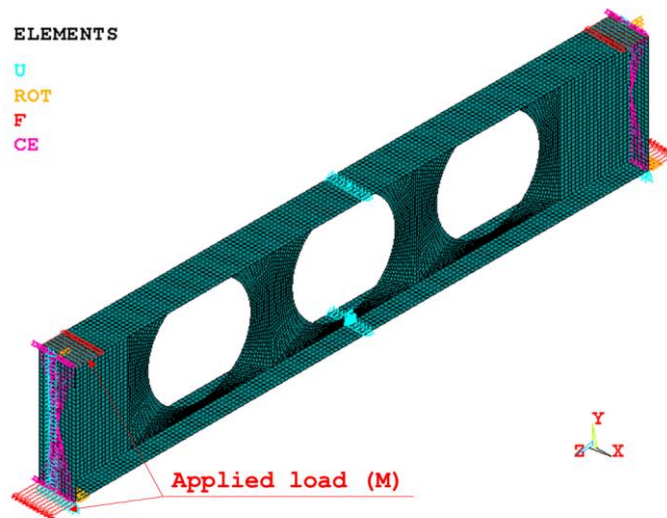


Figure 3-9. Pure bending moments

3.4.2.4. Mechanical model and imperfections

Both material and geometric nonlinearities are considered, as well as imperfections such as residual stresses and initial geometrical out-of-straightness. The stress-strain relationship defined by the Eurocode 3 Part 1-2 [4] is used for the simulations.

The geometric imperfections are implemented by applying the eigenvalues and eigenvectors method to the initial buckling mode of the beam that has a half sinusoidal curve configuration. This approach accounts for the deformation in the flanges and web, as well as the transverse displacement of the beam, as illustrated in Figure 3-10 (a) and (b). The amplitude value of $L/1000$ is allocated to both solid and cellular steel beams, as described in [27] and [24] respectively, where L is referring to the length of the beam span.

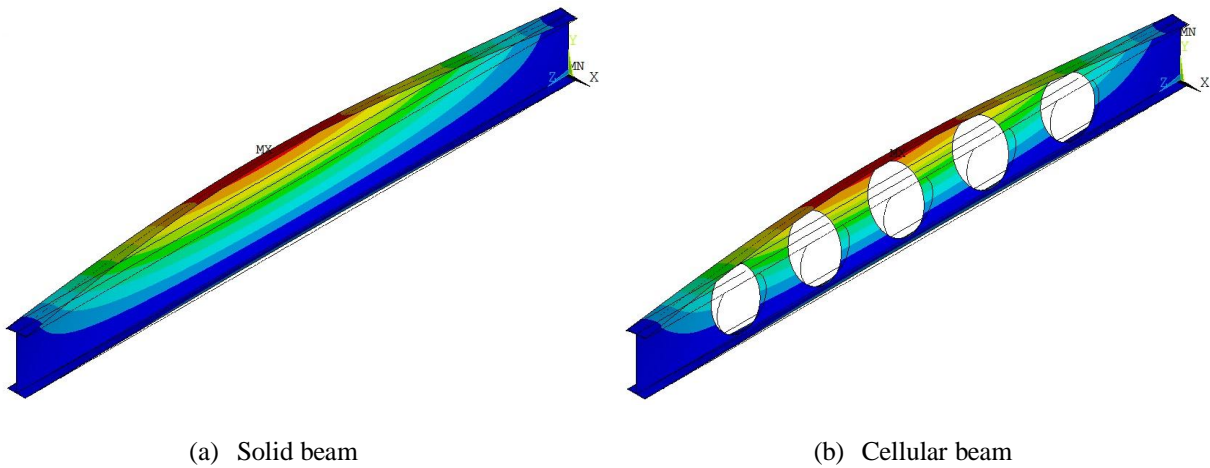


Figure 3-10. Geometric imperfections in (a) solid beam, (b) cellular beam.

Residual stresses for solid and cellular beams were modelled under room and elevated temperature conditions alike and presented in Figure 3-11 as an initial stress state condition. In solid beam section, simplified model of residual stresses for hot rolled section as proposed by [39] was used, Figure 3-11 (a), where the maximum stresses are equal to 30% of the material yield stress. For the cellular beam, the model proposed by [44], presented in Figure 3-11 (b), where residual stresses was disregarded on the web was applied, as presented in Section 1.3. above. All studies were carried out using the Newton–Raphson solution process.

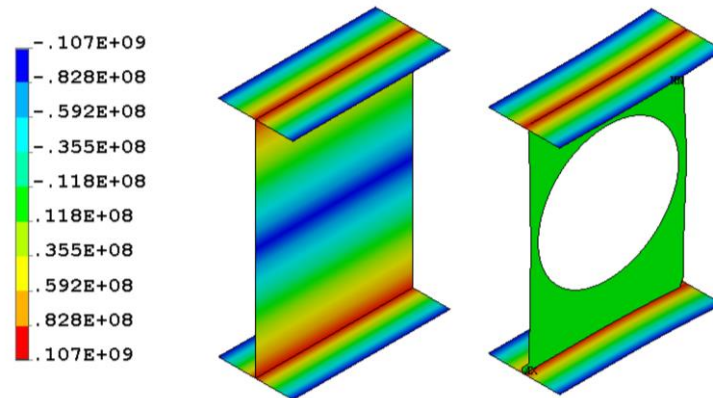


Figure 3-11. Residual stress distributions of rolled sections, S355: (a) solid beam; $H=1.3h$, (b) cellular beam; $H=1.3h$, $a_0=0.8h$.

An ANSYS analysis is submitted in the form of an input file, consisting of four main sections: Eigen Buckling Analysis (including Geometric Imperfections), Residual Stresses, Temperature, and Load Application up to Collapse.

To enable the convergence of the simulation, the solution is divided into three Load Steps. Each load step has a load specification for the beam, as shown in Figure 3-12. In load step 1, residual stresses and geometric imperfections are inserted. In load step 2, temperature is added using a ramped function. Finally, in load step 3, the load/ or bending moment is applied as a function of time (t) relative to each solution increment, with $q=100t$ for steel beams under distributed load and $M =1000t$ for steel beams subjected to pure bending. The simulation ends when the collapse load is reached.

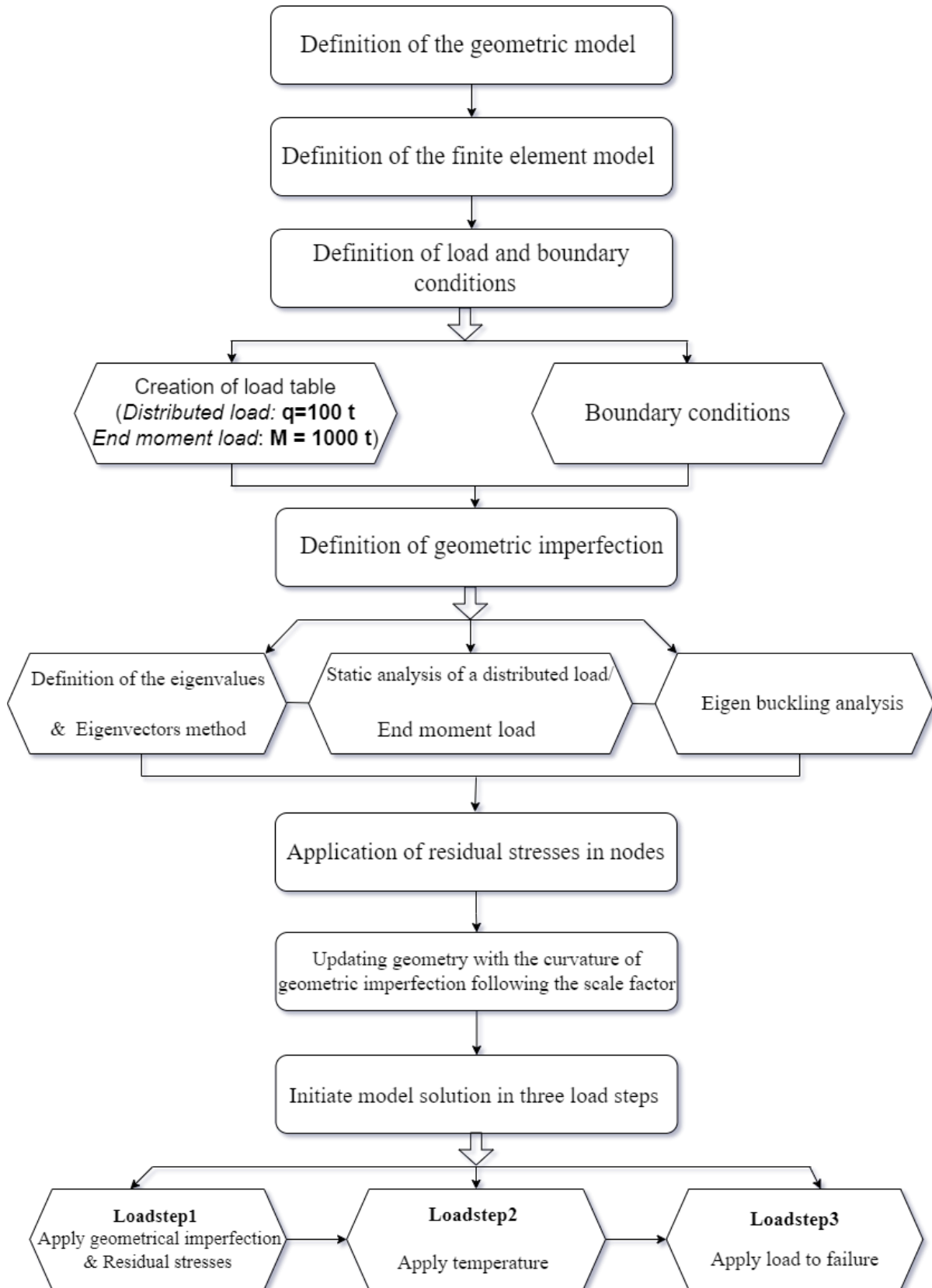


Figure 3-12. Layout and organization of the finite element model implemented in ANSYS.

3.4.2.5. Numerical model validation

The numerical model described in the preceding sections was implemented in the experimental tests of cellular steel beams conducted by Sonck et al. [10, 24], taking the same procedures as those of Faria et al. [84], see Figure 3-13. The load-displacement curves were compared through simulating two experimental tests with four-point bending. Table 3-6 shows the specimen's geometric details, with $f_{y,f}$ and $f_{y,w}$ being the yield strengths of the flange (top and bottom flanges) and the web, respectively. E is the elastic modulus, L and L_f are, respectively, the total beam length and the distance between loads. The tests were done at room temperature.

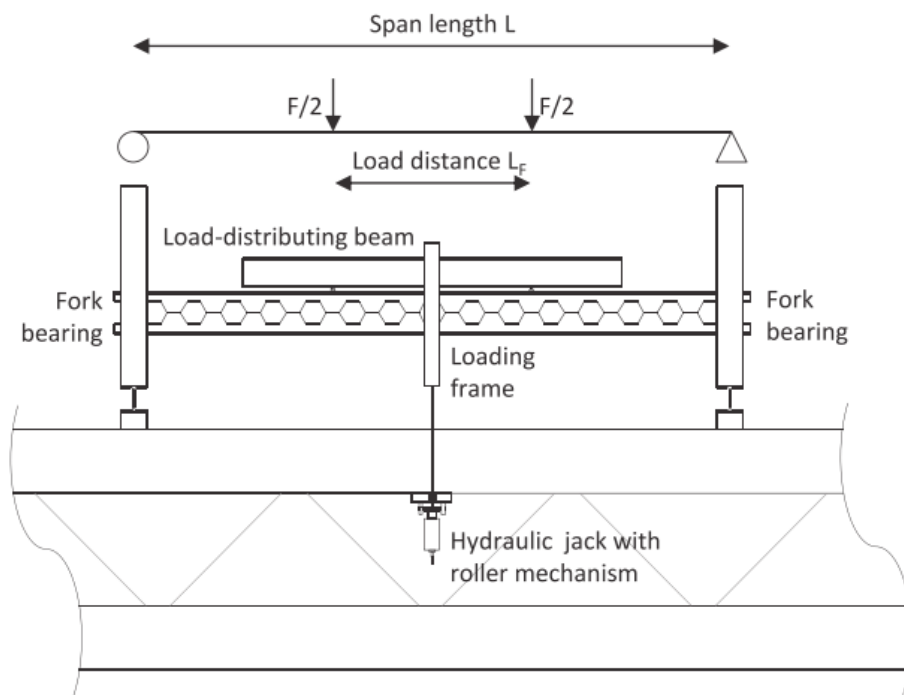


Figure 3-13. Sketch of LTB test according to Sonck et al. [24].

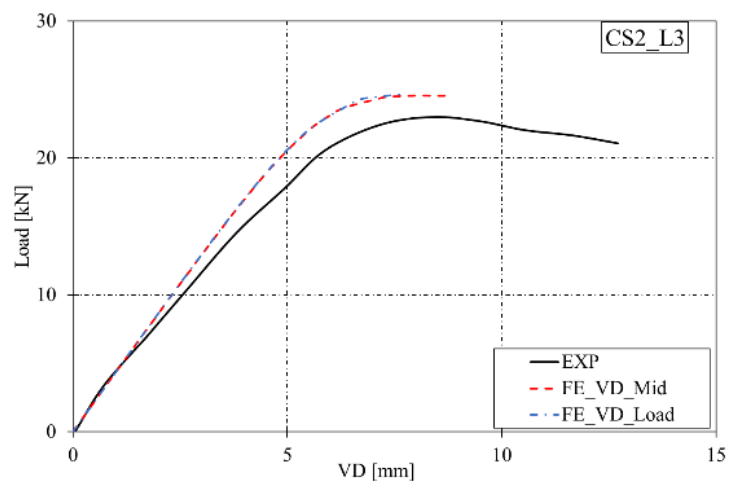
Figure 3-14 presents the load versus vertical displacement from the numerical results (FE), and the experimental results (EXP), measured at the loadings points and mid-span. The numerical collapse load for a beam with a length of 3.15 m was calculated as 23.56 kN, which is slightly higher than the experimentally measured value of 22.34 kN [10]. In the case of the 3.99 (m) beam length, the numerical collapse load obtained was 24.50 (kN) and the experimental maximum load was 23.62 (kN). The numerical model and the experimental results show a high degree of agreement for the overall load and displacement curves, with similar failure modes also seen. A comparison of the two yielded a variance of 5.5% for the CS2_L3 specimen and 3.7% for the CS2_L4 specimen. Considering the simplified residual

CHAPTER 3. SIMULATION AND ANALYSIS OF STEEL SOLID AND CELLULAR BEAMS IN ANSYS

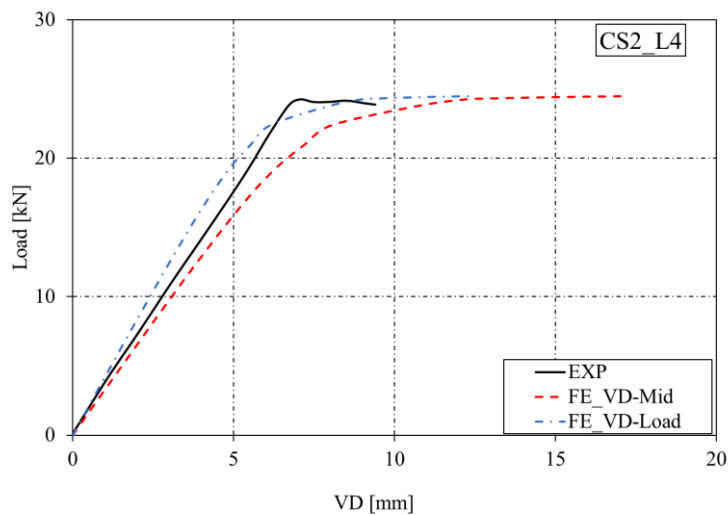
stress pattern used in the model and its influence in the failure load [10, 24] and as the real geometric imperfections were not modelled but a global imperfection, with maximum amplitude of $L/1000$, the numerical results are acceptable, and the model considered suitable for further analysis.

Table 3-6. Geometric details of test specimens

Specimen	H	b	t_w	t_f	a_0	S_0	n	L	L_f	$f_{yt,f}$	$f_{yb,f}$	$f_{y,w}$	E
	(mm)	(mm)	(mm)	(mm)	(mm)	(mm)		(mm)	(mm)	(MPa)	(MPa)	(MPa)	(MPa)
CS2_L3	220	83.1	5.5	7.3	142.8	67.2	15	3150	210	342	341	329	205
CS2_L4	220	83.1	5.5	7.3	142.8	67.2	19	3990	1890	348	351	339	205



(a) Case CS2_L3



(b) Case CS2_L4

Figure 3-14. Comparison between numerical and experimental tests. Load versus vertical displacement.

3.5. Influence of web openings on critical temperature and displacement of steel beams _ Model I

In this section, we will consider Case 1 from Section 3.2. , which is illustrated in the following figure. Figure 3-15 shows the three beams under investigation.

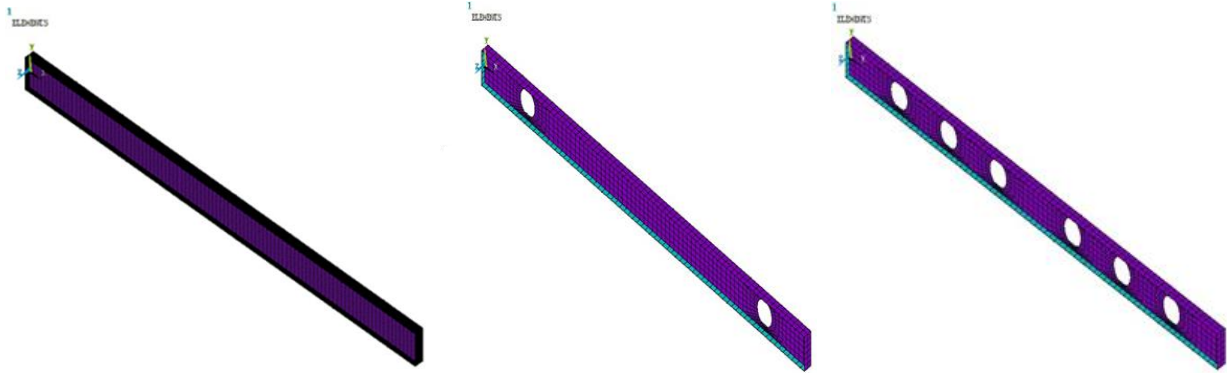


Figure 3-15. Studied steel beams from left to write, P1, P2, P3, respectively.

Table 3-7 displays the vertical displacements and critical temperatures of the various simulated beams P1, P2, and P3.

Table 3-7. Vertical displacements and critical temperatures of the simulated beams.

				P1	P2	P3
At $\theta = 20\text{ }^{\circ}\text{C}$	EC3	Displacement U_y	mm	- 32.13	-	-
	FE			-32.7980	-32.231	-34.1250
At elevated temperatures	FE	Displacement U_y	mm	-	-208.806	-65.4452
			Critical temperature	$^{\circ}\text{C}$	779.1575	773.271
			θ_{cr}			

The results of the study, as seen in Table 3-7, showed that the critical temperatures of the various beams investigated without and with web apertures do not differ appreciably and remain within the range of 700 to 800 $^{\circ}\text{C}$ range as the number of openings increases. The displacements of the beams with web apertures, P2 and P3, on the other hand, were greater than that of the solid beam P1, ranging from 485 (mm) to 65 (mm).

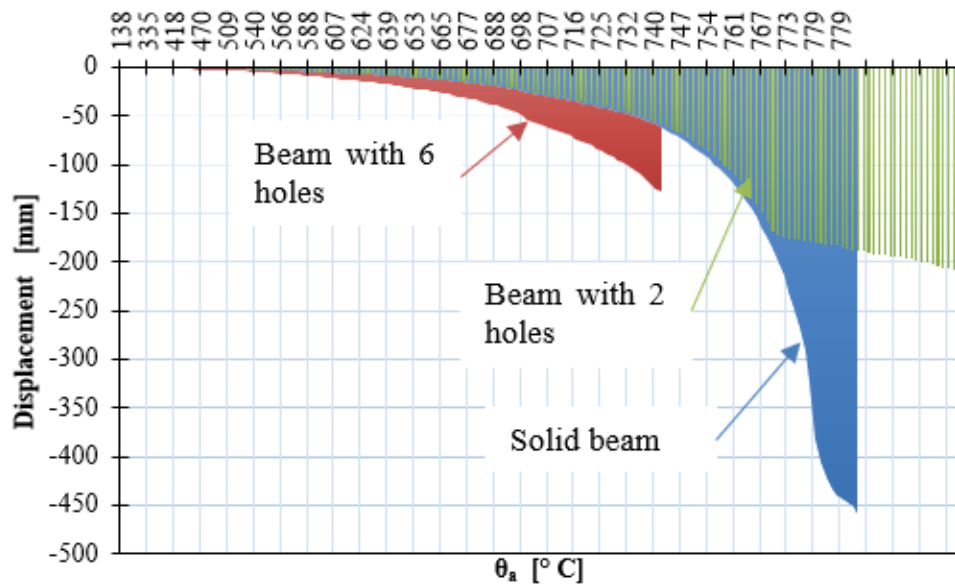


Figure 3-16. Mid-span vertical displacement vs. temperature.

Figure 3-16 demonstrates that when the number of holes in the web of the beam increases, the displacements decrease significantly (from 458 mm to 65 mm), while the critical temperature range remains between 700 and 800 (°C).

3.6. Investigations on beams with multiple web openings in a fire situation with and without imperfections _ Model I

The design and computation of beams with many openings differ from those of solid web beams. As a result, Eurocode 3 reserves a separate part for them, known as Annex N [2], and in order to ease the calculation job, designers (CTICM) have developed software such as ACB+ [111] that is solely dedicated to cellular beams.

The models of the solid, cellular, and hexagonal beams presented in Case 2 in Section 3.2. are the focus of this study. Figure 3-17. depicts the numerical models of the three.

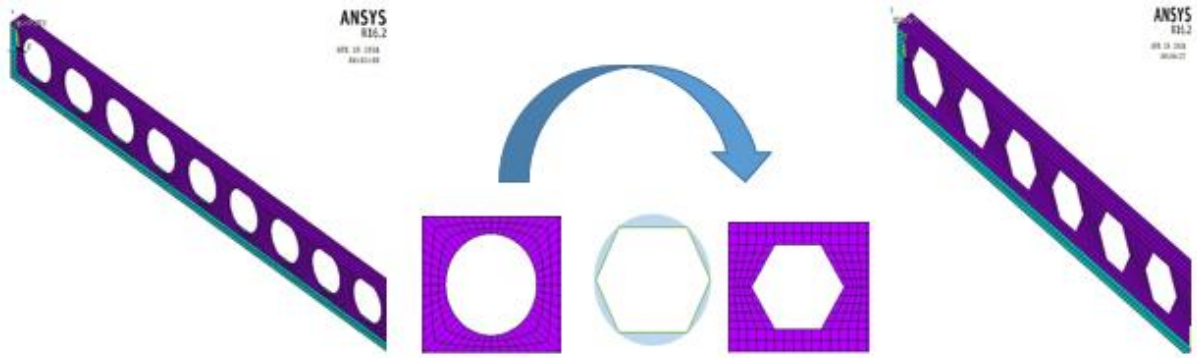


Figure 3-17. Cellular beam and equivalent hexagonal beam.

The parameters investigated are the mid-span vertical displacements U_y , horizontal displacements U_x , and critical temperatures θ_{cr} , Table 3-8.

Table 3-8. Displacements and critical temperatures of the different beams studied.

		Solid beam (PS)	Cellular beam (P cell.)	Hexagonal beam (P hex)
Vertical Displacement at 20 °C	ACB+	-	-42.73	-
	FE	-	-43.906	-
Without imperfection	θ_{cr} [°C]	794.067	764.951	774.6713
	U_y (mm)	-449.870	-164.651	-322.7040
	U_x (mm)	66.314	24.764	48.6182
With imperfection	θ_{cr} (°C)	790.4537	759.4694	773.820
	U_y (mm)	-325.1060	-134.5600	-297.852
	U_x (mm)	48.0289	20.2015	45.010

The results in Table 3-8, show that the maximum beam displacements calculated numerically by ANSYS and ACB+ at ambient temperatures are near and comparable. Additionally, the introduction of geometrical imperfections has a minimal effect on the variation of critical temperatures, ranging from 0.1 to 1%. However, the difference in displacements between the different beams is still considerable, from 10% to 30%.

Figure 3-18 depicts the vertical displacement of the investigated studied steel beams under ISO834 fire curve in relation to the critical temperature. When the load is applied, the vertical displacements of the beams increase gradually and linearly until a temperature of approximately 600°C is reached. Following that, displacements increase very quickly with rising temperatures until they collapse. This suggests that the beams are highly sensitive to temperature variations beyond 600°C.

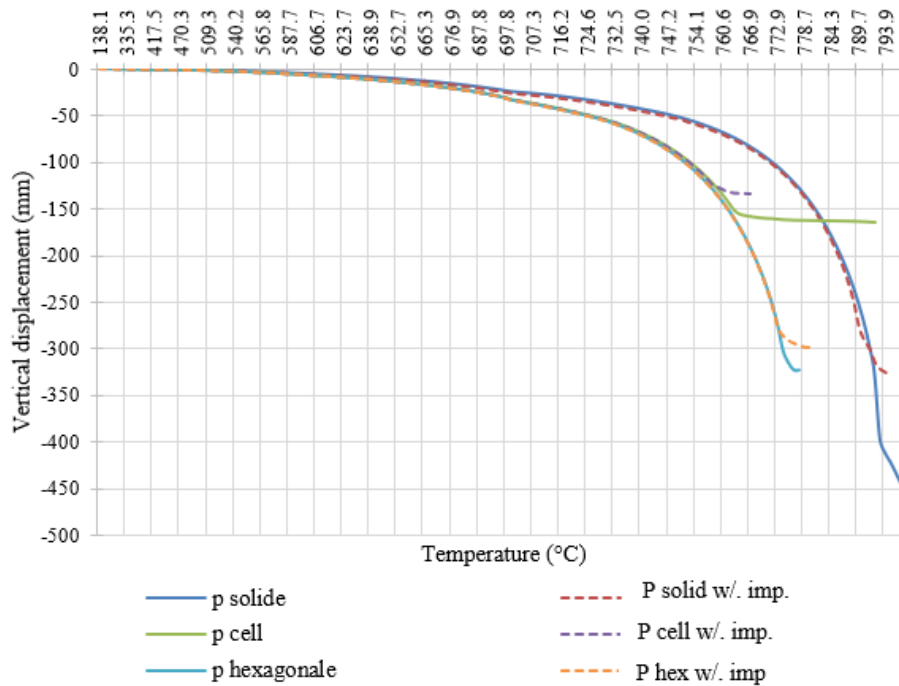


Figure 3-18. Vertical displacement vs. critical temperature under ISO834 fire.

It was also noticed that for the same loading of the three types of beams, the variance in displacement due to imperfections is smaller for the perforated beams than for the solid beam.

3.7. Imperfections and residual stresses' effects on cellular beam LTB _ Model I

To assess the effect of geometric imperfections and residual stress on the lateral torsional buckling resistance of a cellular beam, three cases are studied numerically, as detailed in Section 3.2. , Case 3. The critical load is determined through FE simulations and used to calculate the numerical LTB resistance [107].

In this case, the first structural imperfection investigated was a sinusoidal shape with the same intensity as that used for hot-rolled sections in double tees, with a maximum value of $L/1000$ at mid-span [112], where L is the beam span. A triangular distribution of residual stresses with a maximum value of $0.3 f_y$ was also used. Tensile stresses are applied to the section at the flange-web junction, while the web and the tips of the flanges are compressed.

Figure 3-19 compares the numerical analysis result to the bending resistance $M_{pl,\theta,Rd}$ and the lateral torsional buckling resistance obtained by equation (89) for temperatures ranging from 20°C to 800°C . The moment resistance with geometric imperfections is denoted by MFE_IMP , and the moment resistance with geometric imperfections and residual stresses is

denoted by MFE_IMP_RS. A loading-related component is also explored here, where (M) stands for end moment and (D) stands for distributed load.

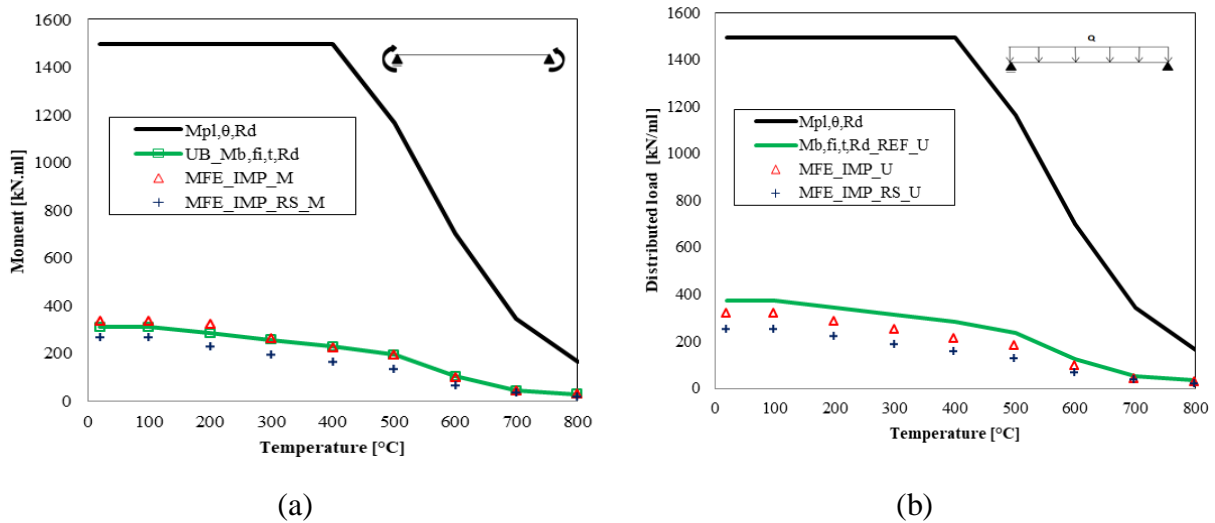


Figure 3-19. Moment resistances of cellular beam vs. temperatures, (a) with end moment load, (b) with distributed load

The results above reveal that the existence of imperfections has a significant impact on beam resistance, implying that they are entering the beam resistance to LTB. The influence of residual stress reduces as temperature rises. This is because of the stress-strain relationship at high temperatures. The effect of residual stress essentially disappears at temperatures close to 500°C. In terms of loading, there is a nearly 5% variation in outcomes between beams loaded with a distributed load and beams loaded with an end moment.

Figure 3-20 depicts the vertical and lateral displacements of various cellular beams as a function of applied load, end moment and distributed load, for temperature values ranging from 20 to 800 (°C).

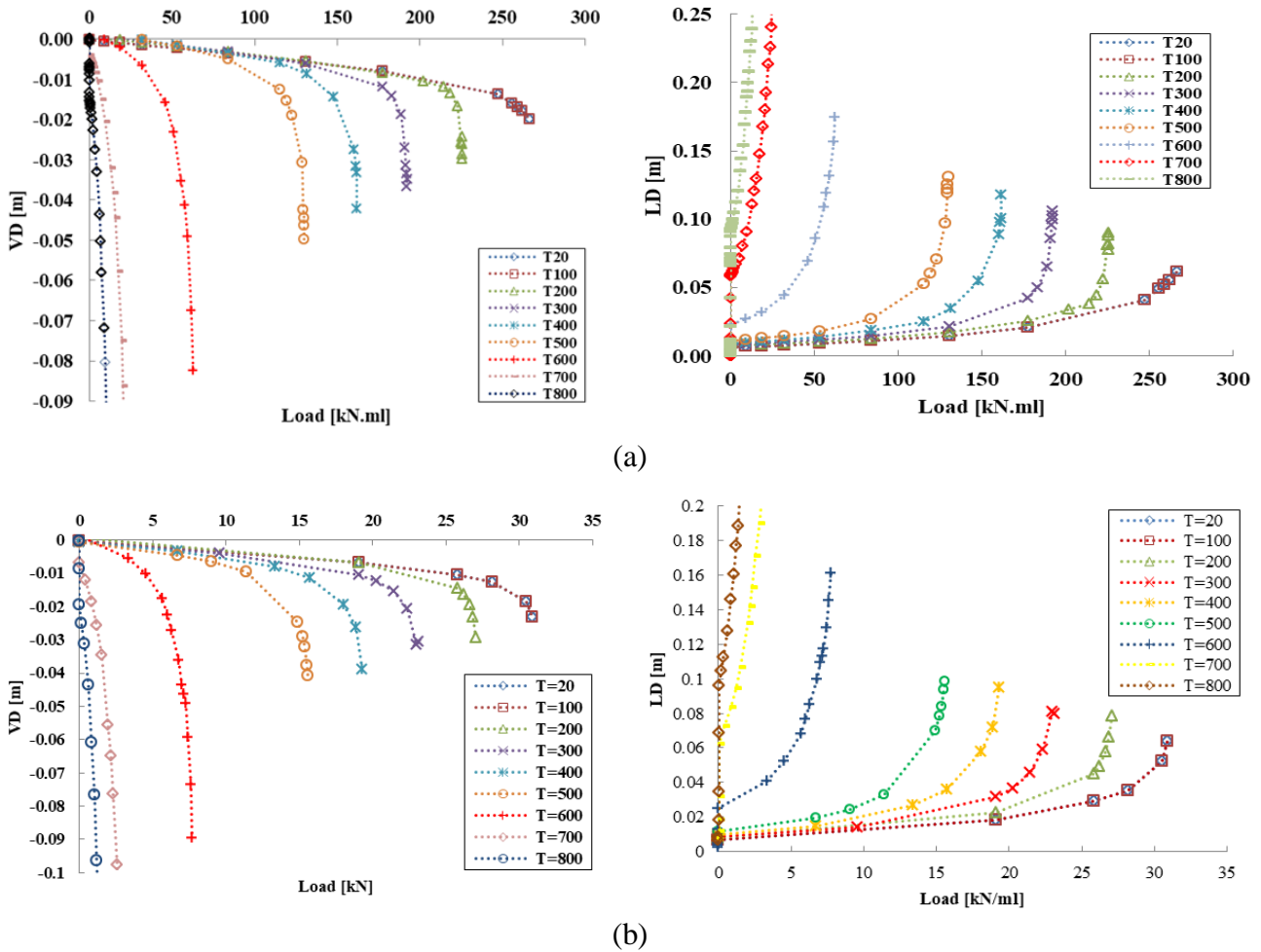


Figure 3-20. Vertical (VD) and lateral displacements (LD) of cellular beams vs. temperature: (a) with an End moment, (b) with a distributed load.

Based on the results in the figure above, the beams have progressively and linearly increased vertical and lateral displacements at temperatures below 500 °C, beyond which the displacement increases sharply with the load.

3.8. Effect of profile section geometry

An analysis of two steel sections, IPE and UB, was conducted as outlined in Section 3.2. , Case 4 [107]. Figure 3-21 depicts the influence of geometry on LTB resistance in both sections for comparison.

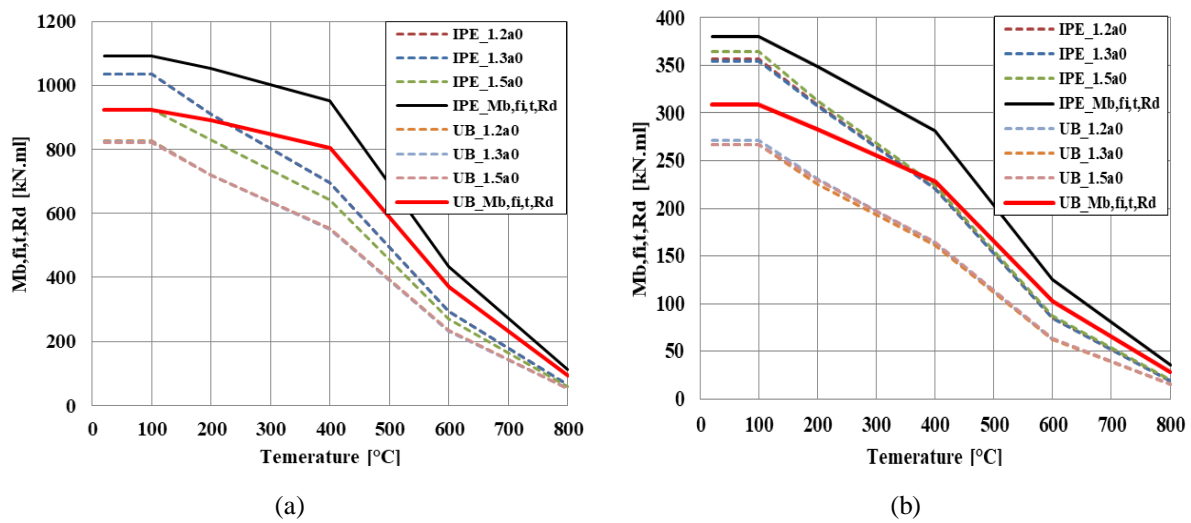


Figure 3-21. Influence of profile section geometry, (a) $L=3$ m, (b) $L=8$ m.

The results reveal that the critical moment determined by numerical analysis is greater than the critical moment determined by equation (89). For UB and IPE cross-sections, the numerical findings of LTB resistance are roughly 10 to 15% lower than the analytical results for lengths of 3 and 8 m. This behaviour was similar for S values less than $1.5a_0$.

When numerical and analytical data for LTB resistance of IPE and UB cross sections are compared, a 20% variation in moment resistance is seen. Figure 3-21 (b) indicates that decreasing the spacing of the apertures, $S/a_0 = 1.2$ and $S/a_0 = 1.3$, has increased the LTB moment resistance over a 3 m span of the beam with IPE cross-section. In the case of the UB cross-section, this emerges marginally. The LTB beam resistance of the cross sections is about the same at temperatures exceeding 500 °C.

3.9. Study of the effect of residual stresses on the fire resistance of unrestrained cellular beams _ Model II

To assess the effect of geometric imperfections and residual stress on the lateral torsional buckling resistance of a cellular beam, we have evaluated the spacing between openings, the height of the cross section, the opening diameter, and the beam length at different temperatures under end moment loading [113].

Table 3-9 presents a comparison of the LTB moment resistance of beams with lengths of 2, 6, and 14 [m] with (W/. RS) and without residual stresses (W/O.RS) at different temperatures ($\theta = 20, 500, \text{ and } 700$ [°C]), where $H/h = 1.3$, $a_0/h = 0.8$, and $S/a_0 = 1.1$. The numerical results indicated that the influence of residual stresses on the LTB moment resistance of cellular

CHAPTER 3. SIMULATION AND ANALYSIS OF STEEL SOLID AND CELLULAR
BEAMS IN ANSYS

beams at ambient temperature was minimal. This effect was further reduced at 500 °C and 700 °C.

Table 3-9. LTB moment resistance of cellular beams with and without residual stresses from numerical results, $H/h = 1.3$, $a_0/h = 0.8$, and $S/a_0 = 1.1$

		θ (°C)	20	500	700
M_{LTB_FE} (kN.m)	L=2 (m)	W/RS	68.56	42.75	12.24
		W/O.RS	69.52	42.98	12.28
		Diff. (%)	1.39%	0.55%	0.39%
	L=6 (m)	W/RS	40.35	19.89	4.31
		W/O.RS	41.02	20.02	4.33
		Diff. (%)	1.66%	0.65%	0.46%
	L=14 (m)	W/RS	13.23	7.11	1.76
		W/O.RS	13.46	7.17	1.77
		Diff. (%)	1.71%	0.84%	0.56%

Figure 3-22 shows the LTB resistance values for solid and cellular beams with $H/h = 1.3$, $a_0/h = 0.8$, and $S/a_0 = 1.1, 1.4$, and 1.7 for temperatures = 20, = 500 °C, and =700°C, as a function of beam length. For each spacing S , the labels $M_s=1.1a_0$, $M_s=1.4a_0$, and $M_s=1.7a_0$ reflect the LTB moment resistances of cellular beams with geometric imperfections and residual stress, while M_{solid} represents the LTB moment resistances of solid beams.

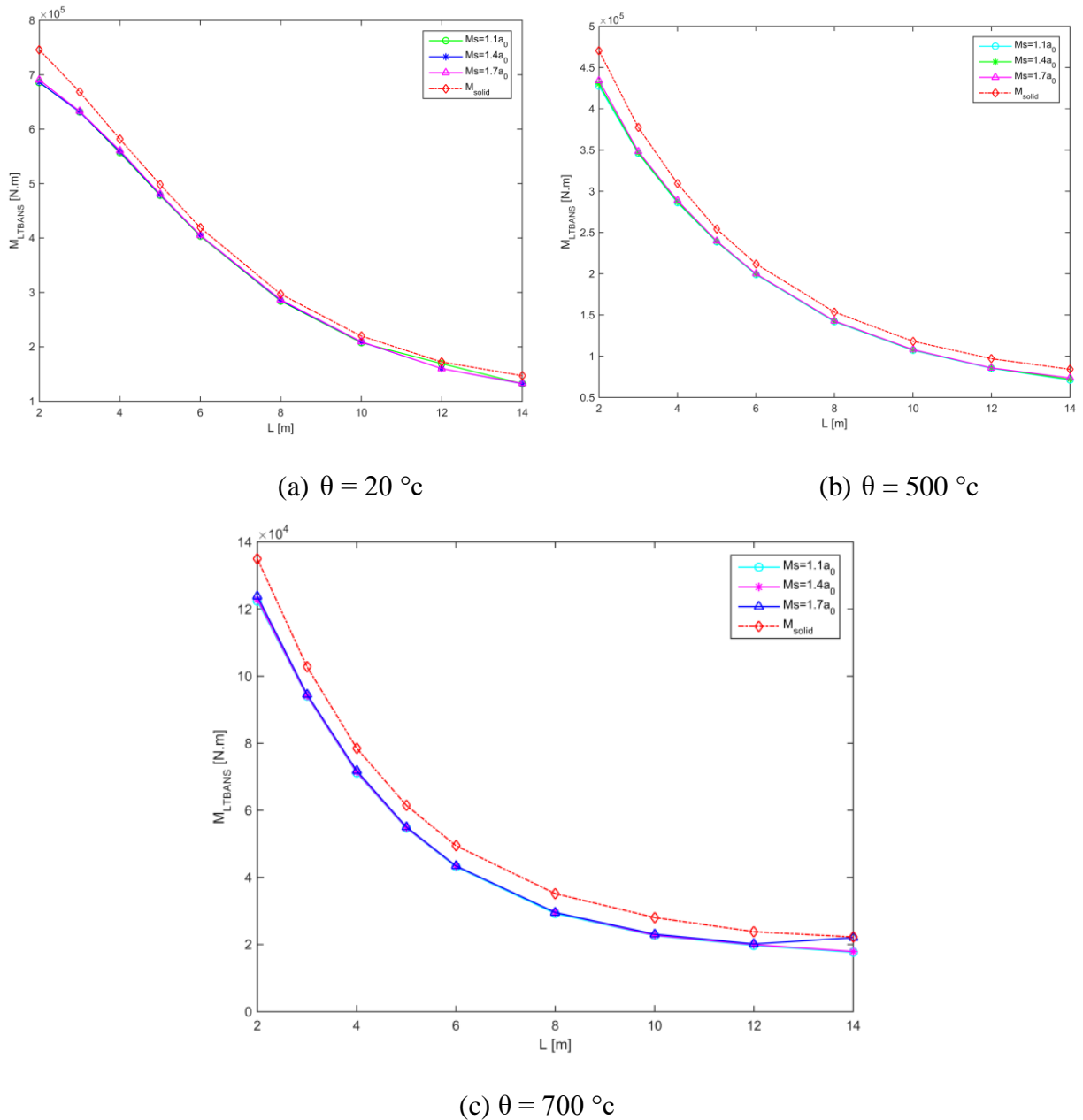


Figure 3-22. Lateral torsional buckling resistance with different openings spacing $H/h = 1.3$, $a_0/h = 0.8$, $S/a_0 = 1.1, 1.4, 1.7$.

LTB resistance decreases as length increases. Figure 3-22 shows a variation in resistance of around 1% between solid and cellular beam at 20 ($^\circ\text{C}$), and about 2 to 9% at 500 and 700 [$^\circ\text{C}$]. It is also found that for various opening spacings, the numerical values for $\theta=20$ ($^\circ\text{C}$) is typically close. For the same beam length, however, the values for $\theta=500$ and 700 ($^\circ\text{C}$) are roughly the same.

To compensate for the steel beam's lack of straightness and residual stresses, after introducing corresponding deflections, it is necessary to monitor the behaviour of beam under fire,

CHAPTER 3. SIMULATION AND ANALYSIS OF STEEL SOLID AND CELLULAR BEAMS IN ANSYS

particularly when it is adjacent to linked other parts. Figure 3-23 depicts the lateral and vertical displacements of distinct cellular beams with $H/h = 1.3$, $a_0/h = 0.8$, and $S/a_0 = 1.1$ as a function of applied load for the various beam length values studied, $L=2$ to $L=14$ (m).

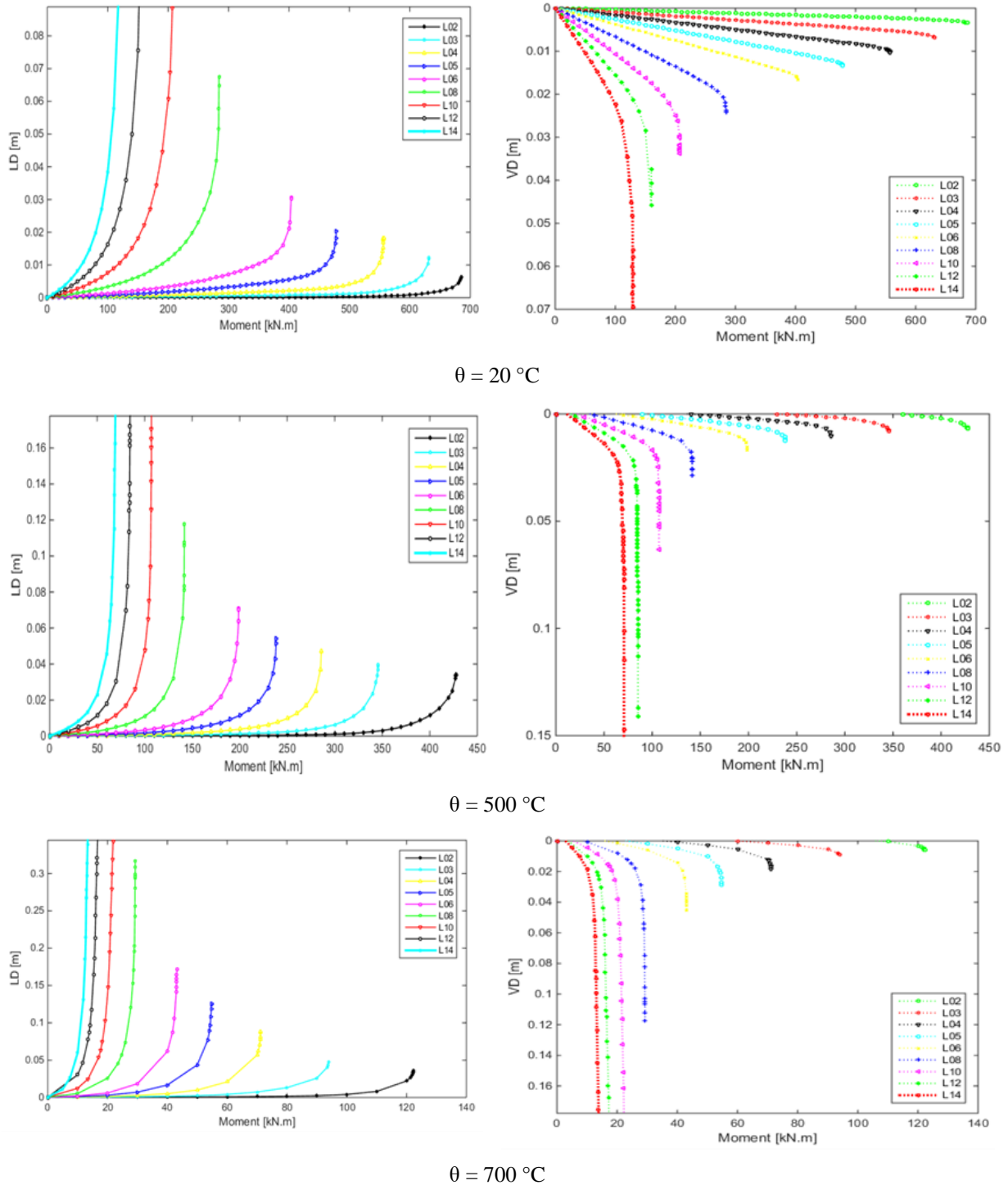


Figure 3-23. Lateral [LD] and vertical [VD] displacements of cellular beams as a function of applied load with $H/h = 1.3$, $a_0/h = 0.8$, $S/a_0 = 1.1$.

CHAPTER 3. SIMULATION AND ANALYSIS OF STEEL SOLID AND CELLULAR BEAMS IN ANSYS

The beams experienced increasing vertical and lateral displacements near the point of collapse, regardless of the temperature. The increase of the length of the cellular beam, with its assumed simply supported boundary conditions, caused a decrease in fire resistance and an increase in vertical and lateral displacements.

Figure 3-24 depicts the findings of the LTB moment resistance loss throughout the beam length for section height variation, $H/h = 1.3, 1.4, \text{ and } 1.5$, $a_0/h = 0.8$, $S/a_0 = 1.1$ at temperatures of 20°C , 500°C , and 700°C .

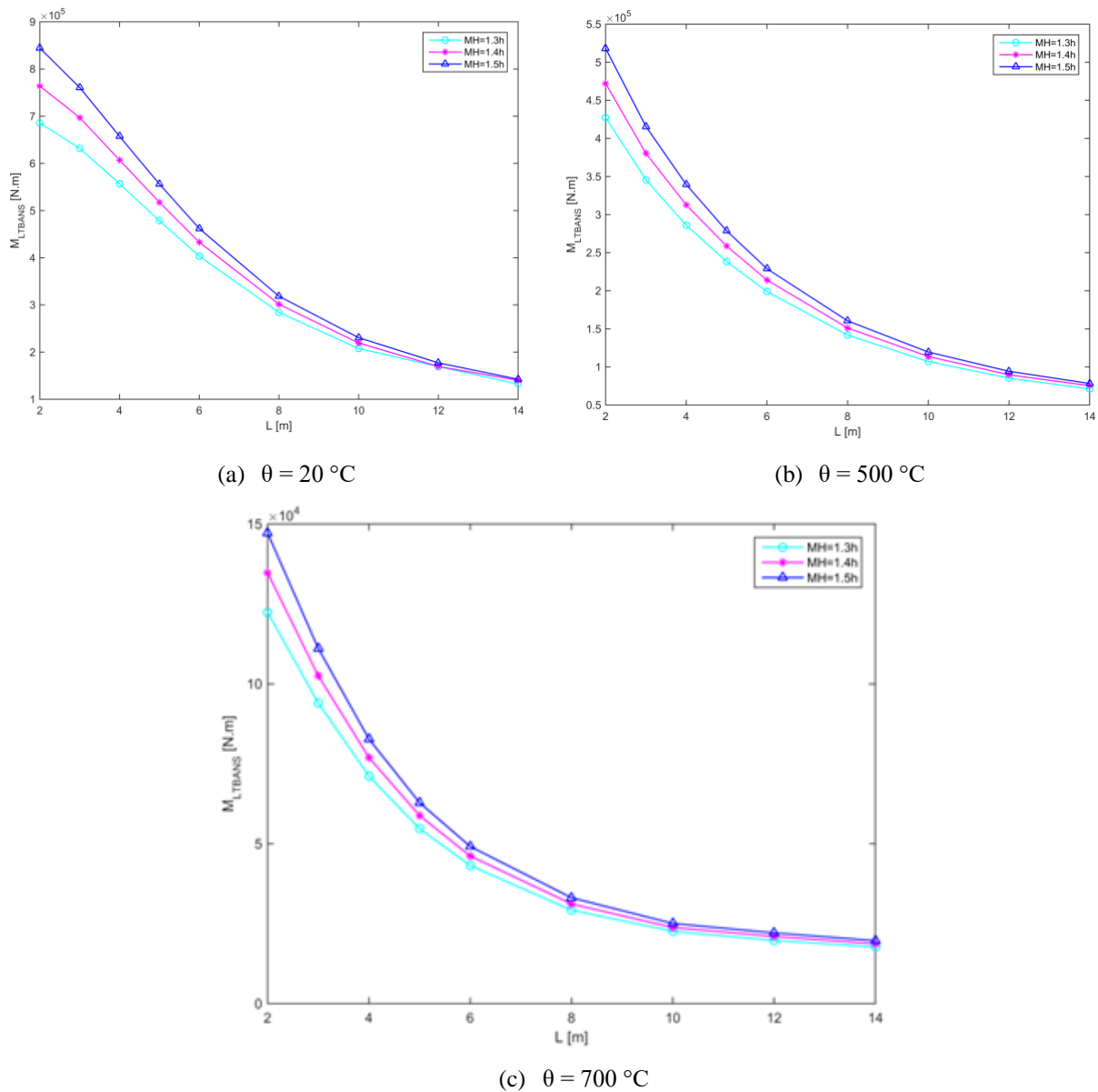


Figure 3-24. LTB moment resistance of cellular beams varying in height with $a_0/h = 0.8$, $S/a_0 = 1.1$.

CHAPTER 3. SIMULATION AND ANALYSIS OF STEEL SOLID AND CELLULAR BEAMS IN ANSYS

The results demonstrate that the beam resistance is affected by the height variation when the length is between 2 and 8 meters. Beyond 8 meters, the resistance of the cellular beam remains unchanged, regardless of the temperature.

Plots of the numerical results of the LTB moment resistance of cellular beams for different opening diameters $a_0/h = 0.8, 1.0, 1.2$ at temperatures of $20^\circ\text{C}, 500^\circ\text{C},$ and 700°C are presented in Figure 3-25.

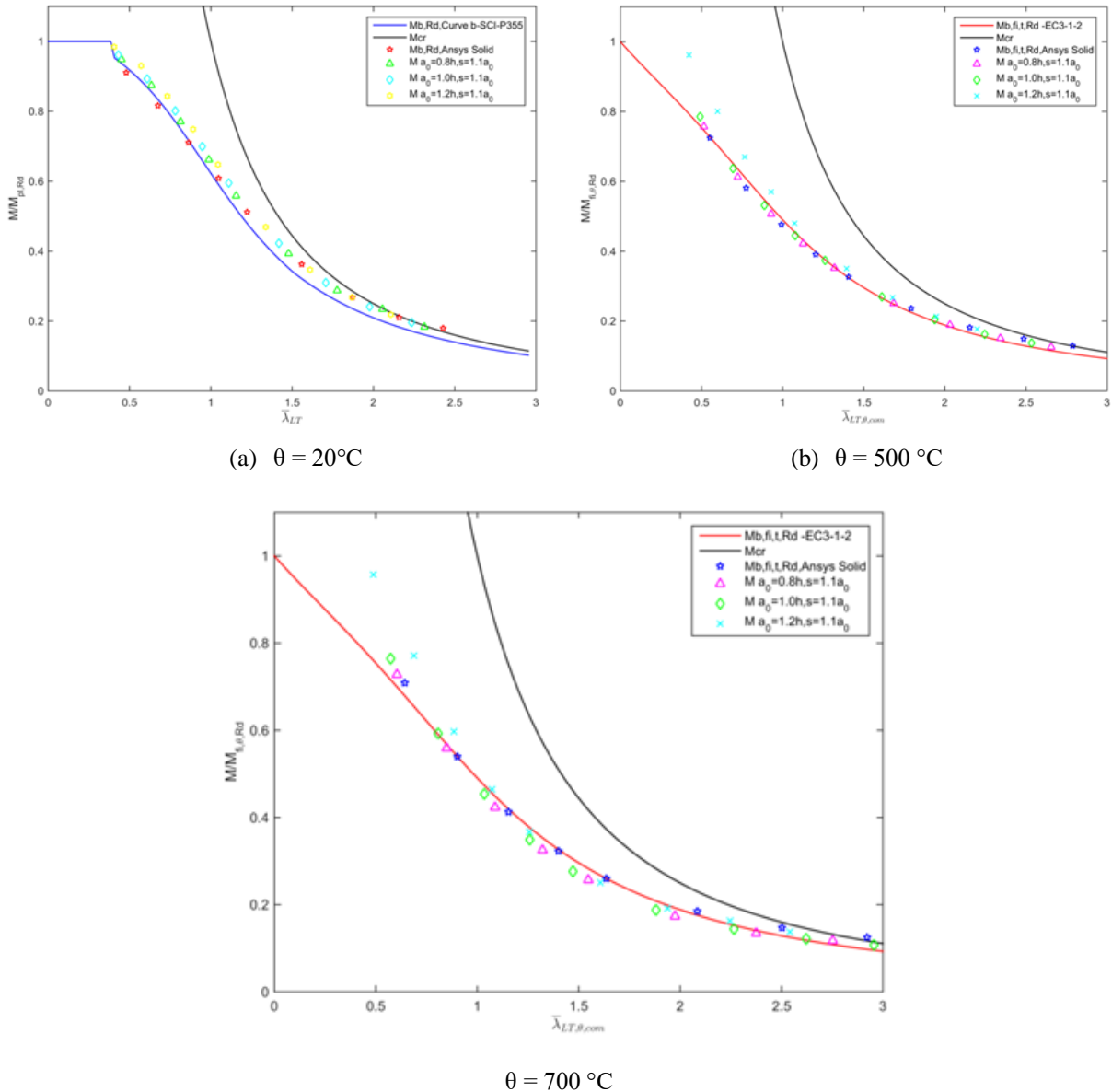


Figure 3-25. LTB moment resistance of cellular beam varying in opening diameter $a_0/h = 0.8, 1.0, 1.2$.

The resistance of steel beams decreases as the opening diameter increases for temperatures of $20^\circ\text{C}, 500^\circ\text{C},$ and 700°C . This effect is more pronounced for beams with lengths greater than 8 meters.

3.10. Conclusions

This chapter examined the effects of web openings, imperfections, residual stresses, and profile section geometry on critical temperature, displacement, lateral-torsional buckling, and fire resistance.

Therefore, it can be inferred that:

- The critical temperatures of the beams with and without web apertures do not significantly differ in the range of 700 to 800 °C, even as the number of openings increases. However, the displacement of beams with web apertures (P2 and P3) is higher than that of the solid beam (P1), ranging from 485 mm to 65 mm.
- The hexagonal beam exhibits a displacement increase of approximately 45 to 50%, in comparison to the cellular beam, regardless of the presence or absence of imperfections.
- It has been proven that the inclusion of geometric imperfections and residual stresses as factors is crucial when assessing the fire resistance of LTB.
- A comparison of the LTB resistance data for IPE and UB cross-sections showed a 20% variation in moment resistance.

**CHAPTER 4. ANALYSIS FOR
GLOBAL LT BUCKLING AND
INTERACTING FAILURE MODES**

4.1. Introduction

Analytical and numerical simulation results are presented for the LTB resistance of cellular beams, with two thorough investigations. The first part of the study focuses on the LTB elastic critical moment at both ambient and elevated temperatures, while the second examines the impact of coupling and end plate thickness on the collapse resistance at ambient temperature.

A parametric study of the studied models was conducted then to analyse global LTB and interacting failure modes. This study included design curves, temperature, loading type, cross-section ratio H/h , opening ratio a_0/h , spacing ratio S/a_0 , and beam span, as detailed in the above, Section 3.3. Three different cellular beam cross-sections were analysed at ambient and elevated temperatures, with values for H/h of 1.3, 1.4, and 1.5. The analytical results were presented by dashed and continuous lines, while the numerical results were plotted as single points with marks.

H/h values of 1.3, 1.4, and 1.5 produced three distinct cellular beam cross-sections, which were examined at ambient and higher temperatures, and numerical resistance curve findings were presented in red, blue, and green, respectively. The analytical results are shown as dashed and continuous lines, while the numerical results are shown as single points with marks.

4.2. LTB elastic critical moment

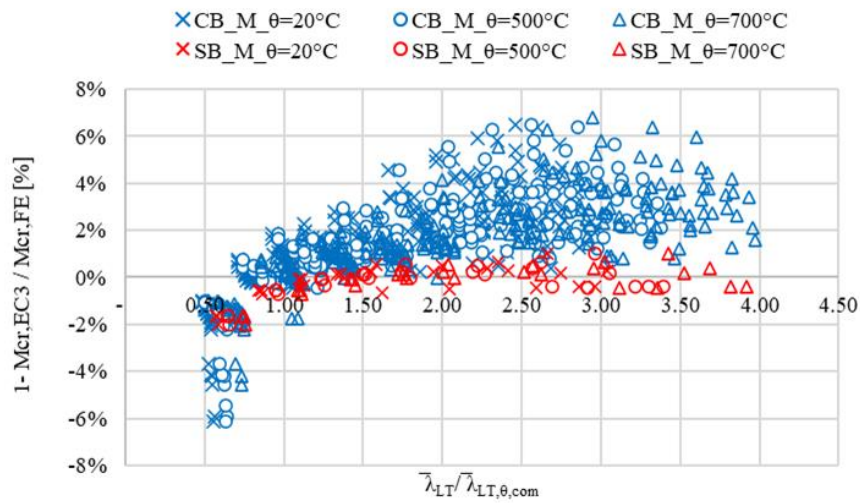
The linear buckling analyses carried out via the FE software ANSYS in [6] enabled the determination of the LTB elastic critical moments under both ambient and elevated temperatures for solid (SB) and cellular beams (CB) subjected to end moment or distributed loads. The FE critical LTB moments ($M_{cr,FE}$) were compared with analytical critical moments ($M_{cr,EC3}$) using the I and 2T approach for solid and cellular beams, respectively. The differences in this comparison as a percent error versus the numerical non-dimensional slenderness are plotted in Figure 4-1. The numerical non-dimensional slenderness to LTB at normal $\bar{\lambda}_{LT,FE}$ and at elevated temperature $\bar{\lambda}_{LT,\theta,FE}$ were determined by following the same approach of the analytical method, equations (62) and (86) in Section 2.6. , considering the respective plastic moment resistances and elastic critical moments. The FE in-plane bending resistance was calculated using the numerical beam models that have been subjected to end moment loads. In over 80% of cases, the global LTB mode was found to be the first to buckle

in simulations conducted both at room temperature and during a fire situation for both loading types.

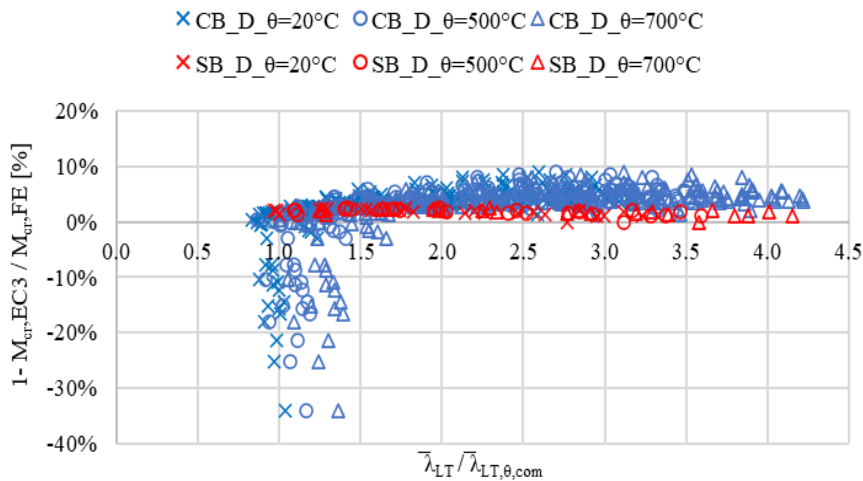
Figure 4-1 (a) shows that for end moment loading case, and at target temperatures of 20, 500, and 700 °C, the percentage differences between the two sets of results vary from -1.99% to 1.04% for the case of SB, and from -6.1% to 6.5% for the case of CB.

For the distributed loading case, Figure 4-1 (b) indicates that the differences were less than 2.5% for SB cases, and were divided into two groups upon on whether the $\bar{\lambda}_{LT}$ being greater or less than 1.5 for CB cases. For $0.5 \leq \bar{\lambda}_{LT} \leq 1.5$ corresponding to a span of 3 m, the LTB buckling mode was observed to be associated with web distortion, which has induced a larger discrepancy between numerical and analytical elastic critical moments. Discrepancies for 5.6% of cases vary from -10% to -35%. The obtained values of the M_{cr} , λ_{LT} , at ambient temperature and $M_{cr,\theta}$, $\bar{\lambda}_{LT,\theta}$ at elevated temperatures by the simplified and numerical methods for cellular beams subjected to distributed loading, are presented in Appendix A.

For $\bar{\lambda}_{LT} \geq 1.5$ corresponding to spans of 4 m and over, the lowest and largest relative errors were 0.03% and 9%, respectively. As beam length increases the effect of web distortion decreases.



(a) End moment loading M



(b) Uniformly distributed load D

Figure 4-1. Analytical and numerical LTB elastic critical moments percental differences for solid and cellular beams at $\theta= 20^{\circ}\text{C}$ and $\theta= 500, 700^{\circ}\text{C}$.

4.3. Effects of coupling and end plates' thickness on the collapse resistance of cellular beams

The coupling procedure, CP, was used in all the studied solid and cellular beam models' Eigen buckling analyses, as is alluded to in Section 3.4. In this part, the impacts of the end plates and the coupling on the LTB capacity and the associated failure mode at ambient temperature are shown using the non-linear FE model.

Four different models, each with a specific configuration, were studied under various conditions: Model 1 is without endplates (W/O.EP) and without coupling (W/O.CP); Model 2

is without endplates (W/O.EP) but with coupling (W/CP); Model 3 has endplates of $2*t_f$ thickness (W/EP. $2*t_f$) and also with coupling (W/CP); and Model 4 has endplates of $1*t_f$ thickness (W/EP. $1*t_f$) but lacks coupling (W/O.CP). Table 4-1 lists all analyses conducted, and corresponding results, M_{COLL} , were compared with appropriate analytical results from EC3 [7], $M_{b, Rd, 2T}$. The studied cellular beams, which were subjected to uniformly distributed load, had a beam height/parent section height ratio of 1.3, an a_0/h ratio of 0.8, and an S/a_0 ratio of 1.1 with differing span lengths. A comparison of the results of Models 1 and 4 revealed an average 5.2% increase in collapse load resistance when end plates (EP) were included, compared to EC3 calculations. Results showed that when end plates were not present, beams with spans of 5 m or less experienced deformation due to plastic yielding (PY).

Additionally, a comparison of Models 1 and 2 indicated that numerical coupling, which was incorporated in the nonlinear analysis, influenced the performance of web posts. It was observed that Model 1, which was uncoupled, experienced failure due to WPB, while Model 2, which was coupled, resulted in plastification of the web post. Examining model 3 for long-span beams where LTB was predominant, it was found that a thickness of $2*t_f$ of EP had an adverse effect on the moment resistance, leading to a 42% difference between the EC3 and finite element (FE) results. Nevertheless, the adoption of a thickness of $1*t_f$ has resulted in improved moment resistance of 10% -19% between EC3 and FE results.

Subsequently, the four models analysed revealed that numerical CP had a significant effect on the web's behaviour, regardless of whether there were plates at the ends of the beam or not. In this study, the FE model employed for the nonlinear analysis included end plates with a thickness of $1*t_f$, and nodes along the beam span were not coupled. The goal of this is to cause an unsteady state on the web page, leading to the expected failure mode of WPB.

CHAPTER 4. ANALYSIS FOR GLOBAL LT BUCKLING AND INTERACTING FAILURE MODES

Table 4-1. Effect of coupling, thickness, and existence of end plates, on the CB's collapse mode.

	L (m)	3	4	5	6	8	10	12	14
	Mb,Rd,2T, EC3 (kN.m)	463.79	345.43	260.83	204.96	141.21	107.8	87.74	74.44
Model 1	M _{COLL} W/O.EP W/O.CP (kN.m)	250.63	224.87	244.26	211.33	150.8	123.37	97.96	84.36
	Diff (1) (%)	-85.10%	-53.60%	-6.80%	3.00%	6.40%	12.60 %	10.40 %	11.80 %
	Collapse mode	WPB+ PY	WPB+ PY	WPB+	LTB+ WPB	LTB	LTB	LTB	LTB
Model 2	M _{COLL} W/O.EP W/CP (kN.m)	338.52	255.04	276.76	227.41	157.59	121.58	97.2	90.63
	Diff (1) (%)	-37.00%	-35.44%	5.76%	9.87%	10.40 %	11.34 %	9.73%	17.86 %
	Collapse mode	WPF+ PY	P- 2T+WPF	P- 2T+WPF	LTB+	LTB	LTB	LTB	LTB
Model 3	M _{COLL} W/EP,2t _f W/CP (kN.m)	380.69	254.84	288.81	317.44	258.06	189.13	147.16	120.9
	Diff (1) (%)	-21.80%	-35.50%	9.70%	35.40 %	45.30 %	43.00 %	40.40 %	38.40 %
	Collapse mode	WPF	P- 2T+WPF	P- 2T+WPF	P- 2T+W PF	LTB+	LTB	LTB	LTB
Model 4	M _{COLL} W/EP,1t _f ; W/O.CP (kN.m)	272.74	236.97	258.39	222.6	158.15	123.92	102.16	92.27
	Diff (1) (%)	-70.00%	-45.80%	-0.90%	7.90%	10.70 %	13.00 %	14.10 %	19.30 %
	Collapse mode	WPB	P- 2T+WPB	P- 2T+WPB	LTB+	LTB	LTB	LTB	LTB

$$\text{Diffy}^{(1)}(\%) = \frac{M_{\text{Coll.FE}} - M_{\text{b,Rd,2T,EC3}}}{M_{\text{Coll.FE}}} * 100$$

4.4. Buckling curves and normalised moment resistance

For uniform steel members in bending, the Eurocode 3 part 1-1 [7] identified two approaches to determining the ultimate LTB strength; the “general case” in clause 6.3.2.2 and the “specific case” for rolled sections in clause 6.3.2.3. According to the cross-section, the concept of buckling curves and the appropriate member slenderness are the basis of both methods; however, the curves to be used differ depending on whether the case is general or specific. In addition, the plateau length for the maximum non-dimensional slenderness $\bar{\lambda}_{LT,0}$ is limited to 0.2 for the general case, and 0.4 for the specific case. For slenderness values of 0.2 or 0.4, the reduction factor χ_{LT} is equal to 1. Supplementary provisions from Eurocode part 1-13 [3] extend the application of EN 1993-1-1 and EN 1993-1-5 to the design of cellular beams made from rolled and welded steel sections and recommends the buckling curve c.

The assumptions provided in Section 3.3.1. were intended to produce the appropriate LTB curve, and the Eurocode recommendation of utilizing buckling curve c for cellular beams need more research to account for a wide range of beam slenderness. As a result, there is a need to define the lower limit of slenderness against LTB at normal temperature and, as a result, improve the buckling curve's tendency toward the safe or conservative state.

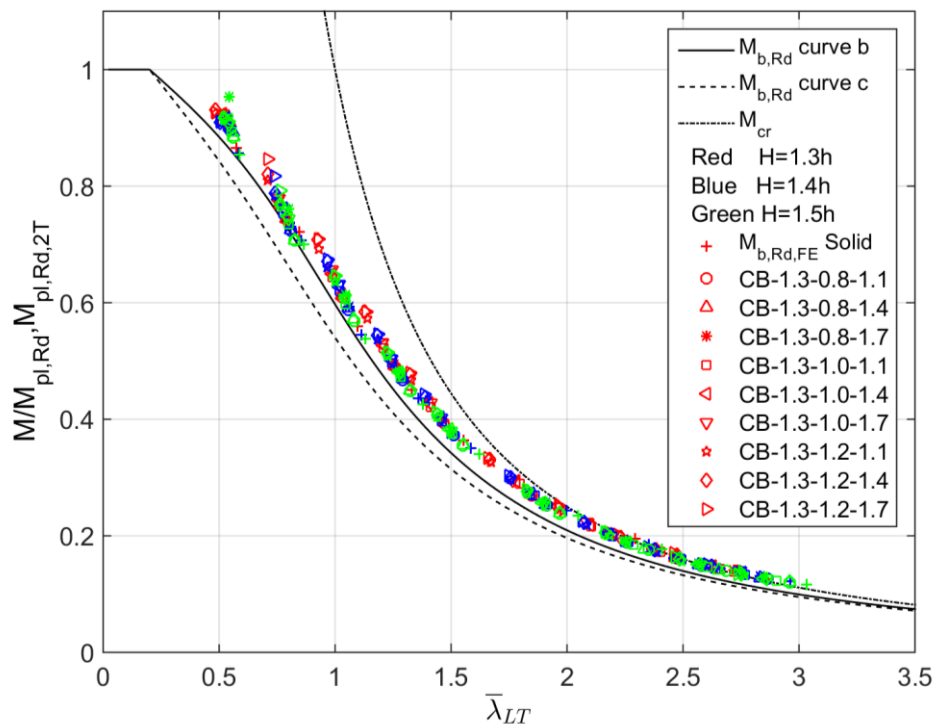
This study includes analytical and numerical analyses for solid and cellular steel beams at ambient and elevated temperatures, including, the in-plan plastic moment resistances, $M_{pl,Rd}$, $M_{pl,Rd,2T}$, $M_{pl,fi,\theta,Rd}$, $M_{pl,fi,\theta,Rd,2T}$, and the LTB moment resistances, $M_{b,Rd}$, $M_{b,Rd,2T}$, $M_{b,fi,t,Rd}$, $M_{b,fi,t,Rd,2T}$. The findings of numerical analysis for various cellular beams include collapse moment resistance M , failure modes, and stress distributions in the deformed state at the collapse time/load. Analytical and numerical results are compared using collapse and plastic moment resistances. The failure modes and stress distributions depicted lead to the establishment of geometric parameters such as a_0 , s , and L that do not favour the preponderance of the LTB behaviour.

Results are plotted for normalized FE collapse moment resistance over the in-plane bending moment resistance, $M/M_{pl,Rd}$ or $M/M_{pl,Rd,2T}$, $M/M_{pl,fi,\theta,Rd}$ or $M/M_{pl,fi,\theta,Rd,2T}$, for solid or cellular steel beams, against non-dimensional slenderness, and comparison is made with analytical curves. At ambient temperature, the flexural buckling curve b [7] is adopted for solid beams, the buckling curve b for equivalent I-sections, and the buckling curve c for cellular beams [3, 7]. At elevated temperatures, the LTB resistance curves provided by ENV 1993-1-2 [4] and by Vila Real [22] are considered in addition to solid beams for cellular beams due to the lack

of a dedicated explicit curve. The FE reduction factor for LTB of cellular beams is calculated using normalized collapse moment resistances derived from numerical resistance curve regression.

4.5. LTB behaviour and failure modes at ambient temperature

The numerical normalized moment resistances and analytical buckling curves for LTB are compared in Figure 4-2 for each investigated beam geometry exposed to either an end bending moment M , Figure 4-2 (a), or a uniformly distributed load D , Figure 4-2 (b).



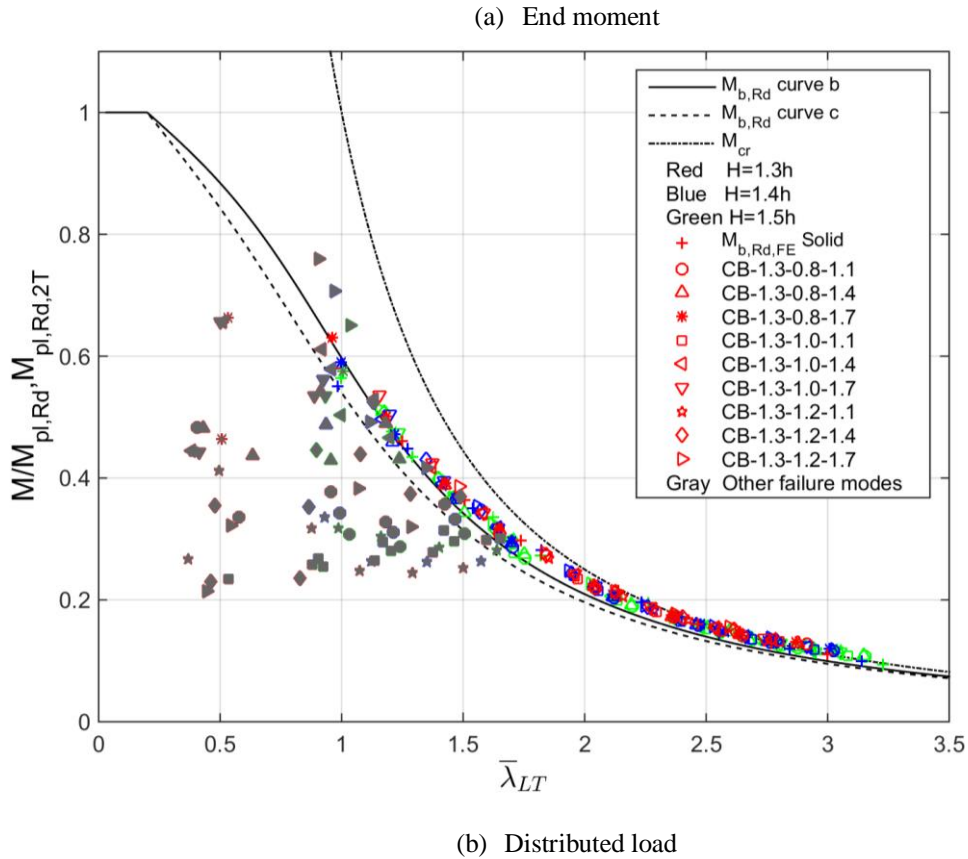


Figure 4-2. Comparison between numerical normalized collapse moments and LTB analytical reduction factors versus non-dimensional slenderness at $\theta=20^{\circ}\text{C}$.

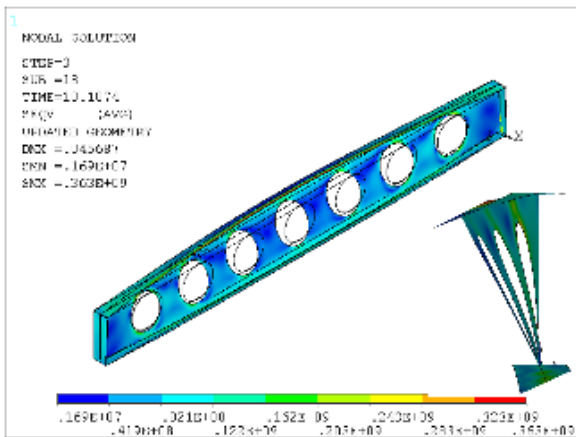
For applied uniform end moment, the LTB failure mode was revealed in most of the simulated cases with short and lengthy span solid and cellular beams, Figure 4-2 (a). The results for FE reduction factors are quite near to the LTB buckling curve b for both solid and cellular beams.

For CBs, with the same cross-section height, where $0,55 < \bar{\lambda}_{LT} \leq 3,0$, the design LTB resistance was conservative by about 11% on average compared with FE resistance. However, for non-dimensional slenderness, $\bar{\lambda}_{LT} \leq 0,55$, small discrepancy between FE and design LTB resistance can be observed. This is because the LTB in combination with the 2T-section failure (LTB+P-2T) was identified as the dominant failure mode. Annex A displays the Von Mises stress distribution and the representation of the ultimate deformation at the point of collapse of solid and cellular beams under end moment loading.

The LTB failure mode was discovered in all simulated solid beam cases with applied uniform load, with the design LTB resistance being conservative by around 9% on average compared to FE resistance, Figure 4-2 (b). Annex B displays the Von Mises stress distribution and the representation of the ultimate deformation at the point of collapse of solid beams under

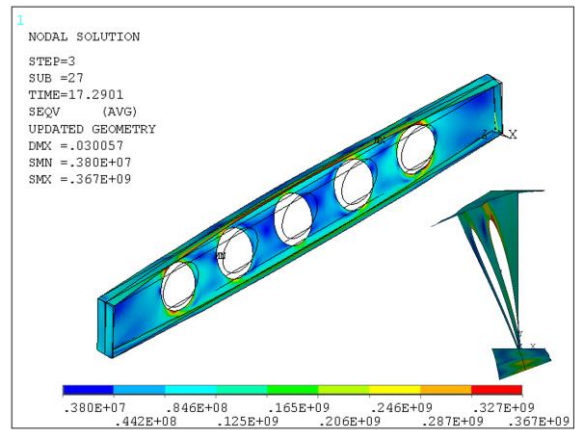
CHAPTER 4. ANALYSIS FOR GLOBAL LT BUCKLING AND INTERACTING FAILURE MODES

distributed loading. Failure mechanisms for cellular beams, on the other hand, occur based on the type of geometrical parameters. The collapse analysis identified the following failure modes: LTB failure; 2T-section failure (P-2T); yielding/bending of the top tee section's flange B-1T, web or web post-buckling (WB or WPB); and Vierendeel mechanism VM. These failure modes are classified as either collapse by plastic yielding (B-1T, P-2T, VM) or collapse by instability (WB/ WPB, LTB). Results are reported in Table 4-2 and the behaviour seen in the non-linear analysis is also reflected in Figure 4-3. Additionally, the corresponding load-displacement curves is presented in Figure 4-4.



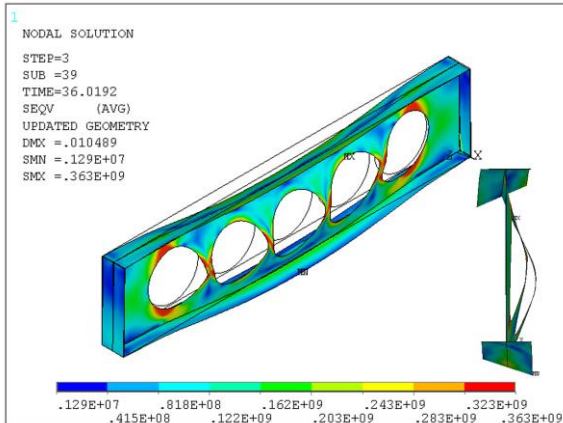
(a) LTB,

$H/h=1.4, a_0/h=1.0, S/a_0=1.7, L=6$ m



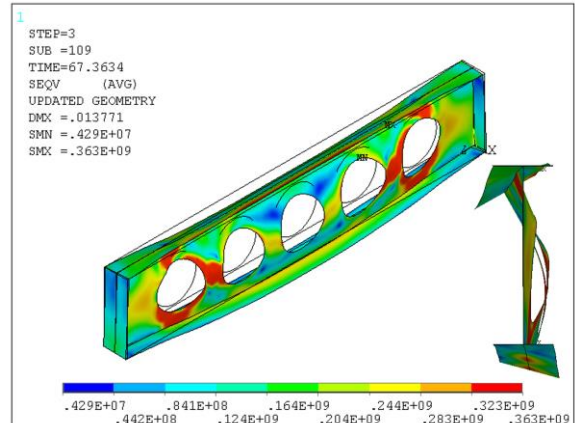
(b) LTB+,

$H/h=1.3, a_0/h=1.0, S/a_0=1.7, L=5$ m



(c) WPB,

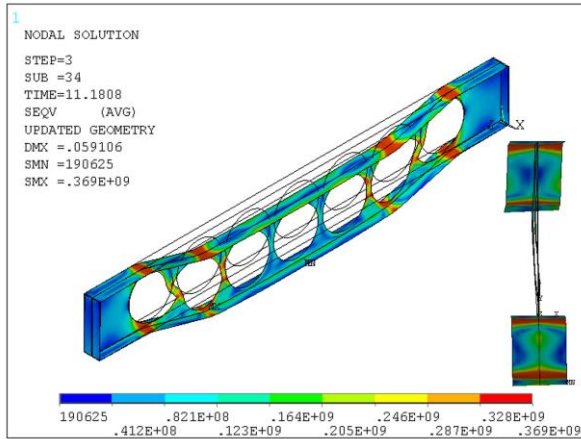
$H/h=1.5, a_0/h=1.0, S/a_0=1.1, L=3$ m



(d) WPB,

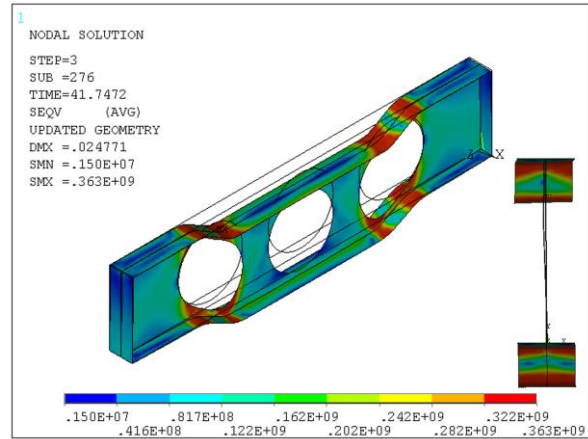
$H/h=1.3, a_0/h=0.8, S/a_0=1.4, L=3$ m

CHAPTER 4. ANALYSIS FOR GLOBAL LT BUCKLING AND INTERACTING FAILURE MODES



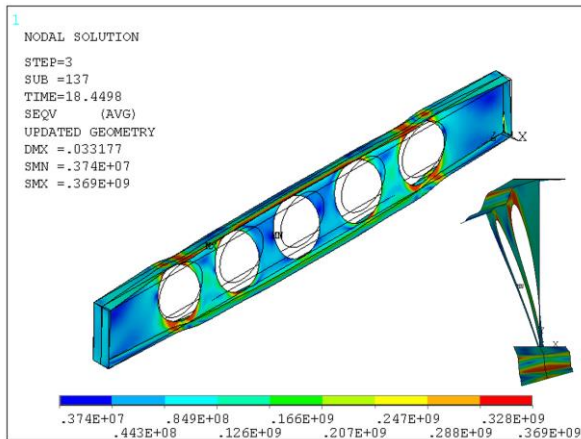
(e) WPB+P-2T,

$H/h=1.4, a_0/h=1.2, S/a_0=1.1, L=5\text{ m}$

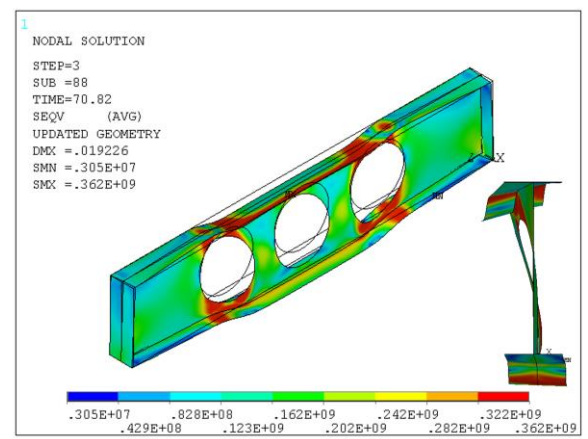


(f) VM,

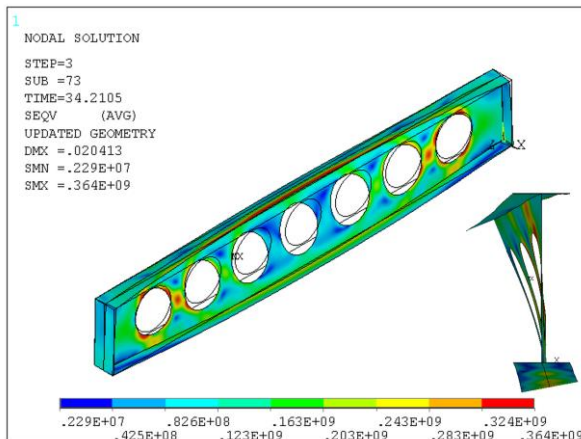
$H/h=1.4, a_0/h=1.2, S/a_0=1.4, L=3\text{ m}$



VM+LTB, $H/h=1.4, a_0/h=1.2, S/a_0=1.4, L=5\text{ m}$

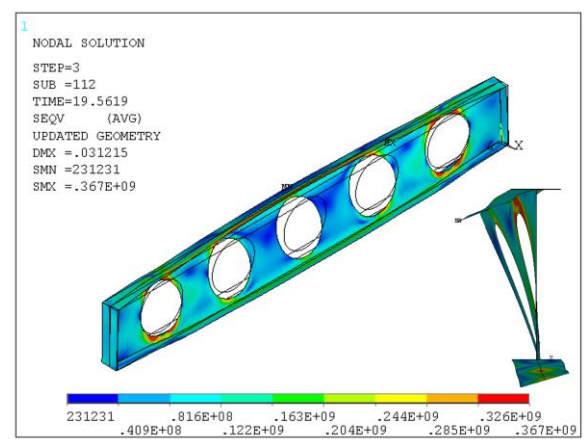


VM+WPB, $H/h=1.3, a_0/h=1.0, S/a_0=1.4, L=3\text{ m}$



(g) WPB+LTB,

$H/h=1.3, a_0/h=0.8, S=1.4a_0, L=4\text{ m}$



LTB+WPB+VM, $H/h=1.5, a_0/h=1.2, S/a_0=1.7, L=5\text{ m}$

CHAPTER 4. ANALYSIS FOR GLOBAL LT BUCKLING AND INTERACTING FAILURE MODES

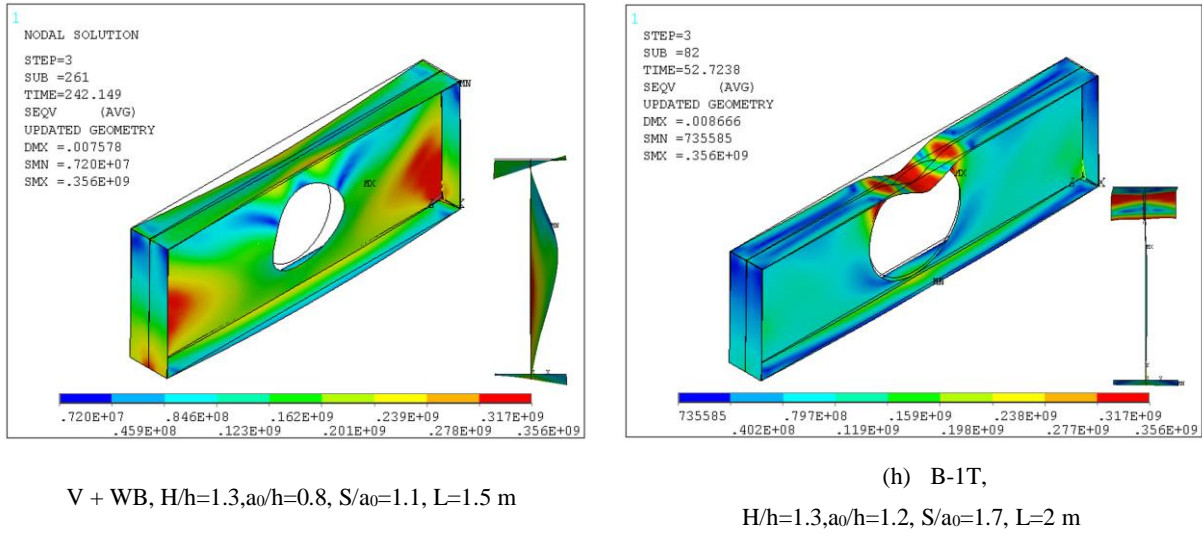


Figure 4-3. Detected failure modes.

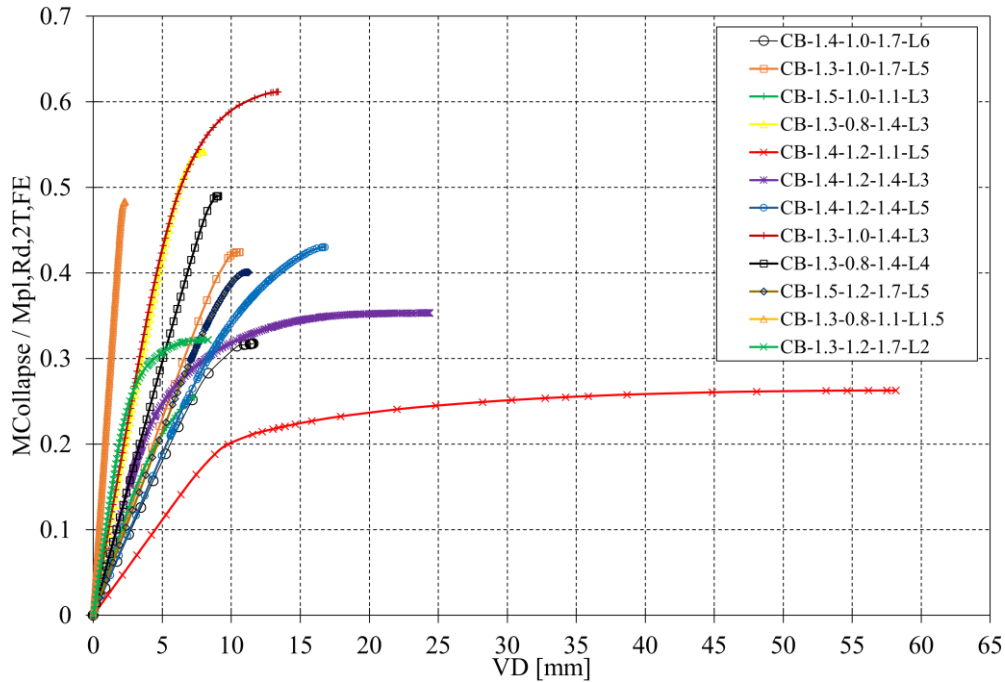


Figure 4-4. Normalized FE collapse moment resistances versus vertical displacements of cellular beams at ambient temperature.

LTB mode was more common in beam models with moderate and large non-dimensional slenderness, where the top flange's upper edge receives the highest compressive stress, as shown in Figure 4-3 (a). It depends on S/a_0 ratios, whatever values for H/h and a_0/h parameters. When $H/h = 1.3, 1.4$, exception is made for $S/a_0 = 1.7, a_0/h = 1.2$, for beams in the interval $1.07 \leq \bar{\lambda}_{LT} \leq 1.35$, the collapse was due to VM, resulting in a lower resistance moment in contrast to the design curve b. For models with intermediate slenderness where the LTB was the main cause of failure, there were also signs of other failure modes labelled

LTB+, see Table 4-2, which appeared in the form of stresses spread around the hole or in the web post's centre, see Figure 4-3 (b).

The parameter ratio S/a_0 , which represents the width of the web post, had a significant effect on the beam's collapse strength. Large S/a_0 values were discovered to boost maximal collapse resistance and allow the local and/or interacted failure modes to fully evolve into the LTB failure mode.

WPB was identified for short spans with narrow web posts of $S/a_0 = 1.1$, as shown in Table 4-2 and was also detected for cases with ratios of $S/a_0 = 1.4$ and 1.7 . Figure 4-3 (c) indicates that for $S/a_0 = 1.1$, all web posts have reached a maximum von Mises stress distribution, and only part of the web of the 2T section near the supports. Whereas, for $S/a_0 = 1.4$ and 1.7 , Figure 4-3 (d), only the web posts closest to the supports were at maximum yield stress and all the web of the 2T section of the opening at the centre line.

As mentioned on Table 4-2, WPB+P-2T was related to cases with $H/h=1.4$, $a_0/h=1.2$, and $S/a_0 = 1.1$, see Figure 4-3 (e).

For relatively short-length beams with $H/h = 1.3, 1.4$, VM was found to be dominant with relatively large tee depths $a_0/h = 1.2$, and $S/a_0 = 1.1, 1.4$, and 1.7 , see Figure 4-3 (f).

Interaction mode VM+ LTB has been revealed in cases with $H/h = 1.3, 1.4$, $a_0/h = 1.0, 1.2$, and $S/a_0 = 1.4, 1.7$, see Figure 4-3 (g). The VM mode was bound to take place when the cross-section height decreased, and when H/h increases, the mode changed to VM+LTB or LTB.

VM+ WPB was observed for short beam models with $H/h = 1.3$, $a_0/h = 1.0$, and $S/a_0 = 1.4$ or $H/h = 1.5$, $a_0/h = 1.2$, and $S/a_0 = 1.4$, see Figure 4-3 (h). This supports the results of the work by Panedpojaman et al. [114], showing that the Vierendeel mechanism may interact with buckling failure.

LTB+WPB was observed for a 4 m beam span with $H/h = 1.3, 1.4, 1.5$, $a_0/h = 0.8$, and $S/a_0 = 1.4$, see Figure 4-3 (i). For a 6 (m) beam span, $H/h = 1.5$, $a_0/h = 1.0$ and $S/a_0 = 1.1$, were also found.

LTB+WPB+VM was observed for $H/h = 1.3, 1.4, 1.5$, $a_0/h = 1.0$, and $S/a_0 = 1.4$, and for $H/h = 1.5$, $a_0/h = 1.2$, and $S/a_0 = 1.4, 1.7$, see Table 4-2 and Figure 4-3 (j).

Short spans of 1.5 and 2 m with $H/h = 1.3$ were studied for cellular beams of a single opening with slenderness less than 0.83, considering the previous parameters a_0/h and S/a_0 , and the

obtained results are red marked points scattered within the margin $0.37 \leq \bar{\lambda}_{LT} \leq 0.63$, Figure 4-2 (b), and Table 4-2. For $\bar{\lambda}_{LT} \leq 0.55$, $S/a_0 = 1.1, 1.4, 1.7$, interaction between shear (V) and web buckling (WB) took place for $a_0/h = 0.8, 1.0$, Figure 4-3 (k), and bending of the top tee section, B-1T for $a_0/h = 1.2$, Figure 4-3 (l).

Figure 4-3 (i) shows that when shear strength is much higher, failure occurs in compression near the supports before web buckling. Figure 4-3 (j) indicates that von Mises stresses were higher at the flanges of the top tee section rather than at the web, owing to the transfer of axial forces and bending moments through the opening.

Figure 4-5 (a) depicts the change in the numerical collapse moment resistance $M_{collapse}$ with beams' length under uniformly distributed load, for web hole sizes $a_0/h = 1.2$, $S/a_0 = 1.4$, and $H/h = 1.3, 1.4, 1.5$. Figure 4-5 (b) depicts Von Mises stress distribution at failure for $H/h = 1.3$ with $L = 3, 5, 8$ m, designated A, B, C, respectively, and $H/h = 1.5$ with $L = 3, 5, 8$ m, designated D, E, F, respectively. The different changes in the $M_{collapse}$ are slenderness related that are, points A and D, B and E, C and F for low, intermediate, and high slenderness, respectively.

It was observed that beams with low or intermediate $\bar{\lambda}_{LT}$ had experienced VM for A and B, LTB for C and F, or VM+WPB for D. The LTB failure mode occurred at high $\bar{\lambda}_{LT}$, and the higher the ratio H/h , the higher the collapse moment resistance, Figure 4-5 (b). Point B, which corresponded to VM, had a significantly lower collapse moment than point E (LTB+), resulting in a reduced beam's ultimate load, Figure 4-5 (a).

CHAPTER 4. ANALYSIS FOR GLOBAL LT BUCKLING AND INTERACTING FAILURE MODES

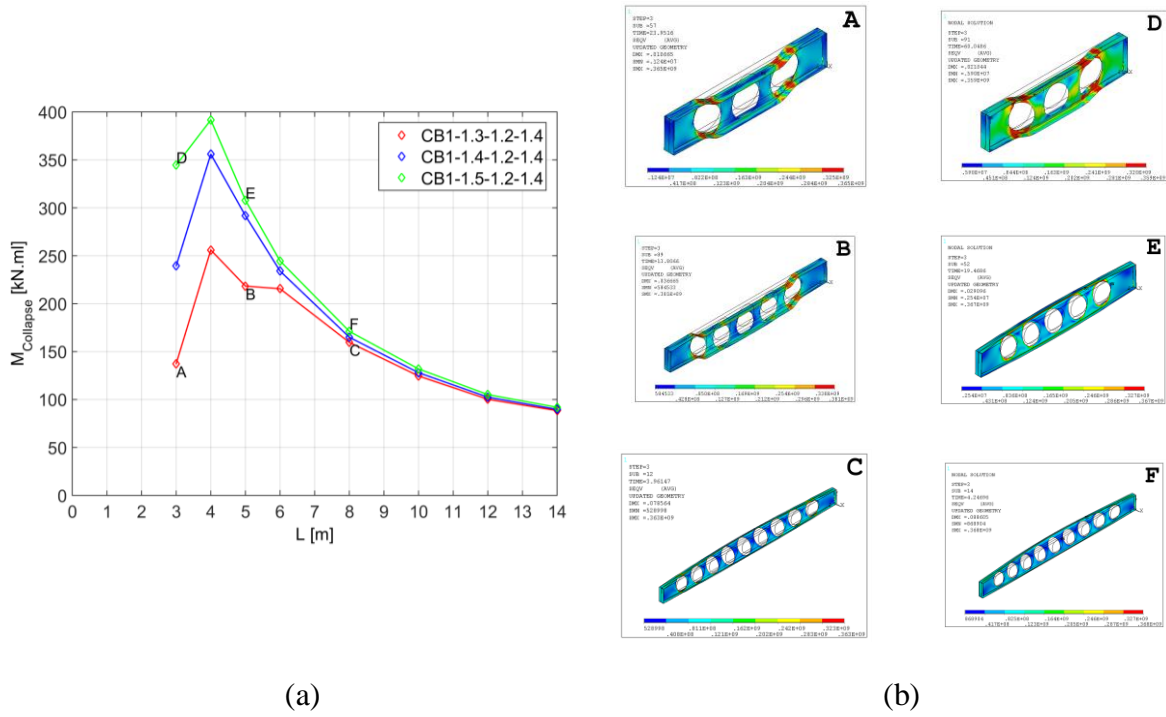


Figure 4-5. (a) Collapse moment resistance against cellular beam lengths at $\theta=20^\circ\text{C}$ with $H/h=1.3, 1.4,$ and 1.5 ; $a_0/h=1.2$; $S/a_0=1.4$. (b) Corresponding Von misses stress at failure for cellular beams with L of 3, 5, and 8 m.

CHAPTER 4. ANALYSIS FOR GLOBAL LT BUCKLING AND INTERACTING FAILURE MODES

Table 4-2. Summary of the failure modes related to the investigated cases at ambient temperature.

Case 1 ($\theta=20$ °C)	L (m)	$\bar{\lambda}_{LT,FE}$	Failure mode	Case 2	L (m)	$\bar{\lambda}_{LT,FE}$	Failure mode	Case 3	L (m)	$\bar{\lambda}_{LT,FE}$	Failure mode
CB-1.3-0.8-1.1	1.5	0.41	V + WB	CB-1.4-0.8-1.1	3-5	0.99-1.74	WPB	CB-1.5-0.8-1.1	3-5	1.03-1.51	WPB
	2-5	0.58-0.1.42	WPB		6	1.70	LTB+		6	1.75	LTB+
	6	1.65	LTB+		8-14	2.12-3.02	LTB		8-14	2.20-3.16	LTB
	8-14	2.04- 2.91	LTB								
CB-1.3-0.8-1.4	1.5	0.43	V + WB	CB-1.4-0.8-1.4	3	0.94	WPB	CB-1.5-0.8-1.4	3	0.95	WPB
	2,3	0.63, 0.91	WPB		4	1.21	WPB+LTB		4	1.24	WPB+LTB
	4	1.18	WPB + LTB		5-14	1.47-3.02	LTB		5-14	1.51-3.15	LTB
	6-14	1.42- 2.88	LTB								
CB-1.3-0.8-1.7	1.5	0.51	V + WB	CB-1.4-0.8-1.7	3	1.00	LTB+	CB-1.5-0.8-1.7	3	1.01	WPB
	2	0.53	WB		4-14	1.22-3.01	LTB		4	1.21	LTB+
	3-4	0.96-1.19	LTB+						5-14	1.46-3.04	LTB
	5-14	1.43-2.87	LTB								
CB-1.3-1.0-1.1	1.5	0.39	V + WB	CB-1.4-1.0-1.1	3-5	0.90-1.42	WPB	CB-1.5-1.0-1.1	3-5	0.93-1.47	WPB
	2, 3, 4, 5, 6	0.54 -1.59	WPB		6	1.65	WPB+		6	1.71	WPB+LTB
	8 - 14	1.97- 2.80	LTB		8-14	2.06-2.95	LTB		8-14	2.13-3.08	LTB
CB-1.3-1.0-1.4	1.5, 2	0.38, 0.51	V + WB	CB-1.4-1.0-1.4	3	0.96	WPB	CB-1.5-1.0-1.4	3	1.00	WPB
	3-4	0.92-1.13	VM+WPB		4	1.17	LTB+WPB+V M		4	1.20	LTB+WPB+VM
	5	1.37	VM+LTB		5-14	1.42-2.92	LTB		5-14	1.45-3.05	LTB
	6-14	1.58-2.77	LTB								
CB-1.3-1.0-1.7	1.5, 2	0.41, 0.50	V + WB	CB-1.4-1.0-1.7	3	0.92	WPB	CB-1.5-1.0-1.7	3	0.93	WPB
	3	0.89	VM		4	1.20	LTB+VM		4	1.24	LTB+
	4	1.15	LTB+VM		5-14	1.42-2.91	LTB		5-14	1.46-3.05	LTB
	5	1.37	LTB+								
	6-14	1.58-2.77	LTB								
CB-1.3-1.2-1.1	1.5, 2	0.37, 0.49	B-1T	CB-1.4-1.2-1.1	3-4	0.93-1.12	WPB	CB-1.5-1.2-1.1	3-6	0.99-1.64	WPB
	3	0.88	VM		5-6	1.35-1.57	WPB+P-2T		8-14	2.04-2.96	LTB
	4, 5, 6	1.07- 1.50	WPB		8-14	1.95-2.81	LTB				

CHAPTER 4. ANALYSIS FOR GLOBAL LT BUCKLING AND INTERACTING FAILURE MODES

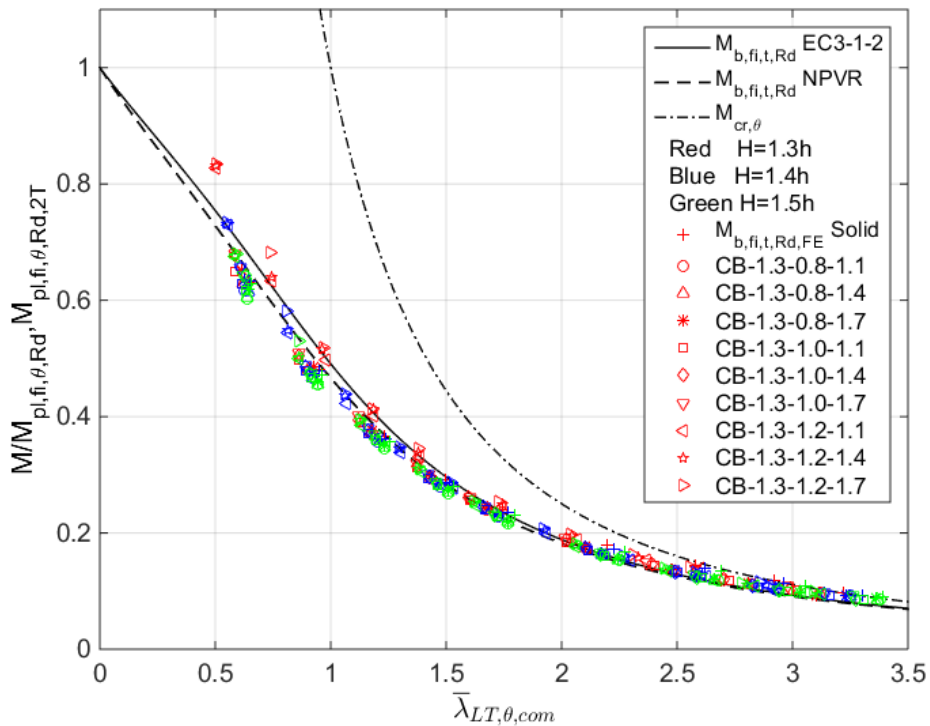
	8-14	1.85-2.64	LTB						
	1.5, 2	0.46, 0.48	B-1T		3	0.87	VM		3 0.90 VM+WPB
	3, 4, 5, 6	0.83-1.49	VM		4	1.13	VM+		4-5 1.18-1.40 LTB+WPB+VM
CB-1.3-1.2-1.4				CB-1.4-1.2-1.4	5	1.35	VM+LTB	CB-1.5-1.2-1.4	
	8	1.84-2.61	LTB		6	1.57	LTB+		6-14 1.63-2.94 LTB
					8-14	1.95-2.79	LTB		
	1.5, 2	0.44, 0.54	B-1T		3	0.97	LTB+WPB		3 1.04 LTB+WB
	3	0.91	LTB+WPB		4-5	1.12-1.35	VM		4-5 1.16-1.40 LTB+WPB+VM
CB-1.3-1.2-1.7	4, 5	1.07, 1.29	VM	CB-1.4-1.2-1.7				CB-1.5-1.2-1.7	
	6	1.48	VM+LTB		6-14	1.56-2.76	LTB		6-14 1.62-2.92 LTB
	8-14	1.83-2.59	LTB						

4.6. LTB behaviour and failure modes under fire condition

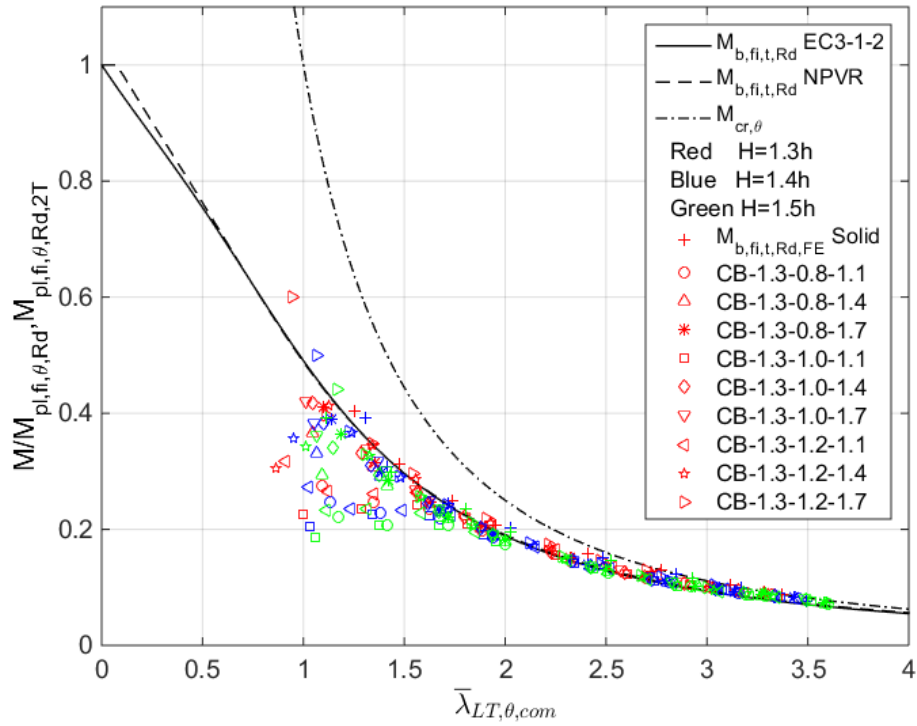
Figure 4-6 presents numerical and analytical results for solid and cellular steel beams against the non-dimensional slenderness $\bar{\lambda}_{LT,\theta,com}$ for both load conditions, end moment Figure 4-6 (a, c) and distributed load Figure 4-6 (b, d), for uniformly elevated temperatures 500 and 700 °C.

The Eurocode LTB resistance curves may satisfactorily represent all FE results for applied end moment loading, as shown in Figure 4-6 (a, c), at 500 °C and 700 °C, and this is also the case for solid beams subjected to distributed load.

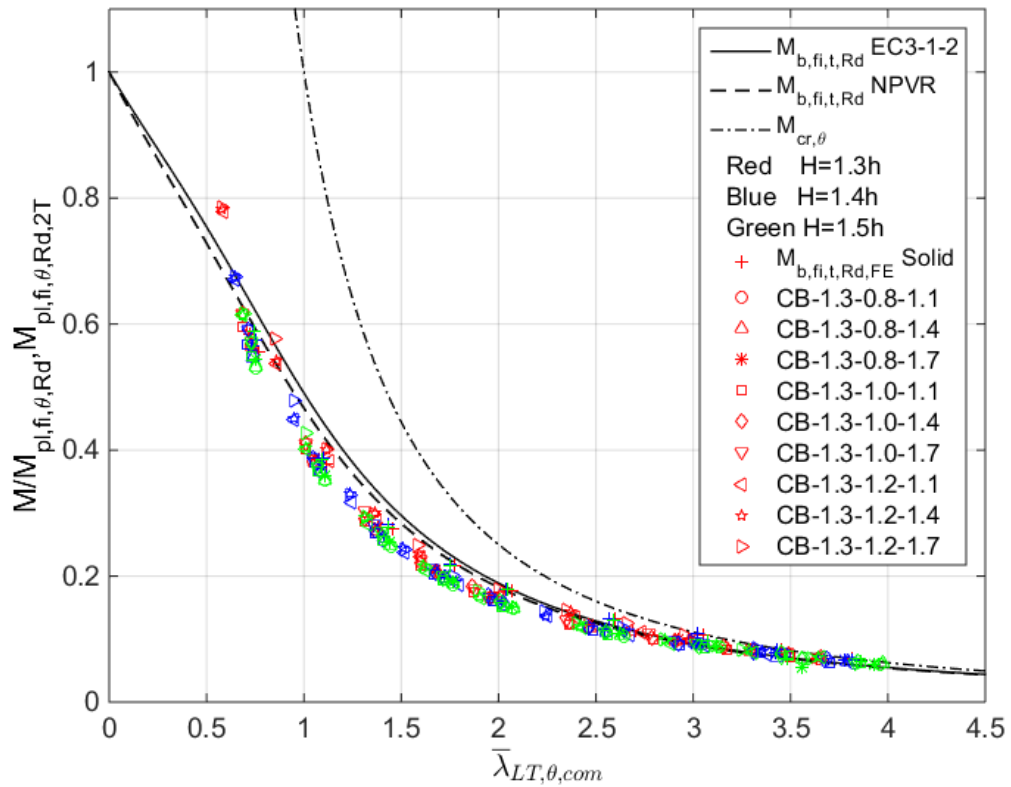
For cellular beams with uniformly distributed loading, numerical resistance curves showed different behaviour for small and intermediate values of slenderness for temperatures, 500°C and 700°C (see Figure 4-6 (b, d)). Table 4-3, and Table 4-4 indicate the typical range of slenderness related to each failure mechanism for each beam subjected to temperatures of 500°C and 700°C, respectively.



(a) End moment, $\theta=500^{\circ}\text{C}$



(b) Distributed load, $\theta=500^{\circ}\text{C}$



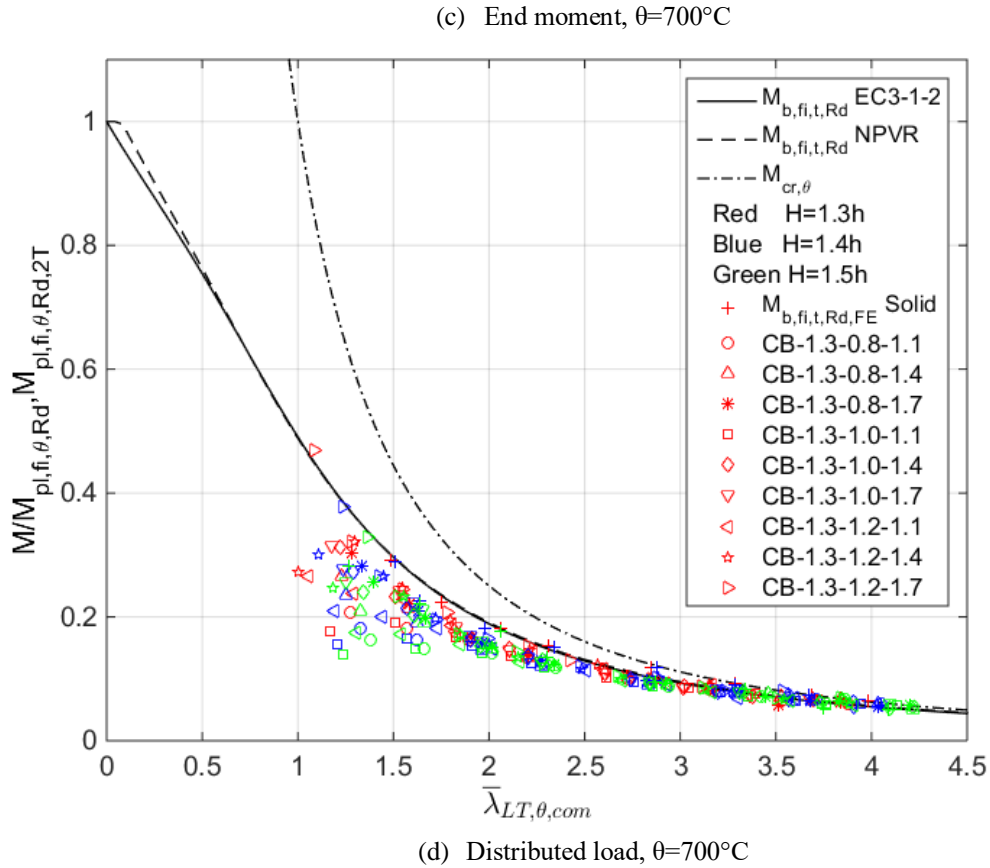


Figure 4-6. Comparison between numerical and analytical reduction factors for LTB against non-dimensional slenderness (a-b) at $\theta=500^\circ\text{C}$, (c-d) at $\theta=700^\circ\text{C}$.

Similarly, to the analysis at $\theta = 20^\circ\text{C}$, the LTB failure mode was observed for intermediate and long-span beams as a function of S/a_0 ; with the range of $\bar{\lambda}_{LT,\theta,com}$ being dependent on the applied temperature.

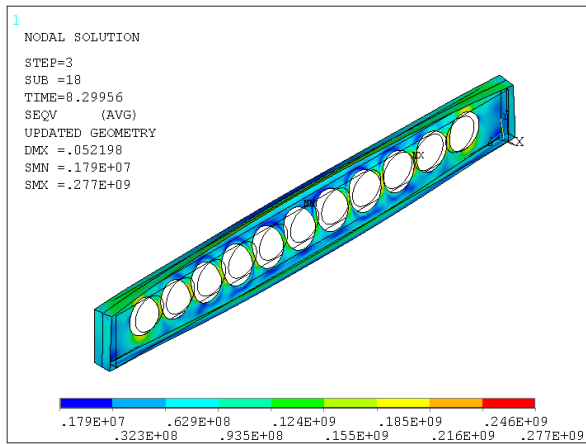
WPB occurred for closely spaced openings with a ratio of $S/a_0 = 1.1$ for $H/h = 1.3, 1.4, 1.5$, and $a_0/h = 0.8, 1.0, 1.2$. It also occurred for $S/a_0 = 1.4, 1.7$, with $a_0/h = 0.8, 1.0$, see Table 4-3 and Table 4-4.

VM was detected for opening diameter ratio of $a_0/h = 1.2$. It occurred at 500°C , for $H/h = 1.3, 1.4$ and it also occurred at 700°C , for $H/h = 1.3$.

The combined failure mode LTB+WPB was observed for $H/h = 1.3, 1.4, 1.5$, $a_0/h = 0.8, 1.0, 1.2$, and $S/a_0 = 1.1, 1.4, 1.7$, at 500°C and 700°C . Combined mode, LTB+VM, was observed for $a_0/h = 1.2$, at 500°C for $H/h = 1.3, 1.4$ with $S/a_0 = 1.4, 1.7$, respectively, and at 700°C for $H/h = 1.3$ with $S/a_0 = 1.4, 1.7$. The last combined failure modes observed were, LTB+, LTB+WPB+VM and WPB+VM, at both temperatures 500°C and 700°C , see Table 4-3 and

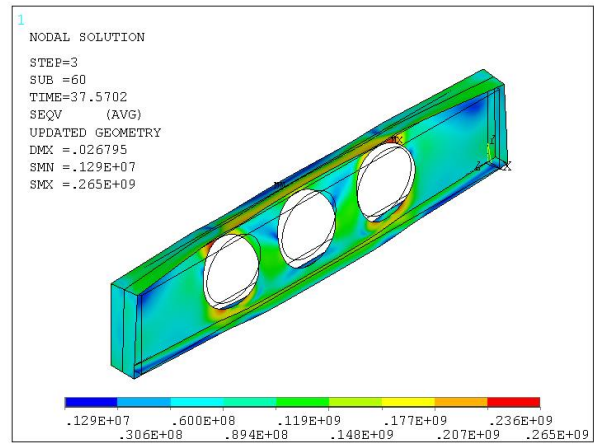
CHAPTER 4. ANALYSIS FOR GLOBAL LT BUCKLING AND INTERACTING FAILURE MODES

Table 4-4. Figure 4-7 and Figure 4-8 also reflected the behaviour seen in the non-linear analysis of cellular beams at $\theta = 500$ and 700 ($^{\circ}\text{C}$), respectively.



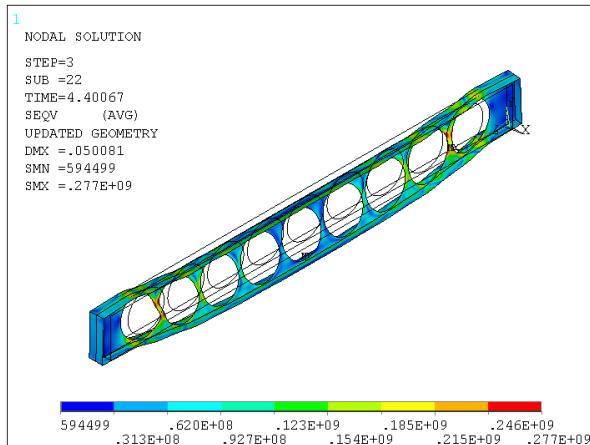
(a) WPB,

$H/h=1.3, a_0/h=0.8, S/a_0=1.1, L=5$ m



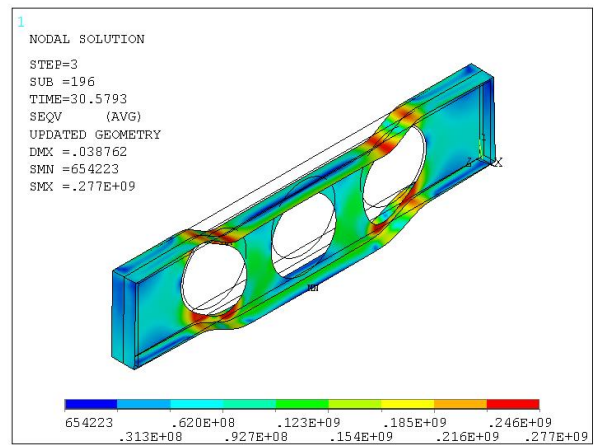
(b) LTB+WPB+VM,

$H/h=1.3, a_0/h=1.0, S/a_0=1.4, L=3$ m



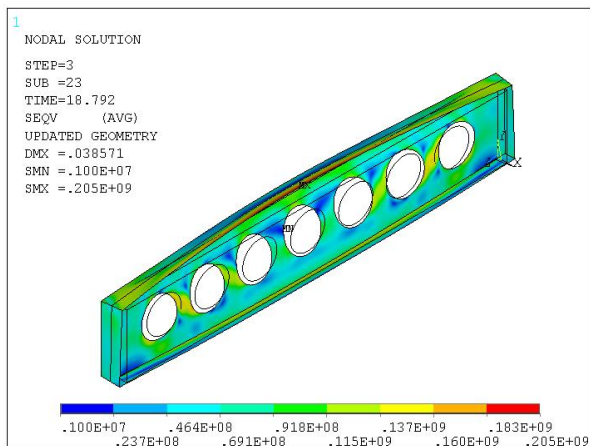
(c) WPB+,

$H/h=1.3, a_0/h=1.2, S/a_0=1.1, L=6$ m



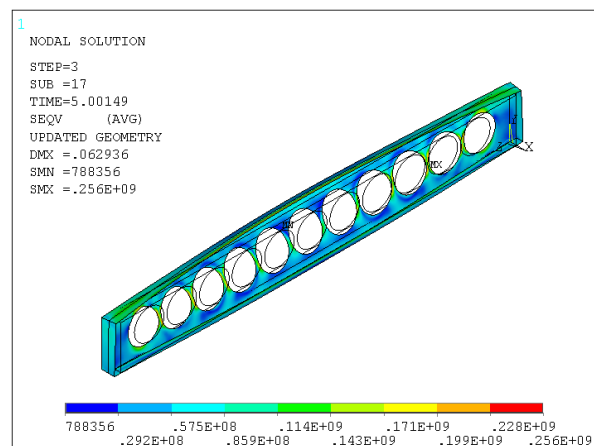
(d) VM,

$H/h=1.4, a_0/h=1.2, S/a_0=1.4, L=3$ m



(e) LTB+WPB,

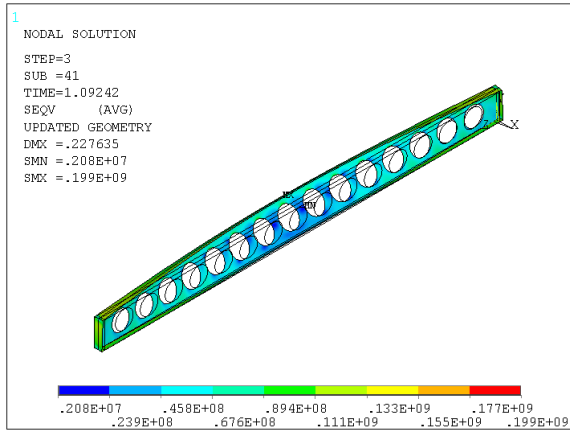
$H/h=1.5, a_0/h=0.8, S/a_0=1.4, L=4$ m



(f) LTB+,

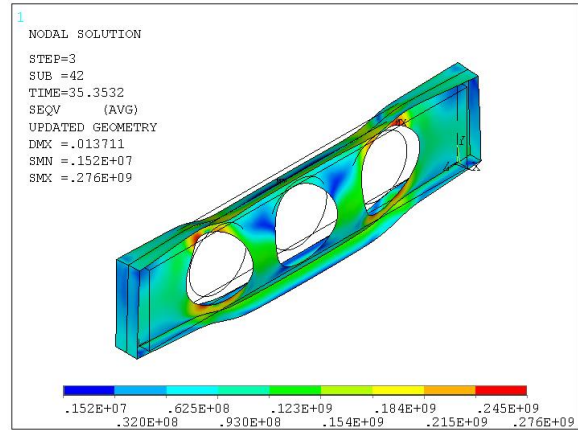
$H/h=1.5, a_0/h=1.0, S/a_0=1.1, L=6$ m

CHAPTER 4. ANALYSIS FOR GLOBAL LT BUCKLING AND INTERACTING FAILURE MODES



(g) LTB,

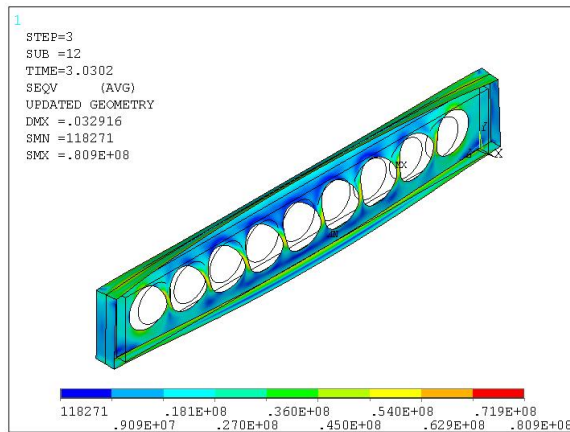
$H/h=1.5, a_0/h=1.0, S=1.4a_0, L=10$ m



(h) WPB+VM,

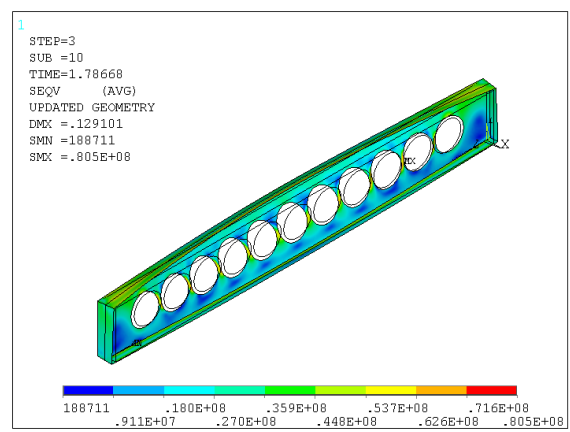
$H/h=1.5, a_0/h=1.2, S/a_0=1.4, L=3$ m

Figure 4-7. Detected failure modes at $\theta = 500$ ($^{\circ}$ C).



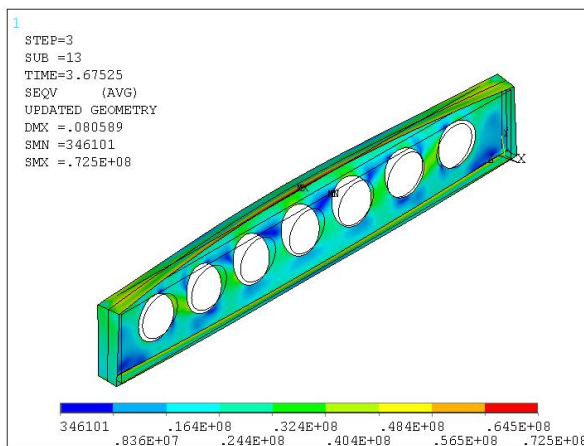
(a) WPB,

$H/h=1.4, a_0/h=0.8, S/a_0=1.1, L=4$ m



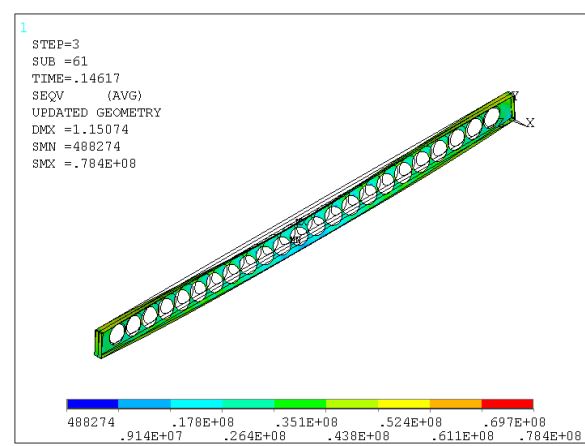
(b) LTB+WPB,

$H/h=1.4, a_0/h=0.8, S/a_0=1.1, L=5$ m



(c) LTB+,

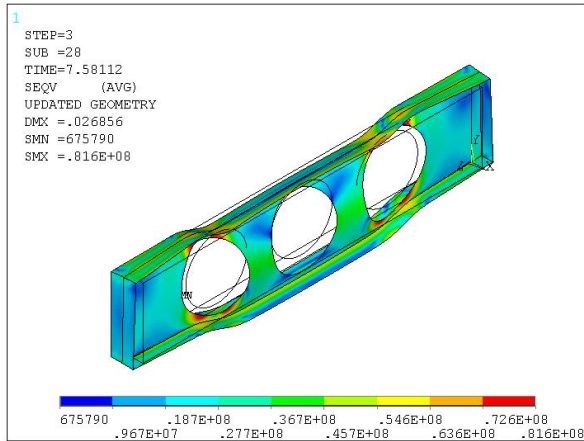
$H/h=1.4, a_0/h=0.8, S/a_0=1.4, L=4$ m



(d) LTB,

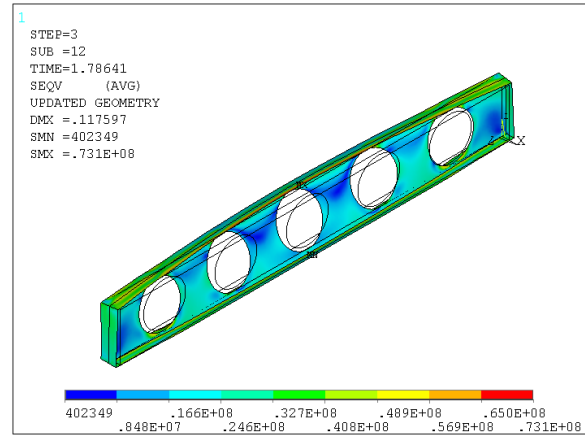
$H/h=1.4, a_0/h=1.0, S/a_0=1.1, L=12$ m

CHAPTER 4. ANALYSIS FOR GLOBAL LT BUCKLING AND INTERACTING FAILURE MODES



(e) WPB+VM,

$H/h=1.4, a_0/h=1.2, S/a_0=1.4, L=3$ m



(f) LTB,

$H/h=1.4, a_0/h=1.2, S/a_0=1.7, L=5$ m

Figure 4-8. Detected failure modes at $\theta = 700$ °C.

Figure 4-9 (a) shows the change in the numerical collapse moment resistance $M_{fi,\theta,collapse}$ with the height ratio H/h varies from 1.3 to 1.4 to 1.5, at 500°C, by setting the ratios a_0/h and S/a_0 to values of 1.2 and 1.4, respectively. It was observed that a sharp fall of the collapse moment resistance for lengths between 4 and 8 m, also, it was observed that beams with low or intermediate $\bar{\lambda}_{LT}$ had experienced VM for A, LTB+VM for B, or VM+WPB for D. The LTB failure mode becomes the dominant failure and occurs at intermediate and high $\bar{\lambda}_{LT}$, for E, C, F, Figure 4-9 (b). Similarly, to the observation made for ambient, the higher the ratio H/h , the higher the collapse moment resistance at elevated temperature. For the beam with $L=5$ m labelled B, at the temperature of 500 °C, the LTB+VM failure mode took place instead of VM at 20 °C.

CHAPTER 4. ANALYSIS FOR GLOBAL LT BUCKLING AND INTERACTING FAILURE MODES

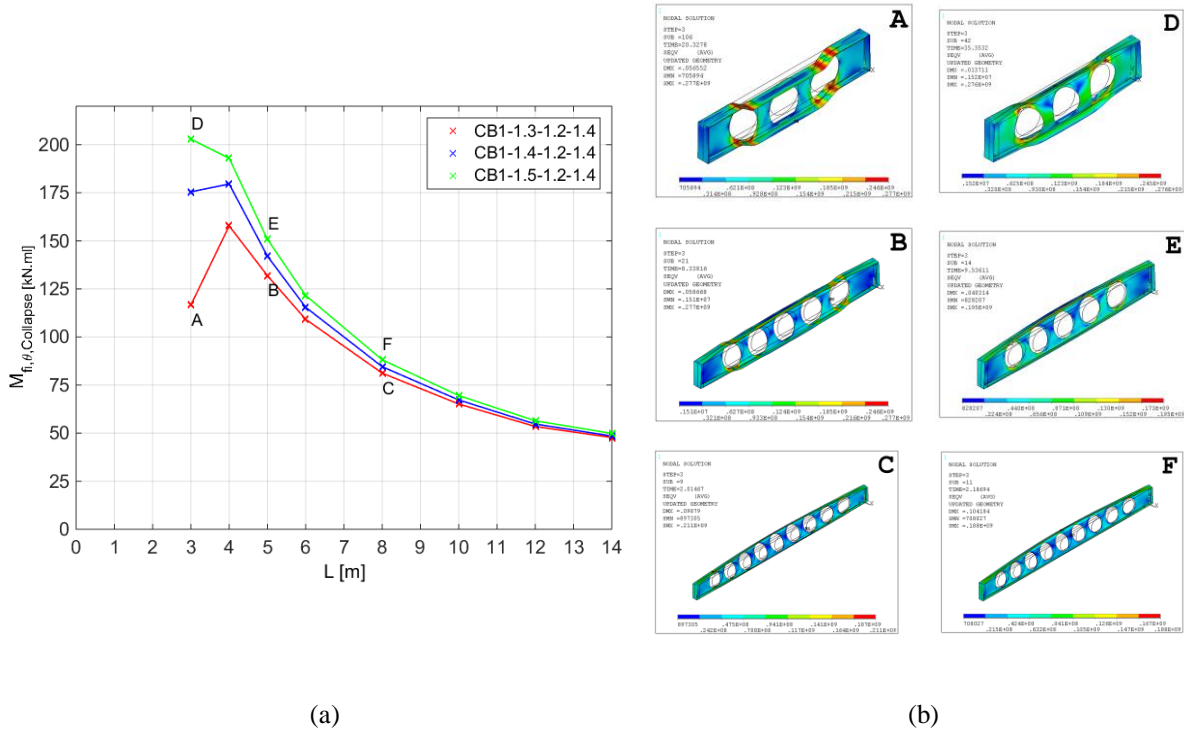


Figure 4-9. (a) LTB moment resistance versus cellular beam length at $\theta=500^\circ\text{C}$ with $H/h=1.3, 1.4,$ and 1.5 ; $a_0/h=1.2$; $S/a_0=1.4$. (b) Corresponding Von misses stress at failure for cellular beams with L of 3, 5, 8 m from left to right.

Figure 4-10 (a) shows the variation in the numerical collapse moment resistance $M_{fi,\theta, \text{collapse}}$ when the ratios a_0/h and S/a_0 are set to 1.2 and 1.4, respectively, and the height ratio H/h is varied between 1.3-1.5 at a temperature of 700°C . It was observed that the collapse moment resistance experienced a sharp decrease for beams with lengths between 4-8 (m); moreover, beams with low- or intermediate $\bar{\lambda}_{LT}$ experienced VM for A or VM+WPB for D, with LTB being the dominant failure mode in beams with intermediate to high $\bar{\lambda}_{LT}$ for B, C, E, and F (Figure 4-9 (b)). Similarly, to what had been observed for $\theta = 20$ and 500°C , the higher the ratio of H/h , the higher the collapse moment resistance at $\theta = 700^\circ\text{C}$. For example, beam B with length $L = 5$ m experienced the LTB failure mode instead of LTB+VM at 500°C when the temperature was raised to 700°C .

CHAPTER 4. ANALYSIS FOR GLOBAL LT BUCKLING AND INTERACTING FAILURE MODES

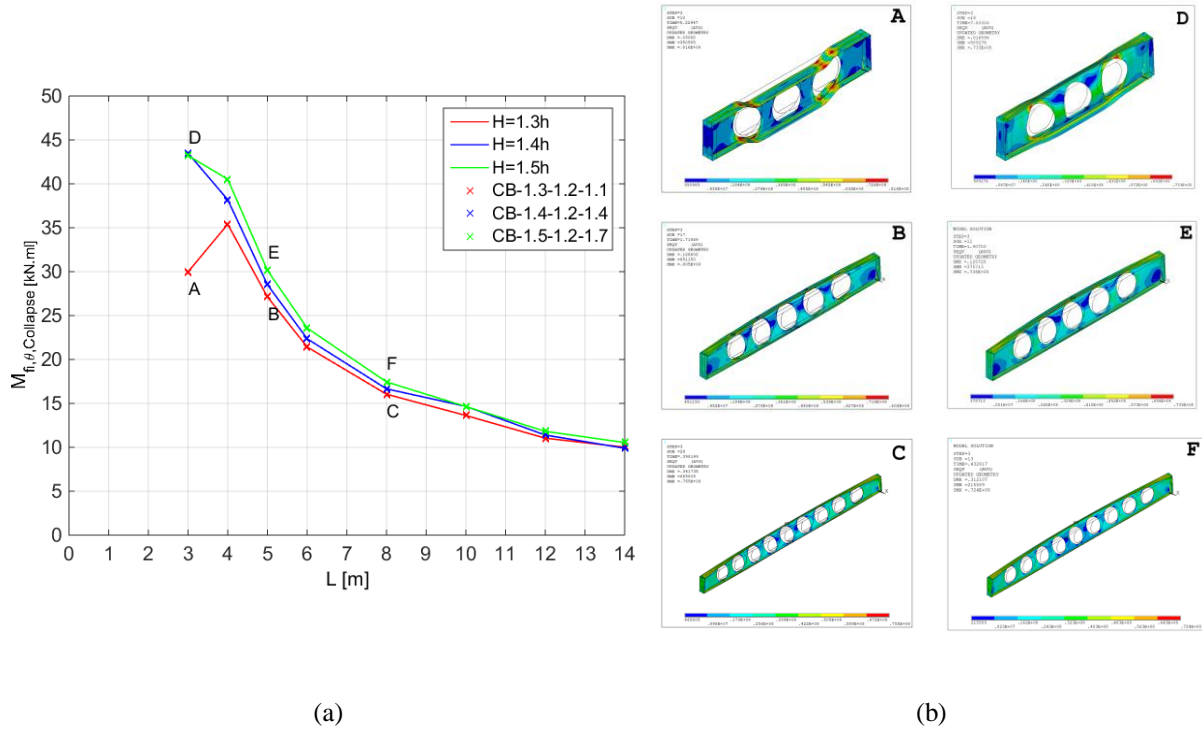


Figure 4-10. (a) LTB moment resistance versus cellular beam length at $\theta=700^\circ\text{C}$ with $H/h=1.3, 1.4,$ and 1.5 ; $a_0/h=1.2$; $S/a_0=1.4$. (b) Corresponding Von misses stress at failure for cellular beams with L of 3, 5, 8 m from left to right.

The average difference between numerical and analytical results for CB cases involving LTB failure modes or combinations of LTB with other local modes approached 10% and 13% at 500°C and 700°C , respectively.

CHAPTER 4. ANALYSIS FOR GLOBAL LT BUCKLING AND INTERACTING FAILURE MODES

Table 4-3. Summary of the failure modes related to the investigated cases at $\theta=500$ °C.

Case 1 ($\theta=500$ °C)	L (m)	$\bar{\lambda}_{LT,0,FE}$	Failure mode	Case 2	L (m)	$\bar{\lambda}_{LT,0,FE}$	Failure mode	Case 3	L (m)	$\bar{\lambda}_{LT,0,FE}$	Failure mode
CB-1.3-0.8-1.1	3-5	1.09-1.62	WPB	CB-1.4-0.8-1.1	3-4	1.13-1.38	WPB	CB-1.5-0.8-1.1	3-4	1.18-1.41	WPB
	6	1.88	LTB+		5	1.67	LTB+WPB		5	1.71	LTB+WPB
	8-14	2.33-3.33	LTB		6-14	1.94-3.45	LTB		6	2.00	LTB+
CB-1.3-0.8-1.4	3	1.04	WPB	CB-1.4-0.8-1.4	3	1.07	WPB	CB-1.5-0.8-1.4	3	1.09	WPB
	4	1.35	LTB+WPB		4	1.38	LTB+WPB		4	1.41	LTB+WPB
	5	1.62-	LTB+		5-14	1.67-3.44	LTB		5-14	1.72-3.59	LTB
	6-14	1.88-3.28	LTB								
CB-1.3-0.8-1.7	3	1.1	LTB+WPB	CB-1.4-0.8-1.7	3-4	1.14-1.39	LTB+	CB-1.5-0.8-1.7	3	1.19	LTB+WPB
	4-14	1.35-3.29	LTB		5-14	1.68-3.43	LTB		4	1.42	LTB+
CB-1.3-1.0-1.1	3-5	1.00-1.56	WPB	CB-1.4-1.0-1.1	3-5	1.03-1.62	WPB	CB-1.5-1.0-1.1	3-5	1.06-1.67	WPB
	6	1.81	LTB+WPB		6	1.89	LTB+		6	1.95	LTB+
	8-14	2.24-3.18	LTB		8-14	2.35-3.37	LTB		8-14	2.44-3.52	LTB
CB-1.3-1.0-1.4	3-4	1.05-1.29	LTB+WPB+VM	CB-1.4-1.0-1.4	3	1.1	WPB	CB-1.5-1.0-1.4	3	1.15	WPB
	5	1.56	LTB+		4	1.34	LTB+WPB		4	1.37	LTB+WPB
	6-14	1.80-3.16	LTB		5	1.62	LTB+		5	1.67	LTB+
CB-1.3-1.0-1.7	3	1.01	LTB+WPB+VM	CB-1.4-1.0-1.7	6-14	1.88-3.34	LTB	CB-1.5-1.0-1.7	6-14	1.94-3.49	LTB
	4	1.31	LTB+		3	1.06	WPB		3	1.07	WPB
	5-14	1.56-3.14	LTB		4	1.37	LTB+		4-14	1.41-3.49	LTB
CB-1.3-1.2-1.1	3-5	0.91-1.35	WPB+VM	CB-1.4-1.2-1.1	5-14	1.62-3.33	LTB	CB-1.5-1.2-1.1	3-5	1.11-1.58	WPB
	6	1.57	WPB+		3-5	1.02-1.49	WPB		6	1.85	LTB+WPB
	8-14	1.93-2.75	LTB		6	1.73	LTB+WPB		8-14	2.31-3.34	LTB
CB-1.3-1.2-1.4	3	0.87	VM	CB-1.4-1.2-1.4	8-14	2.15-3.09	LTB	CB-1.5-1.2-1.4	3	1.01	WPB+VM
	4-5	1.12-1.34	LTB+VM		3	0.95	VM		4	1.33	LTB+
	6	1.55	LTB+		4	1.24	LTB+		5-14	1.58-3.32	LTB
	8-14	1.92-2.73	LTB		5-14	1.48-3.06	LTB				
CB-1.3-1.2-1.7	3	0.94	LTB	CB-1.4-1.2-1.7	3	1.06	LTB	CB-1.5-1.2-1.7	3-4	1.17-1.31	LTB+
	4-5	1.11-1.34	VM/VM+		4	1.23	LTB+VM		5-14	1.58-3.30	LTB
	6	1.55	LTB+		5	1.47	LTB+				
	8-14	1.91-2.70	LTB		6-14	1.71-3.03	LTB				

CHAPTER 4. ANALYSIS FOR GLOBAL LT BUCKLING AND INTERACTING FAILURE MODES

Table 4-4. Summary of the failure modes related to the investigated cases at $\theta=700$ °C

Case 1 ($\theta=700$ °C)	L (m)	$\lambda_{LT,\theta,FE}$	Failure mode	Case 2	L (m)	$\lambda_{LT,\theta,FE}$	Failure mode	Case 3	L (m)	$\lambda_{LT,\theta,FE}$	Failure mode		
CB-1.3-0.8-1.1	3-5	1.28-1.90	WPB	CB-1.4-0.8-1.1	3-4	1.33-1.62	WPB	CB-1.5-0.8-1.1	3-4	1.37-1.66	WPB		
	6-14	2.21-3.90	LTB		5	1.96	LTB+WPB		5	2.01	LTB+WPB		
CB-1.3-0.8-1.4	3	1.22	LTB+WPB	CB-1.4-0.8-1.4	6-14	2.28-4.04	LTB	CB-1.5-0.8-1.4	6-14	2.35-4.22	LTB		
	4	1.58	LTB+		3	1.25	WPB		3	1.28	WPB		
	5-14	1.90-3.85	LTB		4	1.62	LTB+		4	1.66	LTB+WPB		
CB-1.3-0.8-1.7	3-4	1.29-1.59	LTB+	CB-1.4-0.8-1.7	5-14	1.96-4.03	LTB	CB-1.5-0.8-1.7	5-14	2.01-4.21	LTB		
	5-14	1.91-3.84	LTB		3	1.34	LTB+WPB		3	1.39	LTB+WPB		
CB-1.3-1.0-1.1	3-4	1.17-1.51	WPB	CB-1.4-1.0-1.1	4-14	1.63-4.02	LTB	CB-1.5-1.0-1.1	4-14	1.67-4.20	LTB		
	5	1.82	LTB+WPB		3-4	1.21-1.57	WPB		3-4	1.24-1.61	WPB		
	6-14	2.12-3.72	LTB		5	1.91	LTB+WPB		5	1.96	LTB+WPB		
CB-1.3-1.0-1.4	3	1.22	LTB+WPB	CB-1.4-1.0-1.4	6	2.22	LTB+	CB-1.5-1.0-1.4	6-14	2.29-4.13	LTB		
	4	1.51	LTB+		8-14	2.75-3.95	LTB		3	1.34	WPB		
	5-14	1.82-3.69	LTB		3	1.29	LTB+WPB		4	1.61	LTB+		
CB-1.3-1.0-1.7	3	1.18	LTB+WPB	CB-1.4-1.0-1.7	4-14	1.57-3.91	LTB	CB-1.5-1.0-1.7	5-14	1.96-4.10	LTB		
	4-14	1.54-3.68	LTB		3	1.24	LTB+WPB		3	1.25	LTB+WPB		
CB-1.3-1.2-1.1	3	1.24	WPB+VM	CB-1.4-1.2-1.1	4-14	1.60-3.90	LTB	CB-1.5-1.2-1.1	4-14	1.65-4.09	LTB		
	4	1.29	VM		3	1.19	WPB+VM		3-4	1.30-1.54	WPB		
	5	1.55	LTB+WPB+VM		4	1.44	WPB		5	1.85	LTB+WPB		
CB-1.3-1.2-1.4	6-14	1.80-3.17	LTB+	CB-1.4-1.2-1.4	5	1.73	LTB+WPB	CB-1.5-1.2-1.4	6-14	2.16-3.91	LTB		
	3	1.0	VM		6	2.02	LTB+		3	1.18	WPB+VM		
	4	1.30	LTB+VM		8-14	2.50-3.60	LTB		4-14	1.55-3.89	LTB		
	5	1.55	LTB+		3	1.11	WPB+VM		5-14	1.45-3.57	LTB		
CB-1.3-1.2-1.7	6	1.79-3.15	LTB	CB-1.4-1.2-1.7	3-14	1.24-3.53	LTB	CB-1.5-1.2-1.7	3-14	1.36-3.85	LTB		
	3	1.09	LTB		CB-1.4-1.2-1.7	3-14	1.24-3.53		LTB	CB-1.5-1.2-1.7	3-14	1.36-3.85	LTB
	4	1.28	LTB+VM			CB-1.4-1.2-1.7	3-14		1.24-3.53		LTB	CB-1.5-1.2-1.7	3-14
	5	1.54	LTB+		6-14		1.78-3.11		LTB	6-14	1.78-3.11		LTB

4.7. Development of a new plateau length of the LTB curves for cellular beams

The parametric study and the analysis presented in Section 4.5. , for cellular beams subjected to a uniformly distributed load at ambient temperature have revealed that there are significant disparities between numerical and actual LTB design curves provided by EC3-1-1 §§ 6.3.2.2 [7]. These disparities were found to fall within the “non-conservative” side of the $(\bar{\lambda}_{LT}, M/M_{pl,Rd}, M_{pl,Rd,2T})$ plane, pointing to local failure modes and resulting in numerical moment resistances lower than those of code values. These were observed more frequently for "beams with small or intermediate slenderness", but disparities were small for those with high slenderness, which sets the points closer to the buckling curve "b". Numerical results showed also that when using EC3 curves, the actual critical behaviour of a particular section is not adequately represented because most of the properties of the cellular beam sections are based solely on the depth-to-width ratio h/b , particularly in beam cases with ratios S/a_0 indicating narrow web posts or ratios a_0/h indicating large openings.

When confronting the numerical LTB resistance curves with the Eurocode buckling curve, it becomes clear that there is a need to increase the consistency of the latter. This is only possible by setting a new plateau length of the LTB curves based on cellular beam geometric parameters. Lower values of the numerically normalized moment resistance giving rise to local failure and couple modes were disregarded, and the study focuses on the LTB failure mode only.

This proposal considers the statistical method of mean squared error (MSE), to predict a new plateau length of the LTB curves for simply supported cellular beams under uniformly distributed load. The input data required for the model are the key parameters of the cellular beam cross-section (H/h , a_0/h , and S/a_0) and the beam slenderness.

A new equation was worked out based on the MATLAB Curve Fitting App using the Poly21 surface-fitting model. A numerical database for beam parameters together with non-dimensional slenderness, Table 4-5, is used and the FE results chosen are within the limits of 0 to 10% above the buckling curve. It is important to point out that, an improvement of data within the limit in the range of 0 to 10 were adopted, considering two new cases, $a_0/h=1.0$, $S/a_0=1.1$, and $a_0/h= 1.2$, $S/a_0=1.4$, for $L= 7m$.

A suitable equation that best fits the FE results is suggested to be used for predicting the slenderness limit for the LTB design of cellular beams. It can be expressed based on the ratios a_0/h and S/a_0 by the following function:

$$\bar{\lambda}_{LT,0} = 3.64 - 0.86 * (a_0/h) - 2.28 * (S/a_0) + 1.33 * (a_0/h) * (S/a_0) \quad (92)$$

To check the validity and dependability of the suggested equation, its outcomes for the non-dimensional slenderness of the cellular beams were compared to the numerical database. The comparison were made in terms of the goodness-of-fit statistics for the polynomial fit (R^2) and the performance ratio ($\bar{\lambda}_{LT,FE} / \bar{\lambda}_{LT,PV}$), where $\bar{\lambda}_{LT,FE}$ is the numerical value of non-dimensional slenderness, and $\bar{\lambda}_{LT,PV}$ is the value of the non-dimensional slenderness predicted from the fitting equation. Smith's research results [115] showed that a satisfactory state can be reached when the R^2 is greater than 0.8 and the differences between the experienced and predicted values are smallest. We determined that, the coefficient of determination (R^2) of the surface was relatively close to 1.0 (0.9706), showing that the proposed equation was convenient. Furthermore, Table 4-5 shows the ratio of the FE results to the suggested equation ($\bar{\lambda}_{LT,FE} / \bar{\lambda}_{LT,PV}$), which had an average ratio of 1.01. A detailed analysis of the results reveals that for more than 89% of the data, the difference between the parametric numerical results $\bar{\lambda}_{LT,FE}$ and the values predicted $\bar{\lambda}_{LT,PV}$ by the model equation was ± 6 . Consequently, all numerical results have been covered by the suggested equation.

The suggested modification to the EC3 buckling curve closely follows the actual European LTB design rules "general case", except for the use of the maximum value of $\bar{\lambda}_{LT,0}$. A further notable change was that the value of the modified reduction factor, $\chi_{LT,mod}$, becomes a variable that depends on $\bar{\lambda}_{LT,0}$ rather than the constant value 1.

CHAPTER 4. ANALYSIS FOR GLOBAL LT BUCKLING AND INTERACTING
FAILURE MODES

Table 4-5. Performance ratio between FE and predicted results for $H/h= 1.3$.

Model no.	H/h	S/a ₀	a ₀ /h	$\bar{\lambda}_{LT,FE}$	$\bar{\lambda}_{LT,PV}$	Ratio (FE/PV)
1	1.3	1.1	0.8	1.65	1.61	1.02
2	1.3	1.1	1.0	1.79	1.74	1.03
3	1.3	1.1	1.2	1.85	1.86	1.00
4	1.3	1.4	0.8	1.18	1.25	0.94
5	1.3	1.4	1.0	1.37	1.45	0.94
6	1.3	1.4	1.2	1.67	1.65	1.01
7	1.3	1.7	0.8	0.96	0.88	1.08
8	1.3	1.7	1.0	1.15	1.17	0.99
9	1.3	1.7	1.2	1.48	1.45	1.02

Figure 4-11 depicts the comparison of LTB analytical results predicted by Eurocode 3, $M_{b,Rd}$, and overall predicted LTB moment resistances of the proposed equation for $M_{b,Rd,PV}$, with the actual FE collapse moment resistance, $M_{Coll,Rd}$. Prediction error limits of $\pm 10\%$ is plotted with red symbols representing EC3 analytical results, and blue symbols representing theoretically predicted results.

Most of data points were within the conservative zone and the formulation was shown to match the desired conditions and to be able to better estimate the slenderness limit of the perforated beams versus the LTB design when compared to numerical findings. On the other hand, for values $M_{Coll,Rd}/M_{pl,Rd,FE} \leq M_{b,Rd,NP}/M_{pl,Rd,2T}$, odd points that tend towards the non-conservative zone are cases where the slenderness was less than the slenderness limit at which the LTB must be calculated.

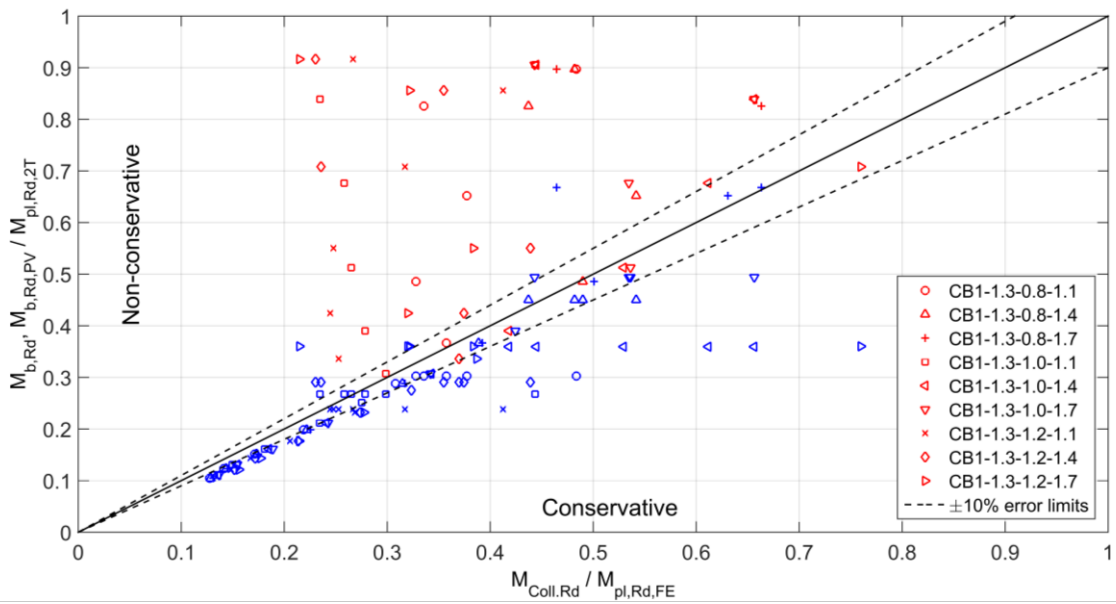


Figure 4-11. Comparisons of numerical results, analytical results predicted by the Eurocode 3 (in red colour), and theoretical results predicted by the proposed equation (in blue colour).

4.8. Comparison of Eurocode and proposed methods for LTB resistance of a cellular beam under distributed load

To compare the EC3 general method to the proposed method, the normalized design LTB resistance and numerical collapse resistance, $M/M_{pl,Rd,2T}$, for a cellular beam model under distributed load were plotted against the non-dimensional slenderness, $\bar{\lambda}_{LT}$, Table 4-6, Figure 4-12, show the cellular beam geometric parameters and the design results for comparison.

Table 4-6. Cellular beam design verification

H/h	a_0/S	S/a_0	L (m)	$\bar{\lambda}_{LT,EC3}$	$M_{b,Rd,EC3}$ (kN.m)	$M_{Coll,FE}$ (kN.m)	$\bar{\lambda}_{LT,0}$ (Eq. (92))	$M_{b,Rd,NP}$ (kN.m)	$M_{b,Rd,EC3}/M_{Coll,FE}$	$M_{b,Rd,NP}/M_{Coll,FE}$
1.3	1.0	1.7	3	0.876	440.04	355.22	1.165	323.61	1.24	0.91

Table 4-6, shows that the EC3 general method overpredicts the LTB design moment in 1.24 times the FE moment resistance value. Applying Equation (92), to determine the slenderness limit, this value is corrected to 0.91 giving a safe estimation of the LTB design resistance. This case is plotted in Figure 4-12, where the FE result and the new plateau are represented together with the Eurocode design curves for comparison.

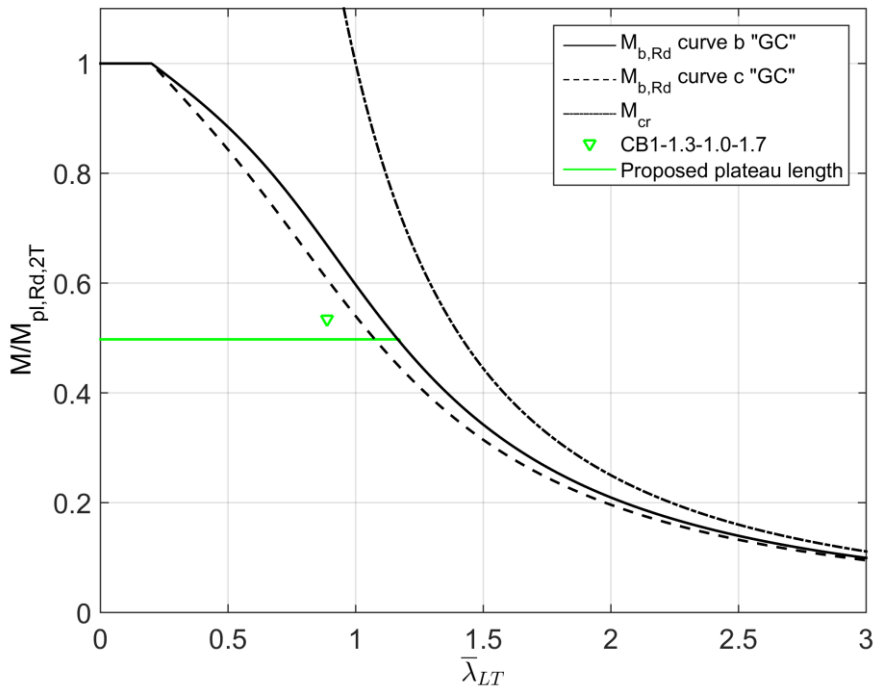


Figure 4-12. Comparison between the proposed and the EC3 methods for a cellular beam with $H/h=1.3$, $a_0/h=1.0$, $S/a_0=1.7$.

4.9. Conclusions

This chapter covers the analytical and numerical analysis of global lateral-torsional buckling (LTB) and interacting failure modes of steel solid and cellular beams.

The final observations are:

- The analytical and the FE results were in excellent agreement, and owing to the small discrepancies, the numerical model was considered validated for computations of LTB elastic critical moment M_{cr} .
- By implementing numerical coupling in the elastic and buckling simulations, the tendency for cross-section local buckling is eliminated. This also enables the accurate prediction of the LTB mode without interference from other buckling modes.
- As S/a_0 increases, the reduction factor χ values approach the LTB curve, and as a_0/h ratio decreases, the LTB resistance increases.
- The cases with a WPB failure mode give, on average, a 59% difference between the numeric and analytic normalized resistances ($M/M_{pl,Rd}$, $M_{pl,Rd,2T}$) for short cellular beams. This variation decreases to 25% for the cases of VM failure modes.

- Independently of the a_0/h ratio, it was noted that for $S/a_0 = 1.1$, 50 % of all cases were on the safe side, for $S/a_0=1.4$, 69% of all cases appeared to be safe, and with $S/a_0 = 1.7$, more than 81% of all cases were safe.
- At both 500 °C and 700 °C, the LTB failure mode was observed for beams with intermediate and long spans, in a similar manner to the analysis conducted at a temperature of $\theta = 20^\circ\text{C}$. The extent of this LTB behaviour, as represented by the range of $\bar{\lambda}_{LT,\theta,com}$, was found to be influenced by the temperature used.
- The suggested approach for determining the LTB curves' plateau length in cellular beams offers a more accurate estimation of the CBs' response to LTB. This approach considers essential geometric factors of the perforated cross-section, namely H/h , a_0/h , and S/a_0 .

GENERAL CONCLUSION

5.1. General conclusion

The work includes a series of parametric studies that look at the effect of Residual stresses, cross-section height, opening size, web-post width, and non-dimensional slenderness on the instability behaviour of cellular beams. Considering a nonlinear analysis with geometric and material imperfections, a uniform bending and a distributed load were analysed at ambient and elevated temperatures. From the analysis results, the predominant failure modes and collapse moment resistance could be obtained for the studied cellular beams. The parametric numerical results have enabled to establish a fit equation to predict the plateau length of the LTB curves for cellular beams.

The following main conclusions can be set:

- We conclude that the introduction of geometrical imperfections that define the almost real shape of the beam has little effect on the variation of critical temperatures (from 0.1 to 1%), but the difference in displacements between the different beams remains significant (from 10% to 30%).
- We also notice that simply changing the geometry of the web opening (from cellular to hexagonal) results in a significant increase in displacement of roughly 45 to 50% for the hexagonal beam compared to the cellular beam, either without or with imperfections.
- Geometric imperfections and residual stresses have been demonstrated to be criteria that should be considered when evaluating the LTB's fire resistance. It is worth mentioning that the presence of imperfections such as residual strains, amplifies LTB.
- The LTB beam resistance at ambient and elevated temperatures is not affected by the spacing between openings when the class of a cross section of cellular beam is the same as the parent section. However, the stresses distribution between openings and the overall beam resistance in relation to its length are impacted by this spacing.
- For spans of less than 8 meters, an increase in the cross-section height results in a noticeable difference in the fire resistance of the beams. Additionally, it is observed that as the diameter increases, the buckling resistance of the beam decreases.
- The case study indicates that residual stresses in the cellular beam have little effect on its lateral torsional buckling resistance.

GENERAL CONCLUSION

- The use of the numerical coupling during the elastic and buckling simulations, cancels the cross-section local buckling, and it allows to capture the LTB mode without being superimposed or combined with other buckling modes.

-For the case of uniform bending the predominant failure modes were LTB and LTB+P-2T. However, for uniform distributed load, the failure modes vary with geometric parameters and generically with the CBs slenderness, noticing failure due to LTB, 2T-section (P-2T), bending of the Top tee section (B-1T), web or web post-buckling (WB or WPB), and Vierendeel mechanism VM.

-The VM mechanism can occur when the perforated steel beam along the span has relatively large openings ($a_0/h = 1.0, 1.2$). A WPB failure mode may occur if the cellular beams have narrow web posts. For all web-post widths analysed with $\lambda_{LT} \leq 0.55$ and $a_0/h = 0.8, 1.0$, the interaction of shear and web buckling V+WB may occur. For $a_0/h = 1.2$, the failure due to bending of top tees section B-1T is verified.

-Over the whole slenderness range of CBs subjected to distributed load, neither of the two LTB design curves, b, and c, provides accurate estimates of the cellular beam design resistance. Additional failure modes must be considered for short beams, which give design resistances smaller than both LTB design curves. For intermediate and high non-dimensional slenderness, the curve b from Eurocode 3 “general case” clause 6.3.2.2, using an equivalent solid beam, gives better predictions.

-At elevated temperatures, similar behaviour is obtained. Nevertheless, due to the loss of stiffness caused by increased temperature, the LTB becomes the dominant failure mechanism even for beams with smaller slenderness.

-On average the difference between numerical and the simplified design results for CB cases involving LTB failure modes or combinations of LTB with other modes, which includes intermediate and high non-dimensional slenderness, approaches 13% at $\theta = 20^\circ\text{C}$, 10% at $\theta = 500^\circ\text{C}$, and approaches 13% at $\theta = 700^\circ\text{C}$.

-The proposed model for the new plateau length of the LTB curves for cellular beams allows a better prediction of the CBs behaviour against LTB. It considers the key geometric parameters of the perforated cross-section: H/h , a_0/h , and S/a_0 . Nonetheless, additional verifications should be developed for other CBs with different height ratios.

In particular, the failure modes of web-post buckling and the Vierendeel collapse mechanism were not deeply addressed in this study, but further work is needed to define the CBs

geometric dimensions and the slenderness threshold that changes the failure mechanisms allowing for a safe design against LTB.

5.2. Suggestions for future research

By examining the topic of the work, we were able to formulate some ideas for potential future research, as outlined below.

- Analyse the behaviour of a cellular beam when subjected to a concentrated load.
- To expand the investigation by simply modifying one geometric parameter, such as analysing the behaviour for various steel grades values or examining the behaviour for different profile sections.
- This study did not thoroughly investigate the failure modes of web-post buckling and the Vierendeel collapse mechanism. Further research is necessary to determine the geometric dimensions of the CBs and the slenderness threshold that can alter the failure mechanisms, thus enabling a secure design against LTB.

BIBLIOGRAPHY

- [1] A.C.S, S.A., ACB® and Angelina® beams - A new generation of beams with large web openings, in: ArcelorMittal (Ed.) 2021, p. 64.
- [2] CEN, NF-EN-1993-1-1, Eurocode 3 «Calcul des structures en acier» et Document d'Application Nationale. Partie 1-1 : Règles générales et règles pour les bâtiments. XP P 22-311/A2:2002., 2002.
- [3] CEN, Draft-EN-1993-1-13, Eurocode 3 part 1.13 steel beams with large web openings, European Committee for Standardization, Brussels, Belgium, 2017.
- [4] CEN, EN-1993-1-2, Eurocode 3: Design of steel structures - Part 1-2: General rules - Structural fire design, European Committee for Standardization, Brussels, Belgium, 2005.
- [5] CEN/TC2503, prEN-1993-1-2, Eurocode 3: Design of steel structures - Part 1-2: General rules - Structural fire design. , European Committee for Standardization, Brussels, Belgium, 2018.
- [6] ANSYS®, ANSYS® Mechanical APDL Product Launcher 2022 R2, 2022.1.0.
- [7] CEN, EN-1993-1-1, Eurocode 3: Design of steel structures - Part 1-1: General rules and rules for buildings, European Committee for Standardization, Brussels, Belgium, 2005.
- [8] R. Lawson, S. Hicks, Design of composite beams with large web openings: in accordance with Eurocodes and the UK National Annexes, Steel Construction Institute 2011.
<https://doi.org/10.13140/RG.2.2.19276.62085>.
- [9] A.M.I. Sweedan, Elastic lateral stability of I-shaped cellular steel beams, Journal of Constructional Steel Research 67(2) (2011) 151-163.
<https://doi.org/10.1016/j.jcsr.2010.08.009>.
- [10] D. Sonck, Global Buckling of Castellated and Cellular Steel Beams and Columns, Ph.D Thesis, Ghent University 2014.
- [11] O. Vassart, Analytical model for cellular beams made of hot rolled sections in case of fire, (2009),
- [12] T. Al-Dafafea, Analyses expérimentale et numérique du comportement de poutres à ouvertures d'âmes raidies, 2018.
- [13] R. THIÉBAUD, Résistance au déversement des poutres métalliques de pont, École polytechnique fédérale de lausanne, 2014.

- [14] J. Valeš, T.-C. Stan, FEM Modelling of Lateral-Torsional Buckling Using Shell and Solid Elements, *Procedia Engineering* 190 (2017) 464-471.
<https://doi.org/10.1016/j.proeng.2017.05.365>.
- [15] K. Rajana, K.D. Tsavdaridis, E. Koltsakis, Elastic and inelastic buckling of steel cellular beams under strong-axis bending, *Thin-Walled Structures* 156 (2020) 106955.
<https://doi.org/10.1016/j.tws.2020.106955>.
- [16] D. Sonck, R. Van Impe, J. Belis, Experimental investigation of residual stresses in steel cellular and castellated members, *Construction and Building Materials* 54 (2014) 512-519.
<https://doi.org/10.1016/j.conbuildmat.2013.12.045>.
- [17] CEN, EN-1993-1-5, Eurocode 3: Design of steel structures - Part 1-5: General rules - Plated structural elements European committee for standardization, Brussels, Belgium, 2006.
- [18] C. Martins, F. Ferreira, A. Rossi, E. Trentini, Numerical Analysis of Physical and Geometrical Imperfections in Cellular Beams, *Open Journal of Civil Engineering* 07 (2017) 116-129. <https://doi.org/10.4236/ojce.2017.71007>
- [19] A. Rossi, D. Hideyuki Saito, C. Humberto Martins, A. Sander Clemente de Souza, The influence of structural imperfections on the LTB strength of I-beams, *Structures* 29 (2021) 1173-1186. <https://doi.org/10.1016/j.istruc.2020.11.020>.
- [20] F. Teixeira, R. Caldas, L. Grilo, Influence of different shapes of geometric imperfections on the structural behavior of beams with large web openings, *ISSN 1816-112X* (2020) 272.
<https://doi.org/10.18057/IJASC.2020.16.3.8>.
- [21] S. Durif, A. Bouchaïr, O. Vassart, Experimental tests and numerical modeling of cellular beams with sinusoidal openings, *Journal of Constructional Steel Research* 82 (2013) 72-87.
<https://doi.org/10.1016/j.jcsr.2012.12.010>.
- [22] P.M.M. Vila Real, N. Lopes, L. Simões da Silva, J.M. Franssen, Parametric analysis of the lateral-torsional buckling resistance of steel beams in case of fire, *Fire Safety Journal* 42(6) (2007) 416-424. <https://doi.org/10.1016/j.firesaf.2006.11.010>.
- [23] E. Ellobody, Nonlinear analysis of cellular steel beams under combined buckling modes, *Thin-Walled Structures* 52 (2012) 66-79. <https://doi.org/10.1016/j.tws.2011.12.009>.
- [24] D. Sonck, J. Belis, Lateral-torsional buckling resistance of cellular beams, *Journal of Constructional Steel Research* 105 (2015) 119-128. <https://doi.org/10.1016/j.jcsr.2014.11.003>.
- [25] F.P.V. Ferreira, A. Rossi, C.H. Martins, Lateral-torsional buckling of cellular beams according to the possible updating of EC3, *Journal of Constructional Steel Research* 153 (2019) 222-242. <https://doi.org/10.1016/j.jcsr.2018.10.011>.

- [26] P.M.M. Vila Real, R. Cazeli, L. Simões da Silva, A. Santiago, P. Piloto, The effect of residual stresses in the lateral-torsional buckling of steel I-beams at elevated temperature, *Journal of Constructional Steel Research* 60(3-5) (2004) 783-793.
[https://doi.org/10.1016/S0143-974X\(03\)00143-3](https://doi.org/10.1016/S0143-974X(03)00143-3).
- [27] N. Boissonnade, H. Somja, Influence of imperfections in FEM modeling of lateral torsional buckling, *Proceedings of the Annual Stability Conference, Structural Stability Research Council Grapevine, Texas, 2012*, pp. 1-15.
- [28] A.C.S, S.A., ACB® and Angelina® beams - A new generation of castellated beams, in: ArcelorMittal (Ed.) Luxembourg, 2015, p. 64.
- [29] E. Ellobody, Chapter 5 - Finite Element Analysis of Steel and Steel-Concrete Composite Bridges, in: E. Ellobody (Ed.), *Finite Element Analysis and Design of Steel and Steel-Concrete Composite Bridges*, Butterworth-Heinemann, Oxford, 2014, pp. 469-554.
- [30] E. Ellobody, R. Feng, B. Young, Chapter 4 - Linear and Nonlinear Finite Element Analyses, in: E. Ellobody, R. Feng, B. Young (Eds.), *Finite Element Analysis and Design of Metal Structures*, Butterworth-Heinemann, Boston, 2014, pp. 56-71.
- [31] L. Tall, Residual stresses in welded plates - a theoretical study, *The Spring Meeting of the AWS, Dallas, 1961*,
- [32] N. NagarajaRao, F. Estuar, L. Tall, Residual stresses in welded shapes. *The Welding Journal*, Vo.. 43, July 1964, p. 295-s, Publication No. 241 (64-4), (1964),
- [33] G.A. Alpsten, Thermal residual stresses in hot-rolled steel members, Lehigh university, 1968, <http://preserve.lehigh.edu/engr-civil-environmental-fritz-lab-reports/329>.
- [34] Y. Kishima, G. Alpsten, L. Tall, Residual stresses in welded shapes of flame-cut plates in astm a572(50) stee, Lehigh University, 1969, <http://preserve.lehigh.edu/engr-civil-environmental-fritz-lab-reports/1907>.
- [35] ECCS, *Manual on stability of steel structures*, European Convention for Constructional Steelwork, [Brussels, Belgium], 1976.
- [36] B.W. Young, Residual stresses in hot rolled members, *IABSE Reports of the Working Commissions* 23 (1975) 25-38. <http://doi.org/10.5169/seals-19798>.
- [37] R.C. Spoorenberg, H.H. Snijder, J.C.D. Hoenderkamp, Proposed residual stress model for roller bent steel wide flange sections, *Journal of Constructional Steel Research - J CONSTR STEEL RES* 67 (2011) 992-1000. 10.1016/j.jcsr.2011.01.009.
- [38] G.A. Alpsten, Prediction of residual stresses in medium-size to heavy welded steel shapes, *IABSE congress report* 9 (1972) <https://dx.doi.org/10.5169/seals-9639>.

- [39] ECCS, Ultimate Limit State Calculation of Sway Frames with Rigid Joints, European Convention for Constructional Steelwork 1984.
<https://books.google.dz/books?id=BJoazgEACAAJ>
- [40] N. Rossini, M. Dassisti, K. Benyounis, A.-G. Olabi, Methods of measuring residual stresses in components, *Materials & Design* 35 (2012) 572-588.
<https://doi.org/10.1016/j.matdes.2011.08.022>.
- [41] J. Nseir, M. Lo, D. Sonck, H. Somja, O. Vassart, N. Boissonnade, Lateral torsional buckling of cellular steel beams, *Proceedings of the Annual Stability Conference Structural Stability Research Council*, 2012, pp. 18-21.
- [42] D. Sonck, N. Boissonnade, V. R, *Instabilities of Cellular Members Loaded in Bending or Compression*, 2012,
- [43] S. Kwani, P. Karta Wijaya, Lateral Torsional Buckling of Castellated Beams Analyzed using the Collapse Analysis, *Procedia Engineering* 171 (2017) 813-820.
10.1016/j.proeng.2017.01.370.
- [44] J. Silva, P. Dalcantal, L. Mesquita, Numerical Analysis of Cellular Steel Beams Failure Modes in Fire Conditions, in: P.A.G. Piloto, J.P. Rodrigues, V.P. Silva (Eds.) *Advances in Fire Safety Engineering. CILASCI 2019. Lecture Notes in Civil Engineering*, Springer, Cham, 2020, pp. 78-92. https://doi.org/10.1007/978-3-030-36240-9_6.
- [45] D. Kerdal, D.A. Nethercot, Failure modes for castellated beams, *Journal of Constructional Steel Research* 4(4) (1984) 295-315. [https://doi.org/10.1016/0143-974X\(84\)90004-X](https://doi.org/10.1016/0143-974X(84)90004-X).
- [46] K.F. Chung, T.C.H. Liu, A.C.H. Ko, Investigation on Vierendeel mechanism in steel beams with circular web openings, *Journal of Constructional Steel Research* 57(5) (2001) 467-490. [https://doi.org/10.1016/S0143-974X\(00\)00035-3](https://doi.org/10.1016/S0143-974X(00)00035-3).
- [47] D. Bitar, P.-O. Martin, Y. Galéa, T. Demarco, Poutres cellulaires acier et mixtes: Partie 1, proposition d'un modèle pour la résistance des montants, *Construction Métallique*, n°1-2006, 2006, pp. 15-39.
- [48] F. Erdal, M.P. Saka, Ultimate load carrying capacity of optimally designed steel cellular beams, *Journal of Constructional Steel Research* 80 (2013) 355-368.
<https://doi.org/10.1016/j.tws.2020.106955>.
- [49] K.D. Tsavdaridis, C. D'Mello, Vierendeel Bending Study of Perforated Steel Beams with Various Novel Web Opening Shapes through Nonlinear Finite-Element Analyses, *Journal of Structural Engineering* 138(10) (2012) 1214-1230. 10.1061/(ASCE)ST.1943-541X.0000562.

- [50] S.A. Elsayaf, M.M. Hassan, Behaviour of structural sub-assemblies of steel beams with openings in fire conditions, *Journal of Constructional Steel Research* 148 (2018) 627-638. <https://doi.org/10.1016/j.jcsr.2018.06.023>.
- [51] S. Demirdjian, *Stability of castellated beam webs*, McGill University Montreal, Canada, 1999.
- [52] J. Warren, *Ultimate load and deflection behaviour of cellular beams*, 2001,
- [53] A. Mustesin, M. Khan, *Analysis of perforated beams in fire using a virtual hybrid simulation approach*, Doctor of Philosophy, Brunel University London, 2019.
- [54] T. Liu, K.F. Chung, *Steel beams with large web openings of various shapes and sizes: finite element investigation*, *Journal of Constructional Steel Research* 59(9) (2003) 1159-1176.
- [55] J.G. Verweij, *Cellular beam-columns in portal frame structures*, Master, Delft University of Technology 2010.
- [56] D.E.-D. Kerdal, *Lateral-torsional buckling strength of castellated beams*, University of Sheffield, 1982.
- [57] F.P.V. Ferreira, R. Shamass, V. Limbachiya, K.D. Tsavdaridis, C.H. Martins, *Lateral-torsional buckling resistance prediction model for steel cellular beams generated by Artificial Neural Networks (ANN)*, *Thin-Walled Structures* 170 (2022) 108592. <https://doi.org/10.1016/j.tws.2021.108592>.
- [58] P. Panedpojaman, W. Sae-Long, T. Chub-uppakarn, *Cellular beam design for resistance to inelastic lateral-torsional buckling*, *Thin-Walled Structures* 99 (2016) 182-194. <https://doi.org/10.1016/j.tws.2015.08.026>.
- [59] R.M. Lawson, J. Lim, S.J. Hicks, W.I. Simms, *Design of composite asymmetric cellular beams and beams with large web openings*, *Journal of Constructional Steel Research* 62(6) (2006) 614-629. <https://doi.org/10.1016/j.jcsr.2005.09.012>.
- [60] Sameer S. Fares, John Coulson, David W. Dinehart, *Steel Design Guide 31: Castellated and Cellular Beam Design*, American Institute of Steel Construction 2016. <https://books.google.pt/books?id=V0SAzQEACAAJ>
- [61] S. Durif, A. Bouchair, O. Vassart, *Validation of an analytical model for curved and tapered cellular beams at normal and fire conditions*, *Periodica Polytechnica Civil Engineering* 57 (2013) 83. <https://doi.org/10.3311/PPci.2144>.
- [62] P. Panedpojaman, T. Thepchatri, S. Limkatanyu, *Novel simplified equations for Vierendeel design of beams with (elongated) circular openings*, *Journal of Constructional Steel Research* 112 (2015) 10-21. <https://doi.org/10.1016/j.jcsr.2015.04.007>.

- [63] S. Durif, Comportement mécanique des poutres cellulaires à ouvertures sinusoïdales: développement d'un modèle analytique adapté, Université Blaise Pascal-Clermont-Ferrand II, 2012.
- [64] L.F. Grilo, R.H. Fakury, A.L.R.d. Castro e Silva, G.d.S. Veríssimo, Design procedure for the web-post buckling of steel cellular beams, *Journal of Constructional Steel Research* 148 (2018) 525-541. <https://doi.org/10.1016/j.jcsr.2018.06.020>.
- [65] M.U. HOSAIN, W.G. SPEIRS, Experiments on Castellated Steel Beams, *Welding research supplement* (1973) 329-342.
- [66] E. Oñate, *Structural Analysis with the Finite Element Method. Linear Statics. Vol. 1: Basis and Solids*, Technical University of Catalonia (UPC), Barcelona, Spain, 2009. <https://doi.org/10.1007/978-1-4020-8733-2>.
- [67] D.V. Hutton, *Fundamentals of finite element analysis*, McGraw-Hill, New York, 2004.
- [68] M.K. Thompson, J.M. Thompson, *ANSYS Mechanical APDL for Finite Element Analysis* Butterworth-Heinemann 2017.
- [69] ANSYS®, *Theory Reference Version 18.2.0.*, 2017, https://www.mm.bme.hu/~gyebro/files/ans_help_v182/ans_thry/ans_thry.html.
- [70] C. Bailey, Indicative fire tests to investigate the behaviour of cellular beams protected with intumescent coatings, *Fire Safety Journal* 39(8) (2004) 689-709. <https://doi.org/10.1016/j.firesaf.2004.06.007>.
- [71] D. Rini, *Critical Behavior of Long Span Cellular Beams in Fire*, 2006,
- [72] A. Nadjai, O. Vassart, F. Ali, D. Talamona, A. Allam, M. Hawes, Performance of cellular composite floor beams at elevated temperatures, *Fire Safety Journal* 42(6-7) (2007) 489-497.
- [73] O. Vassart, A. Bouchair, J.P. Muzeau, A. Nadjai, Analytical model for the web post buckling in cellular beams under fire, 2008, pp. 3-11. <https://www.researchgate.net/publication/273122182>.
- [74] E.-H. Naili, A. Nadjai, S. Han, F. Ali, S. Choi, Experimental and numerical modelling of cellular beams with circular and elongated web openings at elevated temperatures, *Journal of Structural Fire Engineering* (2011),
- [75] L. Mesquita, J. Gonçalves, G. Gonçalves, P. Piloto, K. Abdelhak, Intumescent fire protection of cellular beams, X Congresso de Construção Metálica e Mista, Coimbra, Portugal, 2015, pp. 623-630. <http://hdl.handle.net/10198/12482>.
- [76] K. Abdelhak, *Comportement des Poutres Ajourées sous des Conditions de Hautes Températures dues à l'Incendie*, Docteur en sciences, Université de Hassiba Benbouali de Chlef, 2016.

- [77] B. Lamri, L. Mesquita, K. Abdelhak, P. Piloto, Behavior of cellular beams protected with intumescent coatings, *Fire Research* 1(1) (2017) 27-32. <https://doi.org/10.4081/fire.2017.27>.
- [78] E. Ellobody, B. Young, Behaviour of composite frames with castellated steel beams at elevated temperatures, *Advances in Structural Engineering* 19(7) (2016) 1060-1076. 10.1177/1369433216631620.
- [79] P. Wang, X. Wang, M. Liu, L. Zhang, Web-post buckling of fully and partially protected cellular steel beams at elevated temperatures in a fire, *Thin-Walled Structures* 98 (2016) 29-38. <https://doi.org/10.1016/j.tws.2015.02.028>.
- [80] A. Nadjai, K. Petrou, S. Han, F. Ali, Performance of unprotected and protected cellular beams in fire conditions, *Construction and Building Materials* 105 (2016) 579-588. <https://doi.org/10.1016/j.conbuildmat.2015.12.150>.
- [81] O. Vassart, M. Hawes, I. Simms, B. Zhao, J.-M. Franssen, A. Nadjai, Fire resistance of long span cellular beam made of rolled profiles (FICEB), Bruxelles, Belgique, 2012, <https://doi.org/10.2777/38158>.
- [82] S. Benyettou Oribi, A. Kada, B. Lamri, L.M.R. Mesquita, Numerical analysis of lateral torsional buckling of steel I-beams with and without web-openings under fire, 5th Iberian-Latin-American Congress on Fire Safety _ 5 CILASCI, Porto, Portugal, 2019, p. 10.
- [83] S. Benyettou Oribi, A. Kada, B. Lamri, L.M. Mesquita, Investigation of residual stresses on the fire resistance of unrestrained cellular beams, *ce/papers* 4(2-4) (2021) 1386-1394. <https://doi.org/10.1002/cepa.1436>.
- [84] C. Correa de Faria, H. Carvalho, R. Hallal Fakury, L. Figueiredo Grilo, Lateral-torsional buckling resistance of cellular steel beams at room temperature and fire situation, *Engineering Structures* 237 (2021) 112046. <https://doi.org/10.1016/j.engstruct.2021.112046>.
- [85] A. Kada, B. Lamri, L. Mesquita, A. Bouchair, Finite Element Analysis of Steel Beams with Web Apertures under Fire Condition, *Asian Journal of Civil Engineering* 17 (2016) 1035-1054.
- [86] N. Boissonnade, J. Nseir, M. Lo, H. Somja, Design of cellular beams against lateral torsional buckling, *Proceedings of the Institution of Civil Engineers - Structures and Buildings* 167(7) (2014) 436-444. <https://doi.org/10.1680/stbu.12.00049>.
- [87] L.G. Justino, J.C.L. Ribeiro, G. de Souza Veríssimo, J.L.R. Paes, L.G. Pedroti, Shear buckling strength of web-posts in castellated steel beams in fire, *Engineering Structures* 209 (2020) 109960. <https://doi.org/10.1016/j.engstruct.2019.109960>.

- [88] V.K. Kotapati, A. Khatri, Failure Criteria of Cellular Steel Beams Under Ambient and Elevated Temperature, *International Journal of Steel Structures* 22 (2022) 10.1007/s13296-022-00664-5.
- [89] V.K. Kotapati, A.P. Khatri, Performance of cellular steel beam under fire, *Asian Journal of Civil Engineering* 23(8) (2022) 1267-1276. <https://doi.org/10.1007/s42107-022-00482-4>.
- [90] V.K. Kotapati, A.P. Khatri, A new proposal for the design of laterally unrestrained cellular steel beams under moment gradient at elevated temperatures, *Fire Safety Journal* 140 (2023) 103812. <https://doi.org/10.1016/j.firesaf.2023.103812>.
- [91] L. Thomas, G. Archambault, Sécurité incendie, Office technique pour l'utilisation de l'acier OTUA, Paris, 2005.
- [92] I.J.-F. Denoël, Sécurité incendie et constructions en béton, Choix du béton, réglementations, résistance au feu, risque incendie, « Fire Safety Engineering » et restauration du béton après incendie FEBELCEM Fédération de l'industrie cimentière belge Bruxelles 2007. www.febelcem.be
- [93] C. Ménage, M. Royer-Muller, B. Aldebert, N. Richard, Sécurité incendie, in: C. Acier (Ed.) Construire Acier, France, 2010, www.construiracier.fr
- [94] M. Morys, D. Häßler, S. Krüger, B. Schartel, S. Hothan, Beyond the standard time-temperature curve: Assessment of intumescent coatings under standard and deviant temperature curves, *Fire Safety Journal* 112 (2020) 102951. <https://doi.org/10.1016/j.firesaf.2020.102951>.
- [95] CEN, EN-1991-1-2, Eurocode 1: Actions on structures - Part 1-2: General actions - Actions on structures exposed to fire European Committee for Standardization, Brussels, Belgium, 2002.
- [96] Promat, How hot is a fire? A quick guide to standard time-temperature curves, 2020. <https://www.promat.com/en/tunnels/your-project/expert-area>.
- [97] Promat, International fire curves – useful tool for designing fire safety, 2020. <https://www.promat.com/en/construction/news/33637/international-fire-curves-fire-safety/>.
- [98] J. Outinen, P. Mäkeläinen, Mechanical properties of structural steel at elevated temperatures and after cooling down, *Fire and Materials* 28 (2004) 237-251. <https://doi.org/10.1002/fam.849>.
- [99] A. Santiago, L. Silva, P. Vila Real, J.-M. Franssen, Effect of Cooling on the Behaviour of a Steel Beam under Fire Loading including the End Joint Response, in: B.H.V. Topping (Ed.) The Ninth International Conference on Civil and Structural Engineering, Egmond-an-See, The Netherlands, 2003, <https://doi.org/10.104203/ccp.77.65>

- [100] D. Winful, K. Cashell, S. Afshan, A.M. Barnes, R.J. Pargeter, Behaviour of high strength steel columns under fire conditions, *Journal of Constructional Steel Research* 150 (2018) 392-404. [10.1016/j.jcsr.2018.06.008](https://doi.org/10.1016/j.jcsr.2018.06.008).
- [101] W.I. Simms, Fire resistance design of steel framed buildings In accordance with Eurocodes and the UK National annexes, Steel Construction Institute, UK, 2012.
- [102] S. Durif, Validation du modele analytique de calcul de poutres cellulaires courbes ou a inertie variable sous situation normale et d'incendie Diplôme d'ingénieur, Université Blaise Pascal Polytech' Clermont-Ferrand, 2009.
- [103] N. Boissonnade, R. Greiner, J.-P. Jaspart, J. Lindner, Rules for member stability in EN 1993-1-1; Background documentation and design guidelines, European Convention for Constructional Steelwork 2006. <http://www.steelconstruct.com/site/#>.
- [104] R. Shamass, F.P.V. Ferreira, V. Limbachiya, L.F.P. Santos, K.D. Tsavdaridis, Web-post buckling prediction resistance of steel beams with elliptically-based web openings using Artificial Neural Networks (ANN), *Thin-Walled Structures* 180 (2022) 109959. <https://doi.org/10.1016/j.tws.2022.109959>.
- [105] J. Seputro, Effect of support conditions on steel beams exposed of fire, University of Canterbury Christchurch, New Zealand 2001.
- [106] S. Benyettou Oribi, A. Kada, B. Lamri, Investigation sur le comportement des poutres d'acier sous l'effet des températures élevées, 2^{ème} Conférence Internationale de Construction Métallique et Mixte_CICOMM'2018, Alger, Algérie, 2018,
- [107] S. Benyettou Oribi, A. Kada, B. Lamri, L. Mesquita, Influence of initial imperfections on the lateral torsional buckling of cellular beams under fire, 3^{ème} Conférence Internationale de Construction Métallique et Mixte CICOMM'2021, Oran, Algeria, 2023,
- [108] S.M. Rédha, Modélisation numérique du comportement des poutres métalliques avec des ouvertures dans l'âme Docteur en sciences en Génie Civil Université mantouri de constantine, 2012.
- [109] P.J. Moss, A.H. Buchanan, J. Seputro, C. Wastney, R. Welsh, Effect of support conditions on the fire behaviour of steel and composite beams, *Fire and Materials* 28(2-4) (2004) 159-175. [10.1002/fam.855](https://doi.org/10.1002/fam.855).
- [110] D.L. Kennedy, M.A. Hafez, A study of end plate connections for steel beams, *Canadian Journal of Civil Engineering* 11(2) (1984) 139-149. <https://doi.org/10.1139/184-026>.
- [111] ACB+, Logiciel de conception des poutres cellulaires ACB®, 4.02.

BIBLIOGRAPHY

- [112] L.M.R. Mesquita, P.A.G. Piloto, M.A.P. Vaz, P.M.M. Vila Real, Experimental and numerical research on the critical temperature of laterally unrestrained steel I beams, *Journal of Constructional Steel Research* 61(10) (2005) 1435-1446.
<https://doi.org/10.1016/j.jcsr.2005.04.003>.
- [113] S.B. Oribi, A. Kada, B. Lamri, L.M. Mesquita, Investigation of residual stresses on the fire resistance of unrestrained cellular beams, *ce/papers* 4(2-4) (2021) 1386-1394.
<https://doi.org/10.1002/cepa.1436>.
- [114] P. Panedpojaman, T. Thepchatri, S. Limkatanyu, Novel design equations for shear strength of local web-post buckling in cellular beams, *Thin-Walled Structures* 76 (2014) 92-104. <https://doi.org/10.1016/j.tws.2013.11.007>.
- [115] G.N. Smith, *Probability and statistics in civil engineering - An introduction*, Collins professional and technical books, London, 1986.

ANNEXES

ANNEX A. Elastic critical moment of cellular beams_DL

ANNEX B. Von mises stress distribution of steel beams - end moment load

ANNEX C. Von mises stress distribution of solid beams - distributed load

ANNEX A. Elastic critical moment of cellular beams_DL

H/h	a ₀ /h	S/a ₀	L (m)	θ = 20 (°C)					θ = 500 (°C)					θ = 700 (°C)				
				M _{cr,EC3} (kN.m)	M _{cr,FE} (kN.m)	M _{cr} (FE vs. EC3)	λ _{LT,EC3}	λ _{LT,FE}	M _{cr,0,EC3} (kN.m)	M _{cr,0,FE} (kN.I)	M _{cr,0} (FE vs. EC3)	λ _{LT,0,EC3}	λ _{LT,0,FE}	M _{cr,0,EC3} (kN.I)	M _{cr,0,FE} (kN.I)	M _{cr,0} (FE vs. EC3)	λ _{LT,0,EC3}	λ _{LT,0,FE}
1.30	0.80	1.10	3.00	851.02	790.16	-7.70%	0.91	0.96	510.61	474.10	-7.70%	1.04	1.09	110.63	102.72	-7.70%	1.22	1.28
1.30	0.80	1.10	4.00	505.46	519.05	2.62%	1.19	1.18	303.28	311.43	2.62%	1.35	1.35	65.71	67.48	2.62%	1.58	1.58
1.30	0.80	1.10	5.00	344.74	356.57	3.32%	1.44	1.42	206.84	213.94	3.32%	1.64	1.63	44.82	46.35	3.32%	1.91	1.90
1.30	0.80	1.10	6.00	256.70	265.70	3.39%	1.66	1.65	154.02	159.42	3.39%	1.90	1.88	33.37	34.54	3.39%	2.21	2.21
1.30	0.80	1.10	8.00	167.45	172.98	3.19%	2.06	2.04	100.47	103.79	3.19%	2.35	2.33	21.77	22.49	3.19%	2.74	2.73
1.30	0.80	1.10	10.00	124.35	129.28	3.82%	2.39	2.36	74.61	77.57	3.82%	2.73	2.70	16.17	16.81	3.82%	3.18	3.16
1.30	0.80	1.10	12.00	99.52	103.08	3.45%	2.67	2.65	59.71	61.85	3.45%	3.05	3.02	12.94	13.40	3.45%	3.56	3.54
1.30	0.80	1.10	14.00	83.46	85.14	1.98%	2.92	2.91	50.08	51.09	1.98%	3.33	3.33	10.85	11.07	1.98%	3.88	3.90
1.30	0.80	1.40	3.00	851.02	864.81	1.59%	0.91	0.91	510.61	518.89	1.59%	1.04	1.04	110.63	112.43	1.59%	1.22	1.22
1.30	0.80	1.40	4.00	505.46	519.46	2.69%	1.19	1.18	303.28	311.67	2.69%	1.35	1.35	65.71	67.53	2.69%	1.58	1.58
1.30	0.80	1.40	5.00	344.74	356.02	3.17%	1.44	1.42	206.84	213.61	3.17%	1.64	1.63	44.82	46.28	3.17%	1.91	1.91
1.30	0.80	1.40	6.00	256.70	266.10	3.53%	1.66	1.65	154.02	159.66	3.53%	1.90	1.88	33.37	34.59	3.53%	2.21	2.21
1.30	0.80	1.40	8.00	167.45	173.83	3.67%	2.06	2.04	100.47	104.30	3.67%	2.35	2.33	21.77	22.60	3.67%	2.74	2.73
1.30	0.80	1.40	10.00	124.35	129.72	4.15%	2.39	2.36	74.61	77.83	4.15%	2.73	2.69	16.17	16.86	4.15%	3.18	3.16
1.30	0.80	1.40	12.00	99.52	104.16	4.46%	2.67	2.63	59.71	62.50	4.46%	3.05	3.01	12.94	13.54	4.46%	3.56	3.52
1.30	0.80	1.40	14.00	83.46	87.31	4.41%	2.92	2.88	50.08	52.38	4.41%	3.33	3.28	10.85	11.35	4.41%	3.88	3.85
1.30	0.80	1.70	3.00	851.02	782.46	-8.76%	0.91	0.96	510.61	469.48	-8.76%	1.04	1.10	110.63	101.72	-8.76%	1.22	1.29
1.30	0.80	1.70	4.00	505.46	514.17	1.69%	1.19	1.19	303.28	308.50	1.69%	1.35	1.35	65.71	66.84	1.69%	1.58	1.59
1.30	0.80	1.70	5.00	344.74	354.66	2.80%	1.44	1.43	206.84	212.80	2.80%	1.64	1.63	44.82	46.11	2.80%	1.91	1.91
1.30	0.80	1.70	6.00	256.70	266.29	3.60%	1.66	1.65	154.02	159.77	3.60%	1.90	1.88	33.37	34.62	3.60%	2.21	2.20

ANNEX A. Elastic critical moment of cellular beams_DL

1.30	0.80	1.70	8.00	167.45	174.40	3.98%	2.06	2.04	100.47	104.64	3.98%	2.35	2.32	21.77	22.67	3.98%	2.74	2.72
1.30	0.80	1.70	10.00	124.35	130.12	4.43%	2.39	2.36	74.61	77.06	3.18%	2.73	2.71	16.17	16.70	3.18%	3.18	3.17
1.30	0.80	1.70	12.00	99.52	104.43	4.70%	2.67	2.63	59.71	62.00	3.69%	3.05	3.02	12.94	13.58	4.70%	3.56	3.52
1.30	0.80	1.70	14.00	83.46	87.72	4.86%	2.92	2.87	50.08	52.33	4.32%	3.33	3.29	10.85	11.40	4.86%	3.88	3.84
1.30	1.00	1.10	3.00	847.37	859.14	1.37%	0.88	0.88	508.42	515.48	1.37%	1.00	1.00	110.16	111.69	1.37%	1.17	1.17
1.30	1.00	1.10	4.00	502.00	514.89	2.50%	1.14	1.14	301.20	308.93	2.50%	1.30	1.29	65.26	66.94	2.50%	1.51	1.51
1.30	1.00	1.10	5.00	341.44	351.11	2.76%	1.38	1.38	204.86	210.67	2.76%	1.57	1.56	44.39	45.64	2.76%	1.84	1.82
1.30	1.00	1.10	6.00	253.56	261.15	2.91%	1.60	1.59	152.13	156.69	2.91%	1.83	1.81	32.96	33.95	2.91%	2.13	2.12
1.30	1.00	1.10	8.00	199.95	170.70	3.56%	1.99	1.97	98.77	102.42	3.56%	2.27	2.24	21.40	22.19	3.56%	2.64	2.62
1.30	1.00	1.10	10.00	164.61	126.38	3.64%	2.31	2.29	73.07	75.83	3.64%	2.64	2.61	15.83	16.43	3.64%	3.07	3.04
1.30	1.00	1.10	12.00	121.78	101.20	3.94%	2.59	2.56	58.32	60.72	3.94%	2.95	2.91	12.64	13.16	3.94%	3.44	3.40
1.30	1.00	1.10	14.00	97.20	84.65	3.89%	2.83	2.80	48.82	50.79	3.89%	3.22	3.18	10.58	11.01	3.89%	3.76	3.72
1.30	1.00	1.40	3.00	847.37	786.77	-7.70%	0.88	0.92	508.42	472.06	-7.70%	1.00	1.05	110.16	102.28	-7.70%	1.17	1.22
1.30	1.00	1.40	4.00	502.00	517.26	2.95%	1.14	1.13	301.20	310.36	2.95%	1.30	1.29	65.26	67.24	2.95%	1.51	1.51
1.30	1.00	1.40	5.00	341.44	353.99	3.54%	1.38	1.37	204.86	212.39	3.54%	1.57	1.56	44.39	46.02	3.54%	1.84	1.82
1.30	1.00	1.40	6.00	253.56	264.69	4.21%	1.60	1.58	152.13	158.81	4.21%	1.83	1.80	32.96	34.41	4.21%	2.13	2.11
1.30	1.00	1.40	8.00	164.61	173.16	4.94%	1.99	1.96	98.77	103.90	4.94%	2.27	2.23	21.40	22.51	4.94%	2.64	2.60
1.30	1.00	1.40	10.00	121.78	128.22	5.02%	2.31	2.28	73.07	76.93	5.02%	2.64	2.59	15.83	16.67	5.02%	3.07	3.03
1.30	1.00	1.40	12.00	97.20	103.38	5.97%	2.59	2.53	58.32	62.03	5.97%	2.95	2.88	12.64	13.44	5.97%	3.44	3.37
1.30	1.00	1.40	14.00	81.36	86.32	5.75%	2.83	2.77	48.82	51.79	5.75%	3.22	3.16	10.58	11.22	5.75%	3.76	3.69
1.30	1.00	1.70	3.00	847.37	843.50	-0.46%	0.88	0.89	508.42	506.10	-0.46%	1.00	1.01	110.16	109.65	-0.46%	1.17	1.18
1.30	1.00	1.70	4.00	502.00	498.31	-0.74%	1.14	1.15	301.20	298.99	-0.74%	1.30	1.31	65.26	64.78	-0.74%	1.51	1.54
1.30	1.00	1.70	5.00	341.44	353.10	3.30%	1.38	1.37	204.86	211.86	3.30%	1.57	1.56	44.39	45.90	3.30%	1.84	1.82
1.30	1.00	1.70	6.00	253.56	265.15	4.37%	1.60	1.58	152.13	159.09	4.37%	1.83	1.80	32.96	34.47	4.37%	2.13	2.10
1.30	1.00	1.70	8.00	164.61	173.26	4.99%	1.99	1.96	98.77	103.95	4.99%	2.27	2.23	21.40	22.52	4.99%	2.64	2.60
1.30	1.00	1.70	10.00	121.78	129.42	5.90%	2.31	2.27	73.07	77.65	5.90%	2.64	2.57	15.83	16.83	5.90%	3.07	3.01
1.30	1.00	1.70	12.00	97.20	103.47	6.05%	2.59	2.53	58.32	62.08	6.05%	2.95	2.88	12.64	13.45	6.05%	3.44	3.37
1.30	1.00	1.70	14.00	81.36	86.80	6.27%	2.83	2.77	48.82	52.08	6.27%	3.22	3.14	10.58	11.28	6.27%	3.76	3.68
1.30	1.20	1.10	3.00	843.66	764.68	-	0.83	0.88	506.19	458.81	-	0.94	0.91	109.68	99.41	-	1.10	1.05

ANNEX A. Elastic critical moment of cellular beams_DL

						10.33%					10.33%					10.33%		
1.30	1.20	1.10	4.00	498.49	508.46	1.96%	1.08	1.07	299.10	305.08	1.96%	1.23	1.12	64.80	66.10	1.96%	1.43	1.29
1.30	1.20	1.10	5.00	338.10	352.11	3.98%	1.31	1.29	202.86	211.27	3.98%	1.49	1.35	43.95	45.77	3.98%	1.74	1.55
1.30	1.20	1.10	6.00	250.38	260.89	4.03%	1.52	1.50	150.23	156.53	4.03%	1.73	1.56	32.55	33.92	4.03%	2.02	1.80
1.30	1.20	1.10	8.00	161.73	171.01	5.42%	1.89	1.85	97.04	102.60	5.42%	2.15	1.93	21.03	22.23	5.42%	2.51	2.23
1.30	1.20	1.10	10.00	119.18	125.93	5.36%	2.20	2.16	71.51	75.56	5.36%	2.51	2.25	15.49	16.37	5.36%	2.92	2.60
1.30	1.20	1.10	12.00	94.85	99.61	4.78%	2.46	2.43	56.91	59.77	4.78%	2.81	2.53	12.33	12.95	4.78%	3.28	2.92
1.30	1.20	1.10	14.00	79.22	84.31	6.04%	2.70	2.64	47.53	50.59	6.04%	3.07	2.75	10.30	10.96	6.04%	3.59	3.17
1.30	1.20	1.40	3.00	843.66	847.54	0.46%	0.83	0.83	506.19	508.52	0.46%	0.94	0.87	109.68	110.18	0.46%	1.10	1.00
1.30	1.20	1.40	4.00	498.49	503.02	0.90%	1.08	1.08	299.10	301.81	0.90%	1.23	1.12	64.80	65.39	0.90%	1.43	1.30
1.30	1.20	1.40	5.00	338.10	353.58	4.38%	1.31	1.28	202.86	212.15	4.38%	1.49	1.34	43.95	45.97	4.38%	1.74	1.55
1.30	1.20	1.40	6.00	250.38	262.89	4.76%	1.52	1.49	150.23	157.73	4.76%	1.73	1.55	32.55	34.18	4.76%	2.02	1.79
1.30	1.20	1.40	8.00	161.73	172.08	6.01%	1.71	1.84	97.04	103.25	6.01%	2.15	1.92	21.03	22.37	6.01%	2.51	2.22
1.30	1.20	1.40	10.00	119.18	128.64	7.36%	1.89	2.13	71.51	77.19	7.36%	2.51	2.22	15.49	16.72	7.36%	2.92	2.56
1.30	1.20	1.40	12.00	94.85	101.46	6.52%	2.20	2.40	56.91	60.88	6.52%	2.81	2.50	12.33	13.19	6.52%	3.28	2.89
1.30	1.20	1.40	14.00	79.22	85.33	7.16%	2.46	2.61	47.53	51.20	7.16%	3.07	2.73	10.30	11.09	7.16%	3.59	3.15
1.30	1.20	1.70	3.00	843.66	715.02	- 17.99%	0.83	0.91	506.19	429.02	- 17.99%	0.94	0.94	109.68	92.95	- 17.99%	1.10	1.09
1.30	1.20	1.70	4.00	498.49	513.08	2.84%	1.08	1.07	299.10	307.85	2.84%	1.23	1.11	64.80	66.70	2.84%	1.43	1.28
1.30	1.20	1.70	5.00	338.10	354.05	4.51%	1.31	1.29	202.86	212.43	4.51%	1.49	1.34	43.95	46.03	4.51%	1.74	1.54
1.30	1.20	1.70	6.00	250.38	265.89	5.83%	1.52	1.48	150.23	159.53	5.83%	1.73	1.55	32.55	34.57	5.83%	2.02	1.78
1.30	1.20	1.70	8.00	161.73	174.22	7.17%	1.89	1.83	97.04	104.53	7.17%	2.15	1.91	21.03	22.65	7.17%	2.51	2.20
1.30	1.20	1.70	10.00	119.18	129.61	8.05%	2.20	2.13	71.51	77.77	8.05%	2.51	2.21	15.49	16.85	8.05%	2.92	2.55
1.30	1.20	1.70	12.00	94.85	103.81	8.63%	2.46	2.38	56.91	62.28	8.63%	2.81	2.47	12.33	13.49	8.63%	3.28	2.85
1.30	1.20	1.70	14.00	79.22	87.06	9.00%	2.70	2.59	47.53	52.23	9.00%	3.07	2.70	10.30	11.32	9.00%	3.59	3.11
1.40	0.80	1.10	3.00	911.04	822.24	- 10.80%	0.94	0.99	546.62	493.34	- 10.80%	1.07	1.13	118.43	106.89	- 10.80%	1.25	1.33
1.40	0.80	1.10	4.00	538.13	552.81	2.66%	1.22	1.21	322.88	331.69	2.66%	1.39	1.38	69.96	71.87	2.66%	1.62	1.62
1.40	0.80	1.10	5.00	364.86	377.19	3.27%	1.48	1.47	218.92	226.31	3.27%	1.69	1.67	47.43	49.03	3.27%	1.97	1.96
1.40	0.80	1.10	6.00	270.10	279.23	3.27%	1.72	1.70	162.06	167.54	3.27%	1.96	1.94	35.11	36.30	3.27%	2.29	2.28

ANNEX A. Elastic critical moment of cellular beams_DL

1.40	0.80	1.10	8.00	174.36	179.96	3.11%	2.14	2.12	104.62	107.98	3.11%	2.44	2.42	22.67	23.39	3.11%	2.85	2.84
1.40	0.80	1.10	10.00	128.42	133.38	3.72%	2.49	2.47	77.05	80.03	3.72%	2.84	2.81	16.69	17.34	3.72%	3.32	3.30
1.40	0.80	1.10	12.00	102.16	105.76	3.41%	2.80	2.77	61.29	63.46	3.41%	3.19	3.16	13.28	13.75	3.41%	3.72	3.70
1.40	0.80	1.10	14.00	85.30	88.71	3.84%	3.06	3.02	51.18	53.22	3.84%	3.49	3.45	11.09	11.53	3.84%	4.07	4.04
1.40	0.80	1.40	3.00	911.04	926.44	1.66%	0.94	0.94	546.62	555.86	1.66%	1.07	1.07	118.43	120.44	1.66%	1.25	1.25
1.40	0.80	1.40	4.00	538.13	553.06	2.70%	1.22	1.21	322.88	331.84	2.70%	1.39	1.38	69.96	71.90	2.70%	1.62	1.62
1.40	0.80	1.40	5.00	364.86	376.51	3.09%	1.48	1.47	218.92	225.90	3.09%	1.69	1.67	47.43	48.95	3.09%	1.97	1.96
1.40	0.80	1.40	6.00	270.10	279.63	3.41%	1.72	1.70	162.06	167.78	3.41%	1.96	1.94	35.11	36.35	3.41%	2.29	2.28
1.40	0.80	1.40	8.00	174.36	180.70	3.51%	2.14	2.12	104.62	108.42	3.51%	2.44	2.42	22.67	23.49	3.51%	2.85	2.83
1.40	0.80	1.40	10.00	128.42	133.76	3.99%	2.49	2.46	77.05	80.25	3.99%	2.84	2.81	16.69	17.39	3.99%	3.32	3.29
1.40	0.80	1.40	12.00	102.16	106.77	4.32%	2.80	2.76	61.29	64.06	4.32%	3.19	3.14	13.28	13.88	4.32%	3.72	3.69
1.40	0.80	1.40	14.00	85.30	89.13	4.29%	3.06	3.02	51.18	53.48	4.29%	3.49	3.44	11.09	11.59	4.29%	4.07	4.03
1.40	0.80	1.70	3.00	911.04	811.57	- 12.26%	0.94	1.00	546.62	486.95	- 12.26%	1.07	1.14	118.43	105.50	- 12.26%	1.25	1.34
1.40	0.80	1.70	4.00	538.13	546.54	1.54%	1.22	1.22	322.88	327.92	1.54%	1.39	1.39	69.96	71.05	1.54%	1.62	1.63
1.40	0.80	1.70	5.00	364.86	375.01	2.71%	1.48	1.47	218.92	225.01	2.71%	1.69	1.68	47.43	48.75	2.71%	1.97	1.97
1.40	0.80	1.70	6.00	270.10	279.87	3.49%	1.72	1.70	162.06	167.92	3.49%	1.96	1.94	35.11	36.38	3.49%	2.29	2.28
1.40	0.80	1.70	8.00	174.36	181.23	3.79%	2.14	2.11	104.62	108.74	3.79%	2.44	2.41	22.67	23.56	3.79%	2.85	2.83
1.40	0.80	1.70	10.00	128.42	132.09	2.78%	2.49	2.48	77.05	81.18	5.09%	2.84	2.79	16.69	17.17	2.78%	3.32	3.31
1.40	0.80	1.70	12.00	102.16	107.11	4.62%	2.80	2.75	61.29	64.26	4.62%	3.19	3.14	13.28	13.92	4.62%	3.72	3.68
1.40	0.80	1.70	14.00	85.30	89.58	4.77%	3.06	3.01	51.18	53.75	4.77%	3.49	3.43	11.09	11.65	4.77%	4.07	4.02
1.40	1.00	1.10	3.00	907.62	921.16	1.47%	0.90	0.90	544.57	552.69	1.47%	1.03	1.03	117.99	119.75	1.47%	1.20	1.21
1.40	1.00	1.10	4.00	534.89	548.59	2.50%	1.17	1.17	320.93	329.16	2.50%	1.34	1.34	69.54	71.32	2.50%	1.56	1.57
1.40	1.00	1.10	5.00	361.76	371.78	2.70%	1.43	1.42	217.06	223.07	2.70%	1.63	1.62	47.03	48.33	2.70%	1.90	1.91
1.40	1.00	1.10	6.00	267.14	274.90	2.82%	1.66	1.65	160.28	164.94	2.82%	1.90	1.89	34.73	35.74	2.82%	2.21	2.22
1.40	1.00	1.10	8.00	171.66	177.87	3.49%	2.07	2.06	103.00	106.72	3.49%	2.36	2.35	22.32	23.12	3.49%	2.76	2.75
1.40	1.00	1.10	10.00	125.97	130.67	3.60%	2.42	2.40	75.58	78.40	3.60%	2.76	2.74	16.38	16.99	3.60%	3.22	3.21
1.40	1.00	1.10	12.00	99.93	104.04	3.95%	2.72	2.69	59.96	62.42	3.95%	3.10	3.07	12.99	13.53	3.95%	3.62	3.60
1.40	1.00	1.10	14.00	83.28	86.68	3.93%	2.98	2.95	49.97	52.01	3.93%	3.39	3.37	10.83	11.27	3.93%	3.96	3.95

ANNEX A. Elastic critical moment of cellular beams_DL

1.40	1.00	1.40	3.00	907.62	815.82	-11.25%	0.90	0.96	544.57	489.49	-11.25%	1.03	1.10	117.99	106.06	-11.25%	1.20	1.29
1.40	1.00	1.40	4.00	534.89	549.79	2.71%	1.17	1.17	320.93	329.87	2.71%	1.34	1.34	69.54	71.47	2.71%	1.56	1.57
1.40	1.00	1.40	5.00	361.76	374.22	3.33%	1.43	1.42	217.06	224.53	3.33%	1.63	1.62	47.03	48.65	3.33%	1.90	1.90
1.40	1.00	1.40	6.00	267.14	277.69	3.80%	1.66	1.64	160.28	166.61	3.80%	1.90	1.88	34.73	36.10	3.80%	2.21	2.20
1.40	1.00	1.40	8.00	171.66	179.95	4.60%	2.07	2.04	103.00	107.97	4.60%	2.36	2.34	22.32	23.39	4.60%	2.76	2.74
1.40	1.00	1.40	10.00	125.97	132.20	4.71%	2.42	2.38	75.58	79.32	4.72%	2.76	2.73	16.38	17.19	4.72%	3.22	3.19
1.40	1.00	1.40	12.00	99.93	105.93	5.66%	2.72	2.66	59.96	63.56	5.66%	3.10	3.04	12.99	13.77	5.66%	3.62	3.57
1.40	1.00	1.40	14.00	83.28	88.10	5.48%	2.98	2.92	49.97	52.86	5.48%	3.39	3.34	10.83	11.45	5.48%	3.96	3.91
1.40	1.00	1.70	3.00	907.62	881.08	-3.01%	0.90	0.92	544.57	528.65	-3.01%	1.03	1.06	117.99	114.70	-2.87%	1.20	1.24
1.40	1.00	1.70	4.00	534.89	525.46	-1.79%	1.17	1.20	320.93	315.28	-1.79%	1.34	1.37	69.54	68.31	-1.79%	1.56	1.60
1.40	1.00	1.70	5.00	361.76	372.81	2.96%	1.43	1.42	217.06	223.69	2.96%	1.63	1.62	47.03	48.47	2.96%	1.90	1.90
1.40	1.00	1.70	6.00	267.14	278.47	4.07%	1.66	1.64	160.28	167.08	4.07%	1.90	1.88	34.73	36.20	4.07%	2.21	2.20
1.40	1.00	1.70	8.00	171.66	179.97	4.62%	2.07	2.04	103.00	107.98	4.62%	2.36	2.34	22.32	23.40	4.62%	2.76	2.74
1.40	1.00	1.70	10.00	125.97	133.31	5.51%	2.42	2.38	75.58	79.99	5.51%	2.76	2.71	16.38	17.33	5.51%	3.22	3.18
1.40	1.00	1.70	12.00	99.93	106.00	5.72%	2.72	2.66	59.96	63.60	5.72%	3.10	3.04	12.99	13.78	5.72%	3.62	3.57
1.40	1.00	1.70	14.00	83.28	88.55	5.95%	2.98	2.91	49.97	53.13	5.95%	3.39	3.33	10.83	11.51	5.95%	3.96	3.90
1.40	1.20	1.10	3.00	904.15	784.44	-15.26%	0.86	0.93	542.49	470.66	-15.26%	0.98	1.02	117.54	101.98	-15.26%	1.14	1.19
1.40	1.20	1.10	4.00	531.61	539.40	1.44%	1.12	1.12	318.97	323.64	1.44%	1.27	1.24	69.11	70.12	1.44%	1.49	1.44
1.40	1.20	1.10	5.00	358.63	372.41	3.70%	1.36	1.35	215.18	223.45	3.70%	1.55	1.49	46.62	48.41	3.70%	1.81	1.73
1.40	1.20	1.10	6.00	264.14	274.48	3.77%	1.59	1.57	158.49	164.69	3.77%	1.81	1.73	34.34	35.68	3.77%	2.11	2.02
1.40	1.20	1.10	8.00	168.93	177.88	5.03%	1.98	1.95	101.36	106.73	5.03%	2.26	2.15	21.96	23.12	5.03%	2.64	2.50
1.40	1.20	1.10	10.00	123.48	130.03	5.03%	2.32	2.28	74.09	78.02	5.03%	2.64	2.52	16.05	16.90	5.03%	3.08	2.93
1.40	1.20	1.10	12.00	97.67	102.29	4.52%	2.61	2.58	58.60	61.37	4.52%	2.97	2.84	12.70	13.30	4.52%	3.47	3.30
1.40	1.20	1.10	14.00	81.21	86.16	5.75%	2.86	2.81	48.73	51.70	5.75%	3.26	3.09	10.56	11.20	5.75%	3.80	3.60
1.40	1.20	1.40	3.00	904.15	904.41	0.03%	0.86	0.87	542.49	542.76	0.05%	0.98	0.95	117.54	117.57	0.03%	1.14	1.11
1.40	1.20	1.40	4.00	531.61	530.36	-0.24%	1.12	1.13	318.97	318.22	-0.24%	1.27	1.24	69.11	68.95	-0.24%	1.49	1.45
1.40	1.20	1.40	5.00	358.63	373.58	4.00%	1.36	1.35	215.18	224.15	4.00%	1.55	1.48	46.62	48.56	4.00%	1.81	1.72
1.40	1.20	1.40	6.00	264.14	276.49	4.47%	1.59	1.57	158.49	165.90	4.47%	1.81	1.72	34.34	35.94	4.47%	2.11	2.00

ANNEX A. Elastic critical moment of cellular beams_DL

1.40	1.20	1.40	8.00	168.93	179.03	5.64%	1.98	1.95	101.36	107.42	5.64%	2.26	2.14	21.96	23.27	5.64%	2.64	2.49
1.40	1.20	1.40	10.00	123.48	132.73	6.97%	2.32	2.26	74.09	79.64	6.97%	2.64	2.48	16.05	17.26	6.97%	3.08	2.89
1.40	1.20	1.40	12.00	97.67	104.19	6.26%	2.61	2.55	58.60	62.52	6.26%	2.97	2.80	12.70	13.54	6.26%	3.47	3.26
1.40	1.20	1.40	14.00	81.21	87.24	6.91%	2.86	2.79	48.73	52.35	6.91%	3.26	3.06	10.56	11.34	6.91%	3.80	3.57
1.40	1.20	1.70	3.00	904.15	722.47	25.15%	0.86	0.97	542.49	433.48	25.15%	0.98	1.06	117.54	93.92	25.15%	1.14	1.24
1.40	1.20	1.70	4.00	531.61	543.84	2.25%	1.12	1.12	318.97	326.30	2.25%	1.27	1.23	69.11	70.70	2.25%	1.49	1.43
1.40	1.20	1.70	5.00	358.63	374.18	4.15%	1.36	1.35	215.18	224.51	4.15%	1.55	1.48	46.62	48.64	4.15%	1.81	1.72
1.40	1.20	1.70	6.00	264.14	279.13	5.37%	1.59	1.56	158.49	167.48	5.37%	1.81	1.71	34.34	36.29	5.37%	2.11	1.99
1.40	1.20	1.70	8.00	168.93	180.97	6.65%	1.98	1.94	101.36	108.58	6.65%	2.26	2.13	21.96	23.53	6.65%	2.64	2.47
1.40	1.20	1.70	10.00	123.48	133.54	7.53%	2.32	2.25	74.09	80.12	7.53%	2.64	2.47	16.05	17.36	7.53%	3.08	2.88
1.40	1.20	1.70	12.00	97.67	106.32	8.13%	2.61	2.53	58.60	63.79	8.13%	2.97	2.77	12.70	13.82	8.13%	3.47	3.23
1.40	1.20	1.70	14.00	81.21	88.79	8.54%	2.86	2.76	48.73	53.27	8.54%	3.26	3.03	10.56	11.54	8.54%	3.80	3.53
1.50	0.80	1.10	3.00	971.42	849.37	14.37%	0.96	1.03	582.85	509.62	14.37%	1.09	1.18	126.29	110.42	14.37%	1.27	1.38
1.50	0.80	1.10	4.00	571.15	587.16	2.73%	1.25	1.24	342.69	352.30	2.73%	1.42	1.41	74.25	76.33	2.73%	1.66	1.66
1.50	0.80	1.10	5.00	385.29	398.25	3.25%	1.52	1.51	231.17	238.95	3.25%	1.73	1.72	50.09	51.77	3.25%	2.02	2.01
1.50	0.80	1.10	6.00	283.77	293.10	3.19%	1.77	1.75	170.26	175.86	3.19%	2.02	2.00	36.89	38.10	3.19%	2.36	2.35
1.50	0.80	1.10	8.00	181.47	187.15	3.04%	2.21	2.20	108.88	112.29	3.04%	2.53	2.51	23.59	24.33	3.04%	2.95	2.94
1.50	0.80	1.10	10.00	132.64	137.62	3.62%	2.59	2.56	79.58	82.57	3.62%	2.95	2.92	17.24	17.89	3.62%	3.45	3.42
1.50	0.80	1.10	12.00	104.90	108.53	3.34%	2.91	2.88	62.94	65.13	3.36%	3.32	3.29	13.64	14.11	3.36%	3.87	3.86
1.50	0.80	1.10	14.00	87.22	90.66	3.79%	3.19	3.16	52.33	54.39	3.79%	3.64	3.60	11.34	11.79	3.79%	4.25	4.22
1.50	0.80	1.40	3.00	971.42	989.63	1.84%	0.96	0.95	582.85	593.78	1.84%	1.09	1.09	126.29	128.65	1.84%	1.27	1.28
1.50	0.80	1.40	4.00	571.15	587.53	2.79%	1.25	1.24	342.69	352.52	2.79%	1.42	1.41	74.25	76.38	2.79%	1.66	1.66
1.50	0.80	1.40	5.00	385.29	397.58	3.09%	1.52	1.51	231.17	238.55	3.09%	1.73	1.72	50.09	51.69	3.09%	2.02	2.01
1.50	0.80	1.40	6.00	283.77	293.63	3.36%	1.77	1.75	170.26	176.18	3.36%	2.02	2.00	36.89	38.17	3.36%	2.36	2.34
1.50	0.80	1.40	8.00	181.47	187.90	3.42%	2.21	2.19	108.88	112.74	3.42%	2.53	2.50	23.59	24.43	3.42%	2.95	2.93
1.50	0.80	1.40	10.00	132.64	134.43	1.33%	2.59	2.59	79.58	80.66	1.33%	2.95	2.96	17.24	17.48	1.33%	3.45	3.47
1.50	0.80	1.40	12.00	104.90	109.59	4.28%	2.91	2.87	62.94	65.75	4.28%	3.32	3.27	13.64	14.25	4.28%	3.87	3.84
1.50	0.80	1.40	14.00	87.22	91.12	4.27%	3.19	3.15	52.33	54.67	4.27%	3.64	3.59	11.34	11.85	4.27%	4.25	4.21

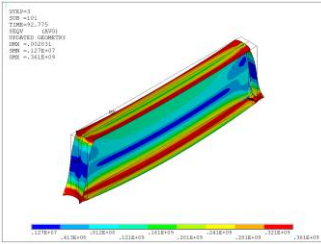
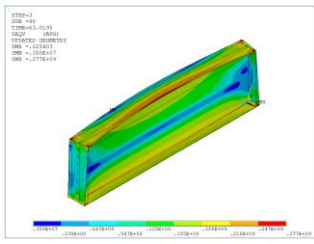
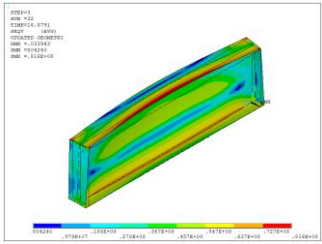
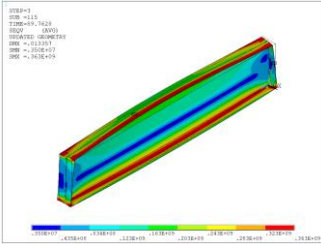
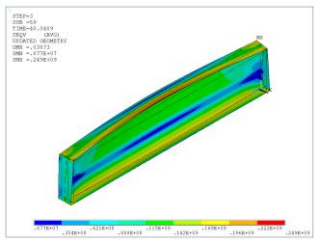
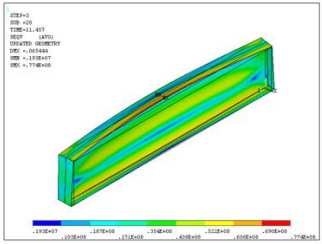
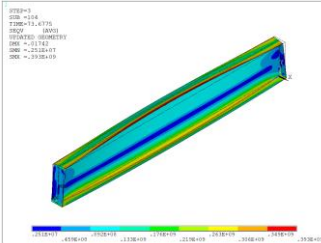
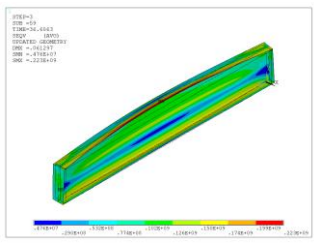
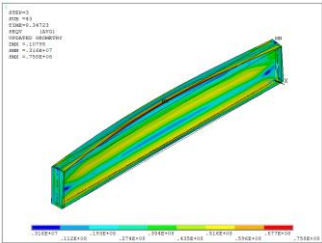
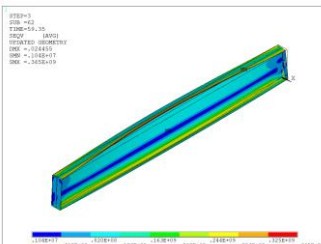
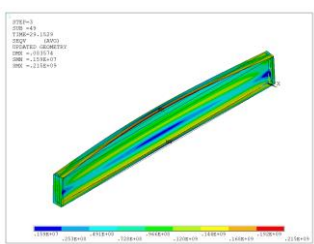
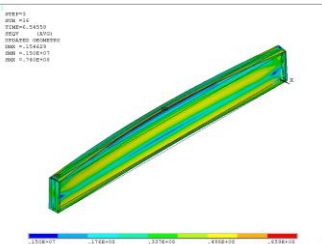
ANNEX A. Elastic critical moment of cellular beams_DL

1.50	0.80	1.70	3.00	971.42	832.99	- 16.62%	0.96	1.01	582.85	499.79	- 16.62%	1.09	1.19	126.29	108.29	- 16.62%	1.27	1.39
1.50	0.80	1.70	4.00	571.15	579.53	1.45%	1.25	1.21	342.69	347.72	1.45%	1.42	1.42	74.25	75.34	1.45%	1.66	1.67
1.50	0.80	1.70	5.00	385.29	395.84	2.67%	1.52	1.46	231.17	237.51	2.67%	1.73	1.72	50.09	51.46	2.67%	2.02	2.02
1.50	0.80	1.70	6.00	283.77	293.81	3.42%	1.77	1.70	170.26	176.29	3.42%	2.02	2.00	36.89	38.20	3.42%	2.36	2.34
1.50	0.80	1.70	8.00	181.47	188.29	3.62%	2.21	2.12	108.88	112.97	3.62%	2.53	2.50	23.59	24.48	3.62%	2.95	2.93
1.50	0.80	1.70	10.00	132.64	135.89	2.39%	2.59	2.49	79.58	81.53	2.39%	2.95	2.94	17.24	17.67	2.39%	3.45	3.45
1.50	0.80	1.70	12.00	104.90	109.90	4.55%	2.91	2.77	62.94	65.94	4.55%	3.32	3.27	13.64	14.29	4.55%	3.87	3.83
1.50	0.80	1.70	14.00	87.22	91.52	4.69%	3.19	3.04	52.33	54.91	4.69%	3.64	3.58	11.34	11.90	4.69%	4.25	4.20
1.50	1.00	1.10	3.00	968.21	983.68	1.57%	0.93	0.93	580.93	590.21	1.57%	1.06	1.06	125.87	127.88	1.57%	1.23	1.24
1.50	1.00	1.10	4.00	568.09	582.66	2.50%	1.21	1.20	340.86	349.60	2.50%	1.38	1.37	73.85	75.75	2.50%	1.61	1.61
1.50	1.00	1.10	5.00	382.37	392.67	2.62%	1.47	1.47	229.42	235.60	2.62%	1.68	1.67	49.71	51.05	2.62%	1.96	1.96
1.50	1.00	1.10	6.00	280.96	288.77	2.70%	1.72	1.71	168.58	173.26	2.70%	1.96	1.95	36.53	37.54	2.70%	2.29	2.29
1.50	1.00	1.10	8.00	178.90	185.06	3.33%	2.15	2.13	107.34	111.04	3.33%	2.45	2.44	23.26	24.06	3.33%	2.86	2.86
1.50	1.00	1.10	10.00	130.29	134.93	3.44%	2.52	2.50	78.17	80.96	3.44%	2.88	2.86	16.94	17.54	3.44%	3.36	3.35
1.50	1.00	1.10	12.00	102.76	106.82	3.80%	2.84	2.81	61.66	64.09	3.80%	3.24	3.21	13.36	13.89	3.80%	3.78	3.76
1.50	1.00	1.10	14.00	85.26	88.64	3.81%	3.12	3.08	51.16	53.18	3.81%	3.56	3.52	11.08	11.52	3.81%	4.15	4.13
1.50	1.00	1.40	3.00	968.21	837.38	- 15.62%	0.93	1.00	580.93	502.43	- 15.62%	1.06	1.15	125.87	108.86	- 15.62%	1.23	1.34
1.50	1.00	1.40	4.00	568.09	583.20	2.59%	1.21	1.20	340.86	349.92	2.59%	1.38	1.37	73.85	75.82	2.59%	1.61	1.61
1.50	1.00	1.40	5.00	382.37	395.14	3.23%	1.47	1.45	229.42	237.08	3.23%	1.68	1.67	49.71	51.37	3.23%	1.96	1.96
1.50	1.00	1.40	6.00	280.96	291.08	3.48%	1.72	1.69	168.58	174.65	3.48%	1.96	1.94	36.53	37.84	3.48%	2.29	2.28
1.50	1.00	1.40	8.00	178.90	187.07	4.37%	2.15	2.11	107.34	112.24	4.37%	2.45	2.42	23.26	24.32	4.37%	2.86	2.84
1.50	1.00	1.40	10.00	130.29	136.46	4.52%	2.52	2.47	78.17	81.88	4.52%	2.88	2.84	16.94	17.74	4.52%	3.36	3.33
1.50	1.00	1.40	12.00	102.76	108.68	5.44%	2.84	2.77	61.66	65.21	5.44%	3.24	3.18	13.36	14.13	5.45%	3.78	3.73
1.50	1.00	1.40	14.00	85.26	90.06	5.32%	3.12	3.05	51.16	54.03	5.32%	3.56	3.49	11.08	11.71	5.32%	4.15	4.10
1.50	1.00	1.70	3.00	968.21	967.65	-0.06%	0.93	0.93	580.93	580.59	-0.06%	1.06	1.07	125.87	125.79	-0.06%	1.23	1.25
1.50	1.00	1.70	4.00	568.09	551.92	-2.93%	1.21	1.24	340.86	331.15	-2.93%	1.38	1.41	73.85	71.75	-2.93%	1.61	1.65
1.50	1.00	1.70	5.00	382.37	392.93	2.69%	1.47	1.46	229.42	235.76	2.69%	1.68	1.67	49.71	51.08	2.69%	1.96	1.96
1.50	1.00	1.70	6.00	280.96	292.15	3.83%	1.72	1.70	168.58	175.29	3.83%	1.96	1.94	36.53	37.98	3.83%	2.29	2.27

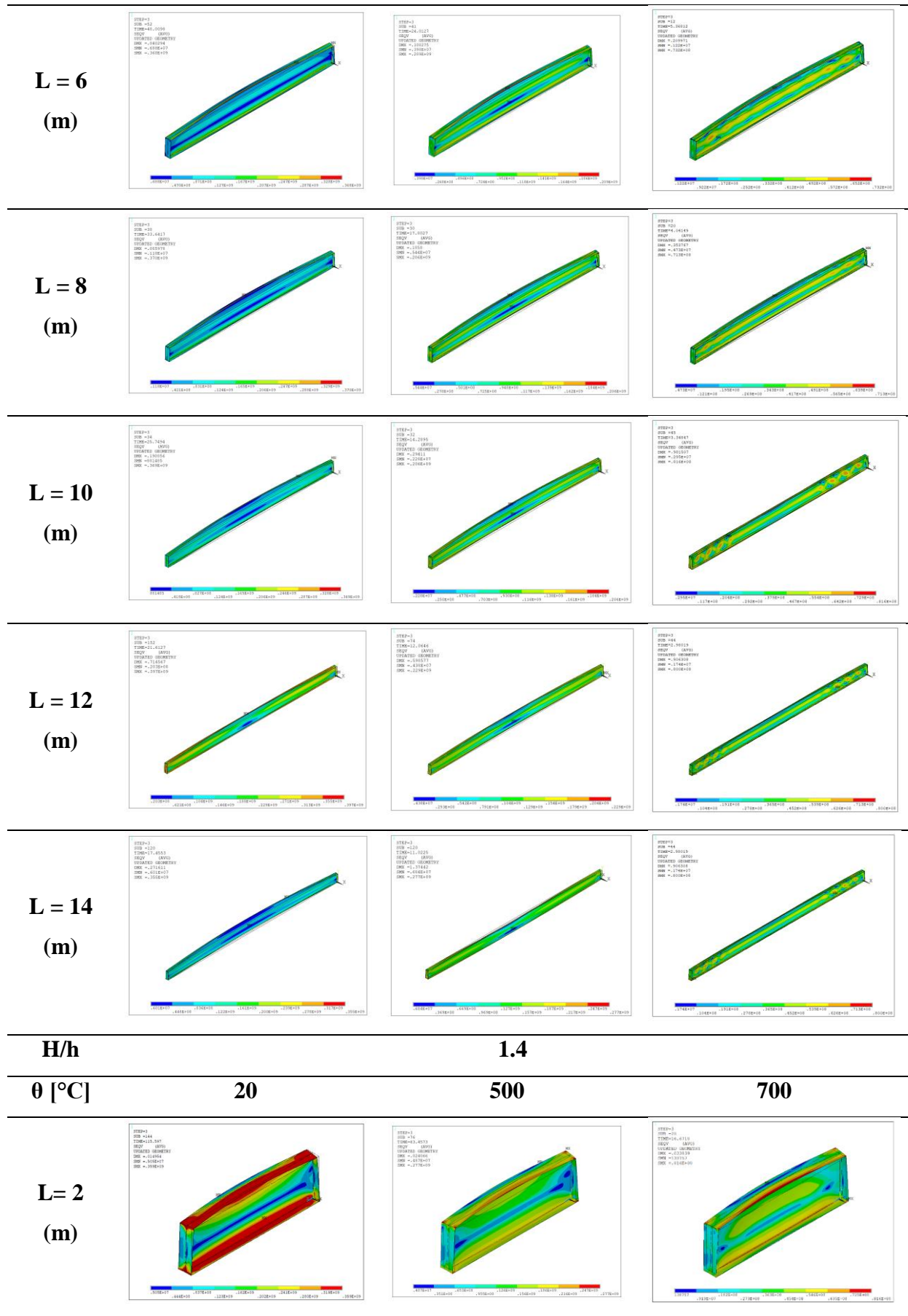
ANNEX A. Elastic critical moment of cellular beams_DL

1.50	1.00	1.70	8.00	178.90	186.92	4.29%	2.15	2.12	107.34	112.15	4.29%	2.45	2.42	23.26	24.30	4.29%	2.86	2.84
1.50	1.00	1.70	10.00	130.29	137.37	5.15%	2.52	2.48	78.17	82.42	5.15%	2.88	2.83	16.94	17.86	5.15%	3.36	3.32
1.50	1.00	1.70	12.00	102.76	107.40	4.31%	2.84	2.80	61.66	64.44	4.31%	3.24	3.20	13.36	13.96	4.31%	3.78	3.75
1.50	1.00	1.70	14.00	85.26	90.37	5.65%	3.12	3.05	51.16	54.22	5.65%	3.56	3.49	11.08	11.75	5.65%	4.15	4.09
1.50	1.20	1.10	3.00	964.95	795.30	-21.33%	0.88	0.99	578.97	477.18	-21.33%	1.01	1.11	125.44	103.39	-21.33%	1.18	1.30
1.50	1.20	1.10	4.00	565.01	570.58	0.98%	1.16	1.16	339.01	342.35	0.98%	1.32	1.32	73.45	74.18	0.98%	1.54	1.54
1.50	1.20	1.10	5.00	379.41	393.28	3.53%	1.41	1.40	227.65	235.97	3.53%	1.61	1.58	49.32	51.13	3.53%	1.88	1.85
1.50	1.20	1.10	6.00	278.13	288.62	3.63%	1.65	1.64	166.88	173.17	3.63%	1.88	1.85	36.16	37.52	3.63%	2.19	2.16
1.50	1.20	1.10	8.00	176.30	185.13	4.77%	2.07	2.04	105.78	111.08	4.77%	2.36	2.31	22.92	24.07	4.77%	2.75	2.70
1.50	1.20	1.10	10.00	127.91	134.48	4.88%	2.43	2.40	76.75	80.69	4.88%	2.77	2.71	16.63	17.48	4.88%	3.23	3.17
1.50	1.20	1.10	12.00	100.59	105.29	4.46%	2.74	2.71	60.35	63.17	4.46%	3.12	3.06	13.08	13.69	4.46%	3.64	3.58
1.50	1.20	1.10	14.00	83.27	88.27	5.66%	3.01	2.96	49.96	52.96	5.66%	3.43	3.34	10.83	11.48	5.66%	4.01	3.91
1.50	1.20	1.40	3.00	964.95	961.04	-0.41%	0.88	0.90	578.97	576.62	-0.41%	1.01	1.01	125.44	124.93	-0.41%	1.18	1.18
1.50	1.20	1.40	4.00	565.01	556.55	-1.52%	1.16	1.18	339.01	333.93	-1.52%	1.32	1.33	73.45	72.35	-1.52%	1.54	1.55
1.50	1.20	1.40	5.00	379.41	393.68	3.62%	1.41	1.40	227.65	236.21	3.62%	1.61	1.58	49.32	51.18	3.62%	1.88	1.85
1.50	1.20	1.40	6.00	278.13	290.21	4.16%	1.65	1.63	166.88	174.13	4.16%	1.88	1.84	36.16	37.73	4.16%	2.19	2.15
1.50	1.20	1.40	8.00	176.30	186.07	5.25%	2.07	2.04	105.78	111.65	5.25%	2.36	2.30	22.92	24.19	5.25%	2.75	2.69
1.50	1.20	1.40	10.00	127.91	136.87	6.55%	2.43	2.37	76.75	82.12	6.55%	2.77	2.68	16.63	17.79	6.55%	3.23	3.14
1.50	1.20	1.40	12.00	100.59	106.91	5.91%	2.74	2.69	60.35	64.15	5.91%	3.12	3.03	13.08	13.90	5.91%	3.64	3.55
1.50	1.20	1.40	14.00	83.27	89.13	6.57%	3.01	2.94	49.96	53.48	6.57%	3.43	3.32	10.83	11.59	6.57%	4.01	3.89
1.50	1.20	1.70	3.00	964.95	719.57	-34.10%	0.88	1.04	578.97	431.74	-34.10%	1.01	1.17	125.44	93.54	-34.10%	1.18	1.36
1.50	1.20	1.70	4.00	565.01	574.41	1.64%	1.16	1.16	339.01	344.65	1.64%	1.32	1.31	73.45	74.67	1.64%	1.54	1.53
1.50	1.20	1.70	5.00	379.41	394.54	3.83%	1.41	1.40	227.65	236.72	3.83%	1.61	1.58	49.32	51.29	3.83%	1.88	1.84
1.50	1.20	1.70	6.00	278.13	292.65	4.96%	1.65	1.62	166.88	175.59	4.96%	1.88	1.83	36.16	38.04	4.96%	2.19	2.14
1.50	1.20	1.70	8.00	176.30	187.94	6.20%	2.07	2.03	105.78	112.77	6.20%	2.36	2.29	22.92	24.43	6.20%	2.75	2.67
1.50	1.20	1.70	10.00	127.91	137.63	7.06%	2.43	2.37	76.75	82.58	7.06%	2.77	2.67	16.63	17.89	7.06%	3.23	3.12
1.50	1.20	1.70	12.00	100.59	108.96	7.68%	2.74	2.66	60.35	65.37	7.68%	3.12	3.00	13.08	14.16	7.68%	3.64	3.51
1.50	1.20	1.70	14.00	83.27	90.62	8.11%	3.01	2.92	49.96	54.37	8.11%	3.43	3.29	10.83	11.78	8.11%	4.01	3.85

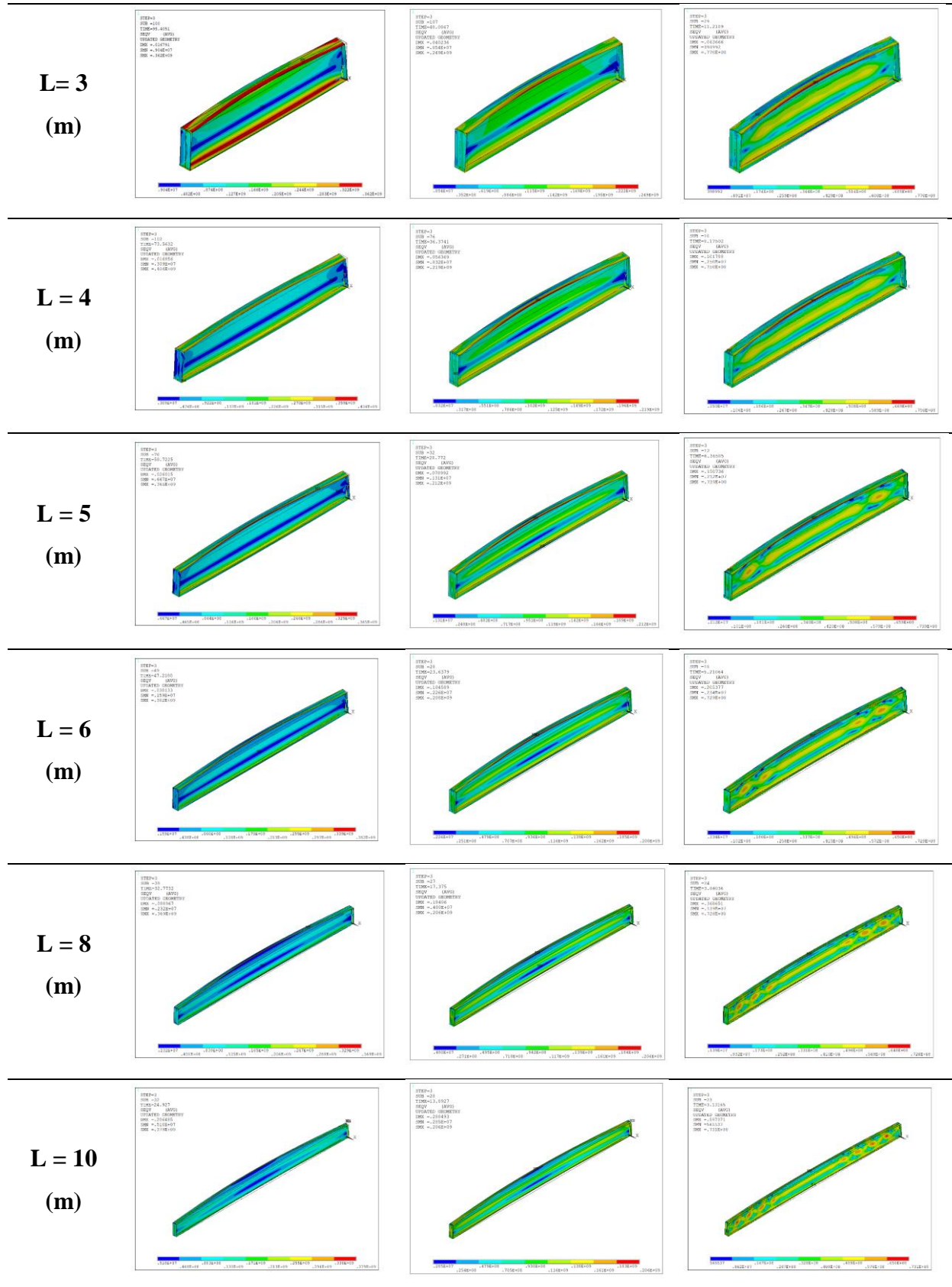
ANNEX B. Von mises stress distribution of steel beams - end moment load

Beam type	SOLID BEAMS		
Loading type	END MOMENT		
H/h	1.3		
θ [°C]	20	500	700
L = 2 (m)			
L = 3 (m)			
L = 4 (m)			
L = 5 (m)			

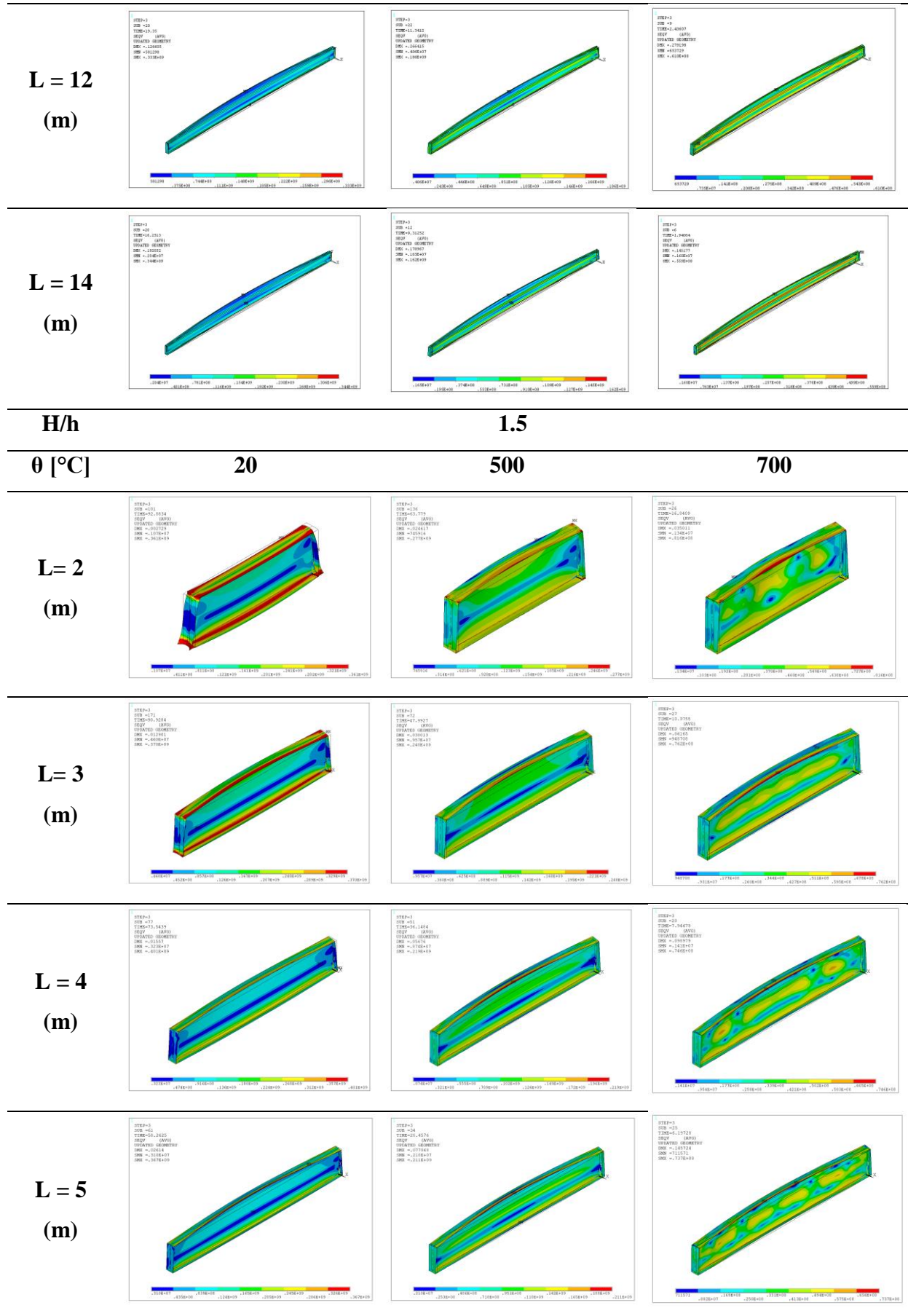
ANNEX B. Von mises stress distribution of steel beams - end moment load



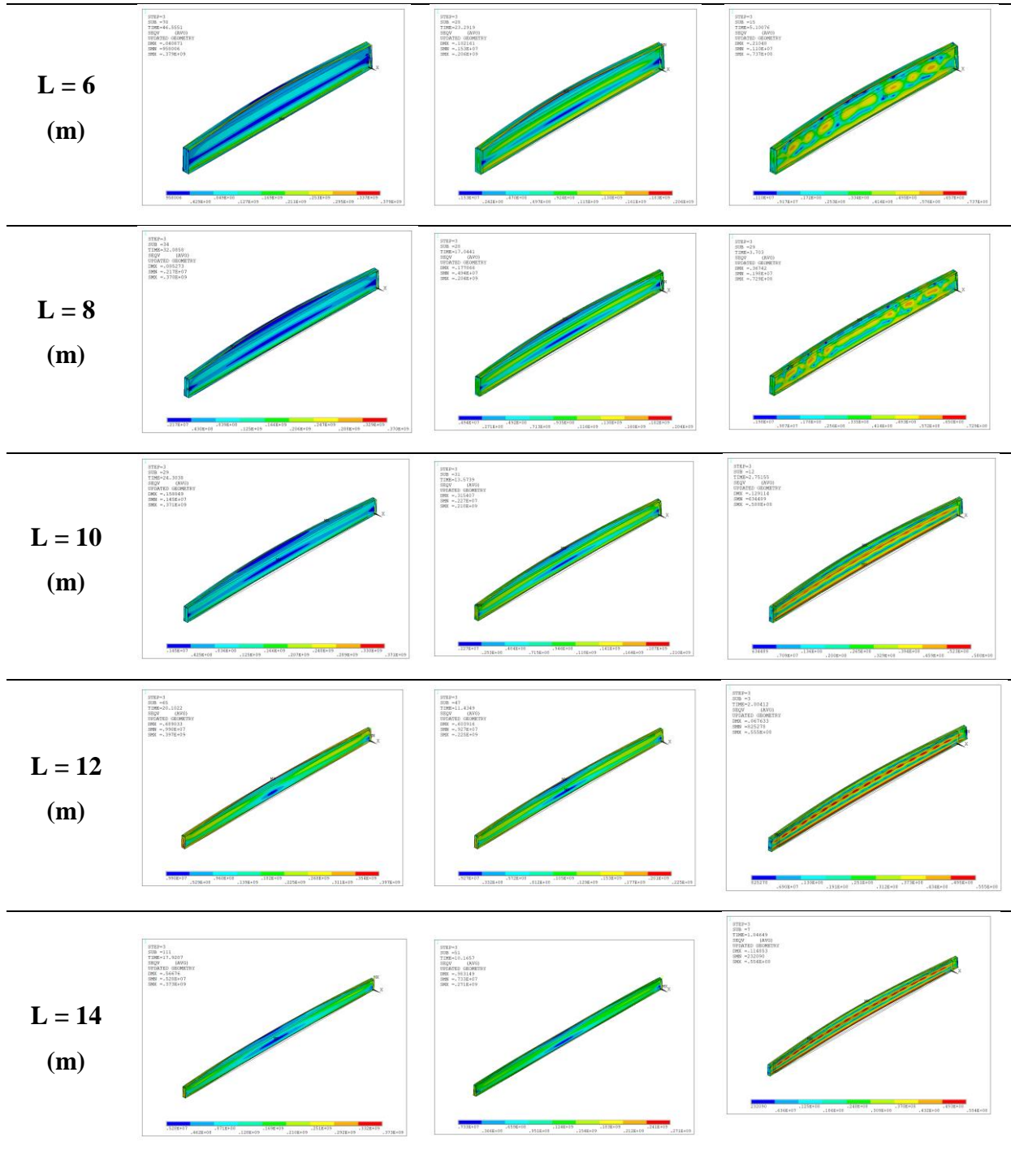
ANNEX B. Von mises stress distribution of steel beams - end moment load



ANNEX B. Von mises stress distribution of steel beams - end moment load

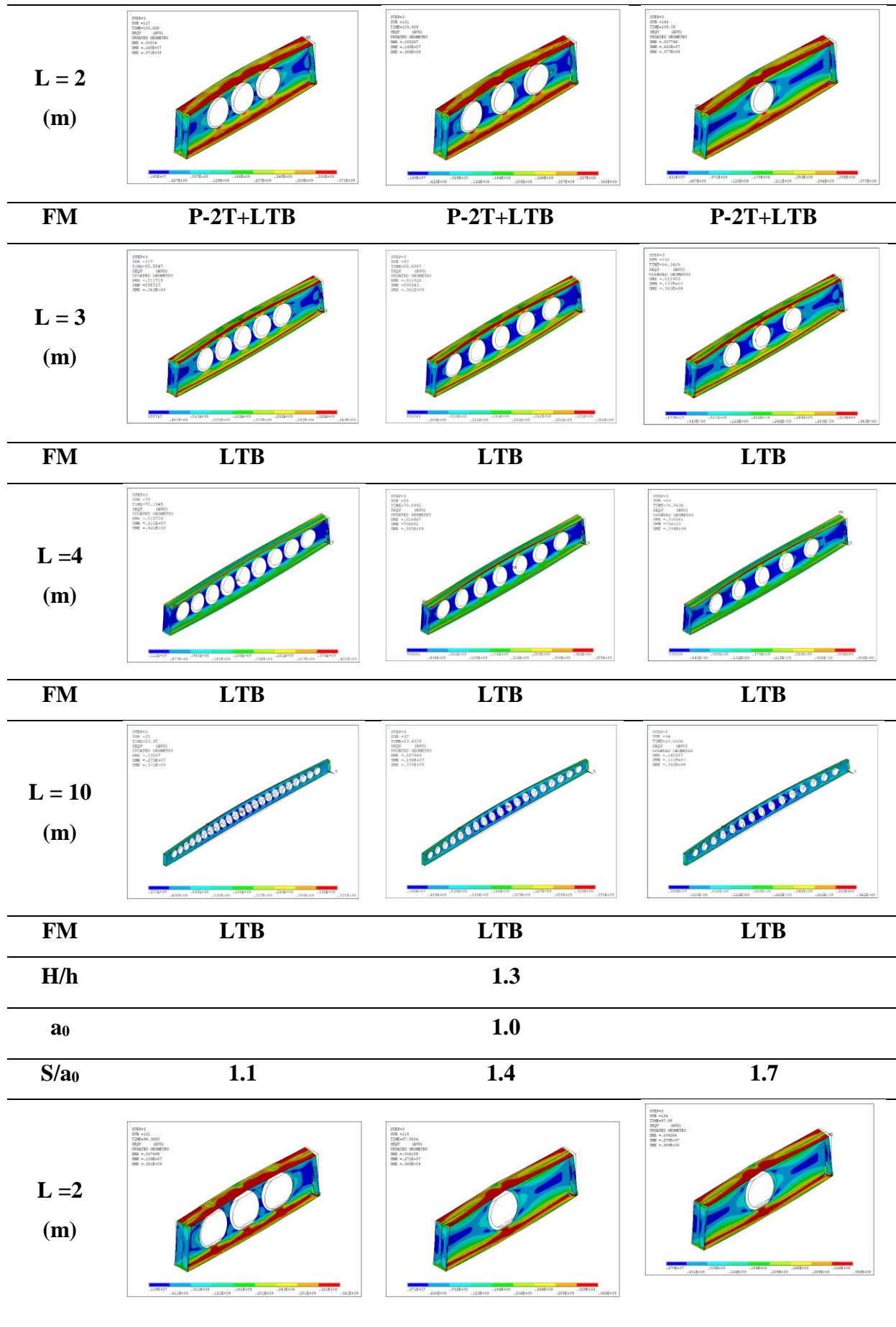


ANNEX B. Von mises stress distribution of steel beams - end moment load

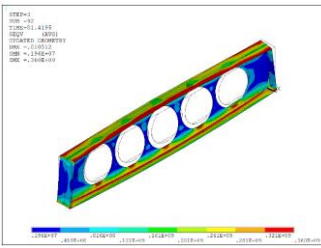
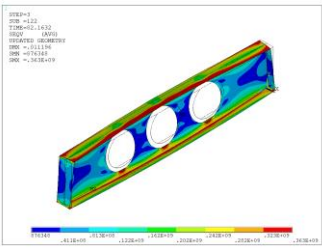
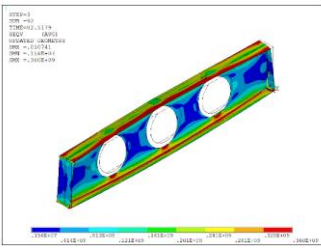
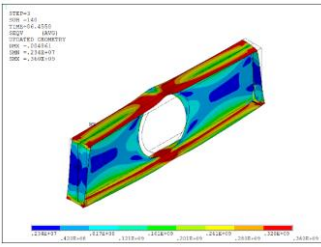
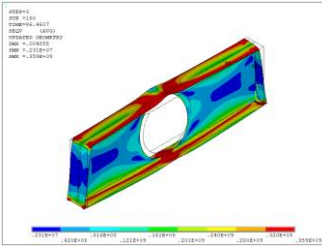
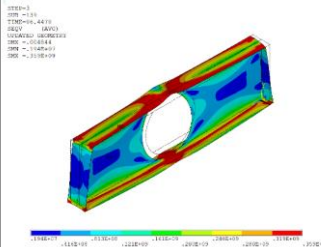
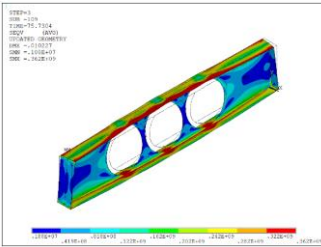
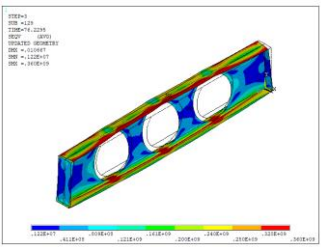
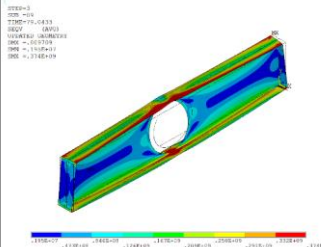
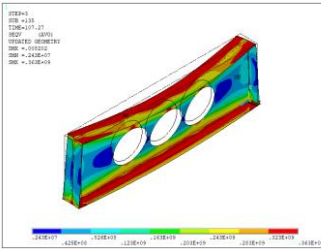
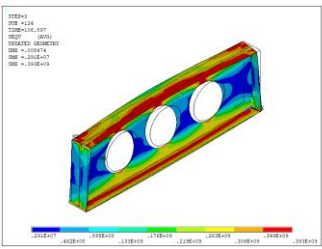
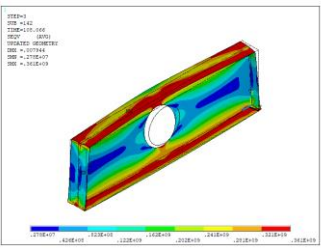


Beam type	CELLULAR BEAM		
θ (°C)	20		
H/h	1.3		
a0/h	0.8	1.0	1.2
S/a0	1.1	1.4	1.7

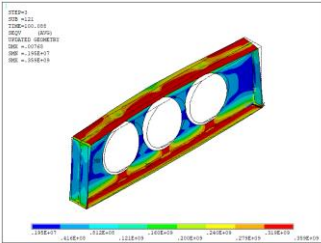
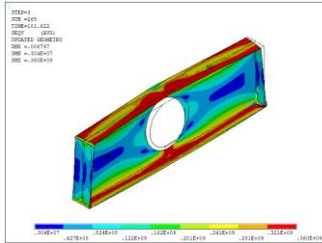
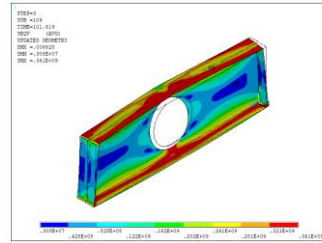
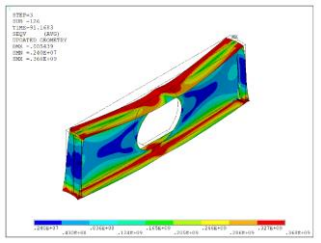
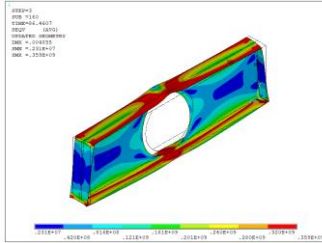
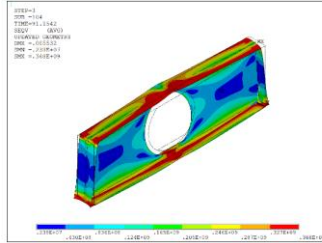
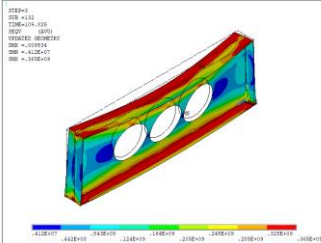
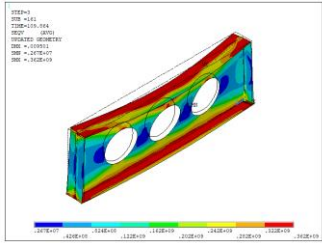
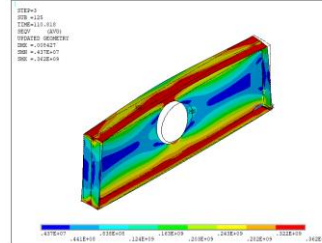
ANNEX B. Von mises stress distribution of steel beams - end moment load



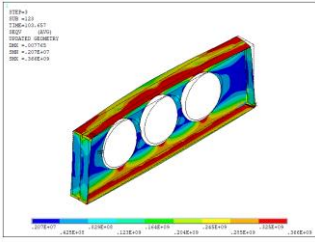
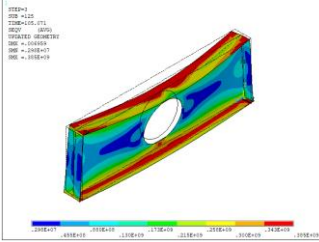
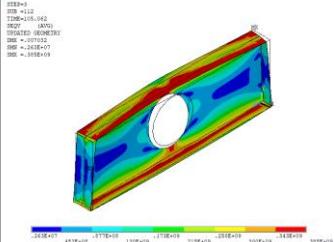
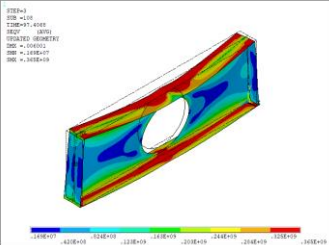
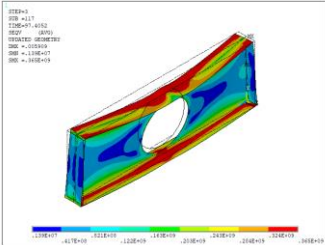
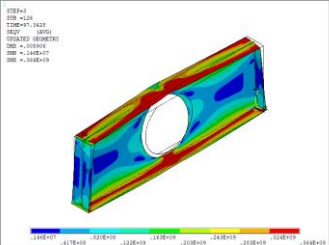
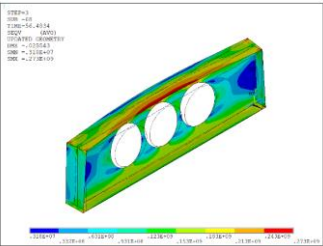
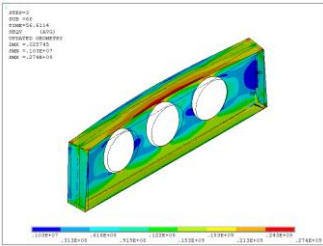
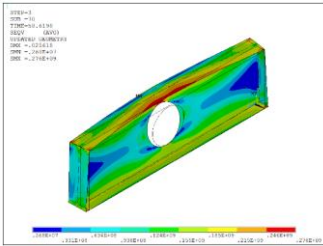
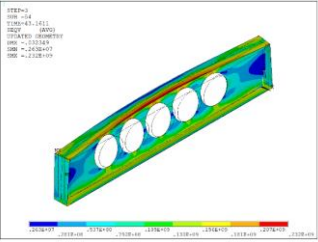
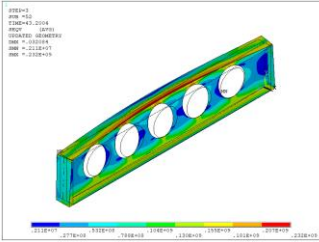
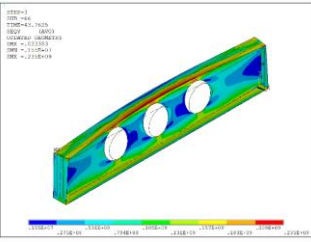
ANNEX B. Von mises stress distribution of steel beams - end moment load

FM	P-2T+LTB	P-2T+LTB	P-2T+LTB
L= 03 (m)			
FM	LTB+	LTB+	LTB+
H/h		1.3	
a ₀ /h		1.2	
S/a ₀	1.1	1.4	1.7
L = 2 (m)			
FM	LTB+P-2T	LTB+P-2T	LTB+P-2T
L = 3 (m)			
FM	LTB+	LTB+	LTB+
H/h		1.4	
a ₀ /h		0.8	
S/a ₀	1.1	1.4	1.7
L = 2 (m)			
FM	LTB+	LTB+	LTB+P-2T

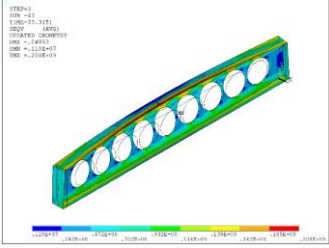
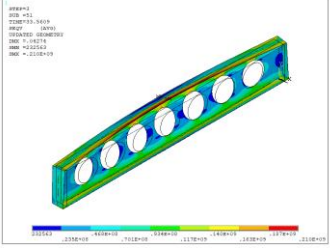
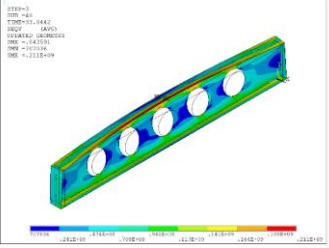
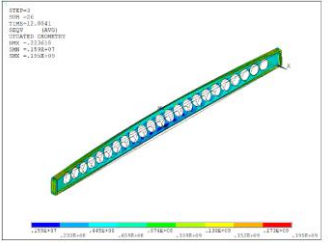
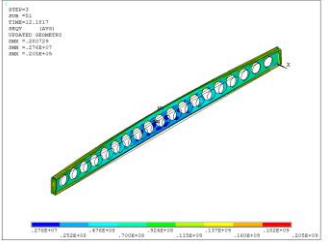
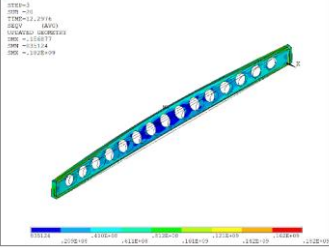
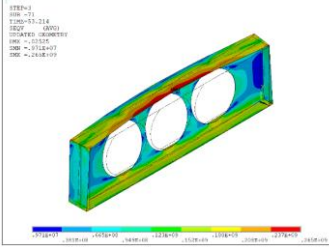
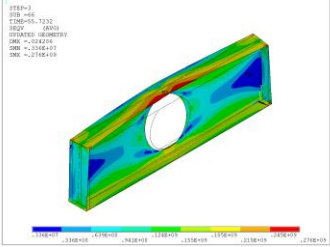
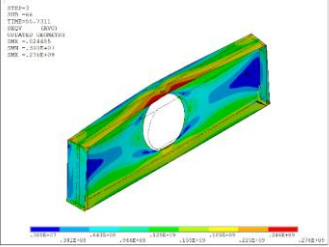
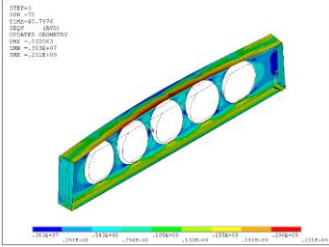
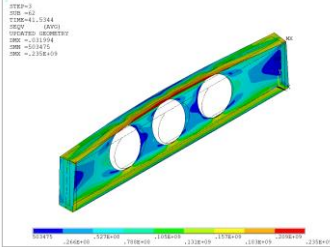
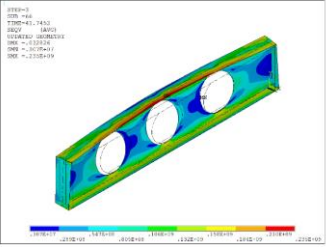
ANNEX B. Von mises stress distribution of steel beams - end moment load

H/h	1.4		
a₀/h	1.0		
S/a₀	1.1	1.4	1.7
L = 2 (m)			
FM	LTB+P-2T	LTB+P-2T	LTB+P-2T
H/h	1.4		
a₀/h	1.2		
S/a₀	1.1	1.4	1.7
L = 2(m)			
FM	LTB+P-2T	LTB+P-2T	LTB+P-2T
H/h	1.5		
a₀/h	0.8		
S/a₀	1.1	1.4	1.7
L=2 (m)			
FM	LTB+	LTB+	LTB+
H/h	1.5		
a₀/h	1.0		
S/a₀	1.1	1.4	1.7

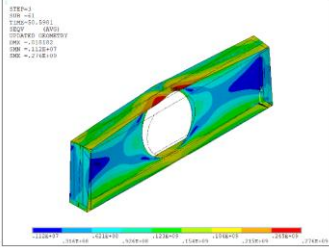
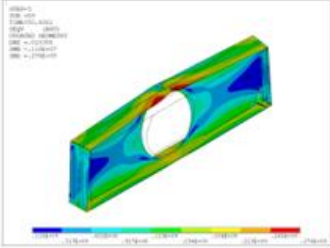
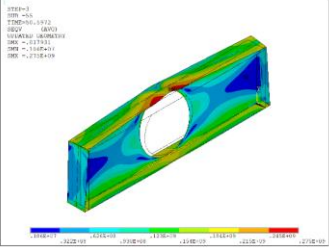
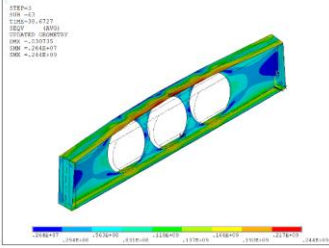
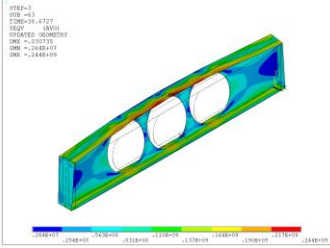
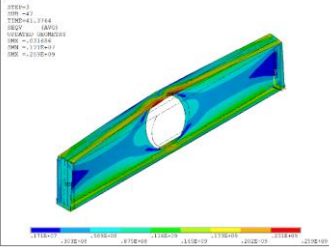
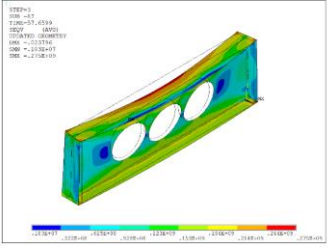
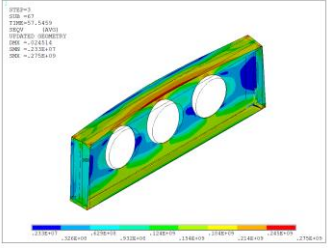
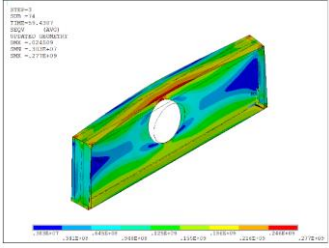
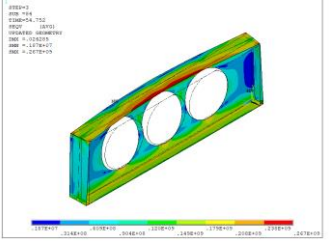
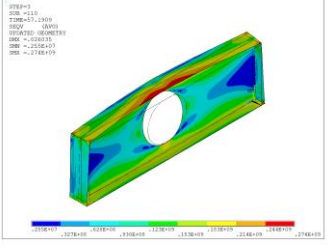
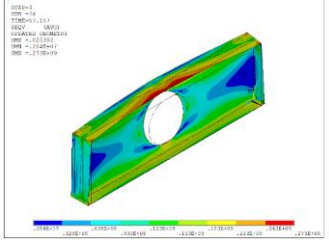
ANNEX B. Von mises stress distribution of steel beams - end moment load

<p>L = 2 (m)</p>				
	FM	LTB + P-2T	LTB + P-2T	LTB+ P-2T
	H/h		1.5	
a₀/h		1.2		
S/a₀	1.1		1.4	1.7
<p>L = 2 (m)</p>				
	FM	LTB+P-2T	LTB+P-2T	LTB+P-2T
	θ (°C)		500	
H/h		1.3		
a₀/h		0.8		
S/a₀	1.1		1.4	1.7
<p>L = 2 (m)</p>				
	FM	LTB	LTB	LTB
	L = 3 (m)			
FM	LTB	LTB	LTB	

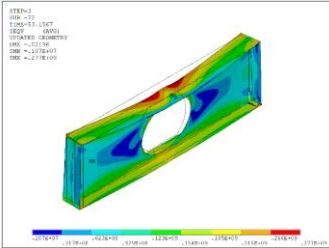
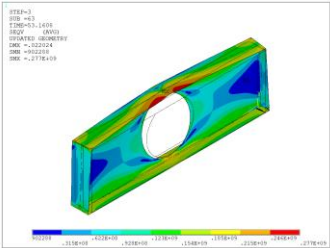
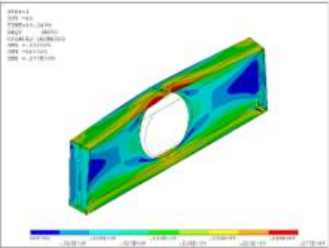
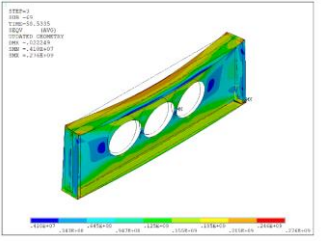
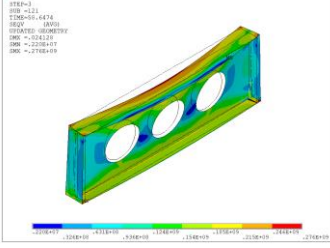
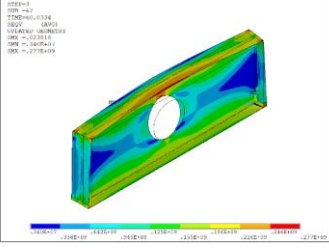
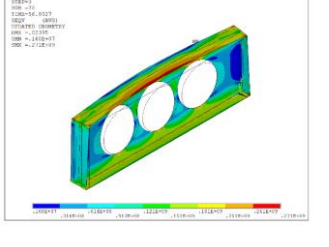
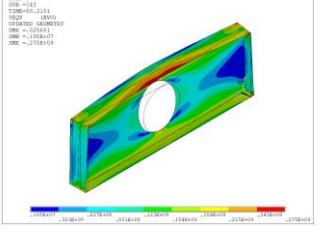
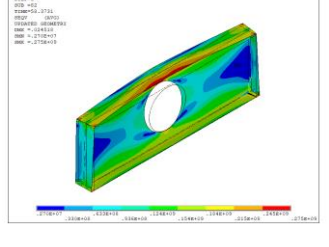
ANNEX B. Von mises stress distribution of steel beams - end moment load

L = 4 (m)			
	FM	LTB	LTB
	FM	LTB	LTB
L = 10 (m)			
	FM	LTB	LTB
	FM	LTB	LTB
H/h		1.3	
a₀/h		1.0	
S/a₀	1.1	1.4	1.7
L = 2 (m)			
	FM	LTB	LTB
	FM	LTB	LTB
L = 03 (m)			
	FM	LTB	LTB
	FM	LTB	LTB
H/h		1.3	
a₀/h		1.2	
S/a₀	1.1	1.4	1.7

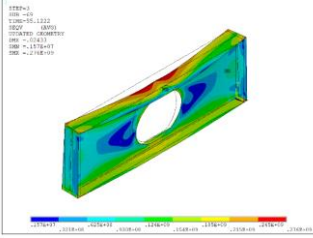
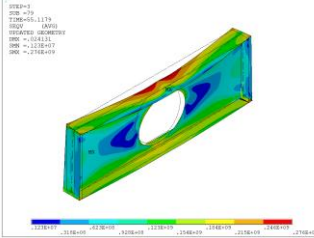
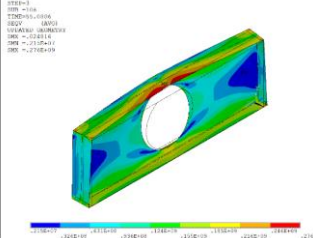
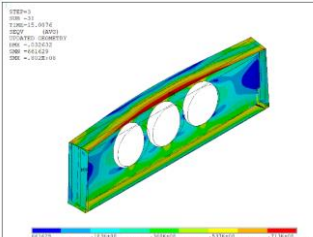
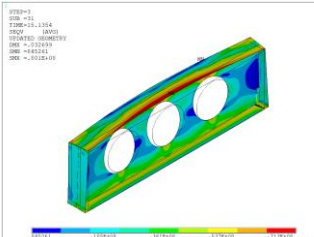
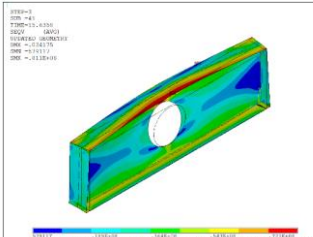
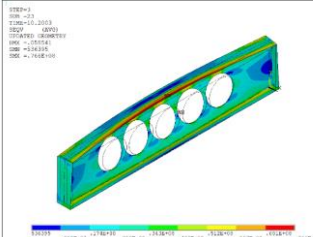
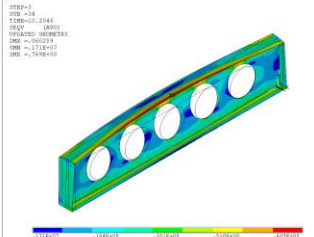
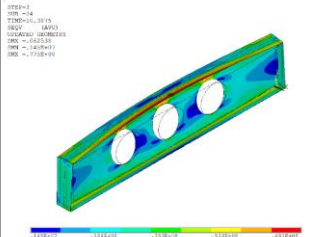
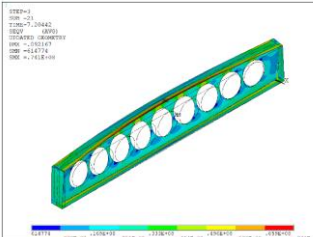
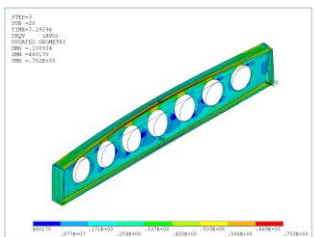
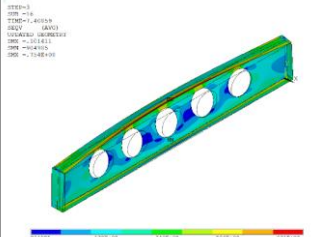
ANNEX B. Von mises stress distribution of steel beams - end moment load

L = 2 (m)				
	FM	LTB+	LTB+	LTB+
	L = 3 (m)			
FM		LTB	LTB	LTB+
H/h		1.4		
a₀/h	0.8			
S/a₀	1.1	1.4	1.7	
L = 2 (m)				
	FM	LTB+	LTB+P-2T	LTB+P-2T
	H/h	1.4		
a₀/h	1.0			
S/a₀	1.1	1.4	1.7	
L = 2 (m)				
	FM	LTB	LTB	LTB
	H/h	1.4		

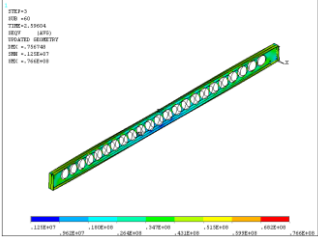
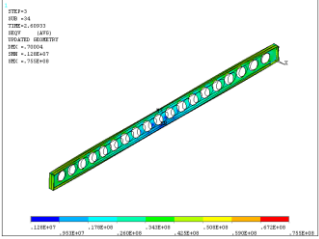
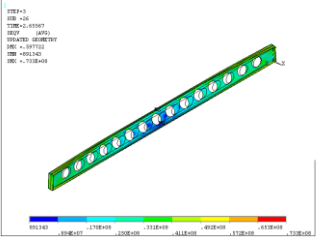
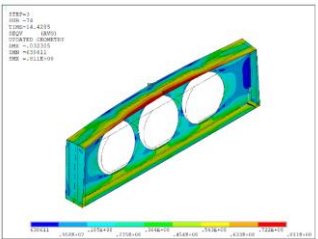
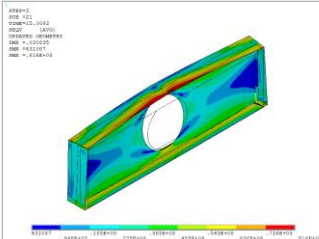
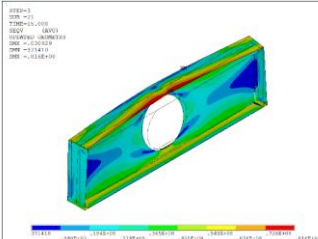
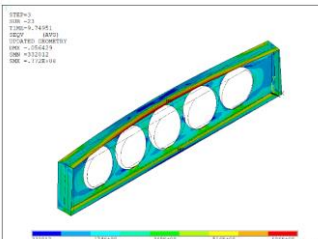
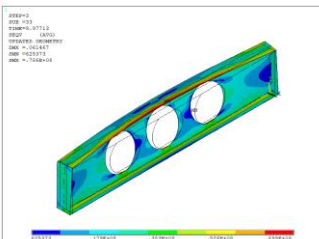
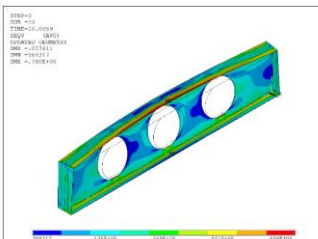
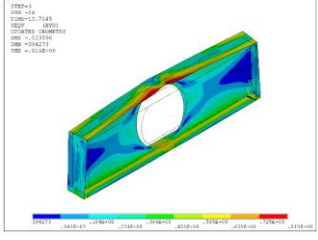
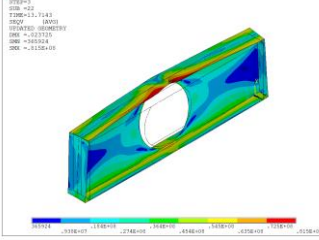
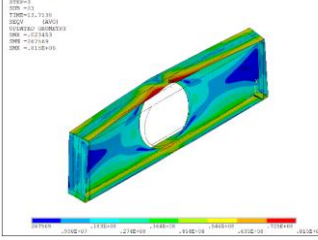
ANNEX B. Von mises stress distribution of steel beams - end moment load

a_0/h	1.2		
S/a_0	1.1	1.4	1.7
$L = 2$ (m)			
FM	LTB+	LTB+	LTB+
H/h	1.5		
a_0/h	0.8		
S/a_0	1.1	1.4	1.7
$L=2$ (m)			
FM	LTB+	LTB+	LTB+
H/h	1.5		
a_0/h	1.0		
S/a_0	1.1	1.4	1.7
$L = 2$ (m)			
FM	LTB	LTB	LTB
H/h	1.5		
a_0/h	1.2		
S/a_0	1.1	1.4	1.7

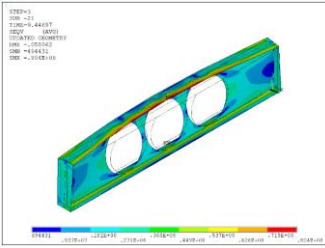
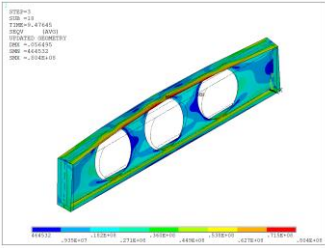
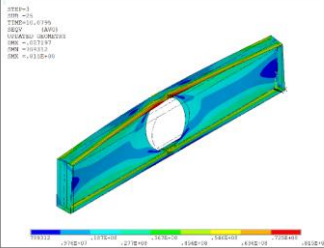
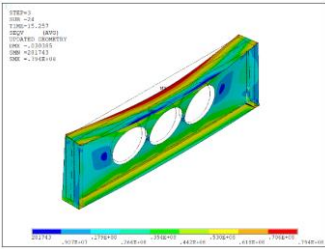
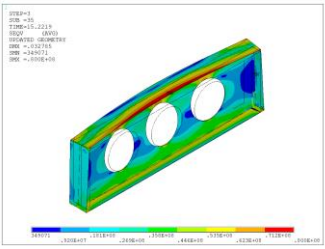
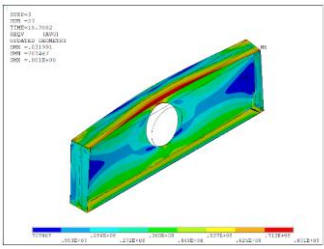
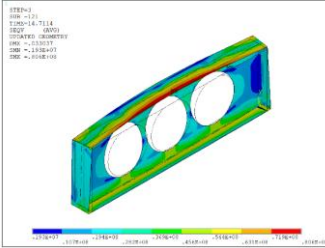
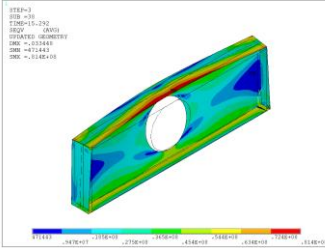
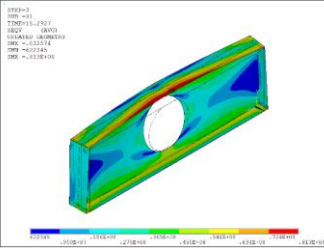
ANNEX B. Von mises stress distribution of steel beams - end moment load

<p>L = 2 (m)</p>				
	FM	LTB+	LTB+	LTB+
	θ (°C)	700		
H/h	1.3			
a₀/h	0.8			
S/a₀	1.1	1.4	1.7	
<p>L = 2 (m)</p>				
	FM	LTB	LTB	LTB
	θ (°C)	700		
H/h	1.3			
a₀/h	0.8			
S/a₀	1.1	1.4	1.7	
<p>L = 3 (m)</p>				
	FM	LTB	LTB	LTB
	θ (°C)	700		
H/h	1.3			
a₀/h	0.8			
S/a₀	1.1	1.4	1.7	
<p>L = 4 (m)</p>				
	FM	LTB	LTB	LTB
	θ (°C)	700		
H/h	1.3			
a₀/h	0.8			
S/a₀	1.1	1.4	1.7	

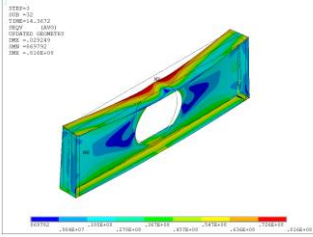
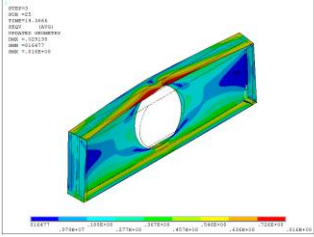
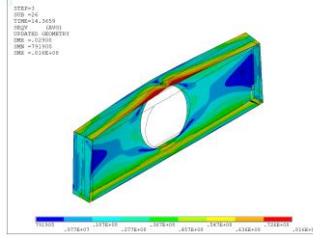
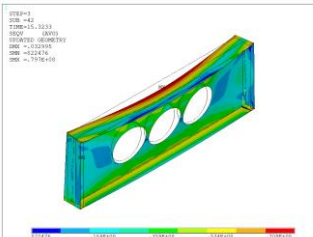
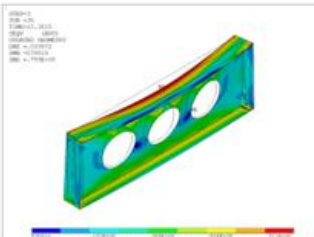
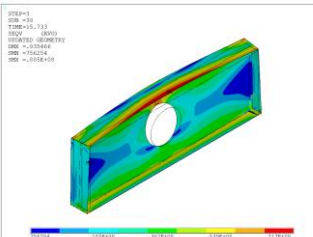
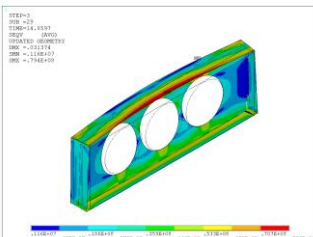
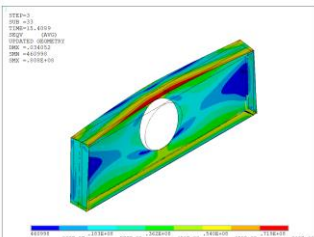
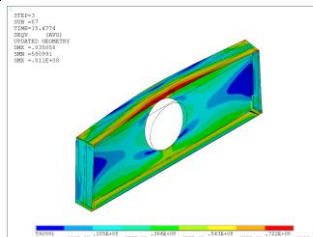
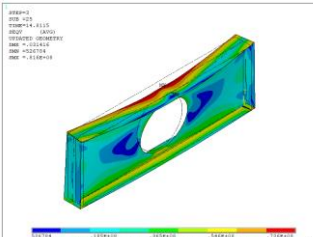
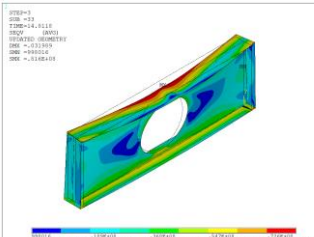
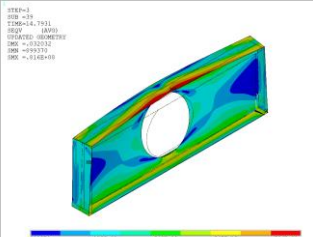
ANNEX B. Von mises stress distribution of steel beams - end moment load

L = 10 (m)			
FM	LTB	LTB	LTB
H/h	1.3		
a₀/h	1.0		
S/a₀	1.1	1.4	1.7
L = 2 (m)			
FM	LTB	LTB	LTB
L = 03 (m)			
FM	LTB	LTB	LTB
H/h	1.3		
a₀/h	1.2		
S/a₀	1.1	1.4	1.7
L = 2 (m)			
FM	LTB+	LTB+	LTB+

ANNEX B. Von mises stress distribution of steel beams - end moment load

L = 3 (m)			
	FM	LTB	LTB
	H/h		1.4
	a₀/h		0.8
	S/a₀	1.1	1.7
L = 2 (m)			
	FM	LTB+	LTB+
	H/h		1.4
	a₀/h		1.0
	S/a₀	1.1	1.7
L = 2 (m)			
	FM	LTB	LTB
	H/h		1.4
	a₀/h		1.2
	S/a₀	1.1	1.7

ANNEX B. Von mises stress distribution of steel beams - end moment load

L = 2 (m)				
	FM	LTB	LTB	LTB
	H/h		1.5	
	a₀/h		0.8	
	S/a₀	1.1	1.4	1.7
L=2 (m)				
	FM	LTB+	LTB+	LTB+
	H/h		1.5	
	a₀/h		1.0	
	S/a₀	1.1	1.4	1.7
L = 2 (m)				
	H/h		1.5	
	a₀/h		1.2	
	S/a₀	1.1	1.4	1.7
	L= 2 (m)			

ANNEX B. Von mises stress distribution of steel beams - end moment load

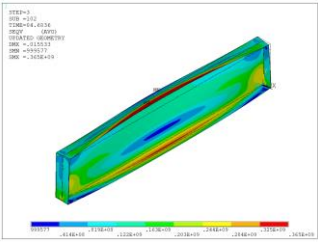
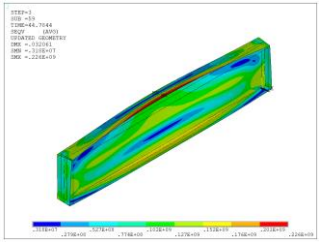
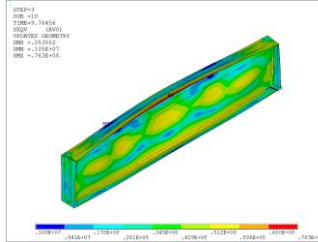
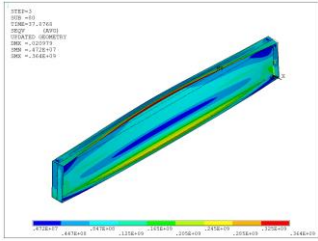
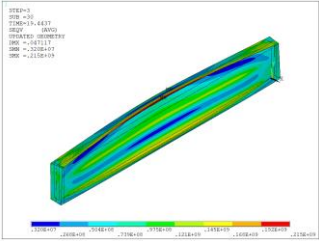
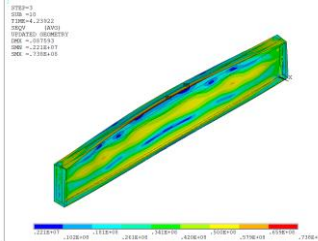
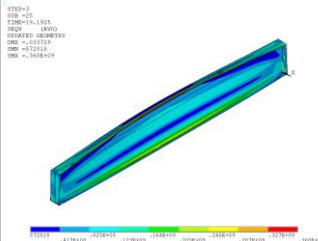
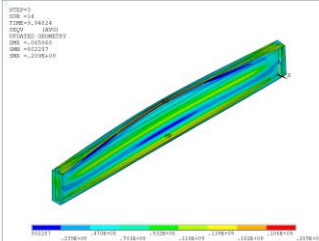
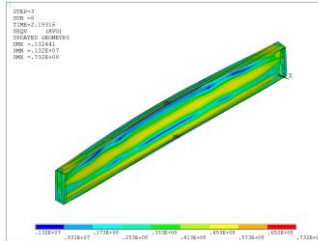
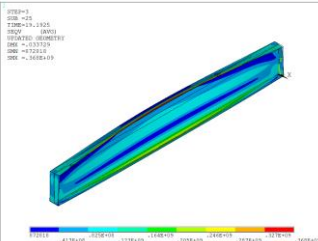
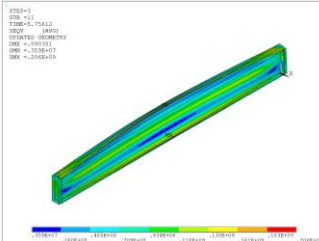
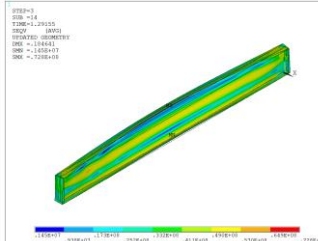
FM

LTB+

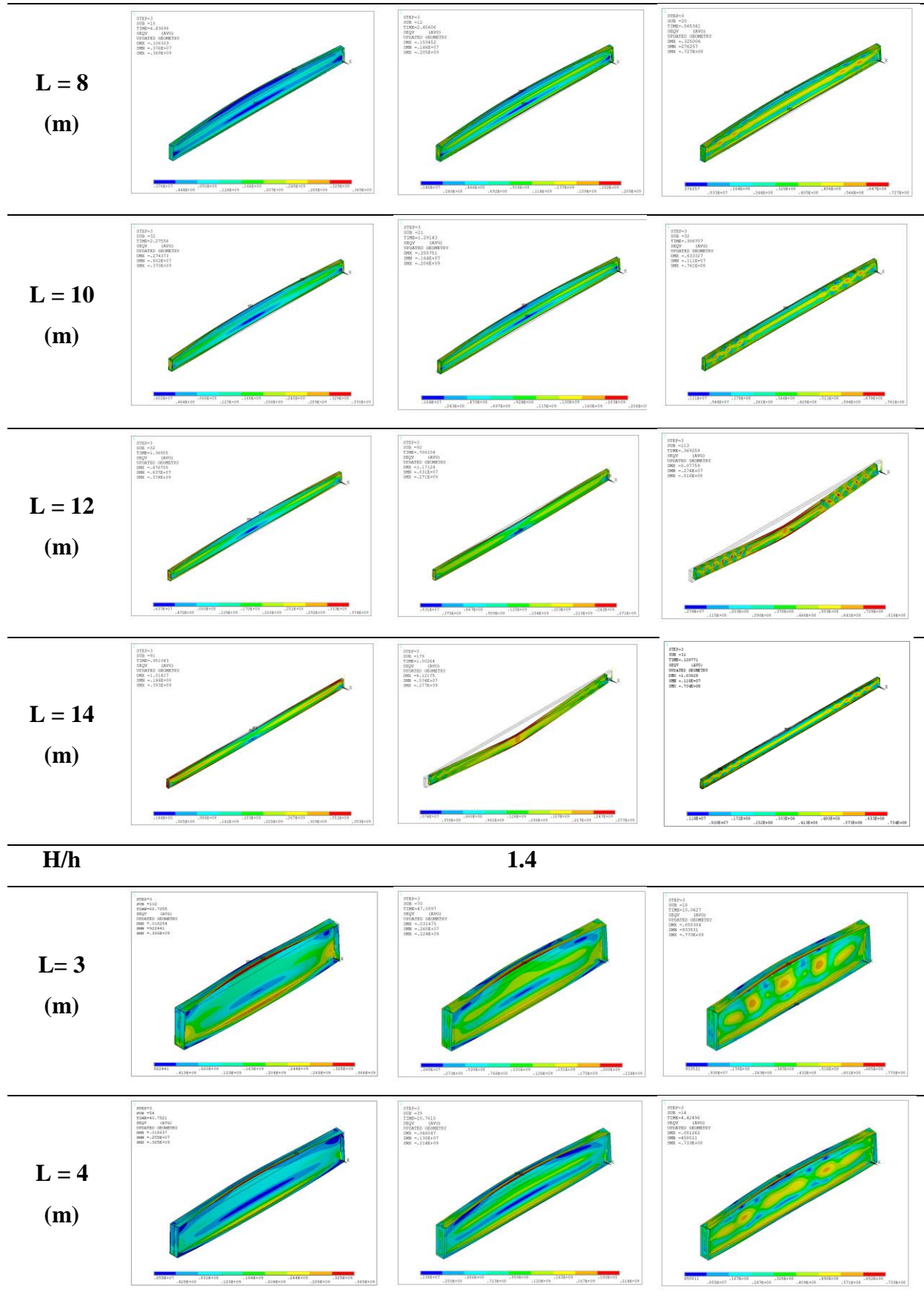
LTB+

LTB+

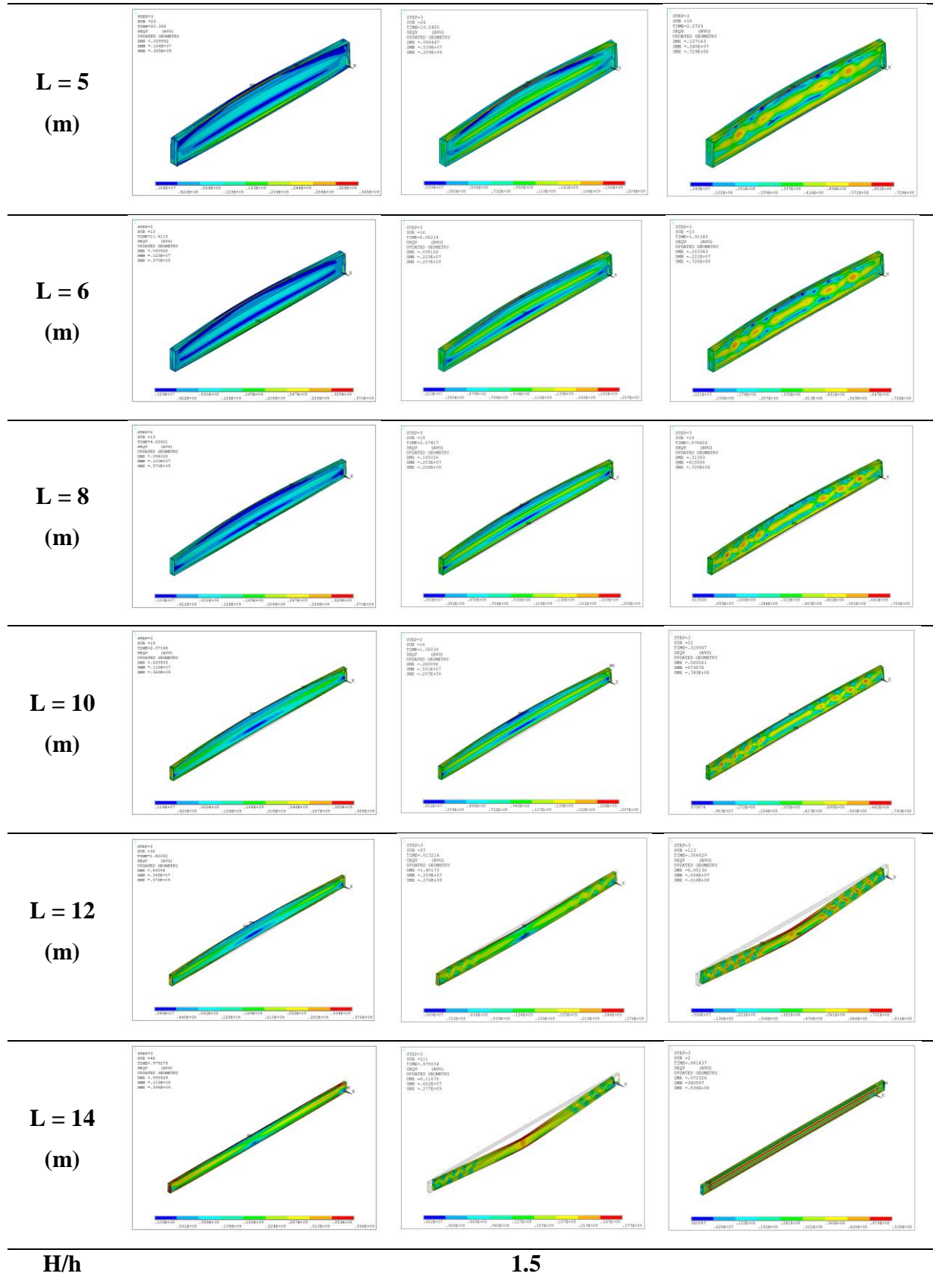
ANNEX C. Von mises stress distribution of solid beams - distributed load

Loading type	DISTRIBUTED LOAD		
H/h	1.3		
θ [°C]	20	500	700
L = 3 (m)			
L = 4 (m)			
L = 5 (m)			
L = 6 (m)			

ANNEX C. Von mises stress distribution of solid beams - distributed load



ANNEX C. Von mises stress distribution of solid beams - distributed load



ANNEX C. Von mises stress distribution of solid beams - distributed load

